Mechanisms and Kinetics of Atmospheric Sphalerite Oxidative and Non-Oxidative Leaching

by

Adriaan Johannes Henning

Thesis presented in fulfilment of the requirements for the Degree

of

MASTER OF ENGINEERING

(EXTRACTIVE METALLURGICAL ENGINEERING)

UNIVERSITEIT
iYUNIVESITHI
STELLENBOSCH
UNIVERSITY

in the Faculty of Engineering
at Stellenbosch University

1918·2018

Supervisor

Dr L. Auret

Co-Supervisor/s

Dr JDT Steyl

March 2018

Declaration

By submitting this thesis/dissertation electronically, I declare that the entirety of the work contained therein is my own, original work, that I am the sole author thereof (save to the extent explicitly otherwise stated), that reproduction and publication thereof by Stellenbosch University will not infringe any third-party rights and that I have not previously in its entirety or in part submitted it for obtaining any qualification.

March 2018

Abstract

A kinetic study of the non-oxidative and oxidative leaching of sphalerite concentrates, under elevated temperatures (75 – 95 °C) and atmospheric pressure is presented in this dissertation. Sphalerite, a zinc sulphide ore, is commonly associated with impurities and other sulphides (*i.e.* chalcopyrite, galena, pyrite etc.). The mineralogical nature of sphalerite concentrates is complex and the chemistry of iron-containing reactive systems is generally poorly understood, especially under aggressive hydrometallurgical conditions.

The aim of this work was the development of an engineering model capable of describing the rate and extent of sphalerite leaching in non-ferric and ferric containing systems. The mathematical framework presented in this thesis consists of various objectives, each addressing thermodynamic and kinetic aspects of the primary leach process. Comprehensive literature investigations are presented which constitutes the mechanisms and rate models, supplemented by phenomenological data obtained from batch experimentation.

The different objectives are each covered in a chapter of this dissertation, and include the following: i) a solution thermodynamic framework, ii) intrinsic oxidation mechanisms and rate expressions and iii) quantification and validation of the intrinsic rate expression.

Thermodynamic considerations provided a rigorous framework for the interpretation of the solution chemistry, with the explicit recognition of the important solution species. Speciation measurements from various literature sources were utilised to construct the Pitzer model for the various subsystems of the $ZnSO_4$ – $Fe_2(SO_4)_3$ – $FeSO_4$ – H_2SO_4 – H_2O system. The model gave accurate speciation trends up to concentrations of 1.5 M $ZnSO_4$, 1.5 M $FeSO_4$, 1.5 M $Fe_2(SO_4)_3$ and 2 M H_2SO_4. The model distinguishes between inner- and outer-sphere complexes, which was achieved through the inclusion of Raman spectroscopic stability constants. Contact ion pair (CIP) formations was predicted by the Pitzer model and shown results with suitable accuracy for the application in modelling the ionic aqueous solution relevant to this metallurgical kinetic study.

A detailed investigation into the electrochemical and mineralogical nature of natural sphalerite gave insights to the leaching mechanism. Iron impurity was found to be integral to sphalerites dissolution mechanism, with the electron exchange at the mineral surface limiting reaction rate. Polarization of sphalerite particle surface by the electrolytic solution caused surface states (barriers) that limits the rate of movement of charge carriers (i.e. electrons). A mechanism was proposed based on the assumption that the first electron or proton transfer step are the rate-

limiting step of the non-oxidative and oxidative leaching mechanism. The resulting electrochemical half reactions from the mechanism was used to define the activation polarisation relationships, the Butler-Volmer equations. Through application of the mixed potential theory of metallic corrosion, rate expression for the non-oxidative and oxidative leaching of sphalerite were derived.

Experimental batch data obtained from Dr JDT Steyl (1996) were used to quantify and validate the rate parameters of the derived rate expressions. The shrinking core model was applied within a batch reactor model to predict the leaching extents of sphalerite under various initial conditions. The rate parameter regression followed a two-fold strategy whereby the model was first linearized and regressed using a linear regression technique, and obtaining preliminary kinetic constants at average solution compositions. The second strategy consisted of a detailed differential batch reactor model including the solution speciation model and concentrate characteristics, which was used to quantify the intrinsic rate parameters using a non-linear regression technique.

A sphalerite leaching mechanism and intrinsic reaction rate model was proposed in this study and the model was quantified using phenomenological batch data. The model was found to be able to predict the leaching rate of sphalerite.

Opsomming

‘n Kinetiese studie van die nie-oksidatiewe en oksidatiewe loging van sfalerietkonsentraat, onderhewig aan verhewe temperatuur (75 – 95 °C) en atmosferiese druk, word in hierde proefskrif voorgelê. Sfaleriet, ’n sinksulfied erts, word tipies geassosieer met onsuiwerhede en ander sulfiede (m.a.w. chalkopiriet, galeniet, piriet, ens.). Die mineralogiese aard van sfalerietkonsentraat is kompleks, en die chemie van ysterbevattende reaktiewe stelsels word in die algemeen nie goed verstaan nie, veral nie onder aggressiewe hidrometallurgiese toestande nie.

Die doel van hierdie werk is die ontwikkeling van ’n ingenieursmodel wat in staat is om die snelheid en omvang van sfalerietloging in nie-femiese en femiese stelsels te beskryf. Die wiskundige raamwerk wat in hierdie proefskrip voorgelê word, bestaan uit verskeie doelwitte wat termodinamiese en kinetiese aspekte van die primêre logingsproses aanspreek.

Die verskillende doelwitte word elk in ’n hoofstuk van hierdie proefskrif aangespreek, en sluit die volgende in: i) ’n oplossing termodinamiese raamwerk, ii) intrinsieke oksidasiemeganismes en snelheiduitdrukkings en iii) kwantifisering en validering van die intrinsieke snelheiduitdrukking.

Termodinamiese oorwegings verskaf ‘n gestrenge raamwerk vir die interpretasie van die oplossingchemie, met die uitdruklike erkenning van die belangrike oplossingspesies. Spesiasie-metings van verskeie beskikbare literatuurbronne is gebruik om die Pitzermodel vir die verskeie substelsels van die $ZnSO_4$ – $Fe_2(SO_4)_3$ – $FeSO_4$ – H_2SO_4 – H_2O stelsel saam te stel. Die model verskaf akkurate spesiasietendense vir konsentrasies tot en met 1.5 M $ZnSO_4$, 1.5 M $FeSO_4$, 1.5 M $Fe_2(SO_4)_3$ en 2 M H_2SO_4. Die model onderskei tussen binne- en buitesfeerkomplekse, wat moontlik gemaak is deur die insluiting van Raman spektroskopiese stabiliteitkonstantes. Kontakioonpaar(KIP)-formasies is voorspel deur die Pitzermodel en toon resultate met genoegsame akkuraatheid vir toepassing in die modellering van die ionise wateroplossing relevant tot hierdie metallurgiese kinetiese studie.

’n Gedetailleerde ondersoek rakende die elektrochemiese en mineralogiese geaardheid van natuurlike sfaleriet het insigte verskaf oor die logingmeganisme. Ysteronsuiwerhede is gevind om integraal te wees tot die sfalerietontbindingmeganisme, met die elektronuitruil by die mineraaloppervlak wat dien as die beperkende reaksiesnelheid. Polarisering van die sfalerietpartikeloppervlak deur die elektrolietoplossing veroorsaak oppervlaktoestande (versperrings) wat die bewegingsnelheid van ladingdraers (m.a.w. elektrone) beperk. ’n

Meganisme is voorgestel gebaseer op die aanname dat die eerste elektron- of protonoordragstop dien as die snelheid-beperkende stap van die nie-oksidatiewe en oksidatiewe logingmeganisme. Die resultante elektrochemiese halfreaksies van hierdie meganisme is gebruik om die aktiveringpolariseringverwantskappe te beskryf deur middel van die Butler-Volmer vergelykings. Snelheiduitdrukkings vir die nie-oksidatiewe en oksidatiewe loging van sfaleriet is afgelei deur middel van die toepassing van gemengde-potensiaalteorie van metaalkorrosie.

Eksperimentele enkelladingdata verkry vanaf Dr JDT Steyl (1996) is gebruik om die snelheidparameters van die afgeleide snelheiduitdrukkings te kwantifiseer en te valideer. Die krimpende kernmodel is toegepas binne die enkelladingreaktormodel om die logingomvang van sfaleriet onder verskeie begintoestande te voorspel. Die snelheidparameterregressie het ’n tweedelige strategie gevolg, waar die model eerstens gelineariseer en geregresseer is deur middel van ’n lineêre regressietegniek, wat die voorlopige kinetiese konstantes vir gemiddelde oplossingsamestelling gelewer het. Die tweede strategie het bestaan uit ’n gedetailleerde differensiaal enkelladingreaktormodel (insluitende die oplossingspesiasiemodel en konsentraateienskappe) wat gebruik is om die intrinsieke snelheidparameters met ’n nie-lineêre regressietegniek te kwantifiseer.

’n Sfalerietlogingmeganisme en intrinsieke reaksiesnelheidmodel is in hierdie werk voorgestel en die model is gekwantifiseer deur middel van fenomenologiese enkelladingdata. Dit is gevind dat die model die logingsnelheid van sfaleriet kan voorspel.

Acknowledgements

I would like to express my sincere gratitude to several people for their support, assistance and fruitful discussions which helped to add this work to the knowledge of the world:

For the never-ending support and guidance, for always guiding with the gold thread in mind and especially for having lots of patience, thank you Doctor Lidia Auret

For technical and theoretical assistance, and most importantly for making this study possible by sharing hard earned exceptional data, thank you Doctor Johann du Toit Steyl

For financial assistance, a thanks to the General Electric Fellowship Fund, and Stellenbosch University merit bursary

A big tank you to Mintek for allowing the publication of data

I would like to thank my parents and family for all their support and love, which made this work possible.

Table of Contents

Chapter 1 Introduction

1.1 Background and Context

Sphalerite, a zinc sulphide mineral, is the most abundant source for zinc (Zn). The mineral is commonly associated with other sulphides (*i.e.* chalcopyrite, galena, pyrite etc.), in low quantity disseminated form. Impurities and relative proportions of metals contained within the ore are among the key factors which determine the processing route, *i.e.*, pyrometallurgical or hydrometallurgical processing techniques or combination of them. The main processing routes for zinc metal production are shown in Figure 1.1.

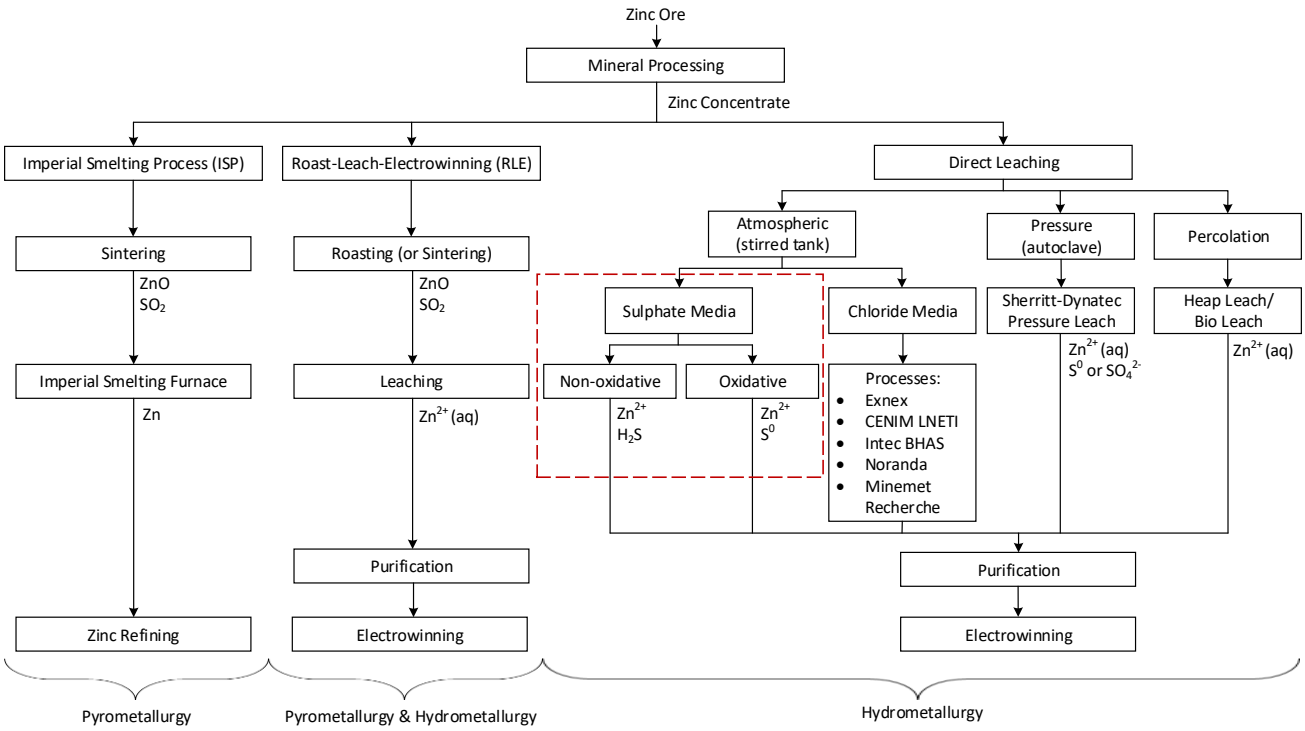

Figure 1.1: Overview of zinc sulphide concentrate processing routes adapted from Fuls and Petersen (2013) and Norgate and Rankin (2002). The area of interest to this project is highlighted.

Pyrometallurgical processing routes (*i.e.* imperial smelting process) have gradually lost their importance and are no longer used in most countries (European Commission, 2014). Imperial smelting (IS) processes reduces zinc ore into a purer metal slag in specially designed furnaces. The furnace typically operates at temperatures of 1000 °C at the surface to > 1500 °C in the centre. IS processes requires excessive energy input (International Zinc Association, 2011). However, pyrometalurgical kinetics are much faster compared to that of hydrometallurgical or hybrid processes. Therefore, greater throughputs could be achieved, but the cost of energy per ton of product is uneconomical and is environmentally unfriendly.

Hydrometallurgical processing routes accounts for approximately 90 % of the world's total zinc production (European Commission, 2014; International Zinc Association, 2011; Norgate & Rankin, 2002). Zinc ore, received from a mine, is concentrated into a high sphalerite containing concentrate. The ore is crushed and milled before being concentrated in flotation cells. The zinc concentrate (a concentrated matte of metallic sulphides) collected from the flotation section is then sent to either a roasting-leaching-electrowinning (RLE) or a direct leaching circuit within the base metal refinery (BMR).

The most common processing route is roasting-leaching-electrowinning (RLE). Roasting (or sintering) involves the oxidation of sphalerite into the more attractive leaching reagent, *e.g.* zinc-ferrous oxides or carbonates, by sparging oxygen-enriched air through a fluidised bed roaster (European Commission, 2014). Sulphide sulphur ($S^{2-}_{lattice}$) reacts with oxygen producing sulphur dioxide, which is sent to the acid plant to be converted to sulphuric acid. The zinc oxide product is then dissolved (leached) with sulphuric acid into an aqueous solution. The zinc rich solution is purified (*i.e.* removing impurities like iron, lead and copper) before being electrowon in a series of electrochemical cells. Metal oxide leaching has much faster kinetics compared to the direct leaching of the sulphide concentrate.

Direct leaching is a process in which zinc sulphide concentrates are leached without prior roasting (or sintering), followed by purification and electrolysis. The direct leaching processing route can be subdivided into three categories, namely percolation, pressure and atmospheric leaching. These processes have been used alongside existing RLE plants to increase zinc production (Fuls & Petersen, 2013). The Dynatec pressure leach, the Albion process and the Outotec atmospheric leach have been installed as standalone facilities.

In considering the percolation route two options are typically available, which are the Geocoat process from Geobiotics and heap bioleach. In the Geocoat process, zinc sulphide concentrate is coated on an inert substance before being stacked and leached in a sulphate medium. The heap bioleach option is aimed at processing the mined ore directly, and is highly dependent on comminution of the ore.

Pressurised leaching involves oxidation of zinc sulphide at temperatures of 150 °C in a sulphuric acid media. Oxygen is sparged into an autoclave to oxidise the sulphide or to regenerate ferrous (Fe^{2+}) to ferric (Fe^{3+}), where ferric may act as the primary oxidant of zinc sulphide. This is a mature technology with successful application at various sites in the gold, platinum, and base metal industries.

Atmospheric leaching can broadly be divided into two categories (based on the solution composition), *viz.* sulphate or chloride (Fuls & Petersen, 2013). The dissolution mechanism of sphalerite varies according the solution composition, which includes non-oxidative, oxidative and alkaline leaching. The leaching rate differs between sulphate and chloride media, with the physicochemical characteristic of the product layer formation being highly dependent of the chemical properties of the oxidant. Various atmospheric leaching processes in chloride media have been developed (see Figure 1.1), but due to the high corrosiveness and difficulties associated with handling and purification of chloride as well as the lack of application on commercial scale makes chloride leaching an inferior process compared to sulphate leaching.

To simplify the discussion of atmospheric leaching of a zinc sulphide concentrate in sulphate media, two conditions of operation is considered. Firstly, in a non-oxidative environment (no oxidant present in the solution); and secondly in an oxidative environment (one or more oxidants present in the solution). Non-oxidative processing involves the direct reaction with acid, where a proton (H^+) reacts with the sulphide to form hydrogen sulphide (H_2S) and a zinc ion (Zn^{2+}). Oxidative processing involves the reduction of ferric (Fe^{3+}) to ferrous (Fe^{2+}) and corresponding oxidation of sphalerite, with the release of Zn^{2+} into solution.

Atmospheric leaching typically operates at temperatures below 100 °C, albeit very close to 100 °C. Pure oxygen or oxygen-enriched air is injected into the stirred tank reactor to regenerate the ferrous to ferric. The success of atmospheric leaching processes is credited to the specially designed reactors that enhance the oxygen dispersion in the slurry and high height to diameter ratios to enhance oxygen solubility through increased hydrostatic pressure. A downside to atmospheric (or direct) leaching in general is that the elemental sulphur product forms a passivating layer around the sphalerite particles which prevents the reactants from reaching the surface reaction sites on the particle core. The kinetics of atmospheric leaching is also much slower in comparison to the pyrometallurgical processes and zinc oxide leaching (since no product are layers). Surfactants (*i.e.* ligosulphonates, sulphonic acid, etc.) are used to enhance the leaching rate and conversions by dispersing the elemental sulphur formed. On the upside, the products formed from direct leaching are more environmentally friendly in comparison to the other processing routes.

1.2 Environmental Impact

Zinc metallurgy has environmental problems such as the emissions of residual sulphur dioxide, acid waste water and release of metals such as lead, arsenic, mercury and cadmium (European Commission, 2014). In some cases, where zinc concentrates are leached with organics (*i.e.* organic surfactants added) it is required to treat organic pollutants according to environmental regulations. Sphalerite concentrates contain large quantities of iron, from which residues are generated (*i.e.* jarosite, goethite, haematite etc.) which must be discarded.

Most upcoming zinc processing plants tend to move away from the conventional RLE process where sulphur dioxide is produced, to elemental sulphur production which is easier to control (control of particulate and gaseous emissions to the atmosphere). A study of the alternative atmospheric direct leaching processing route of sphalerite by ferric is justified.

1.3 Available Data

During full-time employment at Mintek (1996-1999), Dr Johann Steyl undertook a part-time study to investigate the atmospheric leaching of sphalerite in acidic sulphate solutions. Experimental data of high quality were generated, but was never published. As of April 2015, Dr Leon Krüger, manager of the Hydrometallurgy Division at Mintek, formally accepted and authorised the use of the experimental data for this study (refer to Appendix I for formal acknowledgement).

The data consisted of various batch kinetic tests, only selected data (*i.e.* 35 non-oxidative and 129 oxidative batch experimental data, see appendix C, D, E and F; with associated particle and solution characterisation results) were used in this study. At selected time intervals a sample of the batch solution was taken and analysed *via* either atomic absorption spectroscopy (AAS) or atomic emission spectroscopy (AES) or calorimetric titrations to determine the composition. The standardised solutions for analysis were continually calibrated to ensure accurate measurements, and if variance was observed the solutions were freshly prepared and the respective batch experiments were repeated.

The feed concentrate particles were characterised by measuring selected properties. The particle size distribution (PSD) was measured by lased diffraction (Malvern MasterSizer 1000). Particle surface area of each size fraction was determined through the Brunaur-Emmett-Teller (BET) method by using a Micromeritics ASAP 2010 (accelerated surface area and porosimetry) Analyser System.

A chemical analysis was performed to determine the elemental composition of the concentrate by Inductive Coupled Plasma Optical Emission Spectroscopy (ICP-OES). While a bulk modal mineralogical analysis was conducted on the feed concentrate to determine the mineral phase distribution and composition, which include X-ray diffraction (XRD) modal techniques, electron-micro-probe-analysis (EMPA) and scanning electron microscope (SEM) analyses. Through combining these results, a detailed breakdown of the elemental distribution of every particle size fraction was calculated.

The experimental program was initiated to characterise sphalerite leaching under atmospheric non-oxidative and oxidative conditions, in terms of the following effects:

- Temperature
- Sulphuric acid concentration
- Various ferric-to-ferrous ratios (concentrations)
- Hydrogen sulphide sparging (at 1 % and 100 %)
- Particle size effects
- Slurry densities
- Surfactant concentrations (Lignosulphonate)

1.4 Project Elements

1.4.1 Research statement

A kinetic study of the non-oxidative and oxidative leaching behaviour of sphalerite, under various operating conditions with the addition of a surfactant.

Knowledge of the mechanisms and kinetics of dissolution is fundamental to industrial operations and facilitate in the analysis of the complex interactions associated with industrial processing options and economic viability thereof. This research project consist of investigating the atmospheric non-oxidative and oxidative dissolution of sphalerite, within the scope of the typical operating conditions of the zinc refining industry. The following terms are defined:

- Non-oxidative leaching refers to reactions that does not involve a change in valance state, *i.e.*, when then mineral is neither oxidised nor reduced.
- Oxidative leaching refers to reactions that does involve a change in valance state, which entails the oxidation of the mineral.
- Kinetic modelling refers to the mathematical expressions describing the rate (*i.e.* speed) of chemical reactions from the instantaneous bulk properties, which are intrinsic to the reaction mechanism proposed.

1.4.2 Scope of this study

Atmospheric leaching in sulphate medium signifies a complex hydrometallurgical system with many properties and unit operations (section 1.1). With the purpose of developing a comprehensive understanding of these systems' chemistry and a coherent kinetic expression able to predict the warranted behaviour under industrial conditions, the various process parameters need to be examined independently, while remaining cognisant of their inherent relationships associated with the leaching process.

The scope of this project is confined to the experimental data obtained and are summarised in Table 1.1. Note the ranges presented in Table 1.1 are the maximum and minimum values obtained from the batch experiments performed by Steyl (1999), which are given in Appendix C, D, E and F. These conditions will be narrowed (or refined) to capture the desired intrinsic kinetic expression that could predicted the leaching behaviour of sphalerite, yet would still reside within typical operating conditions found in industry.

Table 1.1: Range of bulk properties

Property	Range
Pressure	1 atmosphere
Temperature	50 – 90 °C
Ferric to Ferrous ratio	0.01 – 250
Sulphuric acid concentration	3 – 130 g/L
Slurry density	0.01 – 15 g/L
Surfactant	Lignosulphonate
Surfactant concentration	0 – 10 g/L

1.4.3 Study objectives

The ultimate engineering objective of this study is the development of a kinetic model to characterise the non-oxidative and oxidative leaching behaviour of sphalerite, under atmospheric pressure and various operating conditions with the addition of a surfactant. Such a model will enable enhanced simulation of process flowsheets to highlight key process elements or control feasibility. However, the development of such models is frequently limited by the level of understanding of the fundamental chemistry and ultimately restricts the predictive ability of these models. The predictive capability of kinetic models is also largely dependent on the underlying assumptions on which they are constructed.

Assumptions associated with the quantification of solution phase speciation and the related kinetic data are critical to the development in the case of this specific system. Specifically, with regards to solutions containing soluble iron species where there is a general lack in knowledge in their inherent chemistry, *i.e.*, thermodynamics and kinetic behaviour in an aqueous environment. Leaching under aggressive and concentrated conditions typically encountered in hydrometallurgical operations, would result in substantial speciation of solution complexes and may have a significant impact on the dissolution rate of sphalerite. The characterisation of solution speciation and assumptions regarding the chemistry as well as a detailed review of the relevant literature and acquired data form a central part of the study. The measured data of Steyl (1999) facilitate the development of a modelling framework for predicting sphalerite leaching kinetics in the case-study system.

The objectives of this study are:

1. To develop a self-consistent thermodynamic solution modelling framework of the various sub-systems applicable to the $ZnSO_4 – Fe_2(SO_4)_3 – FeSO_4 – H_2SO_4 – H_2O$ reactive system on which the kinetics of sphalerite leaching with Fe^{3+} and H^+ can be interpreted.
2. To derive intrinsic oxidation mechanism and rate expressions for the non-oxidative and oxidative leaching of sphalerite.
3. To verify the rate expressions for the leaching of the sphalerite concentrate and to quantify the rate parameters on a phenomenological level.

1.4.4 Thesis structure

Chapter 2 reviews the basic theories of thermodynamic (solution) and kinetic modelling, physicochemical properties impacting the mechanism, the fundamental anodic (mineral) dissolution and cathodic (oxidant) reduction mechanism (*i.e.* electrochemical nature of sulphide mineral oxidation) as well as providing an overview of the rate analysis techniques.

Chapter 3 gives an overview of the experimental procedure and analysis methodology.

Chapter 4 presents an investigation into the thermodynamics (solution complexation) of the various sub-systems applicable to this study. Experimentally verified species from the literature were considered and the development of a systematic multi-component Pitzer model was performed that captured the solution chemistry effectively.

Chapter 5 summarises the relevant literature in context of the sphalerite leaching process at elevated temperatures and atmospheric pressure, in terms of the physiochemical nature of the kinetic process and detailed sphalerite crystalline facets. The interaction of the most relevant ionic solution species (oxidants) with sphalerite surface was also described. On the basis of the literature findings, reaction mechanisms are proposed and rate expression derived.

Chapter 6 characterises the concentrate used during the experimental tests, specifically analysing the particle's size and composition. A brief background on the origin and classification of the different particle size fractions is also presented.

Chapter 7 extends the proposed reaction mechanism and rate expression in Chapter 5 to the thermodynamic basis developed in Chapter 4 for the kinetic modelling of the non-oxidative and oxidative leaching of ZnS. Confidence of the experimental data was established, including the identification of the prominent reaction regimes. The intrinsic rate expression parameters were quantified by the response to bulk property changes from the experimental data. The intrinsic reaction rate was then validated by predicting testing ("unseen") data.

Chapter 8 closes with the relevant conclusions for the three objectives stated previously and highlights the most important findings. Further recommendations are also provided.

Figure 1.2 illustrates where the objectives are achieved throughout this project:

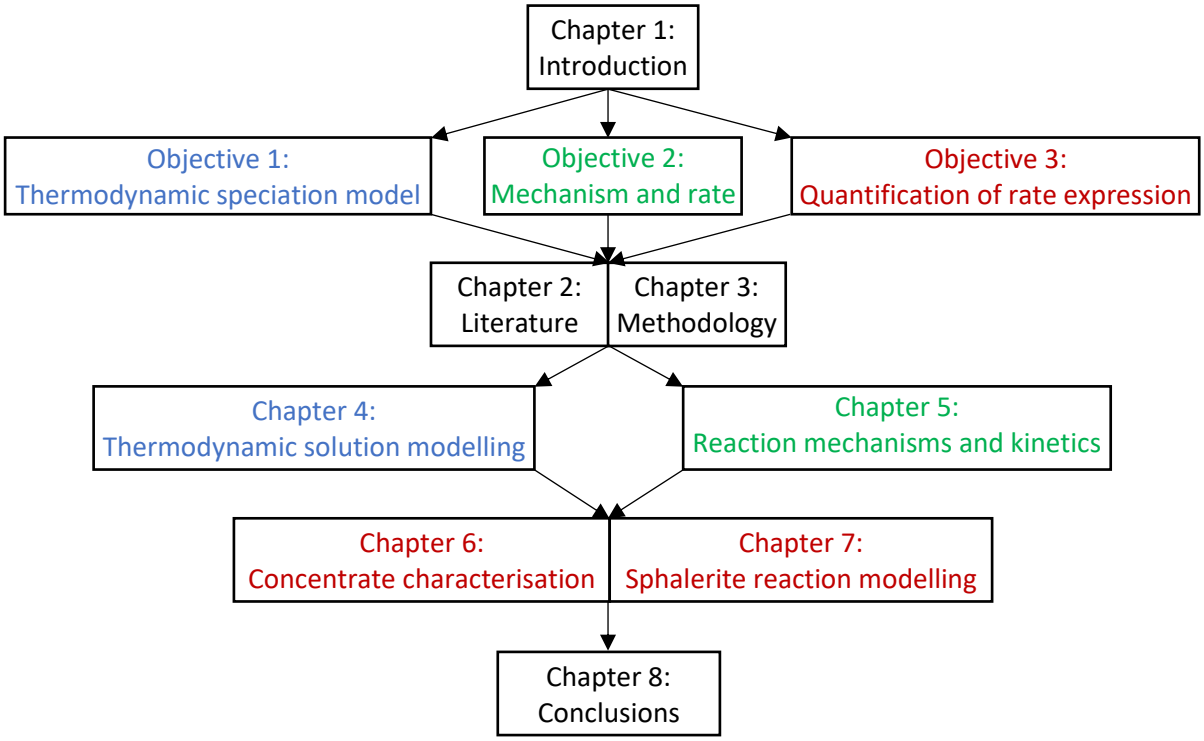

Figure 1.2: Overview of report structure and objectives highlighted

Chapter 2 Literature Review

2.1 Solution thermodynamics

Knowledge of aqueous zinc sulphate solution characteristics at elevated temperatures and pressures forms an integral part of modelling speciation and mass transport equilibria during the hydrometallurgical processing of zinc. Throughout several decades various researchers have studied the association of sulphate with aqueous cations (*e.g.* Zn^{2+}). The key concepts involving thermodynamics and electrolyte solution chemistry, used in this work, are gathered from the two recent studies of Biley (2015) and Steyl (2012).

2.1.1 Inner and outer sphere complexes

The first concept from an electrolytic solution chemistry perspective involves the association of ions to contact ion pairs (CIP) as described in reaction 2.1. Importantly, on the left side of reaction 2.1 the ions are completely dissociated, while a direct chemical bond between the metal and ligand exists within the CIP on the right side of the reaction.

$$M_{aq}^{m+} + X_{aq}^{x-} \rightleftharpoons MX_{aq}^{(m-x)} \qquad 2.1$$

As a result, the free ions and CIP exhibit different chemical behaviour. In reality, according to the relaxation measurements of Eigen and Tamm (1962b), reaction 2.1 occurs in a stepwise association mechanism as follows (Eigen & Tamm, 1962a; Hefter, 2006):

$$\underset{free\ ions}{M_{(aq)}^{m+} + X_{(aq)}^{x-}} \rightleftharpoons \underset{2SIP}{M^{m+}(H_2O)(H_2O)X^{x-}} \rightleftharpoons \underset{SIP}{M^{m+}(H_2O)X^{x-}} \rightleftharpoons \underset{CIP}{MX_{(aq)}^{(m-x)}} \qquad 2.2$$

This stepwise mechanism occurs by the progressive expulsion of water through doubly-separated (2SIP) and singly-separated (SIP) outer-sphere complexes from the free hydrated ions to the contact or inner-sphere ion pairs (CIP) and vice versa.

Traditional thermodynamic analysis of the complexation reactions results in equilibrium constants (or known as dissociation constants) that includes all contributions from 2SIP's, SIP's and CIP's. Certain techniques, such as Raman spectroscopy, detect only the formed CIP's (where a chemical bond exist). As a result, equilibrium constants derived from Raman spectroscopy are not comparable to those measured from techniques that include the outer-sphere complex formations, see Hefter (2006) and Rudolph et al. (1999a) for definitions and descriptions of association constants.

Knowledge of the inner- and outer-sphere may be of importance for certain applications, however, for kinetic processes the formation of contact ion pairs can generally be considered of most importance (Biley, 2015). Kinetic studies of complex electrolyte systems often assume that the effects of outer-sphere complexes are captured in the behaviour of the dissociated ions, *i.e.* included in the electrostatic and short-range interaction terms of the free ions (Biley, 2015; Liu & Papangelakis, 2005a; Steyl, 2012). The implication of complex formation and assumptions from previous researchers on this work are:

1. The formation of inner-sphere complexes (CIP's) are acknowledged and the ions captured within the CIP are assumed to be inert during chemical reaction.
2. Ions in outer-sphere complexes (2SIP and SIP) are assumed to behave like the free hydrated ions in solution and can participate during a chemical reaction.
3. The equilibrium constants, Raman spectroscopy association constants, adopted from Biley (2015) and Steyl (2012) describe the distribution between CIP's and combined free ions (hydrated ions, 2SIP and SIP).

2.1.2 Basic thermodynamic principles

The Gibbs free energy is a key principle in chemical thermodynamics. Enthalpy (H) and entropy (S) of a specific system are related to the Gibbs free energy (G) via the well-known thermodynamic relationship (where T is temperature):

$$G = H - TS \tag{2.3}$$

Of greater importance is the partial molar Gibbs free energy (*i.e.* the chemical potential of a component in a system, μ_i^0), which is mathematically expressed by the partial derivative of the total Gibbs free energy with respect to the amount of component x_i. As with all thermodynamic properties, a reference state is required and the ideal chemical potential can be shown to be equal to:

$$\mu_i^{id} = \mu_i^0 + RT\ln(x_i) \tag{2.4}$$

Real systems, however, consist of non-idealities due to interactions among various components. This is incorporated into the chemical potential by an excess function (Smith *et al.*, 2005). In general terms, all the chemical potentials of the components, in their respective phases, within a system determine the equilibrium state of that system. Since matter always transitions spontaneously from a high chemical potential to a low chemical potential, the point of equilibrium lies thus at a state where all the chemical potentials are equivalent.

To determine the equilibrium point of a specific system, knowledge of the standard state and excess contributions to the chemical potentials are required. These concepts are further developed, specifically for the case of aqueous chemical thermodynamics.

2.1.3 Definition of the equilibrium constant

Mass-action expressions are employed to account for chemical equilibria between dissociated ions and complexes (equation 2.5), as well as species in another phase. Each mass-action equation is accompanied by an equilibrium constant, typically defined as the ratio of concentrations of the associated species. These equilibrium constants are readily measured by traditional thermodynamic means (*i.e.* potentiometry, calorimetry etc.) and extrapolated to zero ionic strength, to give the standard state thermodynamic equilibrium constant, K_j^0. However, these measured equilibrium constants vary with the solution ionic strength, temperature and pressure. Thus, activities are used to capture the variation in *apparent* species concentrations and facilitate the calculation of the thermodynamic equilibrium constant by equation 2.6.

$$M_{aq}^{m+} + X_{aq}^{x-} \rightleftharpoons MX_{aq}^{(m-x)+} \tag{2.5}$$

$$K_{j,T,P}^{o} = \frac{a_{MX_{aq}^{(m-x)+}}}{a_{M_{aq}^{m+}} \cdot a_{X_{aq}^{x-}}} = \frac{m_{MX_{aq}^{(m-x)+}}}{m_{M_{aq}^{m+}} \cdot m_{X_{aq}^{x-}}} \cdot \frac{\gamma_{MX_{aq}^{(m-x)+}}}{\gamma_{M_{aq}^{m+}} \cdot \gamma_{X_{aq}^{x-}}} = K_{j,T,P}^{C} \cdot \Gamma_{j,T,P} \tag{2.6}$$

Where a_i is the activity, m_i the molality (mol/kg) and γ_i the activity coefficient of the respective species i. The equilibrium constant, of reaction j, $K_{j,T,P}^{o}$ is calculated as the product of the concentration equilibrium constant $K_{j,T,P}^{C}$ and the activity quotient $\Gamma_{j,T,P}$. If equilibrium is approached from an association perspective (*i.e.* complex formation), either a step-wise (equation 2.7) or cumulative (equation 2.8) description may be used:

$$MX_{n-1} + X \rightleftharpoons MX_n \tag{2.7}$$

$$M + nX \rightleftharpoons MX_n \tag{2.8}$$

The thermodynamic association constant (denoted by 0) at the thermodynamic transcendent condition of infinite dilution for the step-wise (K°) and cumulative (β°) reaction may then be represented as follows, respectively (Steyl, 2009):

$$K_n^0 = \frac{a_{MX_n}}{a_{MX_{n-1}} \cdot a_X} = \frac{m_{MX_n}}{m_{MX_{n-1}} \cdot m_X} \cdot \frac{\gamma_{MX_n}}{\gamma_{MX_{n-1}} \cdot \gamma_X} = K_n \cdot \frac{\gamma_{MX_n}}{\gamma_{MX_{n-1}} \cdot \gamma_X} \tag{2.9}$$

$$\beta_n^0 = \frac{a_{MX_n}}{a_M \cdot a_X^n} = \frac{m_{MX_n}}{m_M \cdot m_X^n} \cdot \frac{\gamma_{MX_n}}{\gamma_M \cdot \gamma_X^n} = \beta_n \cdot \frac{\gamma_{MX_n}}{\gamma_M \cdot \gamma_X^n} \tag{2.10}$$

Lastly, the equilibrium constant is directly related to the partial molar Gibbs free energy (equation 2.11), of which the activity coefficients describe the excess Gibbs energy contribution.

$$K^{o}_{j,T,P} = \exp\left(-\frac{\Delta \bar{G}^{0}_{j,T,P}}{RT}\right) \qquad 2.11$$

Knowledge of the equilibrium constant and activity coefficients facilitates the calculation of the concentration of the dissociated and associated ions in solution.

2.1.4 Activity

Activity coefficients, introduced above, attempt to describe the apparent solution concentration and account for non-idealities in an electrolyte system, which is related to the excess partial molar free energy of species i:

$$\mu_i^{ex} = RT \ln \gamma_i \qquad 2.12$$

The activity and corresponding partial Gibbs free energy of component i, is calculated by combining equation 2.4 and 2.12:

$$\mu_i = \mu^{id} + \mu^{ex} = \mu^0 + RT \ln \gamma_i = \mu^0 + RT \ln a_i \qquad 2.13$$

These thermodynamic equations have been presented in molal basis (mol solute/kg solvent). This scale is preferred over the mole fraction basis that tends to result in unnecessary complicated models and the volume basis due to its independence on temperature and pressure.

Common practice is to select a standard state for the electrolyte system at $m^0 = 1\ mol/kg$, ideal, hypothetical solution with $\gamma = 1$, and is adopted throughout this work , see Biley (2015) and Steyl (2012). Thus, given the reference potential and activities of the species within solution, knowledge of the change of these quantities would allow the equilibrium state to be solved.

Thermodynamic models are used to set up a framework in which thermodynamic properties can be regressed with experimental data. Various methods, such as freezing point dispersion, boiling point elevation, electromotive force (e.m.f.) of cells, isopiestic measurement (osmotic coefficient) etc., are used to correlate electrolytic solution thermodynamics. However, individual ion activity coefficient cannot be measured, since individual ions cannot be isolated during measurements and electroneutrality limitations. For a salt, $M_m X_x$, the mean activity coefficient, which can be experimentally measured, is defined in equation 2.14.

$$\gamma_{\pm} = (\gamma_M^m \cdot \gamma_X^x)^{\frac{1}{m+x}} \quad 2.14$$

This phenomenon constrains most thermodynamic models, especially those that consider complex formation, as the individual ion activity coefficients are merely convenient representations that are, at best, thermodynamically feasible.

Water activity, a_w, and osmotic coefficient, ϕ, are calculated by the following well known equation via experimental methods which involve measurement of the water vapour pressure:

$$\ln \frac{p_w}{p_w^0} = \ln a_w = -\frac{MW_w}{1000} \phi \sum_i m_i \quad 2.15$$

The fraction of water vapour pressure measured in an electrolyte system to that of pure water is represented as p_w/p_w^0 and ϕ is the osmotic coefficient. Notably, the osmotic coefficient depends on the sum of all the solute molalities.

Lastly the thermodynamics of water as solvent are summarised in the following two derivatives, where the osmotic coefficient (resembling activity) and the activity coefficient of water are directly related to the excess partial molar Gibbs free energy contribution of the system:

$$\phi - 1 = -\frac{[\partial G^{ex}/\partial n_w]_{n_w}}{RT \sum_i m_i} \quad 2.16$$

$$\ln \gamma_w = \left[\frac{\partial G^{ex}/n_w RT}{\partial m_i}\right]_{n_w} \quad 2.17$$

2.1.5 Solution modelling

Broadly there are three types of solution modelling classes which vary in their treatment of the electrolyte entities (Biley, 2015):

1. No electrolyte dissociation occurs (*i.e.* only contact ion pairs exist in the solution), which is typically found to be applicable at high temperature systems (> 300 °C).
2. Complete dissociation of electrolyte (*i.e.* only free hydrate ions), which is valid for very dilute systems.
3. Speciation-type models, which include complexation equilibria (*i.e.* both free ions and contact ion pairs)

There are numerous models that characterise the activity coefficient in electrolyte solutions. Although most of these models have strict limitations, to either dilute solutions (< 0.1 mol/kg) or limited to the experimental data on which the model was regressed. The interactions between solution species with increasing ionic strength can significantly alter the activity coefficients from electrostatic effects and estimations by models become more difficult.

The selection of an appropriate model framework for concentrate electrolyte solutions is often selected arbitrarily and from their prevalence in commercially available simulation packages. Common means of accounting for activity coefficients involves the extended Debye-Hückel models, but are usually limited to low ionic strengths, typically below 0.1 mol/kg. The mixed-solvent electrolyte (MSE) model has received significant attention, which is attributed to the inclusion of explicit solvent effects as well as successful modelling of a wide number of systems and form part the basis of the OLI systems software package (Liu & Papangelakis, 2005b; Wang *et al.*, 2004) .

The complete discussion of the development of activity coefficient modelling theory and selection of the best suited model for this work, while important for understanding the advantages and short-coming of the various models, is not central to the objectives of this study. Hence, the methods and results presented by Biley (2015) and Steyl (2012), that highlighted several benefits of using the Pitzer model, are adopted into this work. The application and validation of the Pitzer model, to the zinc-iron-acid electrolyte system, is shown in Chapter 4.

2.1.6 Pitzer model

The Pitzer model is a linear combination of parameters, of a virial expansion of the excess Gibbs free energy, which characterizes interactions amongst ions and solvents. The most basic form of the Pitzer model is:

$$\frac{G^{ex}}{n_w RT} = f(I) + \sum_i \sum_j m_i m_j \lambda_{ij}(I) + \sum_i \sum_j \sum_k m_i m_j m_k \mu_{ijk} + \cdots \qquad 2.18$$

where, $f(I)$ is a function of the long range electrostatic interactions amongst ions in solution, λ_{ij} is a binary interaction coefficient between species i and j, and μ_{ijk} is a ternary interaction coefficient between species i, j and k.

Some of the important benefits of the Pitzer modelling framework are:

- Interaction parameters as well as the virial-coefficients structure (seen in equation 2.18) are theoretically meaningful, *i.e.* formulated from the fundamental statistical-mechanical theory of electrolyte systems.
- The excess Gibbs free energy is defined, opposed to other activity coefficient models that characterise the activity coefficients directly and make the calculation of the water activity difficult (through the excess Gibbs free energy and the definition thereof). Forms of the derivatives by equations 2.16 and 2.17, makes the calculation of the activity coefficients and osmotic coefficient (water activity) possible. Thus, water activity data can be used to calibrate or enhance the calibration of the model.
- The Pitzer model has shown to predict electrolyte systems successfully up to concentrations of 6 mol/kg, although there are exceptions (Pitzer, 1991).

Several important limitations of the Pitzer model are listed below:

- The model is usually limited to the ternary interactions among the anion-cation pairs, ignoring the higher-order interactions, due to limitations and sensitivity during regression of the model parameters.
- The model is semi-empirical. It does however facilitate extrapolation outside the regions of calibration, but this must be performed with caution.
- The model does not have an inherit dependence on temperature. Inclusion of the effect of temperature can be linear or fixed within a temperature range. Equation 2.19 presents such dependency, where $T_{ref} = 298.15\ K$ and $n < 2$.

$$Par_{Pitzer}(T) = \sum_{i=1}^{n} p_{i-1}\left(T - T_{ref}\right)^{i-1} \qquad 2.19$$

- Some model parameters, *e.g.* the b parameter in the Pitzer-Debye-Huckel term, have no fundamental significance and is solely empirical.

Considering the benefits and short-comings, the model is overall beneficial for the modelling of hydrometallurgical solutions. The Pitzer model was chosen to predict the behaviour of the electrolyte solution of this study, based on the work done by Biley (2015) and Steyl (2012). A well-defined description of the ferric-ferrous aqueous system with sulfuric acid and other metal cations (*i.e.* Zn^{2+}) was presented by them, and is adopted in this study. Refer to these studies and those of Pitzer (1973), Bea et al. (2010) , Burkin (2001), Horvath (1985) and Zemaitis et al. (1986) for the mathematical description of the Pitzer model (see appendix A.4)

2.2 Conventional reaction kinetics

This section presents a broad overview of the intrinsic rate limiting steps during a heterogeneous chemical reaction process. A heterogeneous reaction occurs at a plane (or interface) between two distinct phases (*i.e.* liquid and solid). From a bulk perspective, reaction 2.20 symbolises the solid-liquid reaction occurring.

$$\nu_A A_{(aq)} + \nu_B B_{(s)} \rightleftharpoons \nu_R R_{(aq)} + \nu_P P_{(s)} \qquad 2.20$$

2.1.1 Kinetic expressions

A heterogeneous system can involve various transportation, chemical adsorption and reaction steps. Nine steps occurring in succession (see Figure 2.1) during a leaching process are identified for the three phase reactor of which any one or more of the steps can control the overall reaction rate (Fogler, 2001; Levenspiel, 1999; Missen *et al.*, 1999):

1. Transfer of the gaseous reagent into the liquid phase
2. Transport of reactants from the bulk fluid to the solid interface (film diffusion)
3. Inter and intra-particle transport (diffusion) of the reactant trough the porous particle or solid product phase to the reacting surface
4. Absorption of reactant on reacting surface
5. Surface chemical reaction (transfer of electrons or ions)
6. Desorption of products from particle surface
7. Transport (diffusion) of product through the porous particle or solid product phase to the particle interface
8. Product transportation (film diffusion) into the bulk fluid
9. Transfer of the liquid product into the gas phase

These steps are not absolute and can be included or excluded depending on the conditions of the system, but it clarifies the mass-action during solid-liquid transitions.

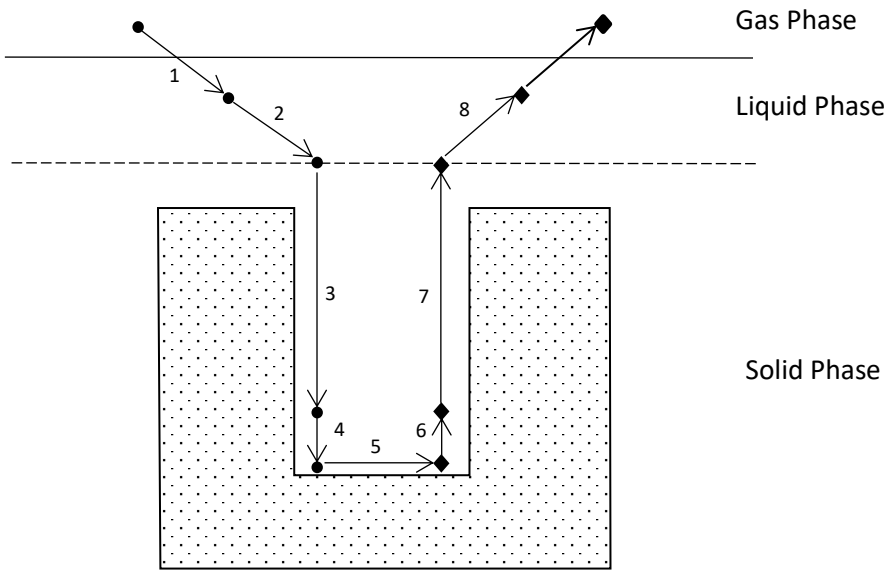

Figure 2.1: Schematic representation of typical transport and reaction scenario of reactants and products during a three-phase system of which any step can be rate limiting

- Gas-Liquid Mass Transfer Model (step 1 and 9)

The rate of mass transfer from the gaseous phase to the liquid phase is dependent on various factors (*i.e.* gas flow rate, bubble size, mixing intensity, reactor configuration, composition and physical properties of both liquid and gas phase). Fick's first law, for equal molar counter diffusion, describes the flux of molecular diffusion through a homogeneous phase:

$$\mathrm{J_i} = -\mathrm{D_i}\frac{\partial \mathrm{C_i}}{\partial \mathrm{x}} \qquad 2.21$$

The molecular flux (J_i) is dependent on the concentration profile ($\partial C_i/\partial x$) multiplied by a diffusivity constant (D_i), averaging the system conditions of component i transfer through the phase. Within different phases, the chemical potential of a component differs which creates a concentration profile at the solid-liquid interface. The two-film model postulates the existence of stagnant gas and liquid films, and describes the rate of transfer of a component by a very simple expression (equation 2.22). The following assumptions are made during the derivation of the two-film model (Missen *et al.*, 1999):

1. The two-film model is a pseudo-steady-state model (*i.e.* the concentration profiles are established instantaneously and remain unchanged).
2. The transport of component i through the stagnant gas film is by molecular diffusion, approximated by a linear concentration profile.

3. Similarly, the transport of component i through the liquid film is by molecular diffusion, approximated by a linear concentration profile.
4. Equilibrium is continually established at the interface, assuming that there is no resistance to mass transfer over the interface.

$$N_i = k_L a(C_i^* - C_i) \qquad 2.22$$

The molar transfer rate (N_i) is dependent on the mass transfer coefficient (k_L), interfacial area per unit volume (a) (*i.e.* average bubble area), the concentration of dissolved component i in the bulk liquid (C_i) and at equilibrium (C_i^*) under the system conditions. In practice it is difficult to determine the exact value of k_L and a independently, and is usually approximated by empirical correlations.

- Film Diffusion Model (step 2 and 8)

Mass transfer in an electrolytic solution is dependent on the movement of mobile ionic species, material balances, current flow, electro-neutrality, and fluid mechanics (Newman & Thomas-Alyea, 2004). The flux density of each dissolved species is described by equation 2.23.

$$\underset{\text{Flux}}{\mathbf{J}_\mathrm{i}} = \underset{\text{migration}}{-\mathrm{z_i u_i F C_i \nabla \Phi}} \underset{\text{diffusion}}{- \mathrm{D_i \nabla C_i}} \underset{\text{convection}}{+ \mathrm{C_i \mathbf{v}}} \qquad 2.23$$

The flux density ($\boldsymbol{J}_i$) of species i, expressed in $mole.m^{-2}.s^{-1}$, is a vector quantity indicating the direction in which the species are moving over an area oriented perpendicular to the flow of the species. The terms on the right side of equation 2.23 represents the three mechanisms describing mass transfer of species in an electrolytic solution in contact with a solid.

The migration term describes the motion of charged species (*i.e.* z_i is the number of proton charges carried by an ion) within in an electric field ($-\nabla\Phi$). This migration term is peculiar to electrochemical systems (leaching), and the quantities (*i.e.* the mobility, u_i, denotes the average velocity of species in the solution by a force of 1 N/mol, independent of the origin of the force) are not easily and directly measurable in a liquid solution. The last two terms in equation 2.23 are the conventional terms to describe molecular movement in non-electrolytic systems. The diffusion term describes the movement of species from regions of high concentration (activity) to regions of lower concentration (activity) due to chemical potential. Lastly, the convection term describes the movement of species due to the motion of the fluid (*i.e.* velocity profiles of fluid motion over a solid surface, laminar or turbulent layers) with the bulk velocity ($\boldsymbol{v}$).

- Product “ash” Diffusion Model (step 3 and 7)

From a molecular viewpoint, diffusion inside a porous particle may occur by molecular, Knudsen and/or surface modes (Missen *et al.*, 1999). Molecular diffusion is the result of molecular collisions in the void space (pores) of the particle. Knudsen diffusion is the result of molecular collisions with the walls of the pores. Knudsen diffusion is negligible in liquid systems, because the mean free path of molecules in the liquid state is very small (*i.e.* the free path for liquids is typically near the diameter of the molecule itself). Surface diffusion results from the migration of adsorbed species along the surface of the pore (*i.e.* migration due to a gradient in surface concentration).

Practically it is near impossible to predict the pore structure of a particles, because the properties of the product “ash” layer are very sensitive to small amounts of impurities in the solid phase and also to small variations in the environment (Levenspiel, 1999). As a result, the conventional phenomenological description of the rate of diffusion, in terms of Fick’s first law, provides the most accurate predictions.

An effective diffusivity coefficient (D_{e_i}), within Flick’s first law, averages all the “ash” layer characteristics (*i.e.* porosity, tortuosity etc.). The diffusivity coefficient can vary greatly with solution composition and impurities. Diffusion through the product layer is described by the following equation:

$$J_i = D_{e_i} \frac{\partial C_i}{\partial x} \qquad 2.24$$

- Absorption Model (step 4 and 6)

Surface bonding of aqueous molecules/ions depends highly on the molecular surface structure, tension, composition, activated sites, ionic species activities, impurities (*i.e.* poisoning the reaction sites) and electrochemical composition (Atkins & Paula, 2013). The following mass-action expression presents the general form of surface bonding:

$$A_{aq} + M_{surface} \underset{k_r}{\overset{k_f}{\rightleftharpoons}} AM_{surface} \qquad 2.25$$

The Langmuir isotherm is a simple model in which to express the adsorption and desorption of aqueous molecules/ions on a reacting surface. The isotherm is based on expressing the dynamic equilibrium of reaction 2.25 by the extent of A absorption coverage (θ_A) in equation 2.26.

$$\theta_A = \frac{K_A a_A}{1 + K_A a_A} \qquad 2.26$$

where the equilibrium constant (K_A) is the ratio of the forward rate constant (k_f) to reverse rate constant (k_r) and a_A is the activity of the solution component A. A further modification to the Langmuir isotherm is the co-absorption of a mixture absorbing species, expressed as follows:

$$\theta_i = \frac{K_i a_i}{1 + K_i a_i + \sum_j K_j a_j} \qquad 2.27$$

Although absorption of species on a reacting surface depends on various factors, these dynamic equilibrium isotherm presents a simplistic method to model highly complex mechanistic systems. It should be noted that the Langmuir isotherm assumes the thermodynamic equilibrium is not influenced by other chemical reactions (Atkins & Paula, 2013).

- Chemical Reaction Model (step 5)

Chemical kinetic theories originated in the 1800's from the "law of mass action" by Guldberg and Waage. An elementary chemical reaction rate law in the conventional (*i.e.* commonly used by researchers) is presented in equation 2.28. The reaction rate depends on the reagent and product species activity, a_i, to the power of their respective reaction coordinates, α_i, *i.e.* thermodynamic orders as anticipated in the mass-action expression.

$$r_j = k_f \prod_{reagents\ i} a_i^{\alpha_i} - k_r \prod_{products\ i} a_i^{\alpha_i} \qquad 2.28$$

The rate (r_j), with the units $mol.time^{-1}.volume^{-1}(or\ area^{-1})$, is expressed as a linear function of the forward (k_f) and backward (k_r) rate constants multiplied by the respective activities. This form of the chemical rate expression originates from ideal gas thermodynamic principles, and at equilibrium state ($r_j = 0$) equates to the equilibrium constant:

$$K_{eq} = \frac{k_f}{k_r} = \frac{\prod_{products\ i} a_i^{\alpha_i}}{\prod_{reagents\ i} a_i^{\alpha_i}} \qquad 2.29$$

Various derivatives of this expression can be used and modified to suit a chemical mechanism which would be most prominent under a specific set of conditions.

The rate constants of the rate-limiting process are expected to vary with temperature. To account for the temperature dependency (*i.e.* thermo-activation of chemical species) on the rate constants, a typical Arrhenius equation is used:

$$k = k_o e^{-\frac{E_a}{RT}} \qquad 2.30$$

Where E_a is the activation energy of the respective reaction, k_o the pre-exponential factor (or frequency factor), T is the absolute temperature, and R is the universal gas constant. Svante Arrhenius proposed the equation in 1889, based on van't Hoff's equation that describes the temperature dependence of equilibrium constants. Furthermore, the assumption of Arrhenius behaviour for inner-sphere electron transfer is in accordance with Marcus' theory of electron transfer (Marcus, 1964).

In practice it is usually found that the frequency factor remains approximately constant over a wide range of temperatures and conditions. If activation energy of a reaction determined by experimentation is higher than 30 kJ/mol, the mechanism can be considered as chemically controlled. It should, however, be regarded as a red flag when the activation energy is lower than 30 kJ/mol since the reaction may be operating in a regime where the rate is influenced or controlled by either external or internal mass transfer.

The Arrhenius equation was determined empirically and the mechanical basis for the pre-exponential factor and activation energy was not understood (Laidler & King, 1983). Research to determine such a mechanical basis led to transition state theory. Proposed in 1935, the theory led to the development of the Eyring equation 2.31, which explains the mechanical basis behind the pre-exponential factor and the activation energy.

$$k = \frac{k_B T}{h} e^{-\frac{\Delta G^{\#}}{RT}} = \frac{k_B T}{h} e^{-\frac{\Delta H^{\#}}{RT}} e^{-\frac{\Delta S^{\#}}{RT}} \qquad 2.31$$

where $\Delta G^{\#}$ is the Gibbs energy of activation, $\Delta H^{\#}$ standard enthalpy of activation, $\Delta S^{\#}$ the standard entropy of activation, k_B is the Boltzmann's constant, and h is Planck's constant. These quantities should not be regarded as fundamental (*e.g.* the enthalpy and entropy of chemical species), but rather as apparent chemical activation values.

The transition state theory is the classical (and most applied) kinetic theory, which explains the reaction rates of elementary chemical reactions. The theory assumes a quasi-equilibrium state (transition state) of activated complexes between the reactants and products.

2.3 Electrochemical nature

2.3.1 Band theory of solids

Quantum mechanics states that inner shell electrons of an atomic nucleus are not free to move in a solid, while outer shell electrons that may be involved in covalent bonding with adjacent atoms, or they may be associated with the solid crystal structure as a whole. Within a solid the quantum mechanical energy states associated with isolated atoms become merged. Creating a band of energies closely spaced within a narrow range of a given energy between isolated atoms within a crystal lattice. In the case where an energy band is full (*i.e.* the number of electrons matches to the number of energy states available, a maximum of two electrons per energy level of a given band), electrons are fixed to the electron shell and not free to move within the solid. The solid would correspond to a pure insulator at low temperatures in this case. (Newman & Thomas-Alyea, 2004)

The transfer of an electron can only occur between adjacent sites of equal or nearly equal energy level (Crundwell, 1988a). According to the band theory of solid state, two bands are described namely the conduction and valence band in defining the electron mobility of a solid. The highest energy completely occupied band is called the valence band, and the lowest energy unoccupied band or highest partially occupied energy band is called the conduction band (see Figure 2.2). The energy levels of the valence and conduction bands at the point of zero charge are E_v and E_c respectively.

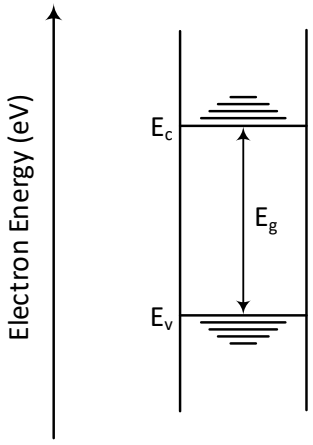

Figure 2.2: Band structure of a semiconductor

Semiconductors form a special group of electronic conductors in that the substance atoms are chemically bonded by valence electrons (forming the valence band), but when energy is supplied externally (*i.e.* by radiation, heat) these bonding electrons are excited to the energetically higher conduction band. This allows the semiconductor to act as an insulator under specific conditions

(*i.e.* low temperature) and a conductor (*i.e.* high temperature). A 'forbidden' band or band gap (E_g) lies between the valence and conductivity bands. (Newman & Thomas-Alyea, 2004)

Defects or impurities in the solid lattice structure can lead to electron energy states that do not correspond with energies of the bands. Solid surfaces involve a discontinuity in the solid crystal lattice structure and therefore creates a concentrated region of defects, called surface states. If an impurity is present in the solid and is of an electron donor tendency a new energy band below the conduction band is formed (see Figure 2.3a). The difference in energy between conductivity band and this new band is smaller in comparison the energy gap (E_g), thus electrons are easily passed from the donor band to the conductivity band. Since electrons are the charge carriers, these type of materials are called n-type semiconductors. Conversely, if the impurity is of an electron acceptor tendency the new energy band will be above the valance band (see Figure 2.3b). Electrons from the valence band passes then readily to the new energy band, leaving holes behind. These positively charged holes are the main charge carries and this type of material is called p-type semiconductors.

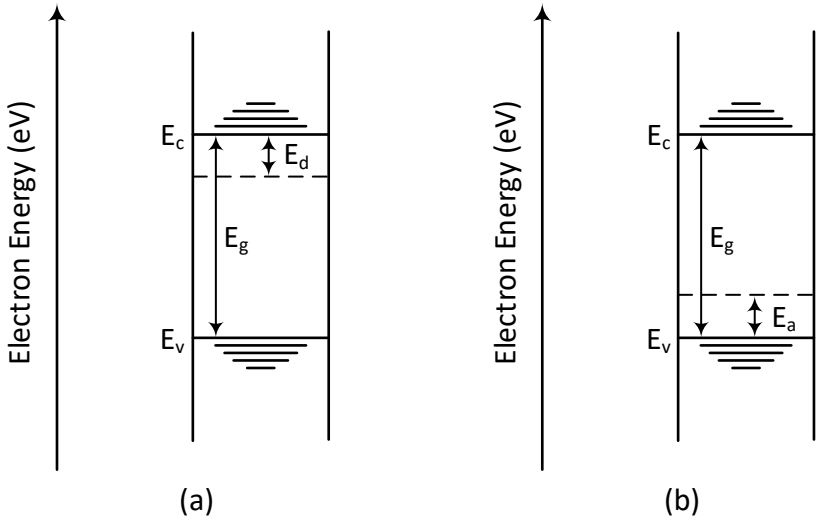

Figure 2.3: Schematic diagram of a semiconductor band structure with an impurity present of an (a) electron donor tendency, n-type semiconductor, and (b) electron acceptor tendency, p-type semiconductor

2.3.2 Structure of electric double layer

This section briefly presents the structure of the electric double layer as described by various researches in the field (Bockris *et al.*, 2000; Havlík, 2008; Koryta *et al.*, 1993; Newman & Thomas-Alyea, 2004; Vignes, 2011). There exists a double layer at a solid-liquid interface, firstly, since specific species in solution may have preference for being near the solid (*i.e.* smaller ions have

a tendency to pack closer to a solid surface in comparison to larger ions). Secondly, the surface charge of the solid (*i.e.* polarized by electrolyte/absorbed species or artificially by applied current) creates a potential difference between the electrolyte and solid, and in response ions get orientated different to that of the bulk fluid (*i.e.* due to coulomb forces) to account for the potential drop. The double layer may be comprised of multiple adsorbed or orientated layers, and it is generally difficult to describe experimental data with a unique model.

The general model of the double layer is presented in Figure 2.3. A charge on the surface (q_m) may be present on the impenetrable surface barrier. The inner Helmholtz plane (IHP) is the position of the centres of ions or molecules that are adsorbed at the surface (*i.e.* generally water in aqueous solution or protons in acidic solution). The outer Helmholtz plane (OHP) is the locus of centres of solvated ions at their distance of closest approach to the surface (*i.e.* solvent or absorbed molecules prevent the solvated ions from interacting with the surface directly). Surface charge in the IHP is denoted as q_1. Outside the OHP is the diffuse layer, with a nett electric charge (q_2) comprising of solvated anions and cations dispersed in the electrolytic solution. The diffuse layer is similar to the bulk of the solution except that it is not electrically neutral. A diffusion layer follows the diffuse layer and is electrically neutral, but has a concentration gradient (non-uniform concentration) of solvated ions (Newman & Thomas-Alyea, 2004) .The whole of the interfacial region is electrically neutral:

$$q_m + q_1 + q_2 = 0$$

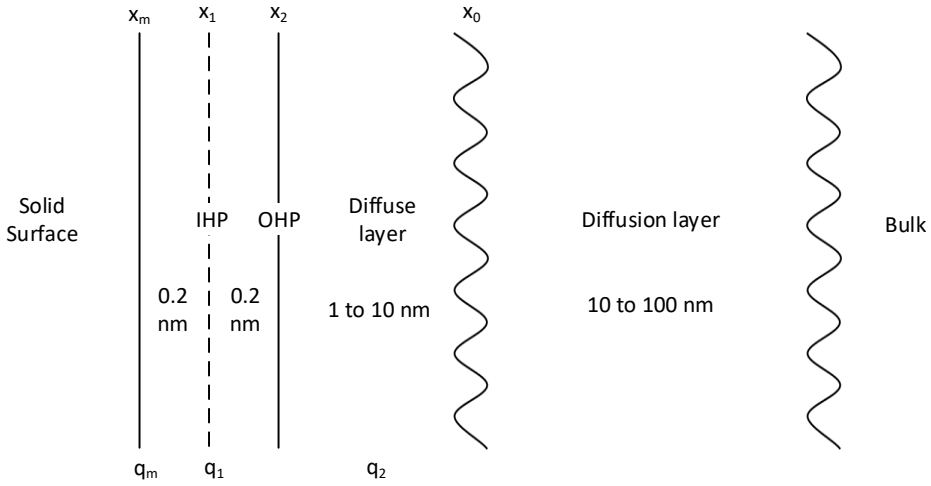

Figure 2.4: Structure of the electric double layer. Redraw from Newman and Thomas-Alyea, (2004).

2.3.3 Electrochemical reaction

The purpose of the detailed description of complex mechanisms is to illustrate the fundamental processes involved to yield a suitable mathematical approximation to the kinetic behaviour, as well as to ensure that the kinetic treatment yields the correct thermodynamic behaviour under equilibrium conditions. Treatment of kinetics involves a great deal of complex elementary steps (as seen in section 2.2 above), phase/state transferal, adsorption layers (*i.e.* at inner Helmholtz plane or a plane of inner surface states), diffusion layers in the solution and space-charge region within the semiconductor, etc. (Newman & Thomas-Alyea, 2004).

An electrochemical reaction is a reaction involving free electron (or hole) transferal, where there is no chemical association between the two half reactions (anodic and cathodic). The elementary electrochemical half reaction is given in equation 2.32.

$$Red \underset{k_b = k_c}{\overset{k_f = k_a}{\rightleftharpoons}} Ox + ne^- \qquad 2.32$$

The symbol Red refers to the reducing species (being oxidized) and Ox to the oxidizing species (being reduced). The forward rate (f) is represented by the anodic reaction (oxidation) and the backward reaction (b) by the cathodic reaction (reduction).

- Interfacial electrochemical kinetics

Interfacial kinetics is rate limiting when the electrochemical potential of the reacting surface limits the overall rate. Chemical interactions are not the rate limiting factor in such instance, even though there may exist some side-reaction involving direct chemical interaction (*i.e.* at the reaction site there is no charge transfer during the chemical interaction). During charge transfer limiting rates the cathodic reduction of the adsorbed oxidant and anodic oxidation of the mineral determines the surface potential at the specific reaction site (Steyl, 2012). The anodic and cathodic reactions occur simultaneously, with respective dependence on the surface overpotential and reactant concentrations. Figure 2.5 illustrate the cathodic half reaction.

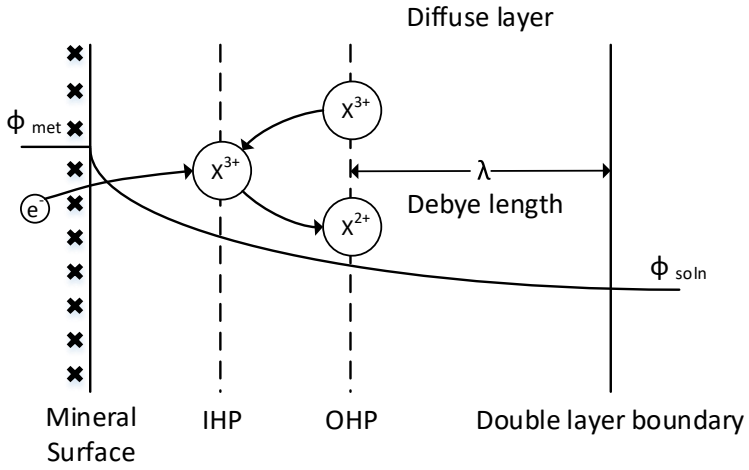

Figure 2.5: Structure of the double layer with potential distribution indicated and cathodic reaction shown. I.e. the 3+ valent ion is adsorbed from the outer Helmholtz plane on the inner Helmholtz plane, where it is able to react with an electron from the metal surface. The resulting 2+ valent ion is then desorbed. Redrawn from Newman and Thomas-Alyea (2004).

A potential difference between the mineral surface and the solution ($\Delta\phi$) is observed as a result of the distribution of the potential within the double layer, denoted as:

$$\Delta\phi = \phi_{\text{min}} - \phi_{\text{soln}} \qquad 2.33$$

Where ϕ_{met} and ϕ_{soln} are the electrostatic potentials of the mineral surface and solution just outside the double layer respectively.

Activation polarisation barriers manifests between the mineral surface and solution as potential barriers, and creates resistance to charge transfer reactions, *i.e.* required activation energy to transfer the atom or electron on the mineral surface to the solution (Steyl, 2012). If an electrochemical transfer reaction is in equilibrium (*i.e.* the free energies of the metallic atoms in the mineral and ionic states in the solution are equal), then the activation energy of electron transfer is the same in both directions, the dissolution rates and precipitation rates on the mineral are identical (Havlík, 2008). At this equilibrium state no current is produced and the mineral is at rest potential. In the instance where the equilibrium state is disrupted, the solid-solution interface becomes polarised. Polarisation means that the surface departs from its rest potential with an overvoltage (η). The extent of the overvoltage depends on several factors, which include the composition of the mineral surface and solution as well as the reaction taking place (Havlík, 2008). The electrochemical potential difference ($\Delta\phi$) therefore limits the leaching rate (Steyl, 2012). For a single reaction the surface overpotential is equal to the electrode potential at the current conditions ($\Delta\phi$) minus the equilibrium electrode potential ($\Delta\phi_e$) corresponding to the considered electrode reaction (Koryta *et al.*, 1993).

$$\eta = \Delta\phi - \Delta\phi_e \qquad 2.34$$

The rest or equilibrium potential is different from the thermodynamic equilibrium potential in that the rest potential is the sum of the anodic and cathodic half reaction potentials, a measured equilibrium potential, leading to the *mixed potential* phenomena. Electrode potential is determined by the rates of the two opposing half reactions of which no chemical interaction exists. The sum of the partial currents corresponding to the two half reactions must equal zero (conservation of charge). The potential attained by the opposing half reactions at the mineral-solution interface is termed the mixed potential ($\Delta\phi_m$).

The theory leading to the derivation of the fundamental relationship between the current density (i_j) and the potential difference ($\Delta\phi$) (the activation polarisation relationship, Butler-Volmer equation) is described by various authors (Burkin, 2001; Havlík, 2008; Newman & Thomas-Alyea, 2004; Steyl, 2012; Vignes, 2011). In the absence of mass transfer limitation (*i.e.* no concentration polarisation) and no ohmic resistance (*i.e.* limiting electron conduction layer within the mineral and solution), the net half reaction rate (r_j) is presented in equation 2.35, using Faraday's equation to relate the exchange current density.

$$r_j = \frac{i_j}{nF} = k_a \left(\prod_{v_{ji}>0} a_{red_i}{}^{v_{ji}} \right) \exp\left(\frac{\beta_j nF}{R_g T} \Delta\phi \right) - k_c \left(\prod_{v_{ji}<0} a_{ox_i}{}^{-v_{ji}} \right) \exp\left(\frac{-(1-\beta_j)nF}{R_g T} \Delta\phi \right) \qquad 2.35$$

Equation 2.35 for an electrochemical half reaction is similar to conventional chemical kinetics, but with the additional potential dependency factor accounting for the activation polarisation barriers. The symbols a and c refers to the anodic and cathodic directions, respectively. The rate (r_j) for half reaction j adopts the units $mol.m^{-2}.\min^{-1}$. The rate constants (k_a & k_c) consist of various factors and are expected to show a Arrhenius dependency on temperature, they also depend on the nature of mineral surface. The anodic and cathodic reactions depend on the activities (a_i) of the respective species (i) partaking in the respective reactions. The symmetry factor or transfer coefficient (β_j) represents the fraction of applied potential ($\Delta\phi$) that promotes anodic reaction, whilst $1-\beta_j$ is the fraction of the applied potential that promotes the cathodic reaction (Newman & Thomas-Alyea, 2004). The value of β_j lies between zero and one. It is frequently found in literature by experimental or approximation that the value of β_j is ½, indicating the applied overpotential is distributed equally between the anodic and cathodic reactions.

- Mixed potential theory or mixed electrode

If two electrochemical (half) reactions occur on the same surface in contact with an electrolyte, then the surface is called a mixed electrode. One reaction produces electrons while the other consumes. In a mixed electrode, with the individual equilibrium potential ($\Delta\phi^*_{1\ or\ 2}$) of both reactions are priori different, the law of conservation of electric neutrality (charge conservation) must be fulfilled. The sum of the two reaction currents is equal (Vignes, 2011):

$$\mathrm{I} = \mathrm{i}_1\mathrm{A}_1 + \mathrm{i}_2\mathrm{A}_2 = 0 \qquad 2.36$$

The mixed potential ($\Delta\phi_m$) corresponds to the position of equality in currents. Its position with respect to equilibrium depends on the activation polarisation relationship (equation 2.35), for as set of given conditions. The current-potential curves are usually presented as illustrated in Figure 2.6, with the anodic and cathodic parts overlapping that gives the mixed potential at equilibrium. It is noted the initial oxidation and reduction overpotential are assumed to be negligible. The resulting current at the mixed potential corresponds to the kinetics of both simultaneous half reactions (*i.e.* the overall leaching rate).

Equation 2.35 can be used to relate the kinetic expression for the phenomenological leaching rate model of non-oxidative/oxidative sphalerite leaching. The anodic branch of the oxidation and cathodic branch of the reduction polarisation curves are used to obtain the expression of the mixed potential and resulting current.

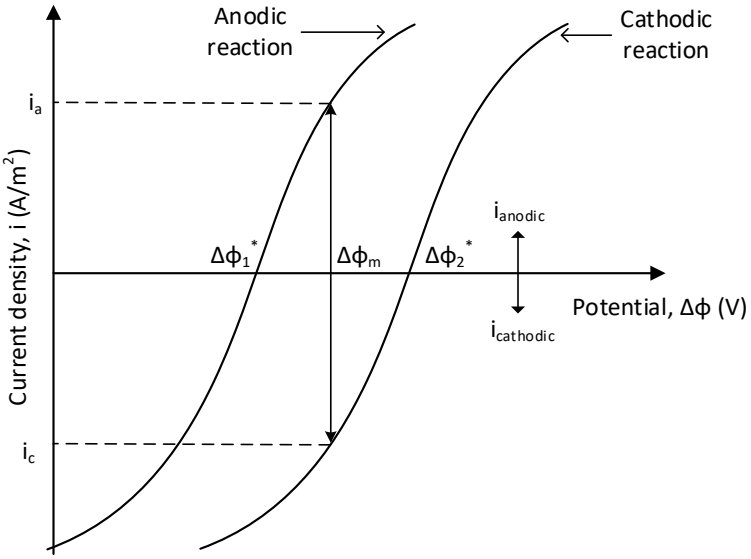

Figure 2.6: Polarisation curves of the elementary (half) reactions. Graphical illustration of the rate of the overall reaction $i_a + i_c = 0$ and for the mixed potential $\Delta\phi_m$. Redraw from Vignes (2011).

- Concentration overpotential

The rate of the electrochemical reaction becomes limited by the transport ion in the diffusion layer above a certain overpotential (Vignes, 2011). The dissolution of the metallic atom from the mineral as well as the reduction of the ionic components lead to rapid changes within the composition in the vicinity of the interface. Transfer takes place by diffusion through the relatively static layer. Consequently, the concentration of the metal ions may increase to a supersaturated level (above the equilibrium value) or decrease to zero in the volume of the solution at the mineral surface. Creating a concentration polarisation. (Havlík, 2008)

For systems containing an excess of supporting electrolyte (*i.e.* neglect conductivity variations in the diffusion layer), the concentration overpotential relationship is (Newman & Thomas-Alyea, 2004):

$$\eta_c = \frac{RT}{nF}\ln\left(\prod_i\left(\frac{C_{i\infty}}{C_{i0}}\right)^{v_i}\right) + \frac{F}{\kappa_\infty}\sum_j z_j D_j\left(C_{j\infty} - C_{i0}\right) \qquad 2.37$$

The last term is frequently orders of magnitude smaller (*i.e.* reactant concentration divided by the supporting electrolyte concentration) in comparison to the first term and is therefore usually neglected.

2.4 Rate analysis

This section discusses various methods for analysing batch experimental tests to obtain rate expression parameters. The shrinking core model (SCM) of solid-liquid reactions is also presented in this section to characterise the reaction regime present in a chemical system.

2.4.1 Analysing batch results

A rate expression characterizes the rate of reaction, and its form may either be interpreted by theoretical considerations or simply the result of an empirical curve-fitting procedure. Once a rate expression is known, it can easily be substituted into appropriate conservation balances (*i.e.* mass and energy balances) to model any system confined to the mechanism of the rate expression. The values of the constant rate parameters are determined by experiments; predictive methods of rate parameters are inadequate to current leaching systems.

In this section, the focus will be on the ways of obtaining and analysing reaction rate data to quantify the rate law, with the focus on a batch reactor configuration. In batch reactor experiments the concentrations of reagents or products are usually measured and recorded at different times during the course of the reaction, under isothermal and isobaric conditions. The concentration data recorded from the batch experiment starts at a set unsteady-state condition and moves toward equilibrium. From the resulting concentration profile, rate parameters are estimated under the specific reactor conditions. Several batch experimental test are therefore computed under various conditions (*i.e.* temperature, initial composition) to observe and quantify the effects into the rate expression.

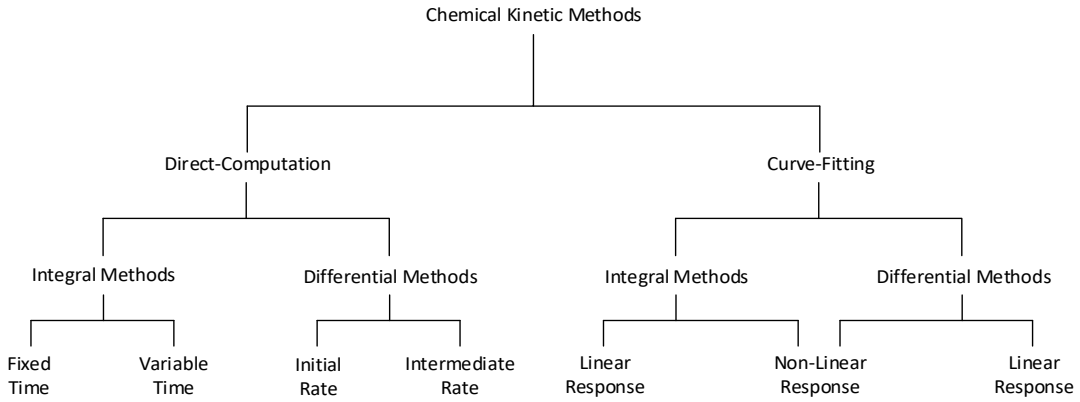

Figure 2.7: Classification of chemical kinetic methods of analysis. Adapted from Pardue (1989).

Figure 2.7 provides one useful diagram for the classification of methods of chemical kinetics analysis (Pardue, 1989). The methods of chemical kinetic analysis are divided into two main categories: Direct-Computation and Curve-Fitting. In a direct-computation method, the rate constants are obtained through keeping select process parameters constant and using the change in another, thus using the experimental data directly for the computation of the rate expression (*i.e.* one or multiple points of concentration measured at a set time during a batch test to obtain the rate parameters). With a curve-fitting method, regression (typically least-squares regression) is used to find the best fit between the data and the known mathematical model for the rate law, as a function of time by varying the parameters.

Both the direct-computation and curve-fitting categories have their advantages and disadvantages in developing or quantifying a rate expression. A direct-computation method is similar to a common factorial design of experiments, where the different factors (*i.e.* initial concentration, temperature, time, etc.) at different levels are used to compute a model. The advantage of this method is that the reverse and side reactions can be eliminated by reducing the reaction (experiment) time, resulting in a higher certainty of capturing a given mechanism

response. The experiment can further be manipulated to operate under a specific mechanism, thus in complex reaction systems each reaction can be investigated individually. The disadvantage of a direct-computation method is that a lot of experiments must be conducted, increasing the costs of a project drastically. The progress of reaction is not captured in these type of methods. Variance also creeps easily into the response variable (*e.g.* concentration) and in order to quantify the variance a series of repeating experiments must be performed. For the curve-fitting category of methods, considerably less experiments are required and a higher certainty in the rate parameters is obtained, since it is regressed over a series of responses over time. The disadvantage, however, is that there exists considerable uncertainty in the mechanism of the proposed rate expression, due to the occurrence of reverse or side reactions.

The overall material (conservation) balance over a batch reactor is given in equation 2.38. The mass change (dM_i/dt) of a component (i) is equal to the rate of generation or consumption (R_i) of the chemical reaction. In the integral method of analysis, a particular form of the rate expression (R_i) is assumed, and after appropriate integration and mathematical manipulation of the conservation balance, an expression relating a select variable (*i.e.* concentration or conversion) as a function of time is yielded. This expression is then used to determine the constant parameters within the rate expression. The differential method of analysis, alternatively, utilizes the differential equation 2.38 directly to obtain the constant parameters within the rate expression. This is done through obtaining the slope of a selected variable over time and calculating a constant parameter at constant conditions.

$$\frac{dN_i}{dt} = R_{i,generated/consumed} \qquad 2.38$$

Four different methods of analysing batch data collected are briefly discussed: (1) fixed/variable time, (2) initial/intermediate rate, (3) linear regression and (4) non-linear regression.

- Direct-Computation: fixed/variable time integral methods

A direct-computation integral method utilizes the integrated form of the rate law. For example, a pseudo-first-order reaction is assumed to occur at constant volume, the integration of the conservation balance (equation 2.38) by application of the rate law yields equation 2.39 for the concentration change of reactant i.

$$C_{i,t} = C_{i,t=0}e^{-kt} \qquad 2.39$$

In a one-point fixed-time integral method, the reagent concentration at a single time is measured with a standard known initial concentration and the resulting reaction rate constant (k) can be estimated. In some cases, it is rather more convenient to measure the reaction products and equation 2.39 can be manipulated if the reaction stoichiometry is known. A one-point fixed-time integral method has the advantage of simplicity, because only a single measurement is required. As with any method that relies on a single measurement, this method cannot compensate for a constant determinate error (Harvey, 2015). In a two (or multi)-point fixed-time integral method a correction for the constant determinate errors is made by making measurements at two (or more) points in time and using the difference between the measurements to determine the reaction rate constant. Since the error creeps into both measurements, the difference between the measurements is independent of the constant determinate error.

A variable-time integral method follows a similar mathematical procedure as the fixed-time integral method, with the difference being that the total time required to effect a specific change in concentration is measured in-stead of the concentration change in a set time. The importance of application of this method is for the quantitative analysis of catalysts.

- Direct-computation: initial/intermediate rate differential method

A differential method utilizes the differential form of the rate law. Again for example, a pseudo-first-order reaction is assumed to occur at constant volume, the integration of the conservation balance (equation 2.38) by application of the rate law yields equation 2.40 for the concentration change of reactant i.

$$\frac{dC_i}{dt} = \frac{\Delta C_i}{\Delta t} = kC_i^{\alpha_i} \qquad 2.40$$

In the method of initial (or intermediate) rates, the presence of significant revers or side reaction could be restricted.

The use of the linear regression differential method of data analysis (following bullet) is clearly one of the easiest methods to determine the reaction orders (α_i) and specific reaction rates. The presence of significant revers reaction or side reaction, could render the differential method ineffective.

In these cases, the method of initial (or intermediate) rates could be used to determine the reaction order and the specific rate constant. A series of experiments are performed at different

initial reagent concentrations and the initial rates calculated. This is done through differentiating the concentration profile at zero time. The data is then used in equation 2.40 by either non-linear regression or linear regression through linearizing the equation by taking the logarithmic to determine rate constant and reaction order. Although regression is applied, the initial rate differential method falls under direct-computation category, since an experimental data point at a specific time and condition is used to directly compute the rate parameters. (Fogler, 2001; Levenspiel, 1999; Missen *et al.*, 1999; Pardue, 1989)

There are several advantages to using the reaction initial rate, because the initial rate provides the greatest sensitivity to a decreasing rate over time and is measured under nearly pseudo-zero-order conditions (*i.e.* concentration change with time is effectively linear or particular desired reagent concentrations are approximately constant). According to (Mottola, 1993), as a general rule, a reaction's initial rate should be measured at a time of conversion of no more than 2% of the reactants (the smaller the percentage, the more linear the change in concentration as a function of time results). A disadvantage of the initial rate method is incomplete mixing for reactants due to insufficient time. This is avoided by using an intermediate rate measured at a later time.

- Curve-fitting: linear regression method

In a curve-fitting method the concentration of a reactant or a product is continuously monitored as a function of time and by usage of a regression analysis to fit the data to an appropriate differential rate law or integrated rate law, the rate parameter can be obtained. In the integral method of analysis, a particular form of the rate expression is assumed (*i.e.* by considering thermodynamics, nature of system and literature), and after appropriate integration and mathematical manipulation (usually linearization) of the conservation balances, a plot of a process variable (*i.e.* concentration) versus time function should yield a straight line. For example, taking the logarithm of equation 2.39 and yielding equation 2.41.

$$\ln(C_i) = \ln\left(C_{i,0}\right) - kt \qquad 2.41$$

In the differential method of analysis, the rate expression is similarly manipulated by linearization of the differential expression. For example, taking the logarithm of equation 2.40 and yielding equation 2.42. The resulting straight line's slope and intercept is used to calculate the rate parameters. In the linear differential method, the derivative of the concentration time plot is required. This can lead to significant error if the data is scattered (*i.e.* the rate between

exceeding data points can vary significantly or even be negative due to variance). In practice this problem is overcome by fitting a polynomial to the data first that represents the concentration curve accurately, thus the derivative at any specific time can easily be calculate. Caution should be taken when applying a polynomial since over fitting can lead to significant derivative errors. In such case of highly scattered data, non-linear regression is usually applied to directly estimate the rate parameters.

$$\ln\left(\frac{dC_i}{dt}\right) = \ln(k) + \alpha_i \ln(C_i) \qquad 2.42$$

The least-squares method of regression is the easiest, well-defined and most applied regression technique in practice. It minimizes the total sum of squared error (*i.e.* the sum of squared residuals between the actual data and model) by varying the model constants.

- Curve-fitting: non-linear regression method

In non-linear least squares analysis, the conservation balance differential (equation 2.38) is integrated over time by an ordinary-differential-equation (ODE) optimisation approach (solver). Many software packages are available to integrate ODE at a very high level of accuracy. The resulting concentration profile in time is compared to the experimental data, by means of residuals analysis. Now the non-linear least-squire analysis is applied to reaction rate data to determine the rate law parameters. Initial estimates of the parameter values are required (*i.e.* reaction order, rate constant) in order to start the regression method and are varied accordingly to minimize the total sum of squared error. The disadvantage of this method is that the resulting optimized rate parameters at some local minima in total squared error is highly dependent on the initial input values.

2.4.2 Shrinking core model (SCM)

After developing a viable chemical or electrochemical mechanism, it is desired to mathematically relate the observed oxidation phenomena (leaching experiments). The shrinking core model (SCM) is a well-defined method to quantify a non-catalytic reaction of particles with surrounding fluid (leaching) in a batch reactor experiment. In the SCM it is assumed that the reaction occurs first at the outer surface of the particle and the zone of reaction then moves into the solid, leaving behind a product “ash” layer and inert solid (see Figure 2.8). There exists therefore an unreacted core of material which continually shrikes in size during the progress of reaction.

Considering the nine possible steps occurring in succession (see section 2.1.1), the resistances of the different steps usually vary significantly. Distinguishing between the first half (*i.e.* reagents to reaction zone, denoted by a dot in Figure 2.1) and the second half (*i.e.* products from the reaction zone, denoted by a diamond in Figure 2.1) is practically also a cumbersome task. Therefore, the treatment of developing the conversion equation for spherical particles considers film diffusion (step 2), product "ash" diffusion (step 3) and reaction (step 5) rate controlling.

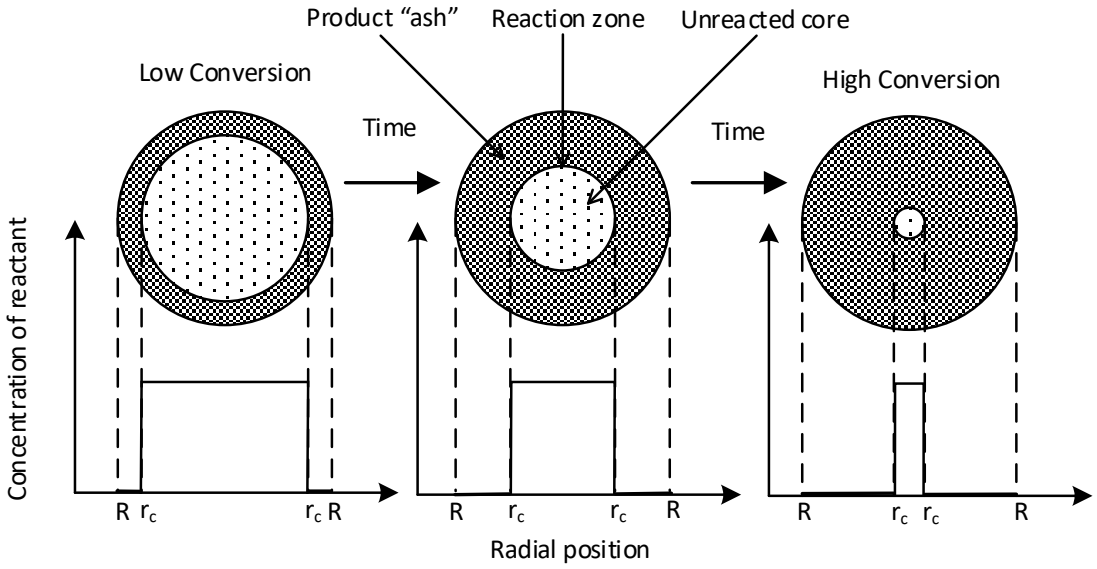

Figure 2.8: Illustration of the reaction process according to the shrinking core model (redrawn from Levenspiel (1999))

The mathematical expressions derived relating the conversion of solid reagent (X) to the three different reaction regimes, displaying topochemical kinetics under approximately constant reaction conditions, are presented in Table 2.1. These relations are under the assumption that the total particle size remains unchanged during the process (*i.e.* under the constant density assumption, solid reagents and products have the same molar density). In practice it is usually found that the SCM approximates a variety of experimental observation of real particles more closely than other models (Levenspiel, 1999).

Table 2.1: Conversion-time expressions for the in-situ transformation of constant size particles controlled by different reaction regimes of the shrinking core model

Relation	Film Diffusion	Product "ash" Diffusion	Reaction Controlled
Conversion – Particles size	$X = 1 - \left(\frac{r_c}{R}\right)^3$	$X = 1 - \left(\frac{r_c}{R}\right)^3$	$X = 1 - \left(\frac{r_c}{R}\right)^3$
Conversion – Time	$X = k_s t$	$1 - 3 \cdot (1 - X)^{\frac{2}{3}} + 2 \cdot (1 - X) = k_s t$	$1 - (1 - X)^{\frac{1}{3}} = k_s t$
Overall rate constant	$k_s = \frac{2 v_b D_A C_{A\infty}}{v_a \rho_B R_o^2}$	$k_s = \frac{6 v_b D_{e_A} C_{As}}{v_a \rho_B R_o^2}$	$k_s = \frac{v_b r_s}{v_a \rho_B R_o}$

If the left-hand side (conversion) term of the conversion-time relation is plotted against time, and a straight line is obtained, it can be assumed that the system is controlled under the respective reaction regime (within reason of the observed kinetic data and designed experimental conditions). This method does also provide the means to capture bulk concentration and state condition effects phenomenologically. The slope would yield the overall rate constant (k_s), which is a function of the initial particle size (R_o), rate determining step (*i.e.* diffusion, $D_A C_A$, or intrinsic reaction rate, r_s), the solid density (ρ_B) and stoichiometric reaction coefficients (v_i). Only when the major bulk parameters affecting the rate (*i.e.* temperature, reagent concentrations etc.) are kept approximately constant, can the overall rate constant and thereof the linear rate constant (k_l, the rate of particle shrinkage) be obtained from the slope. It is obvious from equation 2.43 that to obtain the linear rate constant, the particles have to be screened to a narrow size range.

$$k_s = \frac{k_l}{R_o^n} \qquad 2.43$$

Where n is the order of the initial particle size for the respective reaction regimes (i.e. 1 for reaction controlled regime). If the initial particle size distribution is known, the linear rate constant may be used to integrate over the distribution of the individual particle size conversions to yield the overall conversion (equation 2.44).

$$X = \sum_i X_i W_i \qquad 2.44$$

Where W_i the weight fraction of initial particles in size class i and X_i is the individual conversions of particles of size class i. Noting that the linear rate constant (or rate of particle shrinkage) is independent of particle size and constant throughout the experiment.

Chapter 3 Methodology

The focus of this work is a kinetic study of the non-oxidative and oxidative leaching behaviour of sphalerite, under various operating conditions with the addition of a surfactant. To this end, a reaction modelling framework was developed, incorporating many fundamental and phenomenological aspects. The model framework was used to regress rate parameters for the dissolution of a sphalerite concentrate. Figure 3.1 shows an overview of the techniques, insights and methods address addressing the objective presented in this dissertation.

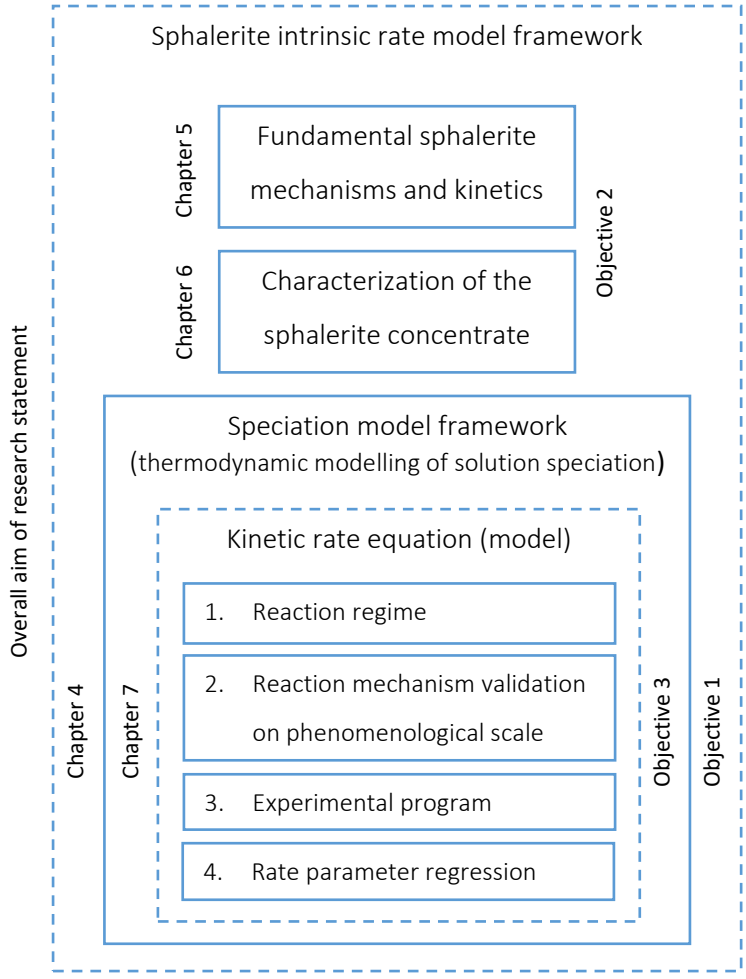

Figure 3.1: Overview of the structure and contributions of this work

The elements of this dissertation build upon each other as seen from Figure 3.1. In order to quantify the reaction regime a detailed fundamental analysis of the minerology and characterization of the concentrate had to be established. While to quantify the kinetic model (sphalerite dissolution rate model) it was first required to build a thermodynamic speciation model, within which sphalerite dissolution could be modelled.

3.1 Thermodynamic modelling

The literature review has highlighted the importance of solution speciation and the behaviour thereof influencing the dissolution of sphalerite. Especially the complexation reactions of acidic aqueous ferric/ferrous solutions. The formation of contact ion pairs may alter the behaviour of sphalerite leaching, by capturing free ions in solution under less acidic conditions. The result would be altering the interfacial electrochemical kinetics on the mineral surface. Hence, it is required to investigate and extract the knowledge of aqueous zinc-ferrous-ferric sulphate solution characteristics at elevated temperatures. The ability to predict solution speciation would therefor form an integral part in modelling zinc leaching reactions.

Explicit recognition of speciation that includes complexation reactions and equilibria is detailed in Chapter 4 (*i.e.* the thermodynamic modelling chapter). After reviewing the literature, it was decided to use the Pitzer model with its linear combination of parameters as a suitable (best fit) model for the solution species activity. A comprehensive methodology of solution model development, modelling speciation using the *Pitzer function* and model validation is described in Chapter 4, and is not repeated here. Thermodynamic model development methodology is broadly performed in the following step:

1. It was firstly required to study the solution speciation to determine a minimum number of solution species to adequately describe the thermodynamic behaviour, *i.e.* warranted to describe the aqueous phase. This was achieved through investigating previous studies and the thermodynamic behaviour of metallic species in an acidic environment.
2. The detailed computational methodology (Figure 4.1) was defined to develop and regress the Pitzer model parameters. Further details regarding the speciation model computational equations, parameters and structure, given in Appendix A.
3. Thermodynamic speciation data from literature sources was then gathered and consolidated for parameter regression of the various species sub-systems.
4. The Pitzer model development consisted of dividing the selected species into binary and ternary sub-systems (*e.g.* $ZnSO_4 – H_2O$ & $ZnSO_4 – H_2SO_4 – H_2O$ etc.). A key focus was to reduce the number of model parameters as much as possible to avoid over-fitting and improve the capability of model extrapolation. The binary sub-systems were firstly regressed independently of one other to obtain their interaction parameters, upon which the ternary sub-systems are applied and selected binary and ternary interaction parameters of the ternary sub-system species fitted to the data. This higher order sub-system regression method upon lower order sub-systems of Pitzer model parameters is

standard practise and a simplistic (accurate) method, with a relatively accurate activity trend predictive capability. Albeit, the regressed parameters from this model cannot be mixed and matched with other Pitzer models from the literature.

Speciation modelling followed the methods and thermodynamic framework of Biley (2015) and (Steyl, 2012).

3.2 Reaction mechanisms and kinetics

The ultimate aim of the project is to develop an intrinsic reaction rate model for the non-oxidative and oxidative leaching of sphalerite on the phenomenological scale. To achieve this goal, it is required to fundamentally understand the mineralogical behaviour of sphalerite under leaching conditions specified in the scope (Table 1.1) of this work (*i.e.* leaching conditions like that of existing processes in industry). Following the thermodynamic study (Chapter 4) a detailed investigation into sphalerite and its leached products was undertaken in (Chapter 5), that lead to deriving intrinsic oxidation rate expressions for both the non-oxidative and oxidative leaching of sphalerite. These fundamentally derived rate expressions will then be used to model the reactive behaviour of sphalerite as obtained from experimental data. The speciation behaviour was used to model the solution phase behaviour during these leaching experiments.

The mechanism of sphalerite dissolution will be deduced by investigating the (1) thermodynamic driving forces, the (2) surface chemistry of the mineral, (3) electrochemical properties and the (4) mechanistic view of research. Based on the conclusions from these four research areas the phenomenological nature of sphalerite will be characterised and a mechanism of sphalerite dissolution will be proposed.

- Thermodynamics

It is appropriate to fist establish the driving force of mineral oxidation from a thermodynamic perspective. The driving force was firstly determined from Pourbaix diagrams, which utilise the electromotive force (EMF) of the half redox reaction couples and pH as the primary variable. Insights into the stability regions of solid and solution species at different solution potentials are obtained from these diagrams, from which the most probable metastable reaction may be deducted. Although these diagrams are useful to describe hydrometallurgical systems, their applicability is often restricted to geological time spans where kinetic factors, such as metastability and diffusion limitations are not dominant. The artificial nature of these diagrams should also be highlighted, since chemical species can be added and neglected as desired when constructing these diagrams (Steyl, 2012).

Other knowledge obtained from a thermodynamic perspective, include sulphur oxidation and rearrangement, melting and transition temperatures of mineral phases, and reaction equilibrium constants. Thermodynamics would also lead to insights into the stoichiometry of the zinc sulphide transformation reactions.

- Surface chemistry

The surface chemistry of sphalerite will lead to insights regarding the electric double layer, the space charge region and absorption tendency of aqueous ions on the mineral surface. Conclusions of the species interaction and mobility may be made, resulting in further insights to the probable mechanism occurring.

- Electrochemistry

Semiconducting properties of sphalerite characterises the electrochemical mechanism of dissolution. The electrochemical nature of the oxidative (incl. non-oxidative as described by Crundwell (2014a)) reactions will be investigated. This may lead to a polarisation curve of the elementary (half) reactions.

- Mechanistic views

Previous proposed leaching mechanism of sphalerite, under identical conditions, from various researchers will be examined, ranging from bulk reactions to elementary electron (or hole) transfer reaction steps. Their viewpoints and research results will ultimately strengthen the mechanistic paths proposed in this dissertation.

3.3 Experimental program

The literature review (Chapter 2) has highlighted different transportation and reaction steps involved during a heterogeneous reaction system. These transportation and reaction steps are influenced by the solution composition and to explain the dissolution behaviour of sphalerite batch tests were conducted in a previous study by Steyl (1999), while the conditions of each batch test were chosen so that the initial condition would dominate throughout the experiment.

The electrochemical model (defined in section 2.4) was adopted in various studies to explain the dissolution behaviour of sphalerite (as defined in Chapter 5). By attempting to mathematically relate the dissolution theories, accurate kinetic data and consideration of all possible rate controlling phenomena are required. The dissolution behaviour is also very specific to sphalerite concentrate and impurity levels (i.e. iron and other oxidants) present in the mineralogical structure.

To obtain the unique rate constants and to confirm (according to theory) the dependence of the leaching rate on selected species in solution, unique batch tests was performed. **The following experimental program was performed by Dr JDT Steyl (1994)**.

Kinetic leaching test under atmospheric conditions

Tests were performed in a glass vessel under accurate well controlled conditions. The apparatus consisted primarily of a glass vessel (5.8 litres), a hot plate, a reflux condenser, an overhead motor and impeller. Figure 3.2 shows the experimental setup and described below.

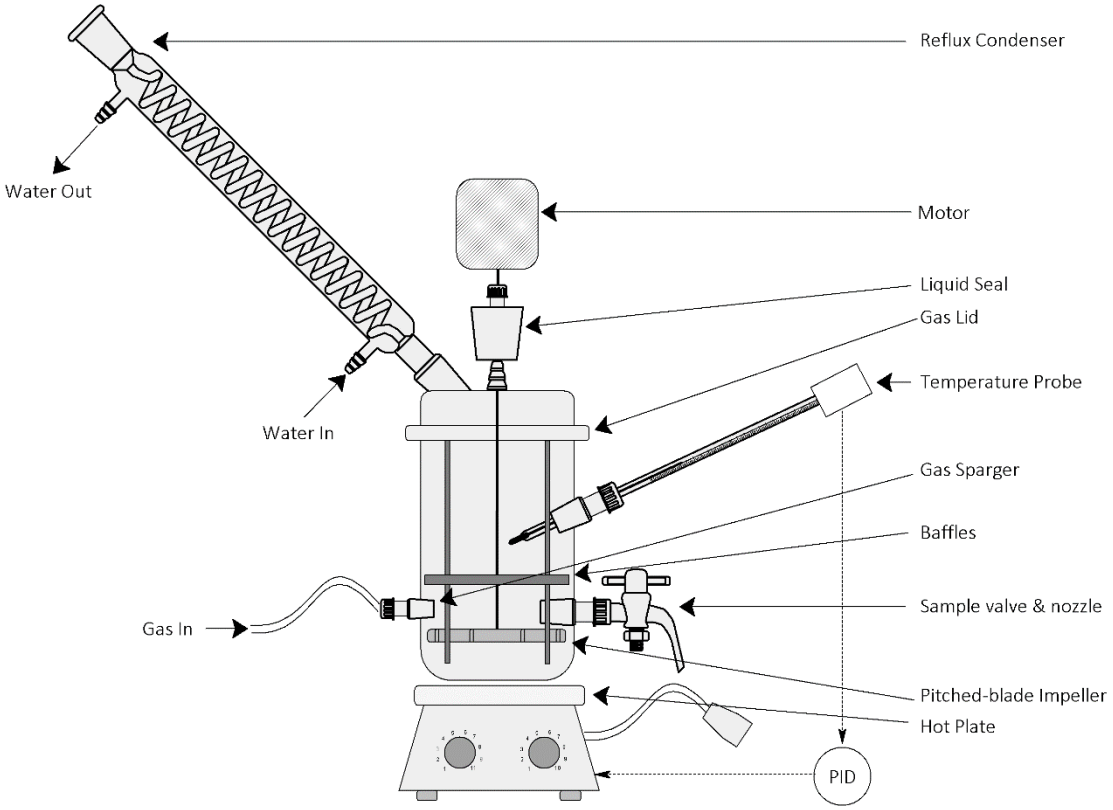

Figure 3.2: Reaction vessel and apparatus (experimental setup)

The pregnant leach solution was heated by a hot plate and controlled within 1 °C with a PID controller (RexC-100) and calibrated temperature probe (PT100). To prevent corrosion of the temperature probe, it was placed within a glass tube (filled with oil). A precision-grade mercury-filled glass thermometer was used in addition to the temperature probe controller, to check the temperature at regular intervals. Water evaporation loss to the environment was limited by the over-sized reflux condenser. An overhead motor was set at the required speed using a tachometer. The agitator consisted of a shaft, down-pumping pitched-blade impeller. The impeller was fitted through a liquid (water) seal to prevent evaporation to the atmosphere. Polypropylene (PP) baffles were fitted inside the vessel, which aided in mass-transfer and solid suspension. Gas was introduced to the reactor using a glass frit, fitted through the side of the

vessel. Samples were then taken through a glass valve and nozzle, also fitted on the side of the vessel at the impeller height.

The following experimental procedure was strictly adhered to:

The reactor vessel and peripherals (i.e. valves, sparger, impeller and baffles) were cleaned overnight in a hydrochloric acid (HCl) bath to remove traces of the sphalerite concentrate. The cleaned and dried reactor was then assembled on the hotplate and all the peripherals attached.

The pregnant electrolyte solution was prepared at 25 °C (room temperature), using accurately weighed analytical grade chemicals and deionized water. A measured pregnant leach solution volume, considering the initial head sample, was then charged into the reactor. Temperature control was switched on and set at the set point. Cooling water (of the reflux condenser) was opened at full capacity and the impeller speed set to the set point. During experimental tests where H_2S had to be sparged, the flowrate was adjusted using a needle valve. The reactor was left to stabilize at a temperature set point.

Before the solid material was added a head sample of the solution was taken, which served as a control (zero-standard) for the kinetic test and sample analysis. An accurately weighed solid sample was then charged into the reactor and the timer started. Solids was introduced into the reactor using a small PP holder that was dropped into the reactor. The solids dispersed immediately into the solution.

During the initial period of reaction, many samples were taken in short time intervals, that was used to evaluate in initial intrinsic reaction rate. A dot sample was always taken before the real sample used for analysis, which eliminated contamination of the sample solution left in the sample nozzle. Samples were filtered immediately using a Buchner funnel (under vacuum) and filter paper; and then cooled to 25 °C in a water-bath. During tests where H_2S gas was present (i.e. non-oxidative conditions), samples were vented, before sealing of the sample holders. All sampling equipment were thoroughly cleaned and dried before use.

Flame Atomic Absorption Spectroscopy (FAAS) was used to analyse all samples during the test program. Filtered residues were washed with deionized water, dried and kept for microscopic investigation.

The experimental program is subdivided into two subsections, *i.e*. tests performed under non-oxidative conditions (testwork C) and test performed under more oxidising conditions

(testworks D, E & F). The experimental program aimed first to establish the rate and mechanism of sphalerite dissolution and then to evaluate the change in rate that took place during the dissolution of sphalerite in sulphuric acid-ferric-ferrous solutions. The results are reported in Appendix C, D, E and F

3.4 Sphalerite intrinsic rate modelling

After quantifying a model for the solution phase (speciation), developing reaction mechanisms and intrinsic rate expressions as well as characterising the concentrate used during the experimental program; a rate model was derived using the insights and conclusions from these sections. The rate model was then used to optimize the rate parameters for sphalerite leaching. A detailed methodology regarding parameter optimisation and batch reactor modelling techniques (*i.e.* leaching extent) used for this work are presented in Chapter 7.

The extent of sphalerite dissolution was calculated for each batch experiment in the experimental program, mentioned in the previous section. The resulting extent data (presented in the form of figures in Appendix C, F, E and F) were used to regress the linear (equation 7.1) and non-linear model (equation 7.4). Rate parameter regression of the intrinsic rate expressions consisted of a two-fold strategy, using the curve-fitting methods (described in section 2.4.1). The first strategy consists of using the *curve-fitting: linear regression* method (see section 2.4.1) to optimize the rate parameters using the linearized SCM at the corresponding average solution composition. The second strategy used the *curve-fitting: non-linear regression* method by solving the differential model dynamically in Simulink (2016b) to obtain the refined optimal rate parameters. Rate parameter results of the linear regression method were used as initial input to the non-linear regression method. Both regression methods results were compared; and final intrinsic rate parameters were proposed in conclusion of this research.

All models were built in either Matlab (2016b) or Simulink (2016b), as specified in Chapter 7. The ode45 (Dormand-Prince) solver was selected to obtain a numerical solution of the differential equations. Relative and absolution tolerances of 1×10^{-10} were selected for all optimization routines, which corresponds to a 1 ppm concentration accuracy ($<1 \times 10^{-5} \frac{mol}{kg}$). The Simulink solver was also restriced to a maximum step size of 1 minute, while the steps were set to be variable in time. The fsolve and generic algorithm (ga) solvers (from Matlab's optimization tools) were used to obtain the minimum total sum of squared error (TSSE) of the selected training data from the experimental program, thus obtaining the intrinsic rate parameters of the kinetic expressions.

Chapter 4 Thermodynamic Modelling

4.1 Objective

The ability to predict solution species behaviour is crucial to the understanding and modelling of sulphide leaching kinetics, especially when considering the electrochemical nature of sphalerite in an aqueous solution containing ionic (oxidising) species.

The objective of this chapter is to develop a self-consistent thermodynamic model of the various sub-systems applicable to the $ZnSO_4 – Fe_2(SO_4)_3 – FeSO_4 – H_2SO_4 – H_2O$ reactive system upon which the kinetics of ZnS oxidation with Fe^{3+} and H^+ can be interpreted. Of primary importance to the modelling of kinetic processes is the ability to predict solution speciation. Hence, the focus of the thermodynamic model is to capture the dominant trends in the systems' speciation.

Within this approach, only experimentally verified species from the literature are to be considered and a minimum number of parameters included to capture the solution chemistry effectively. It is acknowledged that only a simplified representation of the underlying chemistry will be estimated by the model. Given these constraints imposed on the thermodynamic model and the application of the model in the modelling of reaction kinetics, the absolute errors between the model and measured data are expected to be larger than typically observed in thermodynamic modelling studies. Ultimately, errors in the thermodynamic model will be absorbed into the kinetic model parameters. This approach facilitates a reliable basis on which to develop, mechanistically, the important aspects of the oxidative and non-oxidative reactions.

The thermodynamic model is developed based on the research and thermodynamic framework of Biley (2015), which characterised the $Fe_2(SO_4)_3 – FeSO_4 – H_2SO_4 – H_2O$ system. The paper of Steyl (2009) presented a detailed description of the thermodynamics and speciation of $Metal(II)SO_4 – H_2SO_4 – H_2O$ systems for the purpose of kinetic modelling of chemical processes in acid solution at temperatures < 200 °C and was also incorporated into this study. Additional thermodynamic data are gathered from various researches (Albright *et al.*, 2000; Archer & Rard, 1998; Clegg *et al.*, 1994; Clegg & Brimblecombe, 1995; Guendouzi *et al.*, 2003; Guerra & Bestetti, 2006; Holmes & Mesmer, 1992, 1983; Horváth, 1985; Hovey *et al.*, 1993; Li *et al.*, 2014; Liu & Papangelakis, 2005b; Pitzer, 1972; Pitzer *et al.*, 1977; Rard, 1997; Rard & Clegg, 1999; Reardon & Beckie, 1987; Robinson & Jones, 1936; Robinson & Stokes, 1959; Rudolph *et al.*, 1997, 1999a,a; Rudolph & Pye, 1999; Rumyantsev *et al.*, 2004; Scatchard *et al.*, 1938; Snipes *et al.*, 1975; Sobron

et al., 2007; Tartar *et al.*, 1941; Tosca *et al.*, 2007; Miladinović *et al.*, 2002; Velázquez-Rivera *et al.*, 2006; Baes *et al.*, 1993; Hefter, 2006; Yang *et al.*, 2016, 2014).

4.2 Solution speciation

The selection of a minimum number of solution species to adequately describe the thermodynamic behaviour is warranted, particularly considering the general lack of data describing these species. On the basis of reviewing the literature of research done on similar systems and equilibrium spectroscopic measurements (Biley, 2015), a good basis for the selection of the most important species in the various sub-systems has been developed. A detailed breakdown of the solution species structure is presented in Table 4.1.

Table 4.1: Primary and secondary species included into thermodynamic model

Reagent	Primary Species		Secondary Species
H_2SO_4	H^+	SO_4^{2-}	HSO_4^-
$ZnSO_4$	Zn^{2+}		$ZnSO_4^0$
$FeSO_4$	Fe^{2+}		$FeSO_4^0$
$Fe_2(SO_4)_3$	Fe^{3+}		$FeSO_4^+$
			$Fe(SO_4)_2^-$
		H_2O	$Fe(OH)_n^{3-n}$

The sulphate and bisulphate are important species in all sub-systems. Besides the obvious primary species formed from the reagents, a system containing $ZnSO_4$ and $FeSO_4$ reagents will have their respective contact ion pairs (CIP's) in noticeable amounts present, while for the $Fe_2(SO_4)_3$ system, it is expected that both $FeSO_4^+$ and $Fe(SO_4)_2^-$ are present. Additionally, the effect of hydrolysis of ferric is included, due to Fe^{3+} highly oxidative nature (section 4.2.1). Biley (2015) suggested to include a single surrogate $Fe(OH)_n^{3-n}$ specie into the model to account for all hydrolysis effects. The thermodynamic data for the species are given in appendix A.1.

4.2.1 Hydrolysis

As mentioned above hydrolysis of ferric is expected to take place, as found within the literature. This section aims to provide supporting evidence of ferric hydrolysis, while ferrous and zinc hydrolysis are assumed to be negligible.

Ferrous and zinc ions are expected to behave similarly in solution, whereas a significant difference in behaviour for ferric is anticipated. The similarities and differences are explained by their atomic electron structure. This is exemplified when comparing the magnitude of stability

constants of the hydrolysis reactions. Equilibrium data chosen for this study originated from the HSC (2006) database and resulted in the following thermodynamic values for the hydrolysis reactions, presented in Table 4.2.

Table 4.2: Hydrolysis reactions with associated equilibrium constants at 25 °C

Reactions	$\log_{10} K^0$
Zinc	
$Zn^{2+} + H_2O \rightleftharpoons ZnOH^+ + H^+$	-7.83
$Zn^{2+} + H_2O \rightleftharpoons Zn(OH)_2^0 + 2H^+$	-28.02
Ferrous	
$Fe^{2+} + H_2O \rightleftharpoons FeOH^+ + H^+$	-9.32
$Fe^{2+} + H_2O \rightleftharpoons Fe(OH)_2^0 + 2H^+$	-30.2
Ferric	
$Fe^{3+} + H_2O \rightleftharpoons FeOH^+ + H^+$	-2.17
$2Fe^{3+} + 2H_2O \rightleftharpoons Fe_2(OH)_2^{4+} + 2H^+$	-2.91
$Fe^{3+} + 2H_2O \rightleftharpoons Fe(OH)_2^+ + 2H^+$	-6.88
$Fe^{3+} + 3H_2O \rightleftharpoons Fe(OH)_3^0 + 3H^+$	-44.2

The stability constants of the first hydrolysis product formation (*i.e.* hydroxyl species) of zinc and ferrous are approximately five and seven orders of magnitude smaller than the equivalent ferric hydroxyl species, respectively. Zinc and ferrous hydroxide (*i.e.* second hydrolysis product, $M(OH)_2^0$, CIP) stability constants are too small to even be considered. The importance of Zn^{2+} and Fe^{2+} hydrolysis products for solution modelling purposes in multi-electrolyte solutions is assumed to be negligible, especially in concentrated acidic systems. Albeit, aqueous ferric systems have a strong tendency to hydrolyse even at relatively high acid concentrations (pH 2-3) and, as seen in Table 4.2, can form many hydrolytic species, which is influenced by the solution composition and temperature.

To avoid unnecessary complication, a simple surrogate approach for Fe^{3+} hydrolysis was adopted in which only a single $Fe(OH)_n^{3-n}$ species was included in the thermodynamic framework, similar to the study of Biley (2015).

4.2.2 Metal-sulphate speciation

Zn^{2+} and Fe^{2+} have the tendency to form contact ion pairs (CIP's) in sulphate solutions (see section 2.1.1 for details). Raman spectroscopy studies of $FeSO_4$ solutions highlighted that the $FeSO_4^0$ CIP was only formed to a minor extent at room temperature and hydrated Fe^{2+} (*i.e.* typically or most probable $Fe(H_2O)_6^{2+}$) dominates the solution chemistry (Biley, 2015; Rudolph *et al.*, 1997; Sobron *et al.*, 2007). Rudolph *et al.* (1999a,b) investigated aqueous $ZnSO_4$ solutions inner- and outer-sphere complexes from 8 °C to 165 °C by Raman- and infrared-spectroscopy and estimated the association to the $ZnSO_4^0$ CIP to be 10 %, 14% and 30 % at 25 °C, 85 °C and 165 °C, respectively. These studies have highlighted the formation of doubly-separated (2SIP) and singly-separated (SIP) outer-sphere complexes as well as the contact ion pairs in divalent ionic solutions, although they also stated the general difficulties associated with measuring these ions pairs and forewarned large uncertainties.

Typically, studies modelling the thermodynamic behaviour of electrolyte solutions do not take recognition of CIP and adopt only an ion-interaction approach. Steyl (2009, 2012) and Biley (2015) highlighted the benefits of including the contact ion pairs within a modelling framework to properly account for the kinetic interactions of iron-sulphate oxidation and iron precipitation at elevated temperatures. In this study, considering the concentrated sulphate solution and elevated temperatures, it is likely that the Zn^{2+} and Fe^{3+} ions will be captured into neutral species and may be significant for the behaviour of sphalerite oxidation kinetics. Hence, the effects of the $ZnSO_4^0$ and $FeSO_4^0$ CIP's are included within the model.

Stability constants of CIP's (β^0) are significantly lower than the overall stability (equilibrium) constants (K^0) in systems where outer-sphere interactions are important (Table 4.3). The difference in value is formed from the definition of the constant (see section 2.1.3 and Rudolph et al., 1999a; Hefter, 2006). In a thorough review of divalent metal sulphate systems, and supporting static quantum calculations, Steyl (2012) proposed a value of $\log_{10}\beta^0 = 1.5$ for the association of $MgSO_4^0$ and this value was adopted in this study and not the value of 2.2 typically taken for total speciation studies, shown in Table 4.3.

In order to model divalent sulphates in metallurgical solutions, it has been proposed by Steyl (2009) to use the $MgSO_4$ aqueous system as surrogate system. This approach is followed since substantially more thermodynamic data are available in open literature for the $MgSO_4$ system, while there is general lack in data for $ZnSO_4$, as well as the remarkable similarity in the thermodynamic properties (*e.g.* the overall equilibrium constants in Table 4.3) and activities between $MgSO_4$ and other transition metal-sulphates, *i.e.* zinc, copper and iron.

Table 4.3: Reported divalent CIP formation thermodynamic values at 25 °C from the literature

Reactions	[a]$\log_{10} K^0$	[b]$\log_{10} \beta^0$
$Mg^{2+} + SO_4^{2-} \rightleftharpoons MgSO^0_{4\,(aq)}$	2.23	≈ 1.5
$Fe^{2+} + SO_4^{2-} \rightleftharpoons FeSO^0_{4\,(aq)}$	2.20	≈ 1.5
$Cu^{2+} + SO_4^{2-} \rightleftharpoons CuSO^0_{4\,(aq)}$	2.26	≈ 1
$Zn^{2+} + SO_4^{2-} \rightleftharpoons ZnSO^0_{4\,(aq)}$	2.49	≈ 1.5

[a]Values taken from Biley (2015) and [b]values taken from Steyl (2009)

In a $Fe_2(SO_4)_3$ solution hydrolytic Fe^{3+} species may exist at low pH in addition to several ferric sulphate species. A $Fe_2(SO_4)_3$ solution is a complex system associated with various oxidised ionic species, with the structure of these complexes generally not well understood nor applied to kinetic modelling studies. Usually, convenient stoichiometry is assumed that capture the trends observed in experimental data. Hence, within this study's thermodynamic framework the association of ferric-sulphate is done, similarly to the study of Biley (2015), by including only the two most important contact ion pairs, namely $FeSO_4^+$ and $Fe(SO_4)_2^-$. The recommended stability constants and thermodynamic values are presented in Table 4.4.

Table 4.4: Thermodynamic data for $Fe_2(SO_4)_3$ system speciation at 25 °C

Reaction	ΔG^o (kJ/mol)	ΔH^o (kJ/mol)	ΔS^o (kJ/mol.K)	ΔC_p^o (kJ/mol.K)	$\log_{10} \beta^0$
$Fe^{3+} + SO_4^{2-} \rightleftharpoons FeSO_4^+$	-23.75	26.11	167.37	453.79	4.04
$Fe^{3+} + 2SO_4^{2-} \rightleftharpoons Fe(SO_4)_2^-$	-30.7	38.8	235.17	781.62	5.38

An important consideration for the thermodynamic modelling approach is that equilibrium constants typically reported in literature are derived from total solution measurements (*i.e.* calorimetry, potentiometry etc.) which include the contribution of SIP and 2SIP's outer-sphere complexes. For this study, however, only the explicit contact ion pairs are of interest. Their chemical behaviour is different to that of outer-sphere complexes, which could influence the electrochemical behaviour. The stability constant is therefore defined as the ratio of CIP to the relevant free ions in solution and is directly measured by Raman spectroscopy.

Six speciation equilibrium reactions are assumed to occur and are tabulated in appendix A.3.1 with each equilibria's standard state stability constant (β^0) and thermodynamic properties used within the thermodynamic model. The density function (equation A.2) was used to extrapolate each CIP stability constant using the standard values, ΔH^0 and ΔC_p^0 recommended by Biley

(2015), see Table A.2. The temperature dependence of these ionic species are generally not well known nor defined in the literature, but the thorough investigation by Biley (2015) provides great confidence in the accuracy and validity of these values used within this study.

4.3 Computational methodology

Section 2.1.5 broadly defined three types of solution modelling classes which vary in their treatment of the electrolyte entities and stated the benefits and short-comings of the Pitzer model. Explicit recognition of speciation (*i.e.* formation of contact ion pairs) that include complexation equilibria was found to be advantageous to the modelling of real hydrometallurgical systems. The Pitzer model was favourable towards the modelling of an electrolyte solution which can be extended to include the explicit recognition of contact ion pars, and therefore was chosen for this study to model the activity coefficient behaviour. Both these factors form the foundation from which the thermodynamic model was constructed.

The thermodynamic model consists of a *fixed-point iteration* loop (Gilat & Subramaniam, 2011) that solves the extent of every equilibrium reaction (Figure 4.1). This is achieved through the *Pitzer function* (f^{Pitzer}) that calculates each species activity coefficient (appendix A.4) and an *extent function* (f^{extent}) that determines the speciation of each equilibria (appendix A.3). For the *extent function*, the equilibrium constant of each speciation reaction is rewritten in terms of the reaction extents which results in a convoluted polynomial. The resulting (valid) polynomial root is the newly calculated reaction extent (see appendix A.3.1 for function derivation and equations, as well as a blow flow diagram of the calculation method). A concise description of the Pitzer model equations, with the virial expansion terms applicable to this study, are presented in appendix A.4.1. The *Pitzer function* takes the molalities and temperature as input and calculates the activity coefficients for the relevant species. The Pitzer model parameters were either fixed or allowed to vary with temperature, over the region of 25 – 100 °C, as follows (with n ≤ 2 and T_{ref} = 298.15 K):

$$Par_{Pitzer}(T) = \sum_{i=1}^{n} p_{i-1}\left(T - T_{ref}\right)^{i-1} = p_0 + p_1 \cdot \left(T - T_{ref}\right) \qquad 4.1$$

Figure 4.1 presents a flow diagram outlining the iterative calculations followed to solve the thermodynamic equilibrium model. The function takes the temperature and initial molalities as input and calculates the resulting equilibrium concentration of each species in Table 4.1.

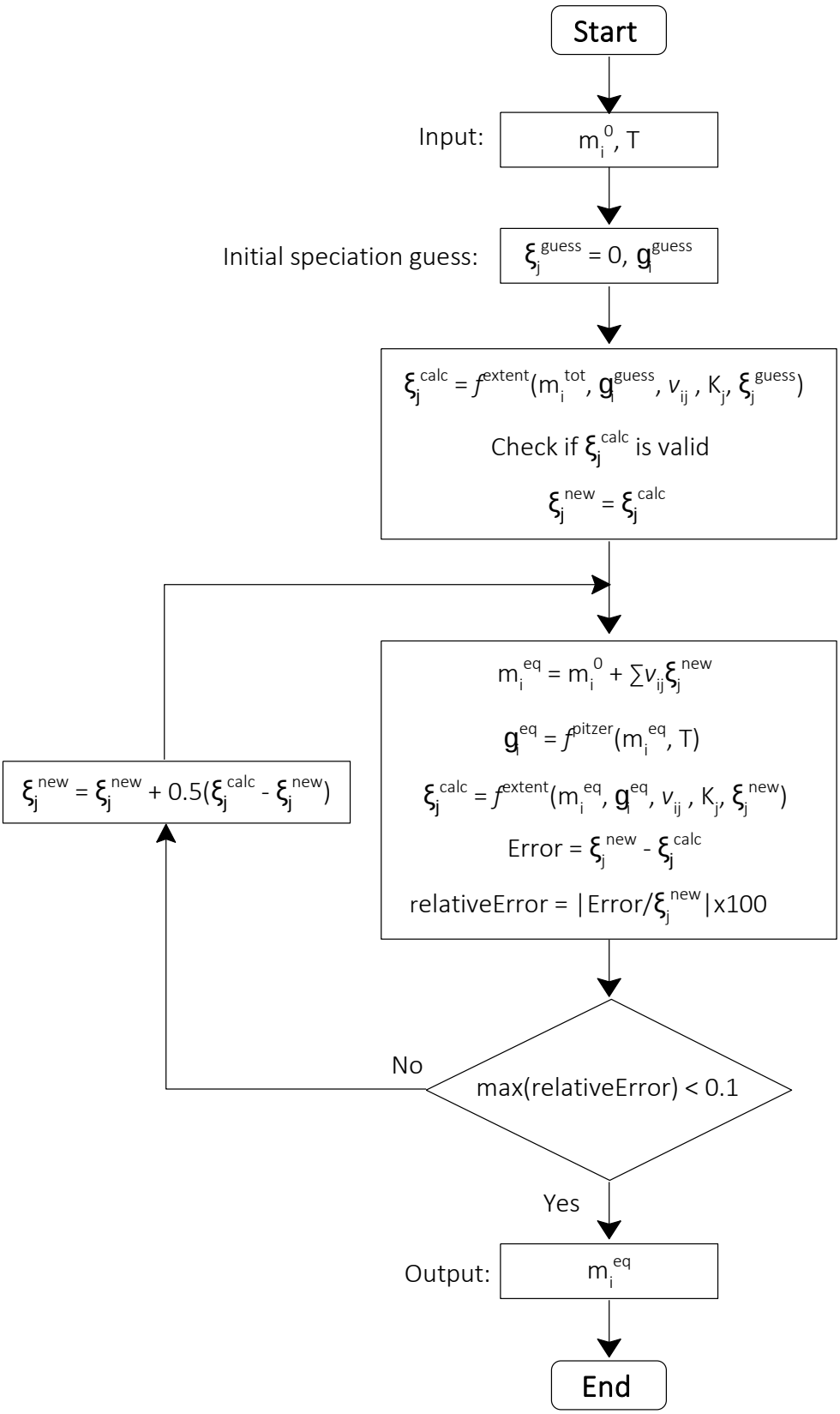

Figure 4.1: Thermodynamic model calculation methodology flow diagram. The inner calculations contain the extent and Pitzer functions as outlined in Appendix A.3 and A.4, respectively.

4.4 Model development and validation

The thermodynamic model was applied to the $ZnSO_4$ – $FeSO_4$ – $Fe_2(SO_4)_3$ – H_2SO_4 – H_2O system on which binary ($\beta^{(i)}$) and ternary (C_i^{ϕ}) model parameters could be regressed. A key focus was to reduce the number of model parameters as much as possible to avoid over-fitting and improve the capability of model extrapolation. Binary sub-systems (*e.g.* $ZnSO_4$ – H_2O) are first regressed independently of one other to obtain their interaction parameters, upon which the ternary sub-systems (*e.g.* $ZnSO_4$ – H_2SO_4 – H_2O) are applied and selected binary and ternary parameters of the ternary sub-system species (*e.g.* Zn^{2+} – HSO_4^-) fitted to the data. Albeit, model accuracy was not a primary focus, parametrisation of the thermodynamic model produced accurate results within the concentration range of this study's objective, whilst keeping the model as simple as possible.

Data from various sources, as listed in section 4.1, were gathered whereupon the thermodynamic model was regressed. The large set of data from various sources extending over a decade of research studies, which compared remarkably well to each other, validates the accuracy and precision of the data and observed speciation trends.

4.4.1 H_2SO_4 – H_2O

The sulphuric acid – water system is probably the most important sub-system in acidic sulphate solutions and must be modelled with great accuracy, since most other sub-systems is regressed upon the parameters obtained from this system. Fortunately, aqueous sulphuric acid solutions are well documented in the literature with several speciation datasets available for regression.

Clegg *et al.* (1994) showed by means of Raman spectroscopic studies that the first dissociation of H_2SO_4, reaction 4.2, is basically complete in solution concentrations smaller than 40 g/L at room temperature. Likewise, $H_2SO_4^0$ constitutes a negligible amount at temperatures below 100 °C (Biley, 2015; Liu & Papangelakis, 2005b; Steyl, 2009). Thus, like most hydrometallurgical studies the first dissociation (or second protonation of the acid) is assumed to be complete. However, the second dissociation of bisulphate (reaction 4.3) is significant especially at temperatures below 100 °C and was incorporated into the model.

$$H_2SO_4 \longrightarrow H^+ + HSO_4^- \qquad 4.2$$

$$HSO_4^- \rightleftharpoons H^+ + SO_4^- \qquad 4.3$$

Formulation of the sulphuric acid complexation model follows that of Steyl (2009). The dissociation (equilibrium) constant and thermodynamic properties of reaction 4.3 are given in Table A.2 (Dickson *et al.*, 1990; Steyl, 2009). Optimized parameters for this system are presented in Appendix A.4.2. The overall fit gave an average absolute relative error (AARD, see Appendix G for definition of errors) of 3.43 %, whilst the model behaviour deviated from experimental data at higher concentrations (> 3 mol/kg). No additional model parameters are warranted, since the acid concentration never exceeded 1.3 M.

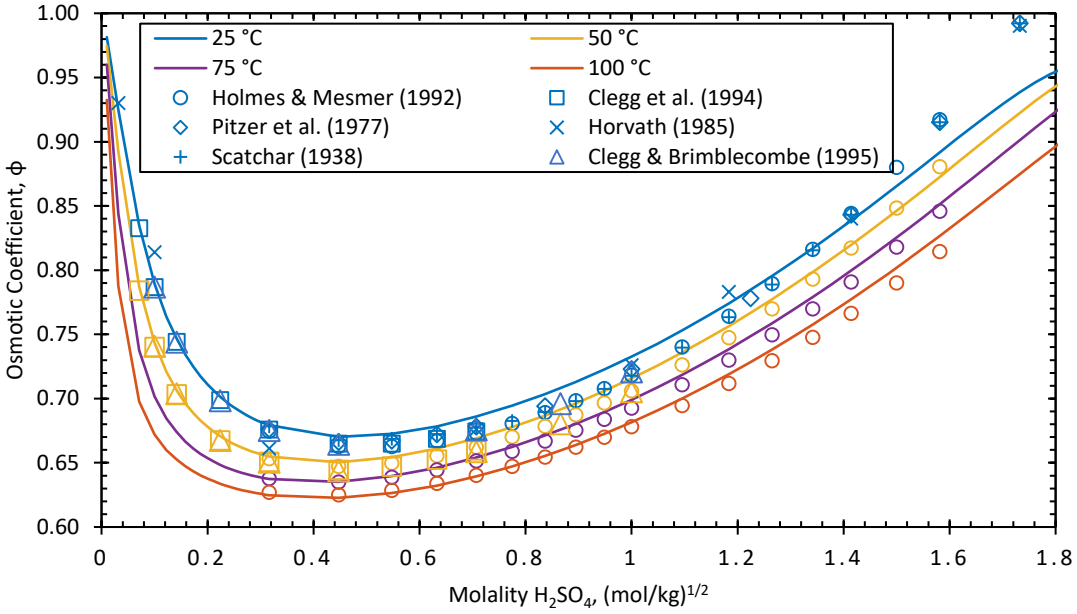

Figure 4.2: Comparison between the reported experimental values and the model output of the osmotic coefficient for the $H_2SO_4 – H_2O$ system. Note the square root of the concentration.

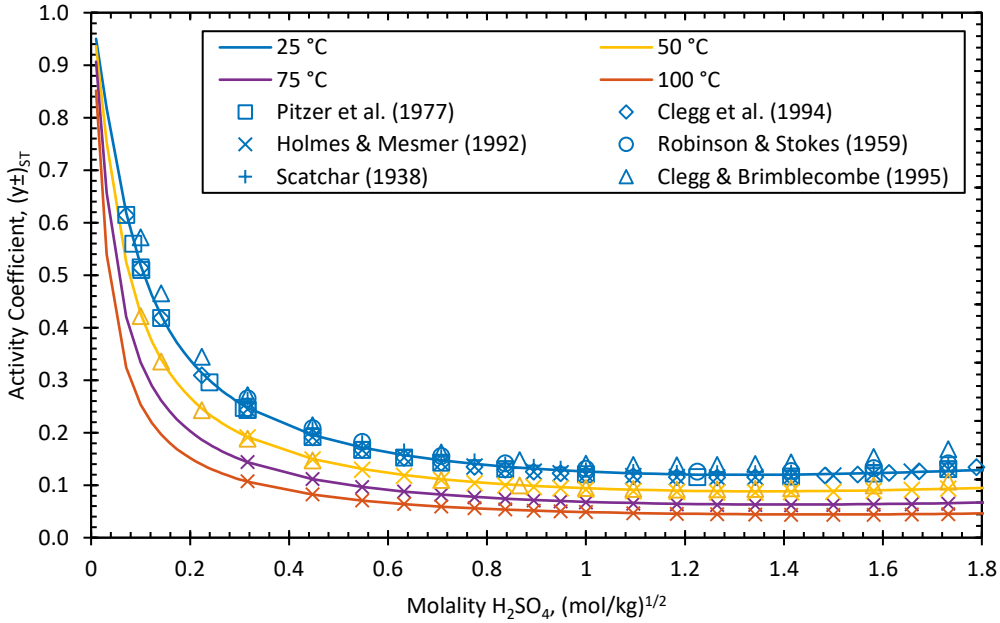

Figure 4.3: Comparison between the reported experimental values and the model output of the mean activity coefficients for the $H_2SO_4 – H_2O$ system. Note the square root of the concentration.

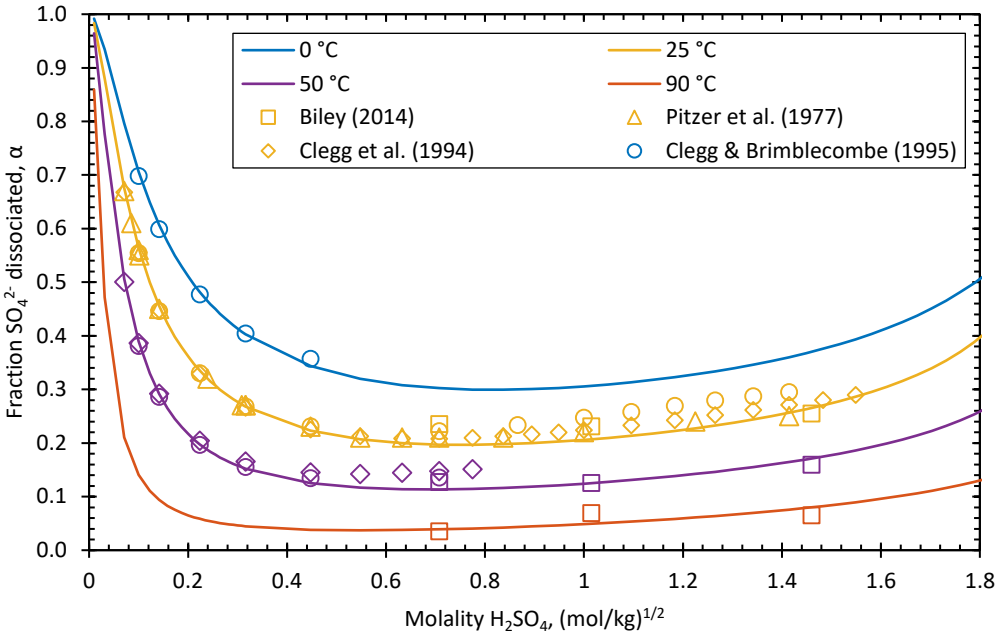

Figure 4.4: Comparison between reported experimental values of the fraction HSO_4^- dissociated and the model output, presented as fraction free SO_4^{2-}. Note the square root of the concentration.

4.4.2 $ZnSO_4 - H_2O$

As mentioned previously, divalent metal sulphate solutions are usually modelled using the $MgSO_4$ surrogate approach and was also adopted into this project by using the Pitzer model parameters of Steyl (2009) and optimizing the parameter to fit the more recent data selected from this study (Yang *et al.*, 2014, 2016). The optimized Pitzer parameters (appendix A.4.2) model output and literature data are presented in Figures 4.5, 4.6, 4.7 and 4.8

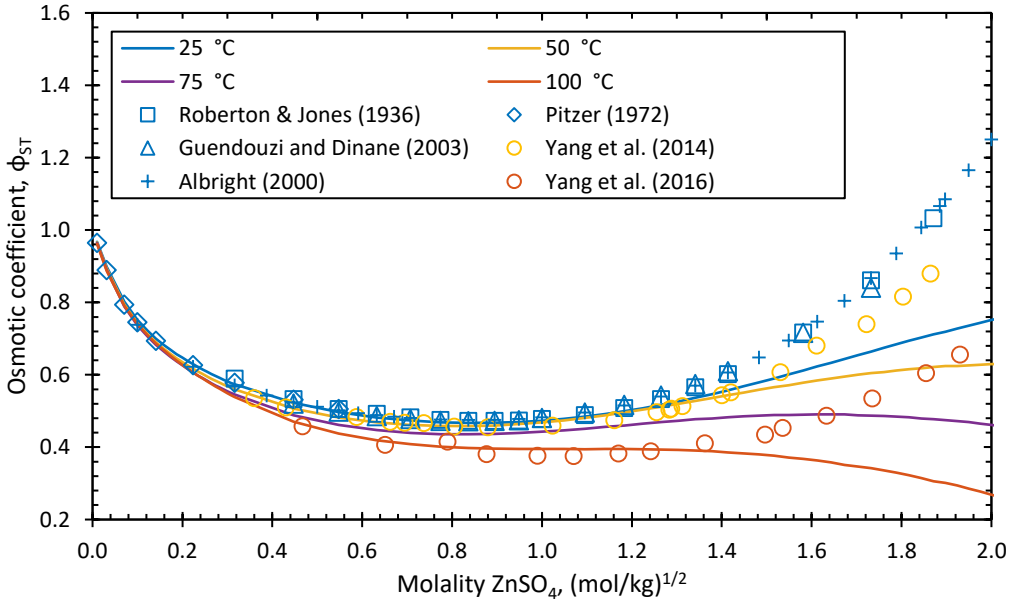

Figure 4.5: Comparison between the reported osmotic coefficients and model output for the $ZnSO_4$-H2O system. Note the square root of the concentration

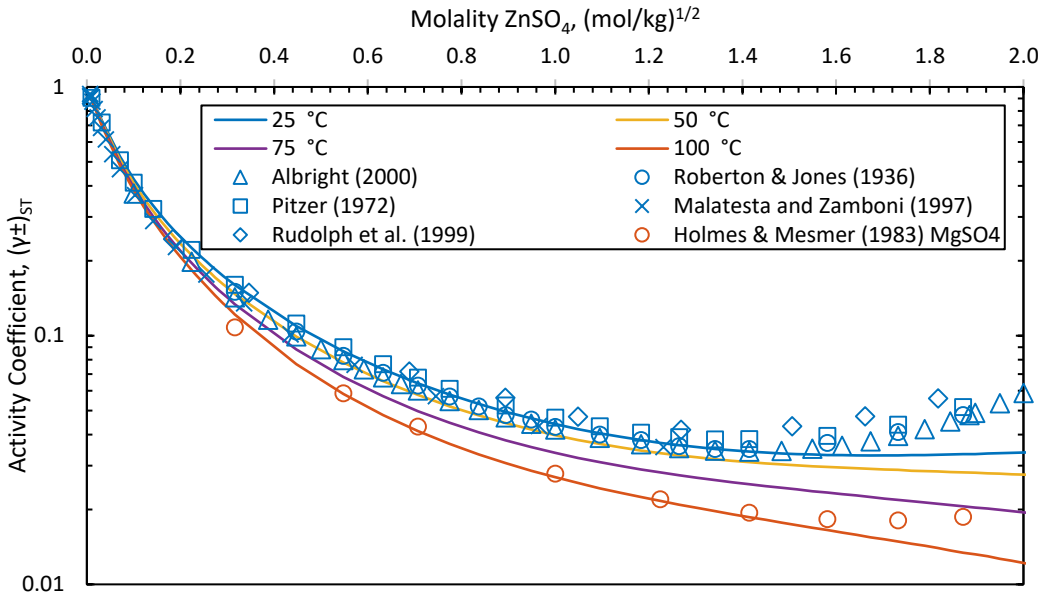

Figure 4.6: Comparison between the reported values and the model output of the mean activity coefficients for the $ZnSO_4$-H2O system. Note the square root of the concentration. The y-axis is presented in the logarithmic scale to improve presentation of data.

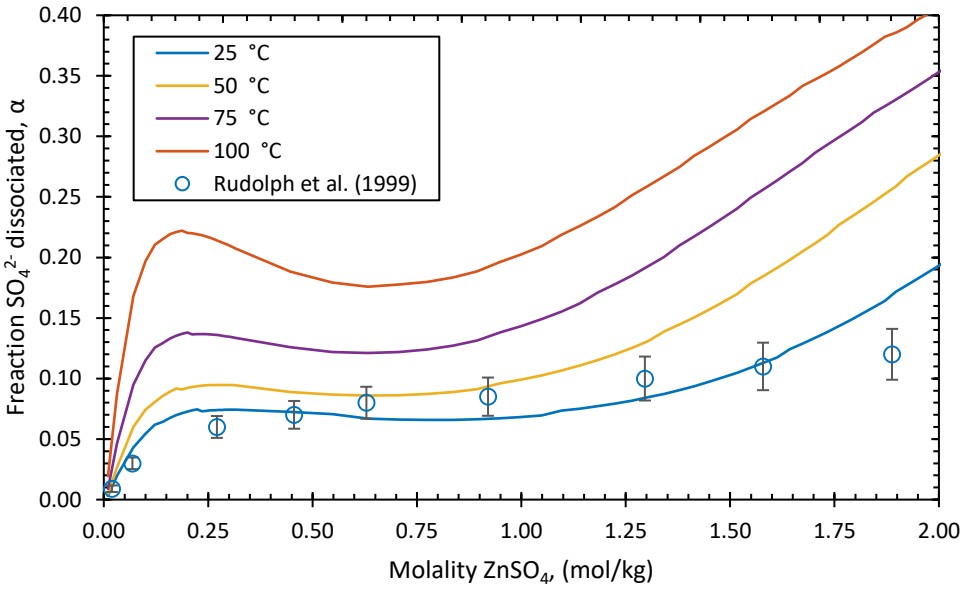

Figure 4.7: Comparison between reported experimental values of the fraction $ZnSO_4$ dissociated and the model output, presented as fraction free SO_4^{2-}. Note the square root of the concentration. Uncertainty estimated by t-statistic propagation from Rudolph et al. (1999a), see appendix G.1.

The thermodynamic model fits the data accurately up to 2 mol/kg $ZnSO_4$. As seen from the figures above, there is very little difference in $ZnSO_4$ speciation between 25 – 50 °C, but with increasing temperature up to 100 °C the effect of $ZnSO_4^0$ becomes significant. This trend is clearly observable from Figure 4.8, showing the fraction sulphate dissociated at various temperatures. Hence, inclusion of the $ZnSO_4^0$ CIP during kinetic modelling is vital.

Speciation trends in Figures 4.7 and 4.8 is not quite captured by the thermodynamic model. Predicted fractional dissociation follows a cubic form, which is an expected behaviour from the inclusion of the ternary interaction parameter of the Pitzer model. Deviation from Rudolph's et al. (1999a) fractional dissociation spectroscopy data becomes greater with increasing temperature, that may be due to the fact that the p_1 values was regressed on the $MgSO_4$ system data. Nevertheless, Raman spectroscopy is known to have quite a significant uncertainty and since the general trends are captured by the model it is assumed to be sufficient for this project.

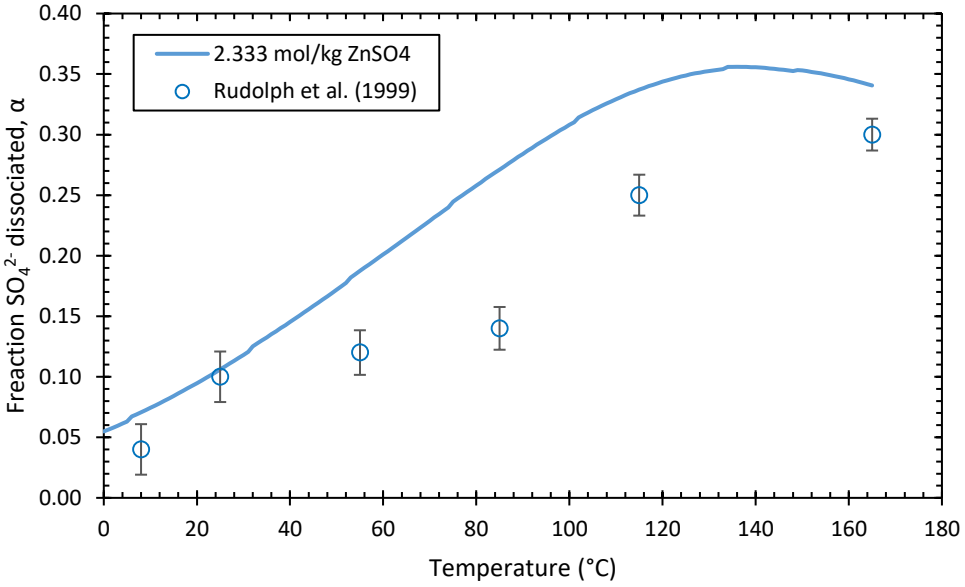

Figure 4.8: Comparison between reported experimental values of the fraction $ZnSO_4$ dissociated and the model output, presented as fraction free SO_4^{2-}, at various temperatures. Reported data was obtained by Raman spectroscopy and uncertainty estimated by t-statistic propagation from Rudolph et al. (1999a), see appendix G.1.

4.4.3 $ZnSO_4 – H_2SO_4 – H_2O$

With the $H_2SO_4 – H_2O$ and $ZnSO_4 – H_2O$ parameters obtained the ternary $ZnSO_4 – H_2SO_4 – H_2O$ systems interaction parameters can now be obtained. Initial Pitzer parameters are again obtained from Steyl (2009) and optimized to selected data from the literature. Tartar et al. (1941) produced accurate isopiestic data and was used to validate the thermodynamic model output. The species' activity results are shown in Figures 4.9, 4.1 and 4.11.

The model predicts the activities exceptionally well between reagent concentrations of 0 – 1.5 mol/kg $ZnSO_4$ and 0 – 2 mol/kg H_2SO_4. These valid concentration regions are partly due to the constraints of the underlying sub-systems limitations (*i.e.* valid concentration regions) and are more than sufficient so that all the species molalities are within these concentration regions.

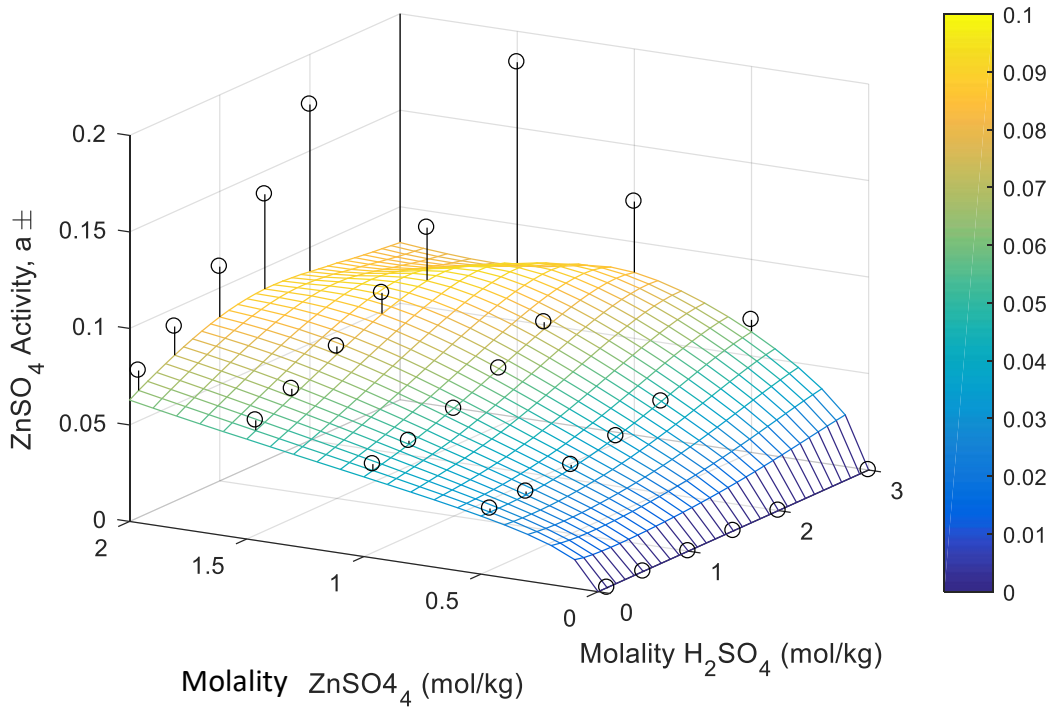

Figure 4.9: Mean activity of zinc sulphate in the ternary $ZnSO_4$-H_2SO_4-H_2O system from the study of Tartar et al. (1941), surface represents the thermodynamic model. AARD = 5.9 %

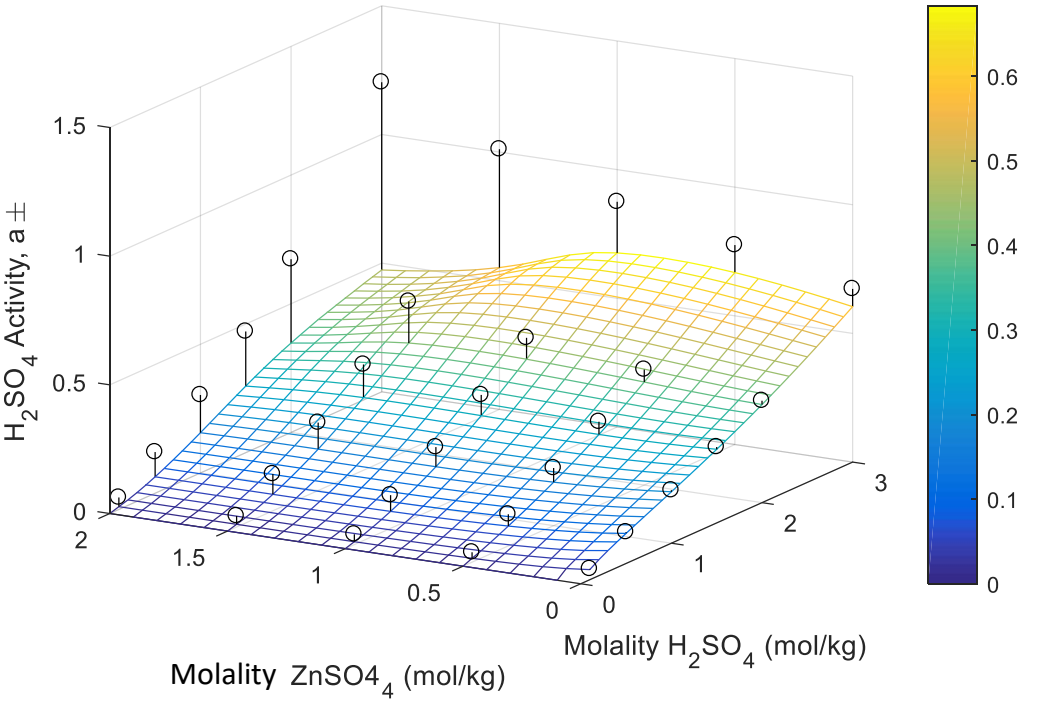

Figure 4.10: Mean activity of sulphuric acid in the ternary $ZnSO_4$-H_2SO_4-H_2O system from the study of Tartar et al. (1941), surface represents the thermodynamic model. AARD = 22.5 %

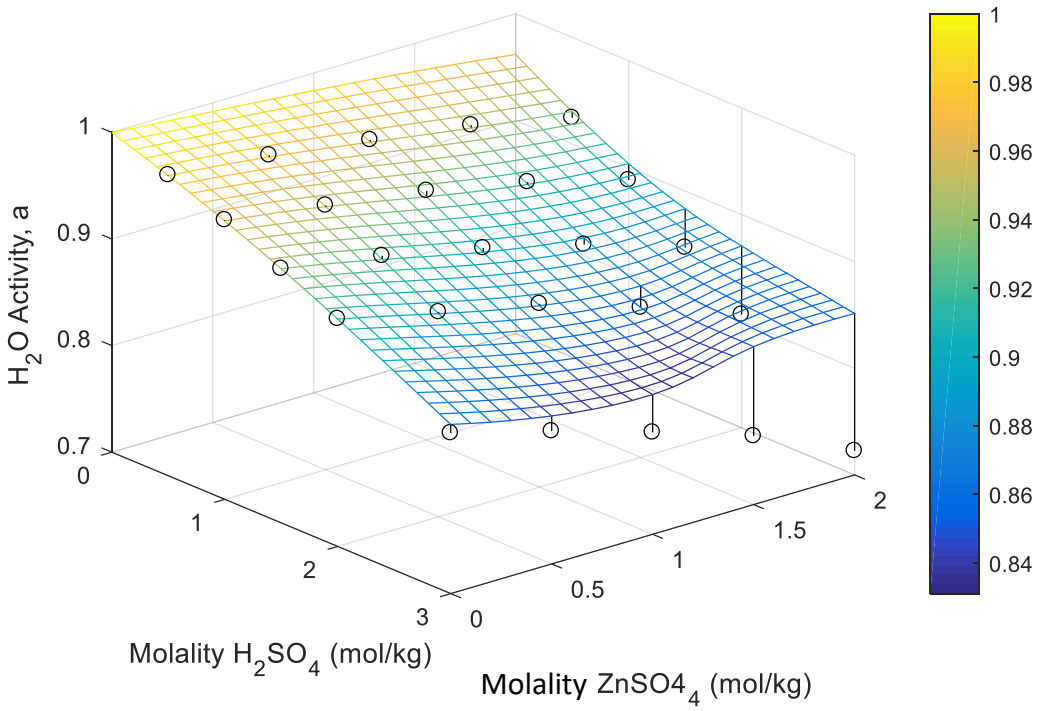

Figure 4.11: Water activity in the ternary $ZnSO_4$-H_2SO_4-H_2O system from the study of Tartar et al. (1941), surface represents the thermodynamic model. AARD = 0.34 %

4.4.4 $FeSO_4 – H_2O$

The $FeSO_4 – H_2O$ systems' Pitzer parameters were obtained from Biley (2015), who used a $FeSO_4^0$ Raman spectroscopy, activity and osmotic coefficient data in combination with $MgSO_4^0$ osmotic and activity coefficient data as enhancement to concentration and temperature regions where there is a general lack of $FeSO_4^0$ data. As discussed in section 4.2.2, a good estimate for the stability constant of the CIP (reaction 4.4) is $\log_{10}\beta^0 = 1.5$, slightly lower than constants typically reported by classical thermodynamic studies (Biley, 2015).

$$Fe^{2+} + SO_4^- \rightleftharpoons FeSO_4^0 \qquad 4.4$$

The thermodynamic properties and Pitzer model constants obtained from Biley (2015) are given in Table A.2. To validate the working of the model and accuracy of the thermodynamic model, literature Raman spectroscopy, activity and osmotic coefficient data were collected and plotted agents the modelled system in Figures 4.12, 4.13 and 4.14. As expected the model fitted the data remarkably well for $FeSO_4$ reagent concentrations of 0 – 3 mol/kg. Again, a cubic form of the fraction $FeSO_4^0$ CIP formed is obtained by the Pitzer model and the speciation of $FeSO_4$ was not perfectly accurate. Nevertheless, the objective is to keep the model simple and to capture the most relevant trends as accurately as possible, thus these results are acceptable for the modelling of sphalerite leaching under atmospheric conditions.

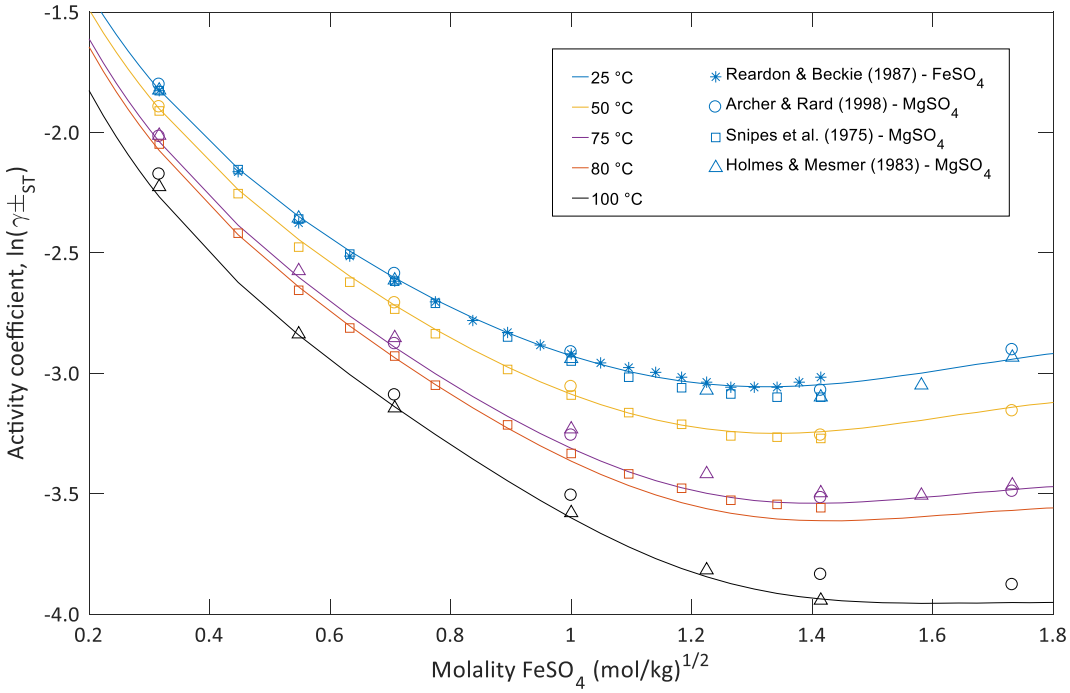

Figure 4.12: Model activity characterisation of $FeSO_4$ and surrogate $MgSO_4$ thermodynamic data from 25-100 °C. Note the square root of concentration and logarithmic of the activity coefficients.

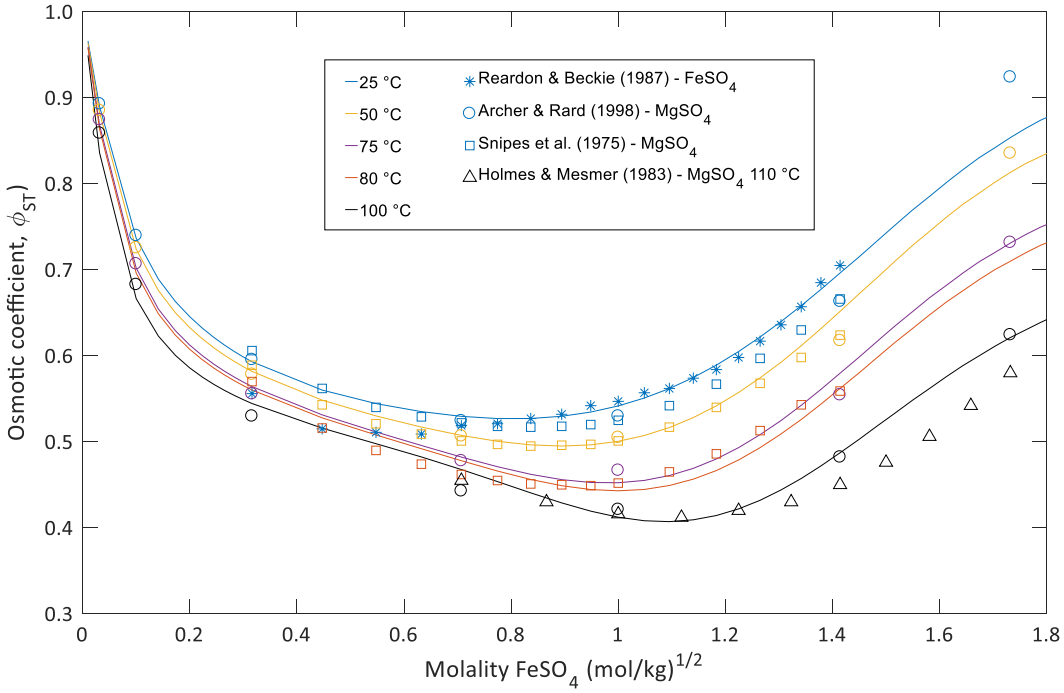

Figure 4.13: Model osmotic coefficient characterisation of $FeSO_4$ and surrogate $MgSO_4$ thermodynamic data from 25-100 °C. Note the square root of concentration.

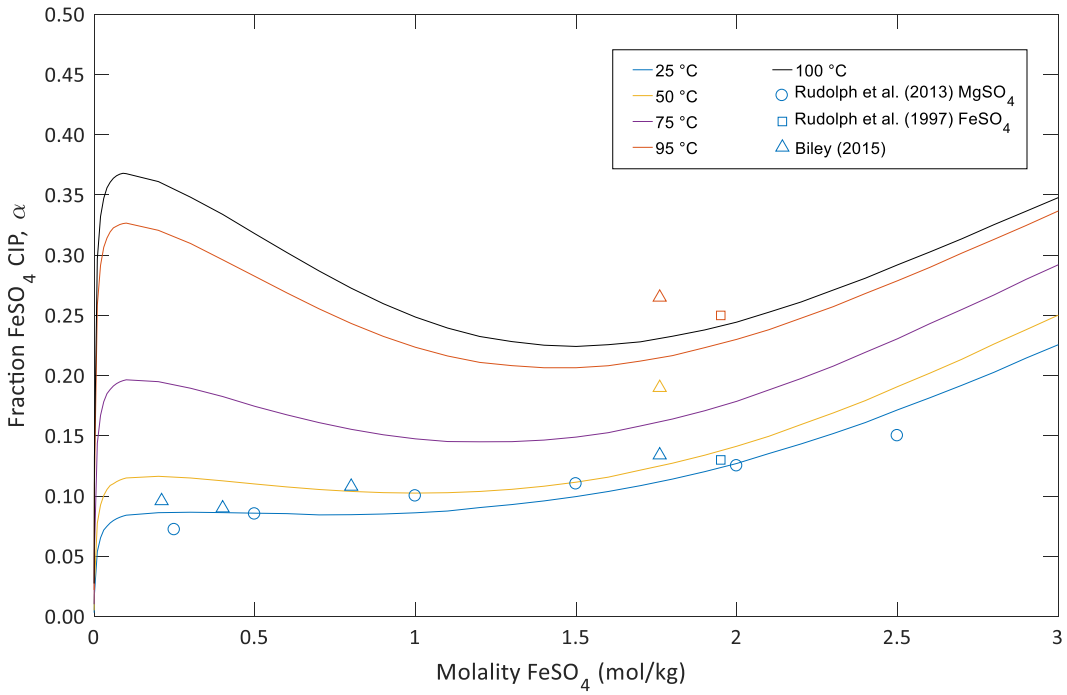

Figure 4.14: Model characterisation of fraction of the $FeSO_4^0$ CIP in $FeSO_4$ solutions as a function of temperature (25 – 125 °C) and concentration (0 – 3 mol/kg). Raman spectroscopy data from Biley (2015) and Rudolph et al. (1997) with surrogate $MgSO_4$ comparison.

4.4.5 $FeSO_4 – H_2SO_4 – H_2O$

No data on which to optimise Pitzer model parameters in the $FeSO_4 – H_2SO_4 – H_2O$ system above 25 °C could be found. Biley (2015) essentially produced optimised parameters on solubility data from Seidell & Linke (1940) and were used to model this system, shown in Figures 4.15 and 4.16.

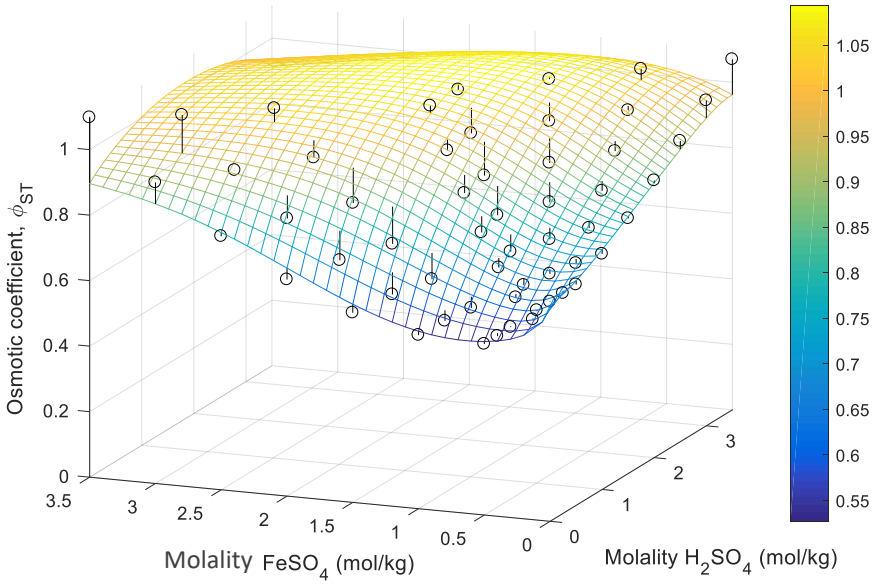

Figure 4.15: Osmotic coefficient characterisation of the ternary $FeSO_4$-H_2SO_4-H_2O system from the studies of Rard (1997) and Rard and Clegg (1999), surface represents the thermodynamic model at 25 °C. AARD = 5.11 %

The predicted osmotic coefficients at 25 °C in Figure 4.15 compare well to the coefficients obtained by Rard (1997) and Rard and Clegg (1999), that measured the activity of water by the isopiestic method. The low AARD of 5.11 % reflects the excellent reproducibility of the real system's activity. It is assumed the model will also be able to predict the system accurately up to a temperature of 100 °C, similar to the results of Biley (2015). To give a reflection of speciation predictability, Raman spectroscopic data from Sobron et al. (2007) are plotted against the thermodynamic model output in Figure 4.16. A clear deviation (lower) is observed from the experimental data, there is some part of the data not captured by the model. Nevertheless, the general trend is captured by the model as well as the fact that temperatures considered within this project are between 75 – 95 °C, the expected behaviour that is predicted by the model is assumed to be correct and accurate enough for the objective of this research.

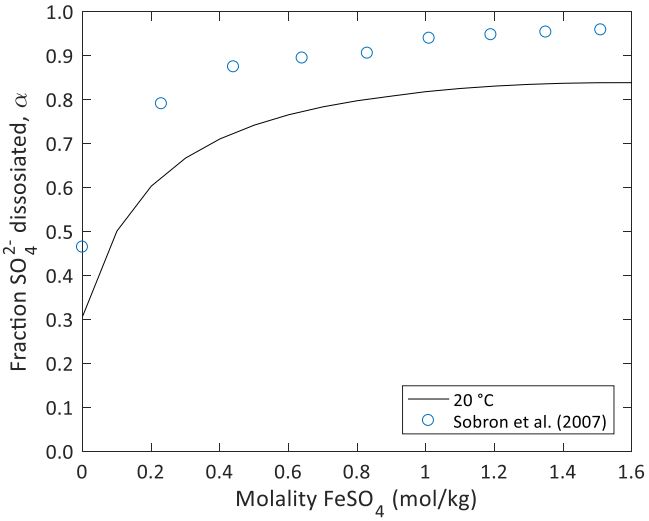

Figure 4.16: Comparison between reported data of the fraction $FeSO_4$ dissociated and the model output, presented as fraction free SO_4^{2-}, with an initial 0.089 mol/L H_2SO_4 concentration.

4.4.6 $Fe_2(SO_4)_3 – H_2SO_4 – H_2O$

One of the most important subsystems, to be optimised and validated, is the aqueous ferric-acid system. Ferric can only exist with acid in a water system, due to the strong hydrolysis tendency, *e.g.* reaction 4.5. Hence, the need for simultaneous optimization of $Fe_2(SO_4)_3$ and H_2SO_4.

$$Fe^{3+} + 2H_2O \rightleftharpoons Fe(OH)_2^+ + 2H^+ \qquad 4.5$$

The possible number of species within this system is large and many interaction parameters can be modelled. Following the description of the two ferric sulphate CIP's in section 4.2.2, a minimum number of species (given in Table 4.1) and model parameters were selected, similar to the study of Biley (2015), and tabulated in appendix A.4.2. Figures 4.17 to 4.21 show the fitted model on literature data (Rumyantsev et al., 2004; Velázquez et al., 2006; Biley, 2015).

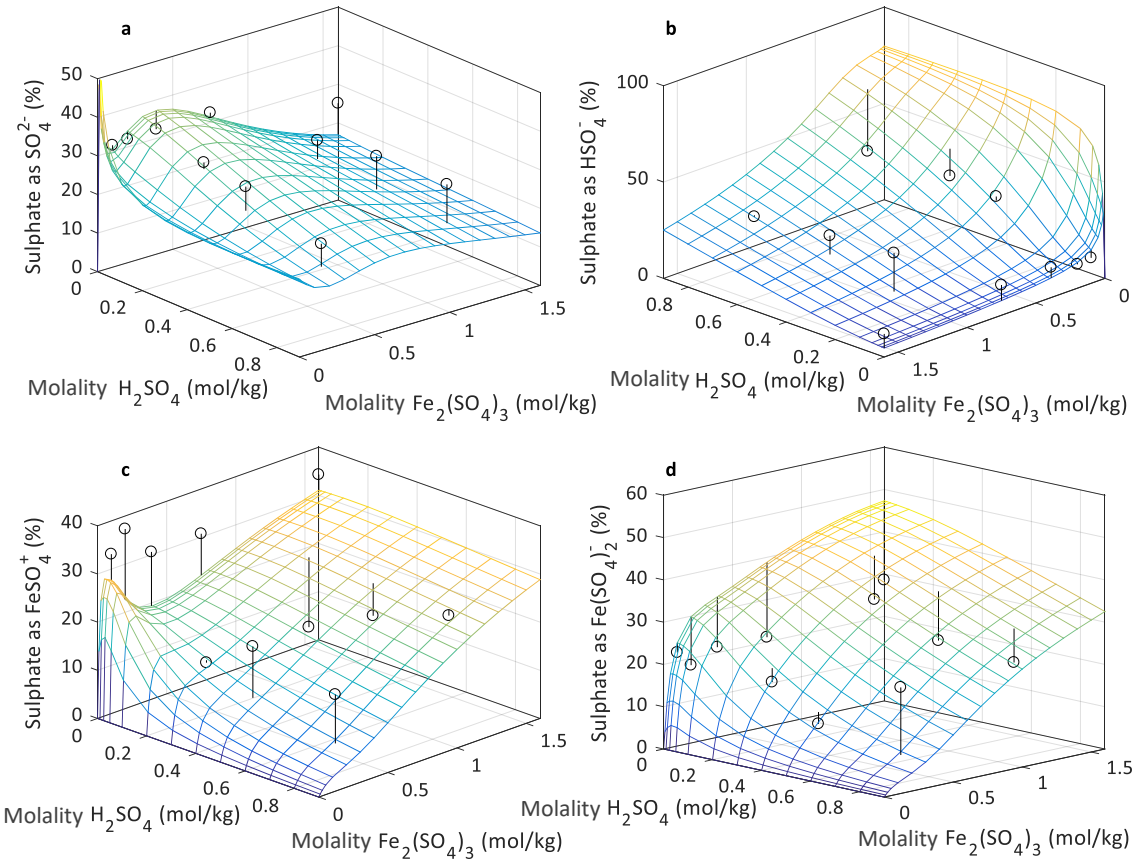

Figure 4.17: Sulphate speciation in the $Fe_2(SO_4)_3$ – H_2SO_4 – H_2O system as measured by Biley (2015) and predicted by the thermodynamic model at 25 °C. Black circles represents Raman spectroscopic data taken from Biley (2015) with conjunction lines drawn to the surface plot of the thermodynamic model.

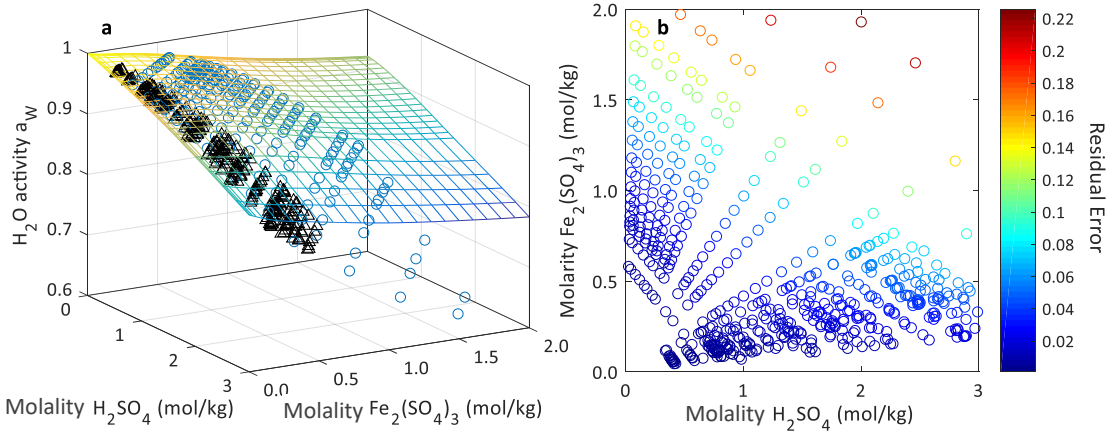

Figure 4.18: Water activity characterisation of the $Fe_2(SO_4)_3$ – H_2SO_4 – H_2O system; a) experimentally measured and predicted water activities, b) residuals between the experimentally measured data and predicted activities as a function of H_2SO_4 and $Fe_2(SO_4)_3$ concentrations. Experimental data is taken from ○: Rumyantsev et al. (2004) and Δ: Velázquez-Rivera et al. (2006)

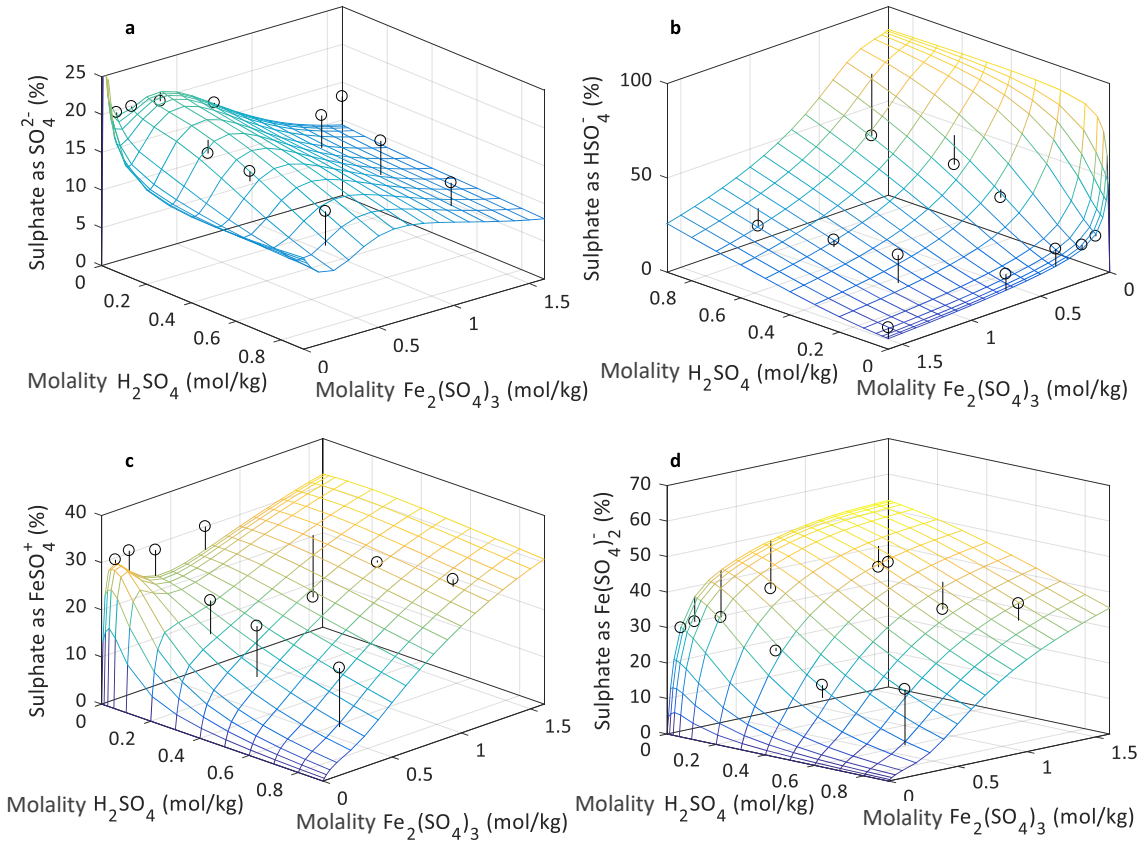

Figure 4.19: Sulphate speciation in the $Fe_2(SO_4)_3$ – H_2SO_4 – H_2O system as measured by Biley (2015) and predicted by the thermodynamic model at 50 °C. Black circles represents Raman spectroscopic data taken from Biley (2015) with conjunction lines drawn to the surface plot of the thermodynamic model.

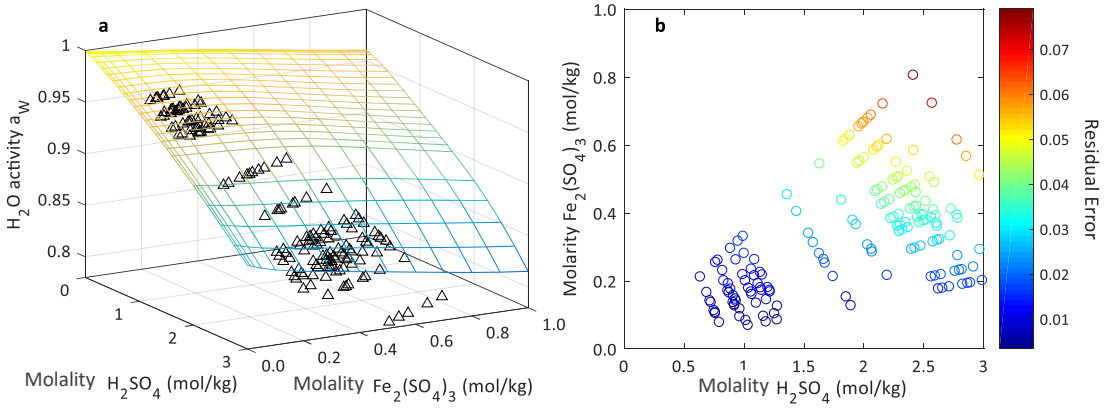

Figure 4.20: Water activity characterisation of the $Fe_2(SO_4)_3$ – H_2SO_4 – H_2O system; a) experimentally measured and predicted water activities, b) residuals between the experimentally measured data and predicted activities as a function of H_2SO_4 and $Fe_2(SO_4)_3$ concentrations. Experimental data is taken from Δ: Velázquez-Rivera et al. (2006).

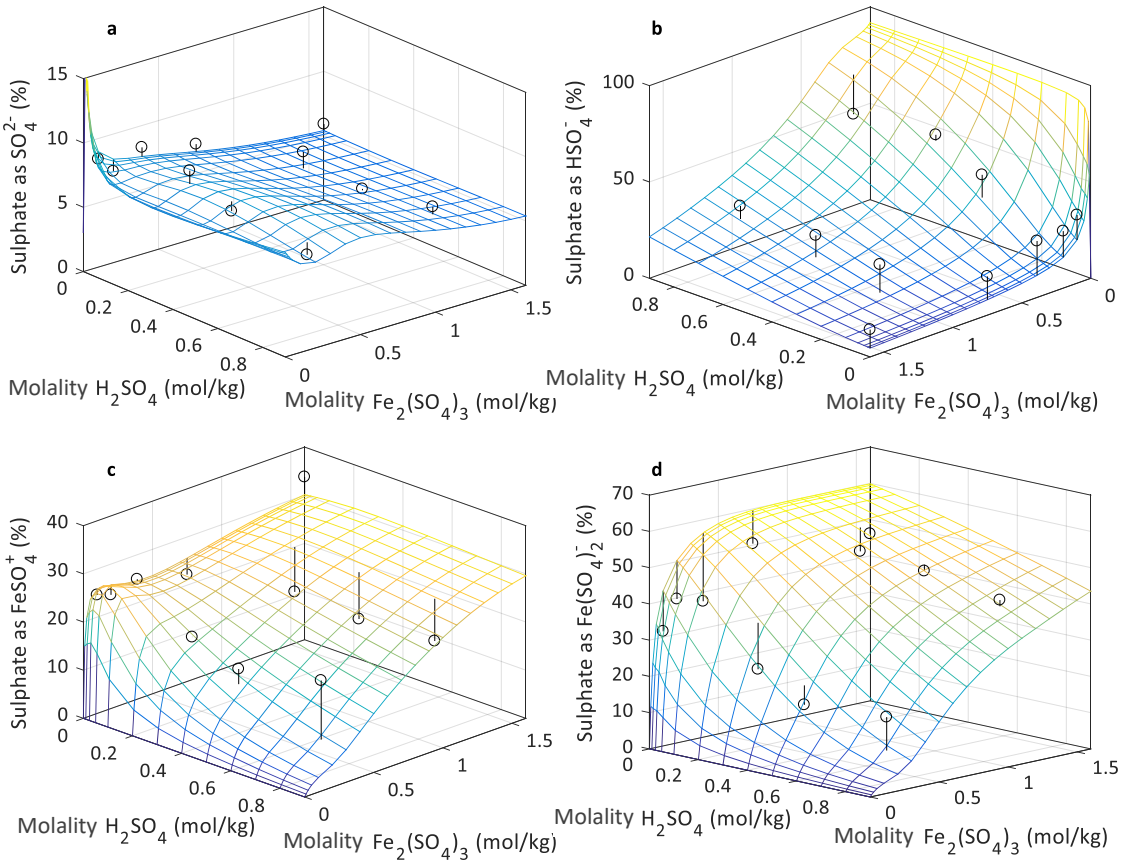

Figure 4.21: Sulphate speciation in the $Fe_2(SO_4)_3$ – H_2SO_4 – H_2O system as measured by Biley (2015) and predicted by the thermodynamic model at 90 °C. Black circles represents Raman spectroscopic data taken from Biley (2015) with conjunction lines drawn to the surface plot of the thermodynamic model.

As shown in the figures above speciation trends are captured remarkably well, even though there are several significant deviations between the measure speciation data (Biley, 2015) and the model predictions. Raman spectroscopic data usually have large variances (Biley, 2015) and given the complexity of this system and the comparative simplistic model being used, the speciation trends are of good fit. Unfortunately, measured water activities could not be predicted above approximately 0.5 mol/kg (even by including all the interaction parameters). The difference may be the result of all interaction between species (including those not incorporated into the model) and water. Deviation from experimentally measured water activity may also be the result of that fact that, in mixed electrolyte systems, the binary short-range interactions between ions of like charge (Φ_{ij}) and ternary interactions (ψ_{ijk}) of the Pitzer model were not accounted for. These parameters were excluded the keep the model as simple as possible. Yet, the general decreasing water activity trend with increasing sulphuric acid and especially towards increasing ferric sulphate concentration is displayed. Similarly, the residual

difference between the model predicted and experimental water activity increases with increasing ferric sulphate and less so to increasing sulphuric acid concentration.

All things considered, the $Fe_2(SO_4)_3 – H_2SO_4 – H_2O$ system's speciation was captured remarkably well and the model is able to predict free Fe^{3+} and H^+ molalities for the objective of this study. Particularly in context of reactive systems where outer-sphere complexes (or more so free ions) are distinguished from inner-sphere complexes. The calibrated model $Fe_2(SO_4)_3 – H_2SO_4 – H_2O$ model has shown to predict speciation trends within 0 – 1 mol/kg $Fe_2(SO_4)_3$, 0 – 2 mol/kg H_2SO_4 concentration ranges and temperatures between 25 – 90 °C (can be extrapolated to 95 °C).

4.4.7 Quaternary systems

No fourth order system, *i.e.* $ZnSO_4 – FeSO_4 – H_2SO_4 – H_2O$, $ZnSO_4 – Fe_2(SO_4)_3 – H_2SO_4 – H_2O$, $FeSO_4 – Fe_2(SO_4)_3 – H_2SO_4 – H_2O$, or all-inclusive quinary system, *i.e.* $ZnSO_4 – FeSO_4 – Fe_2(SO_4)_3 – H_2SO_4 – H_2O$, activity and speciation data could be found in the literature. As the objective is to calibrate the thermodynamic model based on literature data and not to experimentally produce new data, it is assumed that speciation of the aforementioned quaternary and quinary systems may be modelled with the lower order sub-systems parameters, as currently is calibrated. This is a very superficial assumption, which introduces great uncertainty towards the model. However, $ZnSO_4$ and $FeSO_4$ have very similar properties and was both modelled with supplementary data by the $MgSO_4$ surrogate approach, while the $FeSO_4 – Fe_2(SO_4)_3 – H_2SO_4 – H_2O$ system was validated by Biley (2015). Since this model is based on his work and the phenomena of divalent sulphate species similarities, the previous assumption may be considered as valid.

4.4.8 Modelling equilibrium data from literature

Lastly, the thermodynamic model is validated by predicting "unseen" (testing) data relevant to sphalerite leaching. Experimental data from Verbaan (1977) was selected to validate the model. Verbaan (1977) conduced sphalerite leaching experiments in a 1 L reactor by preparing a leach solution and adding various sphalerite concentrates from different sources. The reaction vessel was sealed (closed system) and left to reach equilibrium, while the H_2S partial pressure and zinc solution concentration was measured at selected time intervals. For the purpose of equilibrium modelling the final values of Verbaan's (1977) experiments were used. In order to model the equilibrium, a gas phase model was required in addition to the developed solution model (speciation model) in this chapter. To keep the modelling approach as simple as possible, the gas phase was modelled by the ideal gas law and assuming the fugacity of H_2S is one (ideal). The experimental and model predicted equilibrium results are presented in Figures 4.22 to 4.24.

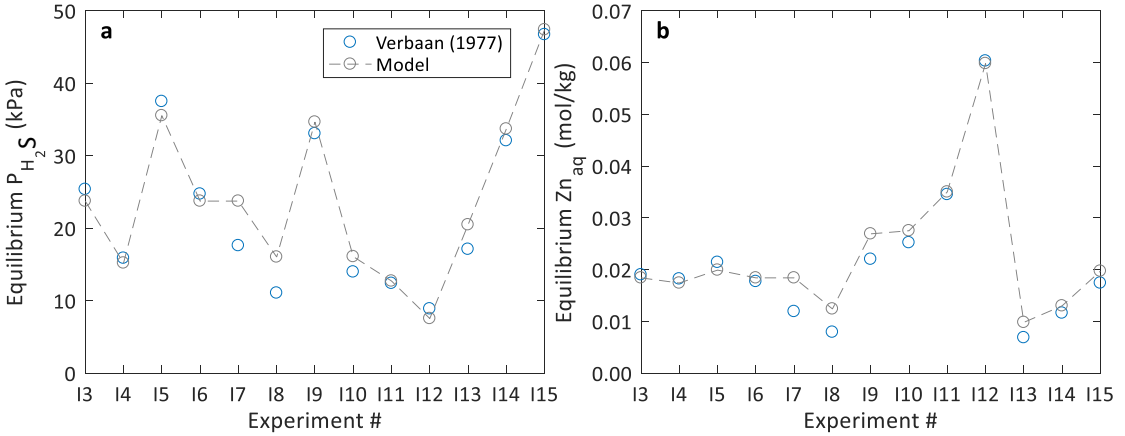

Figure 4.22: Equilibrium a) H_2S partial pressure and b) aqueous zinc concentration as measured by Verbaan (1977) under various experimental conditions compared to the predicted equilibrium values by the thermodynamic model. The feed sphalerite concentrate contained 0.45 % iron. Experiments are numbered as performed by Verbaan (1977).

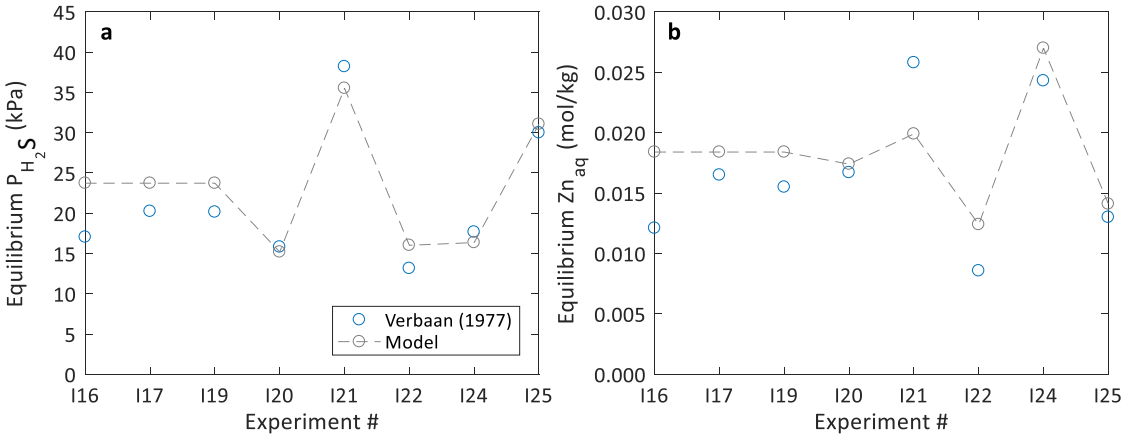

Figure 4.23: Equilibrium a) H_2S partial pressure and b) aqueous zinc concentration as measured by Verbaan (1977) under various experimental conditions compared to the predicted equilibrium values by the thermodynamic model. The feed sphalerite concentrate contained 7.25 % iron.

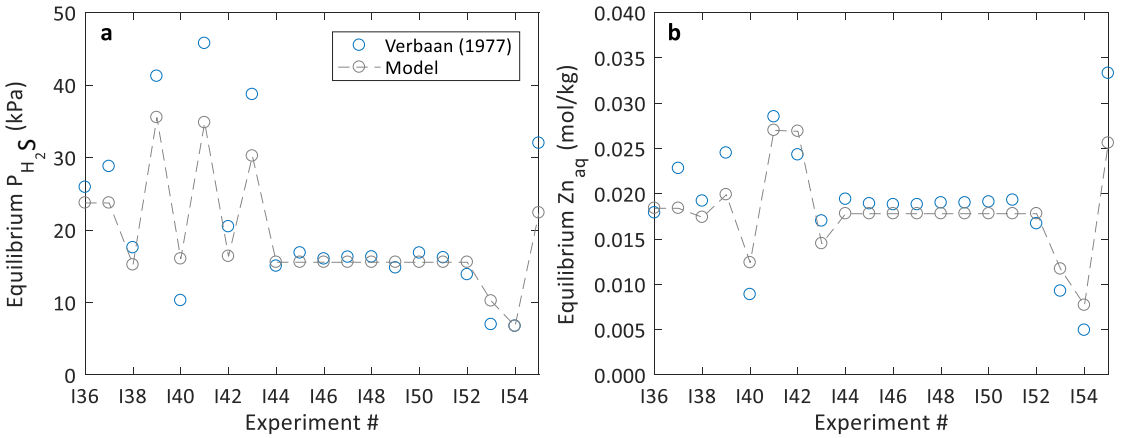

Figure 4.24: Equilibrium a) H_2S partial pressure and b) aqueous zinc concentration as measured by Verbaan (1977) under various experimental conditions compared to the predicted equilibrium values by the thermodynamic model. The feed sphalerite concentrate contained 0.15 % iron.

The distribution of hydrogen sulphide between the gas phase and aqueous phase was modelled using data from Wright and Mass (1932) and were also validated against equilibrium calculation from the HSC (2006) database. While the equilibrium constants for the speciation reaction of $H_2S_{aq} \rightleftharpoons HS^-_{aq} + H^+_{aq}$, where only modelled using the HSC (2006) database.

As seen from Figures 4.22, 4.23 and 4.24, the model predicted the equilibrium H_2S partial pressures and total zinc concentration in the solution accurately. Albeit, small deviations from Verbaan's (1977) data are apparent, which may be result of measurement uncertainties and/or equilibrium could not have been reached since all final measurements were taken within 60 minutes of leaching (but the final change in measured values were small, hence suggesting that equilibrium has been reached). Deviation could also be from impurities within the sphalerite concentrates that Verbaan (1997) used (*i.e.* Cu, Pd and Cd) and was not included into to model. Not excluding the fact that the thermodynamic model also contains some uncertainty, because of the optimisation of the Pitzer parameters. Nevertheless, the overall prediction was good and captured the effect of leaching conditions (*i.e.* solution composition and temperature) on the final equilibrium state.

4.5 Conclusions

This chapter has detailed the development and optimisation of a self-consistent minimum parameter thermodynamic foundation required to describe the $ZnSO_4$ – $FeSO_4$ – $Fe_2(SO_4)_3$ – H_2SO_4 – H_2O system over a temperature range of 25 – 95 °C. The Pitzer model was calibrated by a systematic approach of considering the binary and ternary systems individually and forms the basis from which the overall (higher order systems) could be predicted. Calibration was done by using thermodynamic data from various sources, while the primary (initial) model parameters and speciation data came from studies of Steyl (2009) and Biley (2015).

The model is accurate up to concentrations of 1.5 M $ZnSO_4$, 1.5 M $FeSO_4$, 1.5 M $Fe_2(SO_4)_3$ and 2 M H_2SO_4. A specific focus was to capture speciation of the ions in solution, specifically with regards to distinguishing between inner- and outer-sphere complexes which was achieved through the inclusion of Raman spectroscopic stability constants. Contact ion pair (CIP) formation was predicted by the Pitzer model and has shown results with suitable accuracy for the application in modelling of an ionic aqueous solution relevant to this kinetic study.

The minimum-parameter approach does accurately quantify reported speciation and activity data from the open literature, thus model over-parameterisation was avoided. Validation of the model to testing (unseen) equilibrium data of sphalerite acid leaching from Verbaan (1977) also highlights the applicability of this solution model in the reactive system detailed in the following chapters. A complete set of parameters and thermodynamic data are presented in Appendix A.

Chapter 5 Reaction Mechanisms and Kinetics

5.1 Objective

The literature review (Chapter 2) has pointed out the various transportation and reaction steps involved in a heterogeneous system, and has highlighted the electrochemical nature of solids in an aqueous ionic solution. The purpose of this chapter is to condense the relevant literature in context of the sphalerite leaching process at elevated temperatures and atmospheric pressure. It should be emphasized that is unlikely that a single proposed mechanism would be applicable to sphalerite; and that various mechanistic schemes may be proposed to describe sphalerite dissolution, depending on the particular crystal face and conditions at the surface, *e.g.*, temperature and the nature and concentration of different oxidative species. The following discussions should therefore be viewed in context of this study, *i.e.* to derive intrinsic oxidation rate expressions for the non-oxidative and oxidative leaching of sphalerite, based on insights from the literature.

Sulphide oxidation is embedded within the electrochemical nature of the mineral, which is recognised by various studies in the open literature (Biegler, 1976; Crundwell, 1988b; Gerischer & Mindt, 1968; Osseo-Asare, 1992; Steyl, 2012). A detailed review of the concepts is out of context of this study, since no fundamental electrochemical measurements were conducted. Albeit, the basic application of the mixed potential (MP) theory of metallic corrosion forms an integral part of the rate expressions derived in this chapter. The reader is strongly referred to the papers of Bockris *et al.* (2001), Gerischer and Mindt (1968), Li *et al.* (1992), and Holmes and Crundwell (2000), which cited the MP theory and provides an example of the application of the theory to derive sulphide mineral oxidation rate expressions.

The review and theory are presented in chronological order, from a general overview of the chemistry and thermodynamics, to the sulphide minerals phase mechanisms and the detailed building blocks required to describe the oxidation process phenomenologically.

5.2 Reaction stoichiometry

The oxidation of sulphide (S^{2-}) to higher oxidation states may involve a number of electron transfer steps, see equation 5.1 (Steyl, 2012). With the driving force of each step being dependent on the properties of the solution in contact with the particle and the nature of the oxidant. Elemental sulphur (*i.e.* S^0) is hardly oxidised, if at all, at temperatures below its melting

point of 119°C (Lotens & Wesker, 1987). This is the main reason why elemental sulphur (*i.e.* cyclic or linear chains allotropes) are excluded as an intermediate in sulphate formation.

$$S^{2-}_{(s)} \rightarrow S^{0}_{(s)} \rightarrow SO^{2-}_{4\,(aq)} \quad 5.1$$

Although such a sequential oxidation mechanism is unlikely (see section 5.4.2), the reaction stoichiometry is best dealt with in this manner. The mineralogical analysis (section 6.4.4) has shown that the most prominent phases present in concentrate are sphalerite (ZnS), pyrite (FeS_2) and chalcopyrite ($CuFeS_2$). From a bulk perspective, the leaching reactions of these minerals are divided into groups based on the oxidizing agent:

Sulphuric acid (non-oxidative):

$$ZnS_{(s)} + H_2SO_{4\,(aq)} \rightleftharpoons ZnSO_{4\,(aq)} + H_2S_{(aq)} \quad 5.2$$

$$CuFeS_{2\,(s)} + 2H_2SO_{4\,(aq)} \rightleftharpoons CuSO_{4\,(aq)} + FeSO_{4(aq)} + 2H_2S_{(aq)} \quad 5.3$$

Ferric (oxidative):

$$ZnS_{(s)} + Fe_2(SO_4)_{3\,(aq)} \rightleftharpoons ZnSO_{4\,(aq)} + 2FeSO_{4\,(aq)} + S^{0}_{(s)} \quad 5.4$$

$$CuFeS_{2\,(s)} + 2Fe_2(SO_4)_{3\,(aq)} \rightleftharpoons CuSO_{4\,(aq)} + 5FeSO_{4\,(aq)} + 2S^{0}_{(s)} \quad 5.5$$

$$FeS_{2\,(s)} + Fe_2(SO_4)_{3\,(aq)} \rightleftharpoons 3FeSO_{4\,(aq)} + 2S^{0}_{(s)} \quad 5.6$$

$$FeS_{2\,(s)} + 7Fe_2(SO_4)_{3\,(aq)} + 8H_2O \rightleftharpoons 15FeSO_{4\,(aq)} + 8H_2SO_{4\,(aq)} \quad 5.7$$

Oxygen (oxidative):

$$ZnS_{(s)} + 2O_{2\,(aq)} \rightleftharpoons ZnSO_{4\,(aq)} \quad 5.8$$

$$CuFeS_{2\,(s)} + 4O_{2\,(aq)} \rightleftharpoons CuSO_{4\,(aq)} + FeSO_{4(aq)} \quad 5.9$$

$$FeS_{2\,(s)} + 2O_{2\,(aq)} \rightleftharpoons FeSO_{4(aq)} + S^{0}_{(s)} \quad 5.10$$

$$FeS_{2\,(s)} + \frac{7}{2}O_{2\,(aq)} + H_2O \rightleftharpoons FeSO_{4(aq)} + H_2SO_{4\,(aq)} \quad 5.11$$

Oxygen & Sulphuric acid (oxidative):

$$ZnS_{(s)} + \frac{1}{2}O_{2\,(aq)} + H_2SO_{4\,(aq)} \rightleftharpoons ZnSO_{4\,(aq)} + H_2O + S^0_{(s)} \quad 5.12$$

$$CuFeS_{2\,(s)} + O_{2\,(aq)} + 2H_2SO_{4\,(aq)} \rightleftharpoons CuSO_{4\,(aq)} + FeSO_{4\,(aq)} + 2H_2O + 2S^0_{(s)} \quad 5.13$$

$$FeS_{2\,(s)} + \frac{1}{2}O_{2\,(aq)} + H_2SO_{4\,(aq)} \rightleftharpoons FeSO_{4\,(aq)} + H_2O + 2S^0_{(s)} \quad 5.14$$

Ferrous ions in solution are also oxidized by dissolved oxygen as follows:

$$2FeSO_{4\,(aq)} + \frac{1}{2}O_{2\,(aq)} + H_2SO_{4\,(aq)} \rightleftharpoons Fe_2(SO_4)_{3\,(aq)} + H_2O \quad 5.15$$

Under favourable conditions, elemental sulphur can also be oxidised to sulfuric acid according to the following overall stoichiometry:

$$S^0_{(s)} + \frac{3}{2}O_{2\,(aq)} + H_2O \Rightarrow H_2SO_{4\,(aq)} \quad 5.16$$

These mineral oxidation reactions differ mechanistically, thus their relative oxidation rates would also differ. This study focuses on the non-oxidative dissolution (reaction 5.2) and ferric oxidative dissolution (reaction 5.4) of sphalerite. However, it is also important to know the behaviour of the minor phases (*i.e.* pyrite and chalcopyrite) in acid media, to establish whether or not the effects thereof are detrimental or, most likely, enhance the reaction kinetics. These impurity phases may limit and change the mechanistic behaviour of sphalerite.

5.3 Aqueous mineral thermodynamics

It is appropriate to first establish the driving force of mineral oxidation from a thermodynamic perspective, before determining the mechanisms of sulphide mineral oxidation in acidic media. This is achieved through using Pourbaix diagrams, which utilise the electromotive force (EMF) of the half redox reaction couples and pH. Insights into the stability regions of solid and solution species at different solution potentials are obtained by these diagrams, from which the most probable reactions may be deduced. Although these diagrams are useful to describe hydrometallurgical systems, their applicability is usually restricted to geological time spans where kinetic factors, such as metastability and diffusion limitations are not dominant. The artificial nature of these diagrams should also be highlighted, since chemical species can be added and neglected as desired when constructing these diagrams.

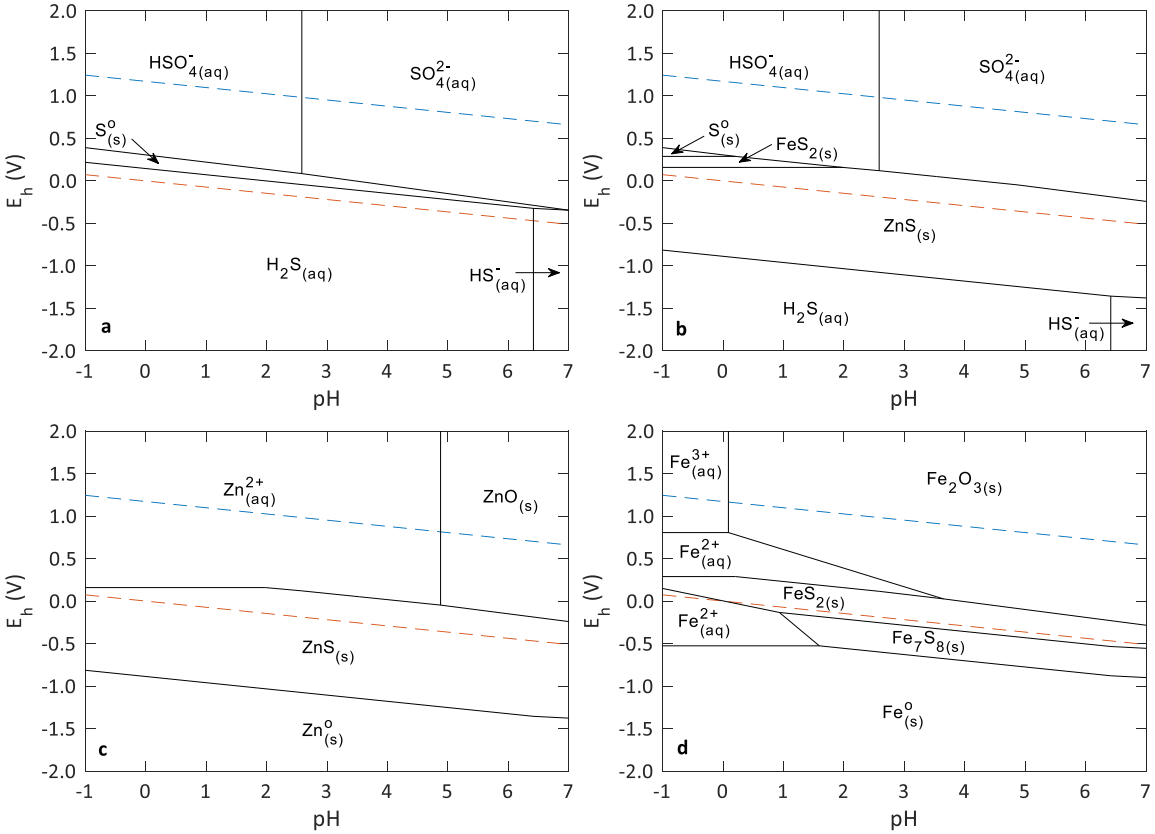

Figure 5.1: E_h-pH diagram in aqueous environment at 95°C & 1 mol/kg ionic strength: (a) S-H_2O system at 0.5 mol/kg S; (b) S-Zn-Fe-H_2O, (c) Zn-Fe-S-H_2O and (d) Fe-Zn-S-H_2O systems at 0.5 mol/kg S, 0.1 mol/kg Zn & 0.1 mol/kg Fe (generated from HSC (2006)).

The water stability region (inside the dotted lines) is of particular interest to hydrometallurgical systems, that is the region below the cathodic reduction of diatomic oxygen (reaction 5.17, blue line) and above the anodic oxidation of diatomic hydrogen (reaction 5.18, red line).

$$O_{2\,(g)} + 4H^+_{(aq)} + 4e^- \rightleftharpoons 2H_2O \qquad 5.17$$

$$2H^+_{(aq)} + 2e^- \rightleftharpoons H_{2\,(g)} \qquad 5.18$$

According to the mineral thermodynamics in a S-H_2O system, shown in Figure 5.1a, sulphur would be expected to be present either as elemental sulphur or sulphate at lower pH, while within the S-Zn-Fe-H2O system sulphur may be present as pyrite, FeS_2, and/or sphalerite, ZnS, as well. Hydrogen sulphide increases in stability in more reducing conditions. Most studies have presented results where the direct reaction of sulphur in sphalerite with acid produces hydrogen sulphide as product (Romankiw, 1962; Verbaan, 1977; Crundwell & Verbaan, 1987; Kammel et al., 1987; Markus et al., 2004b; Weisener et al., 2004; Xie et al., 2007). Thus, giving a reflection of the relevance of the intrinsic mechanisms on a microscopic scale of mineral dissolution, and emphasising that it is risky to infer a reaction mechanism from a bulk stoichiometric perspective.

The E_h-pH diagrams also show an increased stability of elemental sulphur as the acid concentration increases. It is widely known and shown by various researchers that the reaction of sphalerite at < 100 °C in ferric sulphate media generates primarily $ZnSO_4$, $FeSO_4$ and elemental sulphur, with less than ≈ 5% of sulphide converted to sulphate (Verbaan, 1977; Jin et al., 1985; Crundwell, 1988b; Baláž & Ebert, 1991; Baláž, 2000; Markus et al., 2004a; Dutrizac, 2006, 2010; Steyl, 2012). Verbaan (1977) specifically observed that the molar concentrations of $Zn^{2+}_{(aq)}$ and $S^o_{(s)}$ formed after leaching are approximately equal, suggesting that in relation to reaction 5.4 when leaching at relatively high Fe^{3+}: H_2SO_4 ratios (> 1.8) in the absence of oxygen, negligible amounts of elemental sulphur, $S^o_{(s)}$, or sulphide, $S^{2-}_{|lat}$, are oxidise to sulphate species. This may be ascribed to the kinetic resistance of breaking of the S^o_8 ring structure (Lotens & Wesker, 1987; also see section 4.4.2). Yet, the diagrams suggest at high redox potentials (E_h > 0.5 V, *i.e.*, under conditions where most of the iron is present as ferric, Fe^{3+}), elemental sulphur would not be stable. Therefore, the sulphur product species are dependent on the intrinsic oxidation mechanism of sphalerite, rather than supporting the thermodynamic results that elemental sulphur and ferric do not co-exist under atmospheric and elevated temperature conditions.

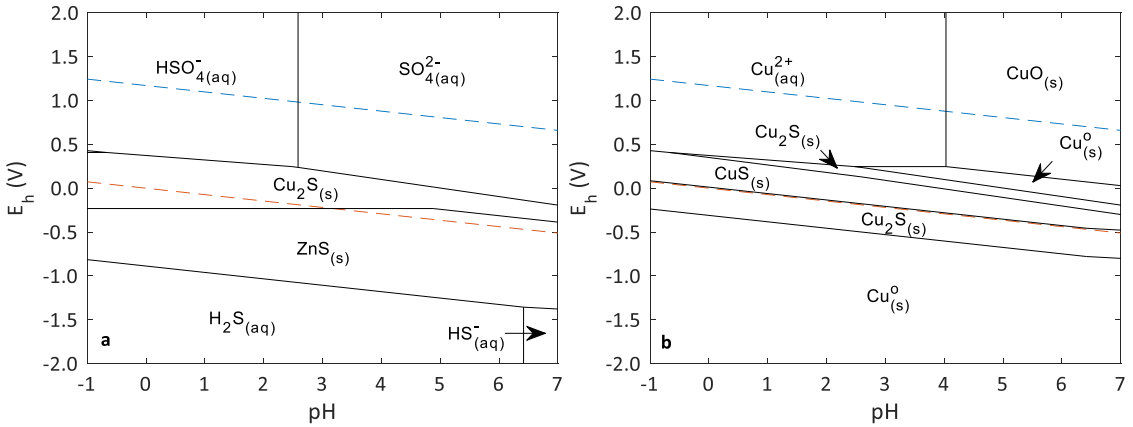

Figure 5.2: E_h-pH diagram in aqueous environment at 95°C & 1 mol/kg ionic strength: (a) S-Cu-Zn-H_2O, Cu-Zn-S-H_2O at 0.5 mol/kg S, 0.1 mol/kg Zn & 0.01 mol/kg Cu (HSC, 2006).

An important observation from the thermodynamic diagrams (Figure 5.1 and Figure 5.2) is the increased stability of pyrite and chalcopyrite as well as the decreased stability of sphalerite at higher acid concentrations. This supports the notion of increased or preferential dissolution of sphalerite compared to pyrite and chalcopyrite dissolution (see section 6.4.5).

In conclusion, thermodynamics alone cannot explain mineral dissolution reactions and observed trends. Thermodynamics should be regarded in terms of chemical speciation limits, while the sulphur species yield is deeply imbedded within the kinetic field, *i.e.* the mechanism by which oxidation of the sphalerite surface occurs (Steyl, 2012).

5.4 Mechanisms of sulphide mineral oxidation

5.4.1 Cathodic reactions

Electrochemical dissolution of metal sulphides occurs by the loss of bonding electrons from the mineral. Before discussing the anodic steps involved on the mineral surface, the coupled cathodic reduction mechanisms of the oxidants are examined. If sufficient excess solvent is present to stabilise ions in the system, the net half-reactions on the mineral surface (applicable to this study) may be represented as follows (Steyl, 2012):

$$Cu^{2+}_{(aq)} + e^- \rightleftharpoons Cu^{+}_{(aq)} \qquad E^o_h = 0.153\ V \qquad 5.19$$

$$Fe^{3+}_{(aq)} + e^- \rightleftharpoons Fe^{2+}_{(aq)} \qquad E^o_h = 0.771\ V \qquad 5.20$$

$$O_{2\,(aq)} + 4H^{+}_{(aq)} + 4e^- \rightleftharpoons 2H_2O \qquad E^o_h = 1.229\ V \qquad 5.21$$

Cupric ions (Cu^{2+}) are much more stable in an acidic aqueous environment compared to cuprous (Cu^{+}) ions, as seen from a thermodynamic perspective in Figure 5.2. Cuprous ions can be stabilised by solutes, *e.g.* chloride ions, enhancing the ability of the cupric ion to be reduced on mineral surfaces (Steyl, 2012). The copper redox couple is a powerful oxidising agent, as seen from the E^o_h value, while ferric ions would regenerate cupric as follows:

$$Fe^{3+}_{(aq)} + Cu^{+}_{(aq)} \rightleftharpoons Cu^{2+}_{(aq)} + Fe^{2+}_{(aq)} \qquad 5.22$$

Reaction 5.30 displays a typical electrochemical (EC) mechanism, and may have a catalytic effect during leaching of the concentrate. Low quantities of chalcopyrite were observed in the coarser size fraction from which copper in the solution originated, while the finer size fraction contained negligible amounts (see Sect. 5.4 for particle composition analysis). The concentration of copper ions was also not observable (*i.e.* under the detection limit) during the kinetic tests of low pulp densities (or very low in high pulp density experiments). As pointed out cuprous species are not very stable in aqueous solution without the presence of stabilising agent. It is doubtful whether such low ion concentration would translate into any meaningful catalytic activity. Albeit, it is important to recognise the effect of these copper ions, which could complicate this kinetic study.

Ferric (Fe^{3+}) ion is an efficient electron acceptor, by the alignment of energy levels of the redox couple with the energy bands, *via* surface states, of the mineral (this phenomenon is discussed in section 5.4.3). The cathodic reduction of ferric would develop the highest anodic mixed potential current, compared to oxygen reduction, and thus according to the MP theory would

be the most effective oxidising agent. Furthermore, Horne and Axelrod (1964) have studied the ferric/ferrous redox couple, which provided conclusive evidence of the Grotthuss-type mechanism. This mechanism involves the formation of a water bridge, so that electron transfer from the mineral surface to the cation could be achieved (*i.e.* over large distances, 100 Å). Water and the mobility of the hydrogen ion (H_3O^+, hydronium) in aqueous solution plays a crucial role in this exchange reaction. It is assumed that a conductive chain between the cathodic site on the mineral surface and solvation shell of the ferric species is formed by water molecules.

In light of the previous discussion, ferric adsorbs onto the outer Helmholtz plane and exchanges electrons with the mineral surface, without having to form a covalent bond (Crundwell, 1988c, 2014a; Steyl, 2012). A polarised barrier then manifests over this water bridge, meaning that additional energy is required for and charge carrier (electron or proton) to move through this barrier. Section 2.3describes the interfacial electrochemical kinetics involved during the charge transfer process. This process is significantly slower in comparison to oxidising agents (such as chloride) that forms a (covalent) bond with the active site.

A detailed review conducted by Steyl (2012) outlines the reduction mechanism of diatomic oxygen, with most of the concepts derived from the first principle study of Shi *et al.* (2006) and oxygen adsorption study of Nørskov *et al.* (2004) at a fuel-cell cathode. The reduction of diatomic dissolved oxygen occurs in a series of consecutive one-electron transfer steps, since the transfer of a single electron is energetically more favourable than multiple electrons.

Table 5.1: Single electron transfer reduction mechanism of diatomic oxygen and potentials

Reaction	[a]E_h^o (V)	
$O_{2\,(aq)} + H^+ + e^- \rightleftharpoons HO_2\cdot$	0.12	5.23
$HO_2\cdot + H^+ + e^- \rightleftharpoons H_2O_2$	$1.42 - 1.49$	5.24
$H_2O_2 + H^+ + e^- \rightleftharpoons OH\cdot + H_2O$	$0.5 - 0.8$	5.25
$OH\cdot + H^+ + e^- \rightleftharpoons H_2O$	$2.6 - 2.9$	5.26

[a]*Values obtained from Steyl* (2012)

It was concluded that the first electron transfer reaction 5.23 is the rate limiting step. The tendency of oxygen to be dissociated is dependent on the reactivity of oxygen during the initial step. The unfavourable thermodynamic driving force of the initial step, to form the perhydroxyle radical ($HO_2\cdot$), is evident from the relatively low reduction potential.

5.4.2 Sulphur transformation and oxidation

Sulphur is a complex substance, with properties not yet fully defined and understood. The average valence of sulphur is usually -2 within sulphides, in combination with other metals (Havlík, 2008). The structure for various orbitals of atomic sulphur is given in Table 5.2. From the main state (1) two non-paired electrons are placed in different p-orbitals, explaining sulphur's divalent tendency and bonding character in solid state. Hybridisation of the s- and p-orbitals (configurations 2 and 3 in Table 5.2) explains the formation of non-divalent (intermediary oxidation) states of sulphur in molecular bonding (*i.e.* SO_4^{2-}).

Table 5.2: Orbital configuration and Ionization Potential (I_v), Electron Affinity (E_v) of atomic sulphur obtained from (Meyer, 1976)

Configuration	Orbital	I_v	E_v
1 – s^2p^2pp	p	12.4	2.4
2 – $(sp^3)^2(sp^3)^2sp^3sp^3$	sp^3	15.5	4.8
3 – $(sp^2)^2(sp^2)^2sp^2\pi$	sp^2	16.3	5.4
	π	12.7	2.8

Elemental (solid) sulphur has two allotropic modifications: intramolecular allotropy (*i.e.* different molecular forms formed by the chemical bonding of the sulphur atoms), intermolecular (*i.e.* different structural arrangements of the molecules in the crystals). Elemental sulphur has more than thirty allotropes (Havlík, 2008; Meyer, 1976), of which twenty of the molecular structures are composed of cyclic rings with six to twenty sulphur atoms each (Diéguez & Marzari, 2009).

Among them, S_8 is the most stable configuration at atmospheric pressure and elevated temperatures (< 100 °C). There also exists polymeric structures formed by molecular chains. Cyclo-octasulphur (S_8) crystallizes to form three solid allotropes, viz. orthorhombic α-sulphur (*i.e.* space group #70, Fddd) that transforms into monoclinic β-sulphur at 95.3 °C, and γ-sulphur (*i.e.* S_8 rings like α-sulfur and β-sulfur and only differs from them in the way that these rings are packed).

Elemental sulphur is hardly oxidized, if at all, at temperatures below its melting point of 119°C (Lotens & Wesker, 1987). Therefore, elemental sulphur (S_8) can be excluded as an intermediate in sulphate formation (SO_4^{2-}).

As mentioned polysulphides can also exist as a stable chemical compound, and as the name indicates, polysulphides are a general class of compound in which sulphur is polymerised and reduced (Klauber, 2008). The formula for polysulphides in general (non-organic) class of components is presented as S_n^{2-} (n > 2). Consisting of a chain of sulphur atoms with an overall negative charge of -2, balanced by monovalent cations. Typically, n is limited to no more than six sulphur atoms in a chain, thus oligomers may therefore be a better description.

Hole formation in the valence band means that one of the bonding electrons has been removed and the bond weakened (Crundwell, 1988b). The formation of holes may be introduced into a metal sulphide mineral by electric current or holes can be injected by an oxidising agent (which is the leaching mechanism of semiconductors with a wide band gap). A narrow enough (≈0.6 eV) band gap, or impurities within the band structure, and also the surface phenomena that allow electronic states in the band gap may improve the energy-level matching between the oxidant and the semiconductor surface so that dissolution via electron capture can occur. This capturing of electrons by an oxidant (*i.e.* the amount of electrons at an energy state) is an important factor when considering the rearrangement and transformation of sulphide to elemental sulphur or sulphate. The average oxidation state of sulphur depends heavily on the nature of the oxidising agent (Steyl, 2012).

Based on the discussion of Gerischer and Mindt (1968) the oxidation of sulphide sulphur may occur via the following sequence:

$$\left(M^{\delta+}S^{\delta-}\right)_{(s)} + (\delta)h^+ \Rightarrow M^{\delta+} + \cdot S_{(s)} \qquad 5.27$$

$$\left(M^{\delta+}S^{\delta-}\right)_{(s)} \Rightarrow M^{\delta+} + \cdot S_{(s)} + (\delta)e^- \qquad 5.28$$

$$\cdot S_{(s)} + \cdot S_{(s)} \Rightarrow (S-S)^o_{(s)} \qquad 5.29$$

$$S^o_{n\,(s)} + \cdot S_{(s)} \Rightarrow S^o_{n+1\,(s)} \qquad 5.30$$

The difference of electronegativity of the components of the semiconductor may initiate the dissolution of the electropositive component by the more electronegative part. Charge transfer can occur either via hole injection (reaction 5.27) or electron withdrawal (reaction 5.28). The more electronegative component, *i.e.* sulphur, may undergo a recombination reaction as by reaction 5.29 or generally by reaction 5.30, which would result in an elementary state of this component.

The sulphur radical, $\cdot S_{(s)}$, on the surface is expected to be highly reactive. It would therefore be expected to react easily with oxidising agents by the capturing an electron, *i.e.* reaction 5.31, one electron transfer or possibly reaction 5.32 by a two-electron transfer, as follows:

$$\cdot S_{(s)} \Rightarrow S^{+}_{(s)} + e^{-} \qquad 5.31$$

$$\cdot S_{(s)} \Rightarrow S^{2+}_{(s)} + 2e^{-} \qquad 5.32$$

Lotens and Wesker (1987) proposed an simplified reaction scheme, based on the formation of higher oxidation products of sulphide. It consists of a series of protonation reactions, known as the Wackenroder scheme, to account quantitatively for the observed yields of elemental sulphur and sulphate. The first step in this mechanism is the oxidation of sulphide, $S^{2-}_{|lat}$, to either $S^{+}_{(s)}$ or $S^{2+}_{(s)}$ depending on the nature of the oxidation agent used, *i.e.* one-electron or two-electron transfer, respectively:

$$S^{2-}_{(s)} \rightarrow S^{-}_{(s)} \rightarrow S^{o}_{(s)} \rightarrow S^{+}_{(s)} \rightarrow S^{2+}_{(s)} \qquad 5.33$$

$$S^{2+}_{(s)} \rightarrow S^{o}_{(s)} \rightarrow S^{2+}_{(s)} \qquad 5.34$$

In the one-electron transfer case, hydrolysis of $S^{+}_{(s)}$-species would lead to the formation of thiosulfurous acid ($H_2S_2O_2$). Subsequently, thiosulfurous species would rearrange and decompose rapidly in acid solution (see Lotens & Wesker, 1987) and would give a theoretical yield of 75% elemental sulphur.

$$2S^{+}_{(s)} + 2H_2O \Rightarrow H_2S_2O_2 + 2H^{+}_{(aq)} \qquad 5.35$$

$$2H_2S_2O_2 \Rightarrow \frac{3}{8}S^{o}_{8} + H_2SO_3 + H_2O \qquad 5.36$$

In the case of two-electron transfer, hydrolysis of the $S^{2+}_{(s)}$-species would form sulfoxylic acid (H_2SO_2). Once more, the sulfoxylic species decomposes rapidly in acid solution and resulting in an theoretical yield of 50% elemental sulphur (Lotens & Wesker, 1987).

$$S^{2+}_{(s)} + 2H_2O \Rightarrow H_2SO_2 + 2H^{+}_{(aq)} \qquad 5.37$$

$$2H_2SO_2 \Rightarrow \frac{1}{8}S^{o}_{8} + H_2SO_3 + H_2O \qquad 5.38$$

Although elemental sulphur in the form of S_8^o molecules is quite unreactive, atomic $\cdot S_{(s)}$ can be contemplated to be easily oxidised further by ether the one- or two-electron transfer reactions, which explains in the different sulphur yields observed during sulphide mineral leaching. Lotens and Wesker (1987) qualitatively verified the above mechanism by the oxidation of sphalerite, pyrite and galena (PbS). However, pyrite behaved unexpectedly by converting virtually all the sulphide to sulphate, this is due to the nature of sulphide, $S_{2\,|lat}^{2-}$, in pyrite. Therefore, the mechanism of pyrite oxidation differs substantially from that of other sulphides and are discussed in detail by Steyl (2012) as well as phenomenological mechanisms are proposed.

According to Steyl (2012) and Harmer *et al.* (2006), if the formation of polysulphides forms an intrinsic part of the oxidation mechanism of sulphide minerals, then sulphide oxidation may be represented by reactions 5.39 and 5.40.

$$(S^{2-})^* + \cdot S_{(s)} \Rightarrow (S_n)_{(s)}^{2-} \quad 5.39$$

$$n(S^{2-})^* \Rightarrow (S_n)_{(s)}^{2-} + (2n-2)e^- \quad 5.40$$

Polysulfide may either be relatively reactive or unreactive to further oxidation to longer chains, depending on the present chain length (Harmer *et al.*, 2006). Either way, the sulphur chain would form crystalline elemental sulphur until end of chain termination reaction occurs. The reduction mechanism of long-chain polysulphides by protons (acid) is an important chain ending step and may follow different pathways as follows:

$$(S_n)_{(s)}^{2-} + (2n-2)H_{(aq)}^+ + (2n-2)e^- \Rightarrow (2n-2)H^+ \cdot n(S^{2-})_{(s)} \quad 5.41$$

$$(S_n)_{(s)}^{2-} + (2n-2)H_{(aq)}^+ + (2n-2)e^- \Rightarrow (n-1)H_2S \cdot (S^{2-})_{(s)} \quad 5.42$$

The short-chained sulphides formed would subsequently be oxidised, which involves a massive structural rearrangement of the surface to form crystallites of elemental sulphur (see Harmer *et al.*, 2006):

$$(2n-2)H^+ \cdot n(S^{2-})_{(s)} \Rightarrow nS_{(s)}^o + (2n-2)H_{(aq)}^+ + (2n)e^- \quad 5.43$$

$$(n-1)H_2S \cdot (S^{2-})_{(s)} \Rightarrow nS_{(s)}^o + (2n-2)H_{(aq)}^+ + (2n)e^- \quad 5.44$$

As seen, there is no stoichiometric difference between these two mechanistic pathways. High acidic conditions may, however, stabilize the hydrogen sulphide entity to such an extent that it can desorb and be released into the solution (Steyl, 2012):

$$(n-1)H_2S \cdot (S^{2-})_{(s)} \Rightarrow S_{(s)}^o + (n-1)H_2S_{(aq)} + 2e^- \quad 5.45$$

5.4.3 Natural sphalerite (Zn,Fe)S

5.4.3.1 Sphalerite's crystalline structure

Zinc sulphide exists in two principal crystalline forms, sphalerite (β-phase, cubic) and wurtzite (α-phase, hexagonal). Cubic zinc sulphide is by far the most abundant zinc sulphide mineral, due to its stability at low-temperatures. Transition from β-phase to α-phase sphalerite occurs at 1293 ± 10 K (Gardner & Pang, 1988). Albeit, wurtzite is metastable under ambient conditions. Numerous other intermediate polytopes or superstructures have also been characterized by researchers. These structures, however, are closely related to the principal forms, while others only crystalize under specific conditions (Farnsworth & Kline, 1973). It is uncommon to find significant quantities of wurtzite and intermediate forms in most natural occurring ores and their thermodynamic properties are similar to those of cubic zinc sulphide. To simplify further discussions, it is assumed that zinc sulphide exists in its cubic type crystalline.

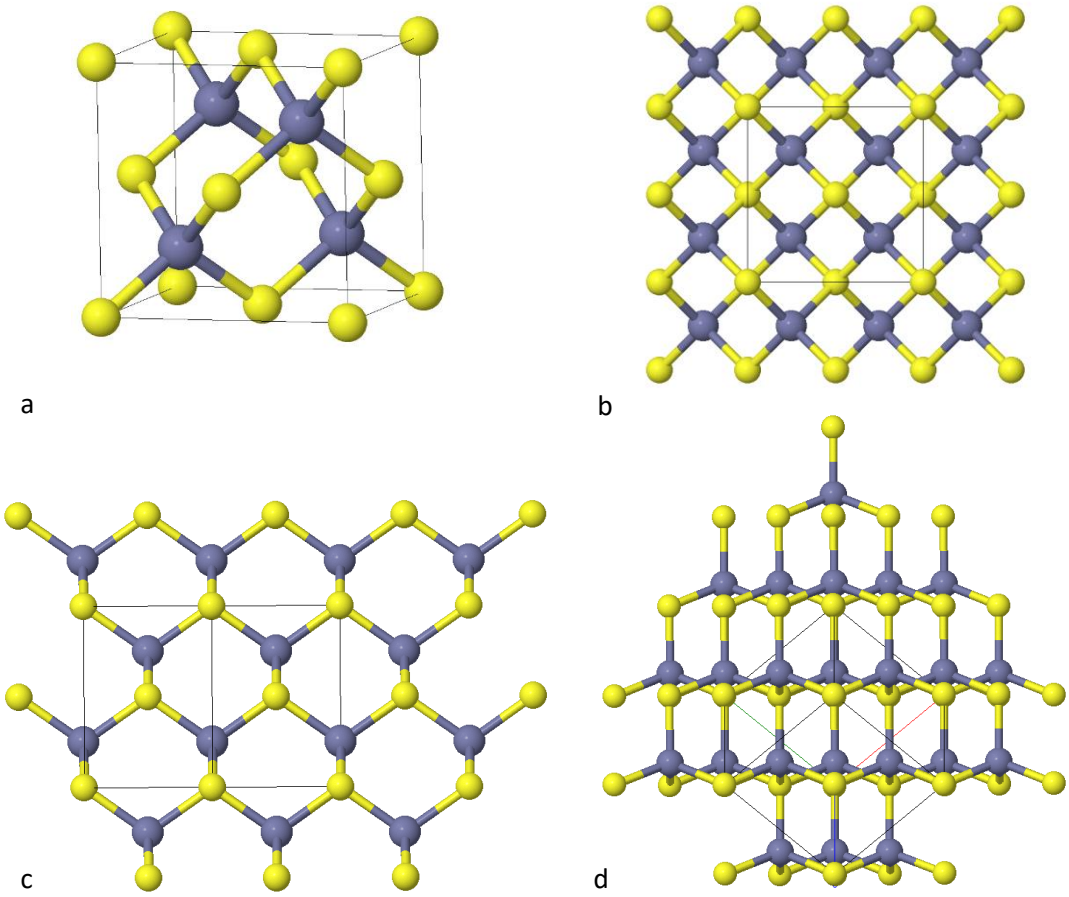

Figure 5.3: (a) Optimised zinc blend unit cell (Jmol, 2016); Zn & S atoms are coloured grey & yellow, respectively (space group F 43m # 216, with experimental lattice parameters: a = b = c = 5.4093Å at room temperature, Smith, 1955; Farnsworth & Kline, 1973); the optimised zinc blend crystal structure faces are shown perpendicular to the (b) 100, (c) 110 and (d) 111 planes, according to the Miller index.

Within sphalerite the zinc and sulphur atoms are tetrahedral coordinated (bonded). The unit cell of the bulk material is presented in Figure 5.3a. Four sulphur atoms, within a unit cell, lie at the centre of a tetrahedron of zinc atoms; and fourteen zinc atoms are positioned at the corners and face centres of the cubic planes (Farnsworth & Kline, 1973; Steyl, 2012).

Each distinct crystalline face of sphalerite has its own particular surface atom bonding strengths and packing, and thus will react in a unique fashion to a solution which it is in contact with. The reaction/interaction of solution species to the particle surface is directly related to the underlying atom structure. The particular shapes of etch figures on the particle surface are partly dependent on factors such as the nature of the solution, but the symmetry of their shape and behaviour on different crystal faces may be considered an indication of the symmetry of the underlying structure (Gatos, 1960). Crundwell (1988c) and Gatos (1960) gives reference and reported evidence of the increased reactivity of the (100) and (110) planes in comparison to the (111) plane of sphalerite (a semiconducting zinc blend). Figure 5.3b-d illustrates the atom orientations from the viewpoint of the different plains.

The outer most surface atoms of the (100) plane are either doubly (the centre atoms) or singly (the corner atoms) bonded to the inner surface atoms, while the inner surface atoms are also bonded to the inner structure (*e.g.* Figure 5.3b). Looking from the (110) plane, the open-framed network of Zn_3S_3-rings in chair conformation is clearly visible. An atom in the outer layer with respect to the (110) plane, can be associated to multiple structural configuration. Despite the various surface configurations of the (110) plane, an atom would also be doubly bonded to other surface atoms and/or singly bonded to the interior structure. There also exist some atoms on the (110) plane which are triply bonded to other surface atoms (*e.g.* left and right side of atomic structure in Figure 5.3c), analogous to the surface structure in the (111) plane. Surface atoms on the (110) plane are packed slightly closer with respect to the (100) plane, which represents a more stable structure.

Surface atoms on the (111) plane, illustrated in Figure 5.3d, are triply bonded to other surface atoms and has a single bond to the internal structure. Hence, atoms on the (111) surface are more tightly packed due to the structural arrangement and since more bonds have to be broken, making it the most stable and therefore the least reactive plane. Both Crundwell (1988c) and Gatos (1960) have concluded in there research that the expected reactivity of the different faces in order is (100) < (110) < (111). Images of the surface topography of two leach residues were produced using a scanning-electron microscope (SEM), to investigate this surface phenomenon, from Steyl (1999). Figure 5.4 shows the hillocks very clearly on some of the particle faces.

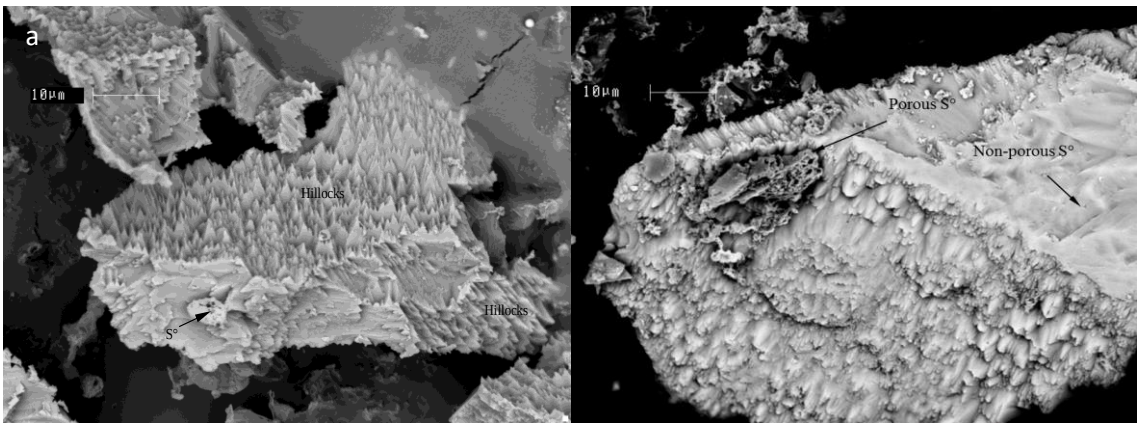

Figure 5.4: Partially leached (120 minutes) particles of size fraction (45-53 µm) in (a) 0.009M $Fe_2(SO_4)_3$, 0.073M H2SO4 and 0 g/L lignosulphonate at 90 °C (test Eb1), and (b) 0.029 M $Fe_2(SO_4)_3$, 0.028 M H_2SO_4 and 0 g/L lignosulphonate at 90 °C (test Ea3) (SEM images produced by Steyl (1999) at Mintek).

Figure 5.4a & b clearly indicate the preferential leaching that causes the formation of the hillocks on the particle surface when it is not parallel to the ideal (111) surface. The flat surfaces observed are probably close and/or parallel to the (111) plane, thus creating less hillocks. These observations are in agreement with discussions of Crundwell (1988c) and Gatos (1960).

To model the kinetics of sphalerite leaching, it is assumed that the cleaved particle surfaces are randomly distributed. The formation of hillocks and deviation due to less reactive surfaces are assumed to be averaged throughout the solution, hence plays a constant average role in the overall dissolution kinetics. A deviation from the expected dissolution rate would only be reflected close to the point of complete leaching.

5.4.3.2 Sphalerite's semiconducting electrochemical properties

Sphalerite is an extreme case of a semiconductor by having a wide band gap, in the range of 3.6 to 3.9 eV, and low rest potential, approximately 0.264 V, at standard temperature and pressure (STP) conditions (Crundwell, 1988b). Making it, in its purest form, a very stable compound; not easily leachable. The electron band structure of sphalerite and the relative positions of the limiting band edges to the standard reduction potential of important redox couples are illustrated in Figure 5.5.

The bottom of the conduction band is derived from the zinc 4s orbital, while the top of the valence band derived from the sulphur 3p orbital (Crundwell, 1988b). This is in agreement with the ionic model that associates the valance band with the anion (S^{2-}) and the conduction band with the cation (Zn^{2+}). Pure sulphide is a poor electrical conductor (almost an insulator), with a high electrical resistivity.

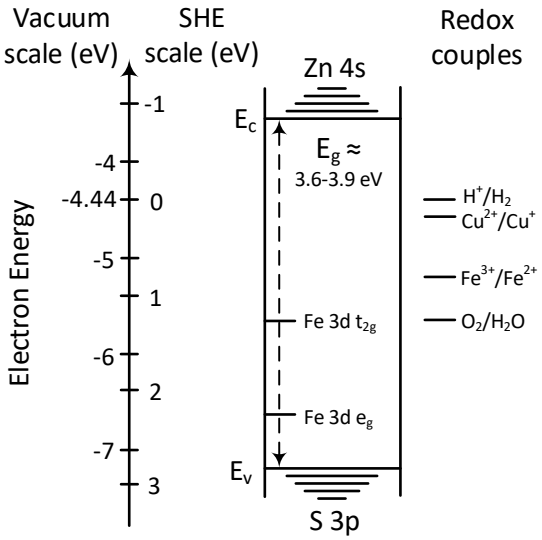

Figure 5.5: Qualitative semiconductor electron band structure of sphalerite, with iron impurity bands and standard reduction potential of the important redox potentials (adopted from Crundwell (1988a) and (Steyl, 2012))

The standard redox potential of the iron redox couple is situated approximately midway between the conduction and valence band edges (see Figure 5.5) and according to the band theory of solids would be an ineffective oxidant for sphalerite, *i.e.* electron transfer cannot occur between the mineral and iron ion since their electrons are not of the same electronic state. However, iron atoms within the crystal structure of zinc sulphide would have the effect of creating impurity bands in the band gap.

Natural sphalerite or concentrates contains a significant amount of iron (or other transitions metals) impurity, replacing the Zn atoms with the Fe atoms in the crystal structure. Iron impurity has a pronounced effect on the lattice parameters as well as the electrical properties of zinc sulphide. Iron impurity could vary between 1 and 15 % depending on the origin of the ore, *i.e.* temperature and pressure of crystallisation during geological formation.

In sphalerite, iron atoms create an impurity band within the band gap of zinc sulphide. Crundwell (1988c) endeavoured a fundamental quantum level description and modelling approach of the effect of iron impurity, in semiconducting sphalerite, to the mineral dissolution rate. The dissolution rate of sphalerite was found to be directly proportional to the concentration of iron substitutes in the zinc sulphide latte without any other impurities present (Crundwell, 1988a). Perez and Dutrizac (1991) have obtained results in agreement with Crundwell (1988a), by showing the linear dependence of the rate on the iron content and an effective decrease in activation energy with an increasing in the sphalerite iron content was observed.

This phenomenon was attributed to the formation of narrow impurity bands within the band gap (E_g) by the iron d-orbital (see Figure 5.5). The localised impurity bands originate from the e_g and t_{2g} d-orbitals of iron (*i.e.* the d-orbitals of transition metals with and face-centred-cubic, FCC, crystal structure) and supply holes (p-type semiconductor) to the conduction mechanism of sphalerite (Crundwell, 1988a, b).

Crundwell (1988c) determined, from quantum calculations, that the e_g and t_{2g} orbital levels are about 0.56 eV and 1.44 eV above the valence band (sulphur 3p orbital), respectively. It was stated that the presence of the iron d-orbital within the band gap has two consequences as a result: (1) it creates a narrow localized band that is energetically more favourable to exchange electrons between the iron d-orbital band and the oxidant (Fe^{3+} or ferric-ferrous redox couple) compared to the sulphur 3p-orbital (valance) band and the oxidant; and (2) it "pins" the Fermi level at a level within the d-orbital band (Crundwell, 1988a).

The transfer of an electron can only occur between states of the same (nearly) energy level; in the absence of energy transfer to the surroundings, or radiation. Therefore, energy levels at the solid-solution interface have a substantial effect on the capture of electrons by electronic carries at the solid surface. Crundwell (1988a,b) stated that the impurity band creates a high density of mono-electric surface states, which has the effect of making the potential charge across the space-charge layer (*i.e.* the solid side of the interface) independent of the solution electrochemical potential. Thus, a variation in the solution potential manifests as a potential change across the Helmholtz layer. The solid solution interface adopts a metal-like behaviour.

Application of the mixed-potential (MP) theory to leaching kinetics requires the potential across the space-charge region to remain constant, with the applied potential difference appearing across the Helmholtz layer. It is therefore imperative that sphalerite assimilates a metal-like behaviour for the application of electrochemical kinetics to the modelling of leaching rates.

Steyl (2012) also performed quantum-level calculations of the surface structures and dissolved solution species adsorption energies using a density functional theory (DFT) plane-wave pseudopotential method, in relation with other theories and density approximation methods. The binding energies were determined by first optimizing the bulk and then surface structures, by finding the minimum energy of the interactive system. The binding energy of aqueous reactant species at selected (most probable) surface mineral facets was calculated as the difference in the optimised total energy of the system before and after adsorption.

For the zinc sulphide (110) surface the binding energy of a proton (H^+) was calculated to be -3.883 eV and for the zinc sulphide (100) surface the binding energy of oxygen (O_2) is -0.4525 eV Steyl (2012). Unfortunately, it was not possible for Steyl (2012) to calculate the binding energy of the proton on the (100) surface, due to the arrangement zinc atom edges. Albeit, other sphalerite surfaces would result in similar (qualitative) measures.

Nevertheless, the unfavourable adsorption characteristics of oxygen are reflected by the end-on interaction of the diatomic molecule on positively charged zinc atoms (Steyl, 2012), while the proton was found to bond relatively strongly to the (110) surface. The strong interaction between the proton with the sulphur atom would be expected to result in a structure that does not resemble the original sphalerite surface, *i.e.* a positively charged surface. Hydrated ferric ions, however, can exchange electrons with the mineral surface without physically adsorbing onto an anodic sulphide site. This reflect the nature of the preferential formation of elemental sulphur (high elemental sulphur yields by various researchers) in comparison to the oxidation of sulphide sulphur to sulphate (SO_4^{2-}).

Chen & Chen (2010) investigated the adsorption of oxygen, O_2, on a sphalerite surface with vacancies and impurities through first principle calculations based on the density functional theory (DFT). Their results suggest that a perfect sphalerite (110) surface cannot adsorb oxygen, while the presence of vacancies (*i.e.* Zn-vacancy or S-vacancy) and impurity atoms (*i.e.* Fe, Mn, Cu and Cd) energetically favoured oxygen adsorption. Among the four impurities, the Fe-bearing surface was found to be the most energetically favourable site for oxygen adsorption. Followed by the Mn and Cu bearing surfaces of favourable oxygen adsorption, whilst the Cu baring surface was the least energetically favourable. This was attributed to the 3p orbital of S and 3d orbitals of Fe, Mn and Cu atoms, which donated electrons to the antibonding orbital π_{2p}^* of the O atom.

In contrast, the band theory of sphalerite (Figure 5.5) shows that oxygen would be a very effective oxidising agent (better than ferric) by alignment of the energy level of the redox couple with the iron impurity 3d-orbital energy level. This is true for the overall oxygen reduction reaction 5.21, but oxygen reduction involves a series of one electron transfer steps as shown in section 5.4.1. Steyl (2012) and Crundwell (1988c) has proven the first electron step (reaction 5.23) to be rate limiting and has a standard reduction potential, E_h^o, of 0.14 V. This low reduction potential of the diatomic oxygen molecule is situated approximately midway between the conduction band and the iron impurity band, similar the hydrogen and cupric reduction potentials. Hence, from a thermodynamic perspective, oxygen would be an ineffective oxidising agent, due to this mismatch of energy levels.

Taking previous research results, the latter, into account and the fact that this study's experiments were conducted under oxygen free conditions (*i.e.* no oxygen sparging, but autoclave was exposed to air), or extremely low solubility of oxygen at atmospheric and elevated temperature conditions, it can be assumed that sphalerite dissolution *via* oxygen reduction is negligible compared to H^+ and Fe^{3+} oxidation.

5.4.3.3 Sphalerite's leaching mechanism

The anodic dissolution reaction of sphalerite is coupled with the cathodic ferric redox reaction. Mechanisms proposed throughout the remainder of this study should be viewed in light of iron as oxidising agent. The reduction of ferric ion on sphalerite surfaces involves a single-electron transfer step at lower mixed potentials, thus yielding elemental sulphur as primary sulphur product. Sphalerite dissolution may also occur by direct acid attack, where a proton reacts with the sulphur atom and losses the bonding of zinc to the sphalerite surface. Due to the strong interaction between the proton with the sulphur atom, it would be expected that the resulting surface structure does not resemble that of the original sphalerite surface. Dissolution of sphalerite may occur *via* both proton and hole transformations as well. The first electron or proton transfer reactions are presented in Table 5.3, and as seen sphalerite leaching is proposed to be leached by either one of the three mechanisms.

Table 5.3: The first electron or proton transfer reaction of the sphalerite dissolution mechanisms

Mechanism	Reaction	Reference	
1: Oxidative	$ZnS_{(s)} + 2h^+ \Rightarrow Zn^{2+}_{(aq)} + \cdot S^*$	Gerischer and Mindt (1968)	5.46
2: Non-oxidative	$ZnS_{(s)} + H^+ \Rightarrow Zn^{2+}_{(aq)} + HS^{-*}$	Crundwell (1988c, 2014a)	5.47
3: Oxidative	$ZnS_{(s)} + H^+ + h^+ \Rightarrow Zn^{2+}_{(aq)} + HS\cdot^*$	Steyl (2012)	5.48

*Where * denotes a site on the surface, h^+ - hole's formed (opposite of electrons)*

The radical sulphur species, $\cdot S^*$, formed during the first oxidative mechanism may either react with other sulphur radicals to form elemental sulphur (reaction 5.30) or be oxidised to higher oxidation sates (reaction 5.31 and 5.32) to form sulphates or can react to form polysulphides (reaction 5.39). Refer to section 5.4.2 for sulphur transformation and rearrangement reactions at elevated temperatures (25 °C < T < 100 °C) and atmospheric pressure. The primary sulphur product from mechanism 1 is expected to be elemental sulphur, S^o, at lower acid concentration and high oxidative species concentrations. Mechanism 1 would also predominate over the other mechanisms when there is a surplus of hole formation, even at low redox potentials.

At high acid concentrations and low redox potential (*i.e.* low aqueous zinc, ferric and ferrous concentrations), the non-oxidative mechanism 2 would be expected to predominate over oxidative mechanisms. Aqueous hydrogen sulphide may subsequently be produced:

$$HS^{-*} + H^{+} \Rightarrow H_2S_{(aq)} \qquad 5.49$$

Hydrogen sulphide can also be produced by the termination process during the polymerisation of sulphur (see reaction 5.45). In a non-limiting case (*e.g.* hole formation/propagation or acid attack), the sulphide sulphur atom may react with a proton loosening the zinc-sulphur bond; and with the supply of an additional hole zinc ion would be released into solution. The subsequent oxidation of radical surface species would be expected to be comparatively fast (Steyl, 2012):

$$HS\cdot^{*} + h^{+} \Rightarrow S^{o} + H^{+} \qquad 5.50$$

Alternatively, this radical species may be reduced by remnant ferrous species of the first electron transfer step, leading again to the formation of hydrogen sulphide:

$$HS\cdot^{*} + e^{-} \Rightarrow HS^{-*} \qquad 5.51$$

The former discussion emphasises the difficulty to assign a specific reaction path to characterise the product formed during the leaching of sphalerite. Regardless, the importance of ferric as oxidising agent is highlighted and three mechanisms are proposed based on the first electron or proton transfer reactions.

Evidence supporting the mechanistic pathways, Table 5.3, is found in the study of Verbaan (1977). He investigated the dissolution kinetics of natural and synthetic sphalerite (*i.e.* low and high iron content in sphalerite) in various aqueous sulphuric acid and ferric sulphate media. The reported results show that an increase in iron impurity results in a decrease in hydrogen sulphide generation and increased solid sulphur production. This is in-line with the phenomenon where iron impurity causes increased hole formation by the alignment of valence electron energy levels from the band theory of solids, thus resulting in the preferential dissolution of sphalerite *via* mechanism 1 producing primarily elemental sulphur. High acid concentrations ($> 0.5\ M$) promoted the formation of hydrogen sulphide, while at higher redox potentials (hihger ferric connections) less hydrogen sulphide and more elemental sulphur was produced. Leaching of sphalerite was characterised as follows (Verbaan, 1977):

1. the S^{2-} sulphide species react with adsorbed Fe^{3+} to form S^{o} in situ (oxidative leaching)
2. the S^{2-} sulphide species react with adsorbed H^{+} to form H_2S (non-oxidative leaching)
3. the H_2S and Fe^{3+} react homogeneously

The concepts and mechanism described by Verbaan (1977) incorporated neither any solid state band theories nor the electrochemical nature of the solid-solution interface.

It is expected from the proposed mechanistic pathways that concentrates containing high iron impurity would be less sensitive (almost insensitive) to varying acid concentration, since no acid is involved during the reaction path. While concentrates containing low iron impurities would reflect a stronger dependency on the acid concentration, due to less hole formations and hydrogen involvement during the reaction path. This is reflected in the studies of Markus *et al.* (2004b) which used a concentrate containing 5.1 wt.% iron and reported that the sulphuric acid concentration (0.2 – 1.02 M) had no influence on the rate, while Markus *et al.* (2004a) used a synthetically produced pure zinc sulphide reagent and reported that sulphuric acid (0.41 – 1.02 M) had a great impact on the reaction kinetics. Dutrizac (2006) observed an increasing rate with increasing acid concentration > 0.1 M H_2SO_4, but the rate became insensitive to more dilute acid concentrations in an 0.3 M ferric media and using a sphalerite concentrate containing 7.23 ± 0.58 wt.% iron. He concluded from results of his research, the existence of a possible parallel direct acid leaching mechanism at the higher acid concentrations.

The insightful study of Weisener *et al.* (2004) has provided conclusive evidence, with XPS and ToF-SIMS analysis, of increased surface concentration of oxidised sulphur species, S_n^o, as the concentration of iron in sphalerite increased. They also observed higher leaching rates of zinc for the sphalerite samples containing greater concentrations of iron. Their results provide additional confidence for the proposed mechanistic behaviour.

There is overwhelming evidence from the literature supporting the proposed mechanistic behaviour of sphalerite leaching in sulphuric acid-ferric sulphate media, with the major distinction made between the oxidative and non-oxidative first transfer reactions.

The electrochemical nature is emphasised regarding ferric ions' role in the charge transfer mechanism of sphalerite dissolution, while acid may involve a direct chemical interaction, *i.e.*, no transfer of charge between separate reaction sites. The different proposals (covered above) are relatively consistent up to the point of surface adsorption, but differ substantially with regards to the route that sulphide follows to higher oxidation states. In the three reaction pathways proposed, physical distinction between mechanism 3 and other two mechanisms is problematic (almost impossible). A comprehensive quantum-level simulation may reveal a complete representation of the mechanism of sphalerite oxidation, but falls well outside the scope of this study. An empirical approach is therefore adopted in the rest of this study.

Sphalerite dissolution within the scope of this study is divided into two mechanistic pathways termed *non-oxidative* and *oxidative*. Non-oxidative sphalerite leaching refers to the direct reaction with acid (proton), while oxidative leaching refers to sphalerite oxidation by ferric ions. These two reaction paths will capture the prominent characteristics of sphalerite leaching. Figure 5.6 depicts the oxidative and non-oxidative mechanism, with the first electron or proton transfer step assumed to be the rate-limiting step. This model also assumes that the hydrogen ion prevents the direct adsorption of Fe^{3+} species on sulphide sites and presumes that electron transfer may occur *via* the relatively slow Grotthuss-type conduction mechanism at a high redox potential. Whilst at high acid concentrations the sulphide will undergo a protonation reaction.

$$Fe^{2+}_{(aq)} + h^+ \Leftrightarrow Fe^{3+}_{(aq)}$$

$$ZnS_{(s)} + 2h^+ \Rightarrow Zn^{2+}_{(aq)} + \cdot S^*$$

$$ZnS_{(s)} + H^+ \Rightarrow Zn^{2+}_{(aq)} + HS^{-*}$$

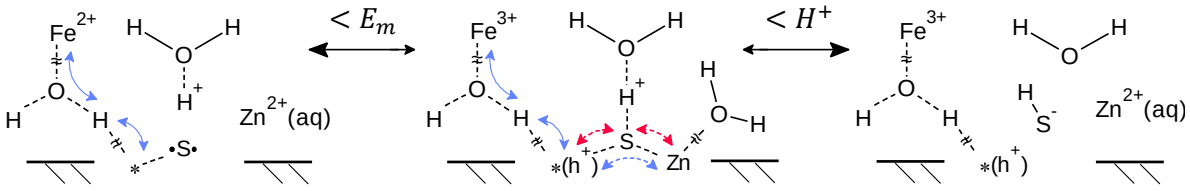

*Figure 5.6: A simple schematic diagram of sphalerite leaching: a) oxidative dissolution via electron exchange between t_{2g} orbital of aqueous Fe^{3+} species and surface states * (e.g. iron on the surface), namely hole creation mechanism, followed by an internal electron transfer from adjacent sulphide sites (represented by the blue paths); b) Protonation of surface sulphide site, with internal electron transfer from adjacent zinc sites (represented by the red paths).*

5.5 Intrinsic kinetic expression

The previous detailed review highlights the complex nature of sphalerite mineral oxidation and presented a suit of intrinsic rate-limiting steps from the proposed mechanism. The simplest conceptualised pathways are now used to develop intrinsic kinetic expressions suitable to model the rate of sphalerite leaching.

5.5.1 Electrochemical framework

Implicit in using this approach is a basic understanding of semiconducting electrochemistry and solid-state electronic structure theory, which was briefly discussed in the literature review (section 2.3). Bockris *et al.* (2001) provided a comprehensive study of all the aspects concerning the modern understanding of electrochemistry fundamentals. A detailed description of the fundamental concepts is outside the scope of this paper, and the reader is referred to review the literature. However, the basic application of the mixed potential theory is central to intrinsic kinetics derived in this section.

A metal-deficient compound, such as sphalerite (ZnS), is most likely to display *p*-type semiconducting behaviour (hole-decomposition pathway). The supply of electrons may be mitigation-limited in *p*-type semiconductors, which may explain why saturation effects are sometimes observed. An electric field developed at the solid-solution interface causes the transportation of charge carries across this region to be the rate-limiting step of sulphide mineral oxidation. Solid-state electronic structure and semiconductor electrochemistry is therefore used during the development of mechanisms and intrinsic sulphide mineral dissolution rates.

The cathodic reduction rate of the oxidant and anodic oxidation rate of the mineral govern the mineral surface potential at a specific reaction site. Activation energy barriers determine the intrinsic rate of these redox reactions, *i.e.* potential barriers creating resistance to charge transfer reactions. With the assumption that the Fermi energy is pinned, the electric potential would predominantly reside across the Helmholtz layer, that allow application of the MP theory to describe the rate of mineral dissolution (Bockris *et al.*, 2001; Crundwell, 1988c; Steyl, 2012).

The famous Butler-Volmer (BV) equation is central to phenomenological electrode kinetics, valid for systems containing excess supporting electrolyte with no mass transfer limitations (concentration polarisation) and no ohmic resistance, due neither to non-conducting surface layers nor to limiting conduction of electrons within the semiconductor. The rate would therefore be controlled by the electric charge transfer at the interface (Bockris *et al.*, 2001). The theory leading to the derivation of the fundamental relationship between the current density, i_j, and the potential difference, $\Delta\phi$, (the activation polarisation relationship) is presented in the literature review, section 2.3.3. The net current density of the anodic (i_a) and cathodic (i_c) reactions are represented as follows, for convenience square bracket notation for molality is adopted (Bockris *et al.*, 2001; Burkin, 2001; Havlík, 2008; Newman & Thomas-Alyea, 2004; Steyl, 2012; Vignes, 2011):

$$i_a = F \cdot \overrightarrow{k_a} \cdot [red] \cdot \exp\left(\frac{\beta_A F \Delta\phi}{RT}\right) - F \cdot \overleftarrow{k_c} \cdot [ox] \cdot \exp\left(\frac{-(1-\beta_A) F \Delta\phi}{RT}\right) \qquad 5.52$$

$$i_c = F \cdot \overrightarrow{k_a} \cdot [red] \cdot \exp\left(\frac{\beta_C F \Delta\phi}{RT}\right) - F \cdot \overleftarrow{k_c} \cdot [ox] \cdot \exp\left(\frac{-(1-\beta_C) F \Delta\phi}{RT}\right) \qquad 5.53$$

The subscripts a and c refer to the anodic and cathodic half-cell reactions, respectively. The rate constants k adopt the units of the molality scale and are a combination of various coefficients, e.g. water and species activity coefficients, free energy of activation of the reaction etc., which are lumped together to form a constant parameter. This rate constants characterises and

captures all uncertainties within the given system and is assumed to vary only with temperature. The transfer coefficient of the nett anodic and cathodic reactions are denoted as β_a and β_c, respectively. As mentioned, in literature the transfer coefficient is usually assumed to be $\beta_A = \beta_C = \beta = 0.5$. These concepts are now applied to sphalerite, in terms of the non-oxidative and oxidative dissolution mechanisms derived in the previous section of this chapter.

5.5.2 Non-oxidative kinetic expression

The non-oxidative mechanism is an instance where there exists chemical interaction between the sulphide sulphur atom and a proton. Meaning there does not exist two separate half reactions occurring on the sulphide surface. However, some researchers have presented theories and application of electrochemistry towards the dissolution of minerals by direct acid reaction (Bockris *et al.*, 2001; Crundwell, 2014a). Treatment of non-oxidative dissolution kinetics is therefore two-fold, *viz.*, derivation of kinetic expression based on conventional chemical kinetics and electrochemical kinetics based on charge transfer limitations.

During the overall non-oxidative reaction 5.2, the first protonation reaction 5.47 is assumed to be the rate-limiting reaction step, while the second protonation reaction 5.49 is expected to be comparatively fast. In the absence of any mass transfer and absorption limitations, the kinetic expression based on the conventional rate expression formula is:

$$r_{sph} = \vec{k} \cdot [H^+]^{\alpha_{H^+}} - \overleftarrow{k} \cdot [Zn^{2+}]^{\alpha_{Zn^{2+}}} \qquad 5.54$$

where the forward, $\vec{k}$, and backward, $\overleftarrow{k}$, rate constants are only temperature dependent and behave according to the Arrhenius relationship. The reaction orders with respect to acid concentration, α_{H^+}, and aqueous zinc ions concentration, $\alpha_{Zn^{2+}}$, are both expected to be equal to unity, according the stoichiometry of the reaction. Since discrepancies often arise and the order or reaction with respect to each species can be obtained by the method of initial rates from experimental batch data, α_i is left in variable format.

Crundwell (2014a,b, 2015) published a series of papers regarding the theoretical framework and application of electrochemistry, especially focussing on the Helmholtz layer, to the non-oxidative dissolution of minerals in acid solutions. His mechanism is based on the breaking of bonds at the dissolving surface and the transfer of charge across the interface, *i.e.* proton and/or metal cations. Bockris *et al.* (2001) gave a more detailed description of the structure of electrified interfaces, and the transfer of ions through the polarised (electric) Helmholtz layer.

Both imbedded the activation barriers theory, due to the potential difference across the surface layer surrounding the particle, in their derivation of mineral dissolution kinetics.

Removal of the zinc atom and formation of the zinc ion is given by the following expression:

$$Zn^{2+}_{|lat} + wH_2O + 2h^+ \rightleftharpoons Zn(H_2O)^{2+}_w \qquad 5.55$$

where $Zn^{2+}_{|lat}$ represents the zinc atom in a lattice position on the surface, w represents the stoichiometric coefficient with respect to water, which holds the zinc ion in solution. The anodic current density, due to direct reaction with the hydrogen ion (reaction 5.55) may be represented as follows:

$$i_A = F \cdot k_{a_1} \cdot [H_2O]^w \cdot \Psi_{Zn^{2+}_{|lat}} \cdot \exp\left(\frac{\beta_A F \Delta\phi}{RT}\right) - F \cdot k_{c1} \cdot [Zn^{2+}] \cdot \exp\left(\frac{-(1-\beta_A) F \Delta\phi}{RT}\right) \qquad 5.56$$

The surface concentration of zinc atoms in the lattice is denoted as $\Psi_{Zn^{2+}_{|lat}}$. By definition the water molality is 55.55 mol/kg and the surface concentration of zinc is assumed to remain constant and is therefore lumped with the rate constant, k_{a_1}. The dissolution of sulphide atoms from the lattice may occur by the reaction with a proton, expressed by the following first protonation reaction:

$$S^{2+}_{|lat} + H^+ \rightleftharpoons SH^{-*} + 2h^+ \qquad 5.57$$

where $S^{2+}_{|lat}$ represents the sulphide atom in a lattice position on the surface. It is assumed that the concentration of SH^{-*} remains very low (negligible) at high acid concentrations, since the second protonation reaction 4.49 is expected to be comparatively fast. The cathodic current density, due to the removal of sulphur atom on the surface and the formation of hydrogen sulphide ion, is given by the following rate expression:

$$i_C = -F \cdot k_{c2} \cdot [H^+] \cdot \Psi_{S^{2-}_{|lat}} \cdot \exp\left(\frac{-(1-\beta_C) F \Delta\phi}{RT}\right) \qquad 5.58$$

The surface concentration sulphide atom in the lattice is denoted as $\Psi_{S^{2-}_{|lat}}$.

If it is assumed that these anodic and cathodic reactions take place randomly over the particle surface, in the absence of copper in the solution, the total anodic and cathodic surface areas may be assumed to be equal. Assuming $\beta_A = \beta_C = \beta$ and applying equation 2.36 ($i_A = -i_C$), resulted in a potential-rate relationship described in equation 5.59.

$$\frac{\beta F \Delta\phi_m}{RT} = \ln\left(\frac{k_{c_1}[Zn^{2+}] + k_{c_2}[H^+]}{k_{a_1}}\right)^{\beta} \quad 5.59$$

The constants in equation 5.59 are lumped together to form the anodic and cathodic rate constants, k_i. The exchange current density (i_o) is the current at the mixed potential $\Delta\phi_m$, *i.e.*, where the net anodic and cathodic current densities are equal (see Figure 2.6). The relationship between the exchange current density and the intrinsic oxidation rate ($mol/m^2.min$) is expressed by Faraday's equation (Steyl, 2012):

$$r = \frac{i_o}{|n|F} \quad 5.60$$

Substitution of equations 5.60 and 5.59 into equation 5.56 and assuming $\beta = 0.5$, leads to an expression for the intrinsic formation rate of non-oxidative sphalerite dissolution, r_{sph}:

$$r_{sph} = \left(k_{a_1}k_{c_2}\right)^{0.5}\left([H^+] + \frac{k_{c_1}}{k_{c_2}}[Zn^{2+}]\right)^{0.5} - \frac{k_{c_1}k_{a_1}^{0.5}}{k_{c_2}^{0.5}}\left([H^+] + \frac{k_{c_1}}{k_{c_2}}[Zn^{2+}]\right)^{-0.5} \quad 5.61$$

Alternatively, substitution of equations 5.60 and 5.59 into equation 5.58 leads to:

$$r_{sph} = \frac{\left(k_{a_1}k_{c_2}\right)^{0.5} \cdot [H^+]}{\left([H^+] + \frac{k_{c_1}}{k_{c_2}}[Zn^{2+}]\right)^{0.5}} \quad 5.62$$

Both equations 5.61 and 5.62 give the exact same rate value, but differ in their formula. The overall protonation rate of the surface (per kg of H_2O), R_{sph}, is simply related to the phenomenological intrinsic rate, as follows:

$$R_{sph} = A_p \cdot \frac{k_1 \cdot [H^+]}{([H^+] + k_2 \cdot [Zn^{2+}])^{0.5}} \quad 5.63$$

where $k_1 = \left(k_{a_1}k_{c_2}\right)^{0.5}$, $k_2 = k_{c_1}/k_{c_2}$ and A_p refers to the surface area available for reaction. No enhanced oxidation effect at higher pulp density, *e.g.* due to the possible catalytic effect of pyrite and chalcopyrite and/or passivation of cupric which would form covellite like surface on the sphalerite particles, is deemed significant and equation 5.63 represents the most simplistic representation of sphalerite's non-oxidative dissolution.

5.5.3 Oxidative kinetic expression

Hydrated ferric ion may exchange electrons with the mineral surface *via* a water-bridge, without physically adsorbing onto an anodic sulphide site. Natural sphalerite contains iron substitutes, which creates 3d-orbital bands within the band gap. Hence, electron tunnelling between the sulphide 3p-orbitals in the valence band and holes in the surface 3d-orbitals of iron substitutes would occur through the injection of holes by ferric ion in solution (after Crundwell, 1988b). This electron transition process is followed by the concomitant release of Zn into solution, highlighting the role of iron and the oxidative nature of sphalerite leaching by ferric. To present a more conclusive picture in alignment with electrochemical nature of sphalerite leaching, oxidative kinetic expressions based on electrochemical principles and derived from a phenomenological view point.

For the overall oxidative reaction 5.4 to take place, it is assumed there is an excess supply of holes injected by ferric without the presence of an intermediary hydrogen ion interaction with sulphide, as illustrated by reaction 5.48. This is a very superficial and vague assumption, since it is difficult to prove or be conclude from batch experiments. The strong interaction of the hydrogen ion and sulphide is illustrated (qualitatively) by the binding energies from literature (Steyl, 2012). Reaction 5.48 also represents the intermediary mechanism as oxidative dissolution transforms to non-oxidative dissolution, and the first electron transfer step may become rate limiting. For the purpose of simplicity and due to the difficulty associated with defining the region of this possible intermediary mechanism, the extreme limiting non-oxidative and oxidative cases are assumed to capture the pronounced sphalerite leaching behaviour.

The MP methodology is followed to derive the current density of sphalerite oxidation by ferric ion. The anodic current density, due to direct reaction with ferric ion (reaction 5.46), may be represented as follows:

$$i_A = 2 \cdot F \cdot N_{Fe} \cdot k_{a_1} \cdot \exp\left(\frac{\beta_A F \Delta\phi}{RT}\right) - 2 \cdot F \cdot k_{c1} \cdot N_{Fe} \cdot [Zn^{2+}] \cdot \exp\left(\frac{-(1-\beta_A) F \Delta\phi}{RT}\right) \qquad 5.64$$

The current density is first order dependent on N_d, the number of occupied states in the d-band, *i.e.*, the concentration of iron substitutes (mol Fe/mol Zn) in the sphalerite lattice sites (Crundwell, 1988b,a). The cathodic current density, due to the reduction of ferric ions to ferrous ions (reaction 5.20), may be represented as follows:

$$i_C = F \cdot N_{Fe} \cdot k_{a_2} \cdot [Fe^{2+}] \cdot \exp\left(\frac{\beta_A F \Delta\phi}{RT}\right) - F \cdot k_{c2} \cdot N_{Fe} \cdot [Fe^{3+}] \cdot \exp\left(\frac{-(1-\beta_A) F \Delta\phi}{RT}\right) \qquad 5.65$$

Assuming these anodic and cathodic reactions takes place randomly over the particle surface, with no side reactions or passivation effects, the total anodic and cathodic surface areas are assumed to be equal. By assuming $\beta_A = \beta_C = \beta$ again and applying equation 2.36 ($i_A = -2i_C$, from stoichiometry), the following relationship of the activation energy over the polarised barrier is obtained:

$$\frac{\beta F \Delta\phi_m}{RT} = \ln\left(\frac{k_{c_2}[Fe^{3+}] + k_{c_1}[Zn^{2+}]}{k_{a_2}[Fe^{2+}] + k_{a_1}}\right)^{\beta} \qquad 5.66$$

Substitution of equation 5.66 with 5.60 back into either equation 5.64 or 5.65 and assuming the transfer coefficient is equal to ½ ($\beta = 0.5$), leads to an expression for the intrinsic oxidative dissolution rate of sphalerite, r_{sph}, respectively:

$$r_{sph} = 2N_{Fe}\left(k_{a_1}k_{c_2}\right)^{0.5}\left(\frac{[Fe^{3+}] + \frac{k_{c_1}}{k_{c_2}}[Zn^{2+}]}{1 + \frac{k_{a_2}}{k_{a_1}}[Fe^{2+}]}\right)^{0.5} - \frac{2N_{Fe}k_{c_1}k_{a_1}^{0.5}}{k_{c_2}^{0.5}}[Zn^{2+}]\left(\frac{[Fe^{3+}] + \frac{k_{c_1}}{k_{c_2}}[Zn^{2+}]}{1 + \frac{k_{a_2}}{k_{a_1}}[Fe^{2+}]}\right)^{-0.5} \qquad 5.67$$

$$r_{sph} = 2N_{Fe}\left(k_{a_1}k_{c_2}\right)^{0.5}[Fe^{3+}]\left(\frac{[Fe^{3+}] + \frac{k_{c_1}}{k_{c_2}}[Zn^{2+}]}{1 + \frac{k_{a_2}}{k_{a_1}}[Fe^{2+}]}\right)^{-0.5} - \frac{2N_{Fe}k_{a_2}k_{c_2}^{0.5}}{k_{a_1}^{0.5}}[Fe^{2+}]\left(\frac{[Fe^{3+}] + \frac{k_{c_1}}{k_{c_2}}[Zn^{2+}]}{1 + \frac{k_{a_2}}{k_{a_1}}[Fe^{2+}]}\right)^{0.5} \qquad 5.68$$

Again, both equations 5.67 and 5.68 give the exact same rate value, but differ in their formula.

The overall oxidation rate of the surface (per kg of H_2O), R_{sph}, is simply related to the phenomenological intrinsic rate, as follows:

$$R_{sph} = A_p\left(k_1\left(\frac{[Fe^{3+}] + k_2[Zn^{2+}]}{1 + k_3[Fe^{2+}]}\right)^{0.5} - k_1k_2[Zn^{2+}]\left(\frac{[Fe^{3+}] + k_2[Zn^{2+}]}{1 + k_3[Fe^{2+}]}\right)^{-0.5}\right) \qquad 5.69$$

Or

$$R_{sph} = A_p\left(k_1[Fe^{3+}]\left(\frac{[Fe^{3+}] + k_2[Zn^{2+}]}{1 + k_3[Fe^{2+}]}\right)^{-0.5} - k_1k_3[Fe^{2+}]\left(\frac{[Fe^{3+}] + k_2[Zn^{2+}]}{1 + k_3[Fe^{2+}]}\right)^{0.5}\right) \qquad 5.70$$

With the constants defined as $k_1 = \left(k_{a_1}k_{c_2}\right)^{0.5}$; $k_2 = k_{c_1}/k_{c_2}$; $k_3 = k_{a_2}/k_{a_1}$ and are assumed to follow the Arrhenius-type extrapolation of the rate constants. A_p refers to the surface area available for reaction. Equations 5.69 and 5.70 represents the most simplistic representation of the oxidative dissolution of sphalerite with ferric as oxidant.

Chapter 6 Concentrate Characterisation

The focus of this chapter is to characterise the sphalerite concentrate used in this study for modelling the intrinsic oxidation behaviour. The literature review has pointed out the requirement of mono-sized particles for the application of the shrinking core model, as well as that the dissolution kinetics of sphalerite is very specific to the source of the material.

The concentrate characterisation procedure followed from the following chronological order:

- A description of the sphalerite concentrate origin (where it came from).
- The classification procedures (*i.e.* milling and screening) used to prepare the various particle size fractions are outlined.
- Reviewing the literature of the most important features and analysis methods of a population of particles, and through analysing the prepared size fractions, the mono-sized particle assumption and surface discrepancies are addressed.
- A chemical and mineralogical analysis of each size fractions will further lead to insights into the reactivity of the different sulphide phases and their expected behaviours.
- A mineralogical inspection of the unreacted core of partially leached particles.

The experimental work was performed by Dr Johan Steyl (1999).

6.1 Origin of the concentrate

Zincor (Zinc Corporation of S.A. Limited) supplied chemical analysis of concentrates from a number of mines, with varying mineralogy, from which the purest concentrate was chosen. In view of Chapter 5, concentrates with high impurity content could lead to undesirable reaction pathways (*e.g.* galvanic interactions). Several mines contained galena in their concentrate, which will form a film of insoluble lead sulphate on reacting particle surfaces and inhibit sphalerite dissolution from the phenomenological mechanism as described in Chapter 5. Crundewell (1985) observed such an inhibition effect during the leaching of Black Mountain concentrate (Pb ≈ 3.5%) in sulphate solution.

The feed concentrate used in this study was selected to be from the Miranda Mineral Holding Ltd. mine, because it had the lowest lead (<0.01%), magnesium (<0.05%), manganese (< 0.05%) and other impurity levels, excluding iron and minor amounts of other base metal sulphides. The Maranda mine is situated near Letsitele in Limpopo Province of South Africa. The classification procedure of the sphalerite concentrate was performed by Steyl (1996), on the next page.

6.2 Classification of the sphalerite concentrate

Two tons of sphalerite concentrate was received from Miranda Mineral Holding Ltd. A maximum particle top size fraction of 150 µm was an operation requirement for proper suspension in the pilot-scale autoclave. The concentrate was wet-screened to pass 150 µm using a Sweco vibratory separator. Oversized particles were crushed in a ball mill and then re-screened. Figure 6.1 shows the comminution procedure.

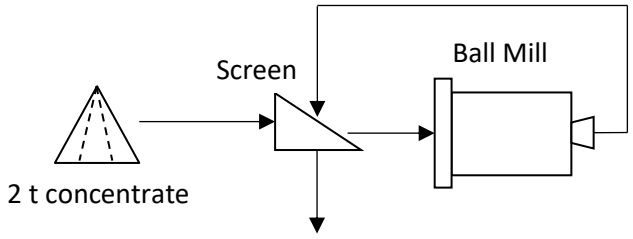

Figure 6.1: Process flow diagram of feed concentrate milling

Undersize material was passed (dry) through an air swept classifier (British Rema Aerosplit Classifier) to produce three batches of feed concentrate. The operating conditions were different during each campaign, *i.e.* different cut sizes were used, and thus slightly different particle size distributions were obtained. For further referencing these three batches are termed feed concentrate Fc1, Fc2 and Fc3, respectively, and presented in Figure 6.3. The method used to determine the particle size distributions, as well as the detailed size distribution data, can be found in Appendix H.1.

A batch of 100 kg was removed from feed concentrate 1 (Fc1) to produce the material for the lab-scale kinetic leaching tests. The milled feed sample was then separated into six different size fractions with a Sweco vibratory separator. The undersize (<38µm) material was then hand-screened to produce an additional size fraction of 20-38 µm. Ultra-fine particles, clinging to the surface of the particles, were ultrasonically removed from all size fractions and followed by another wet screening by hand. The samples were dried and then a final dry screen by hand was performed on each size fraction, producing the final head concentrate.

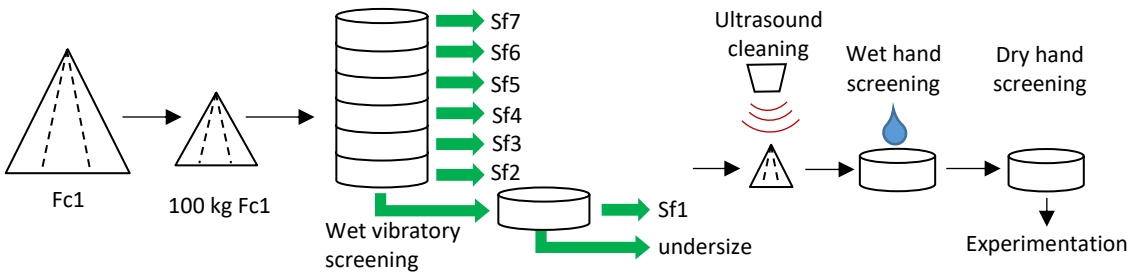

Figure 6.2: Classification procedure (screening) into seven size fractions

A sample from each size fraction was sent for particle size analysis to determine the respective size distributions (see appendix H.1 for detailed distribution results and Figure 6.4 for graphical presentation). The size fractions used in the batch test are shown in Table 6.1 below.

Table 6.1: Sieve range of each size fraction class (Steyl, 1996)

Size fraction	Sf1	Sf2	Sf3	Sf4	Sf5	Sf6	Sf7
Range (µm)	+25/-38	+38/-45	+45/-53	+53/-75	+75/-90	+90/-106	+106/-150

6.3 Particle size analysis

6.3.1 Objective

Mineral oxidation (leaching) reactions are topochemical of nature, *i.e.*, occurring at a specific region on the surface of a particle. It is therefore important to establish the nature of the surface and volume of particles in the respective size fractions. The objective of analysing the particles is to confirm whether or not the median diameters of each distribution can be used as approximation of the average particle size (*i.e.* inspecting the validity of assuming mono-sized particles in the kinetic analysis techniques). To achieve this objective two distribution and one particle characteristic needs to be defined, which include the (1) form of the particle size distribution, the (2) measures of a particle size distribution, and the (3) particle angularity and porosity analysis.

6.3.2 Methodology

This section presents the analysis methodology of a particle size distribution. The statistics are outlined and how they address the three characteristics of a particle size distribution.

Form of a particle size distribution

Particle size distribution can be represented as a histogram of discrete sizes or as a continuous curve. A particle size density function can be defined in terms of either the number, surface area or the volume (mass) of particles within a given size range. These density functions are also interconvertible with each other, *i.e.,* area distribution can be converted to volume distribution.

In practice the distribution of milled ore is often found to be quite skewed, with a sharp increase at small particle sizes and slowly decreasing with increasing particle size. A distribution called the lognormal distribution describes particle populations exhibiting such a form. That is, with the logarithm of the particle size, the particle size distribution follows the normal or Gaussian distribution in semi-log scale (Fan & Zhu, 1998).

This phenomena of observing lognormal particle size distributions as product from milling is rationalised in the literature based on the central limit theorem (Bender, 2012; Epstein, 1947; Rice, 2006; Rumpf, 2012; Wasserman, 2002). In practical terms, suppose that particles of some initial size is subjected to repeated, but independent, impacts and after each impact a proportion of the original particle size remains. After many of such impacts the distribution would conform to a lognormal distribution.

The feed concentrates particle size distribution results (Appendix H.1) indicate that the volume distribution follows the rational of a lognormal distribution, and has the characteristics thereof. Four statistical parameters are introduced to characterise the distributions, namely the logarithmic mean, standard deviation, skewness and kurtosis. The method and calculations for each statistical parameter are obtained from (Blott & Pye, 2001), and summarised in Table 6.2.

Table 6.2: Lognormal distribution statistics

Mean	Standard deviation	Skewness	Kurtosis
$x_g = e^{\sum f_v ln x_i}$	$\sigma_g = e^{\sqrt{\sum f_v \cdot (ln\, x_i - ln\, x_g)^2}}$	$Sk_g = \frac{\sum f_v \cdot (ln\, x_i - ln\, x_g)^3}{\ln \sigma_g^3}$	$K_g = \frac{\sum f_v \cdot (ln\, x_i - ln\, x_g)^4}{\ln \sigma_g^4}$

[a]Sorting (σ_g)		[b]Skewness (Sk_g)		[c]Kurtosis (K_g)	
Very well	< 1.27	Very left	< -1.3	Very platykurtic	< 1.7
Well	1.27-1.41	Left	-1.3 to -0.43	Platykurtic	1.7-2.55
Moderately well	1.41-1.62	Symmetrical	-0.43 to 0.43	Mesokurtic	2.55-3.70
Moderately	1.62-2	Right	0.43 to 1.3	Leptokurtic	3.70-7.40
Poorly	2-4	Very right	> 1.3	Very leptokurtic	> 7.40
Very poorly	4-16				
Extremely poorly	> 16				

The sum of frequencies adds up to one ($\sum f_v = 1$), [a]*Sorting* is a measure of the spread of the sizes around the average, [b]*Skewness* is a measure of the symmetry of the distribution *and* [c]*Kurtosis* is a measure of the peakedness or flatness of the distribution

The statistical parameters in Table 6.2 would indicate, in conjunction with visual inspection, if the semi-log plot of the volume percentage passing versus particle size is normally distributed. A lognormally distributed particle population has the same shape in area and volume.

Measures of a particle size distribution

There are three important measures for a given particle size distribution, viz. the mode, median and mean (Ahmed & Ahmed, 2008). The purpose of such measures is to represent a population of polydispersed particles by a single comparable particle size. Other measures include the distribution percentiles and span, which gives an indication of the accuracy of the average particle size.

- Mode

The mode is defined as the most frequent size, *i.e.*, the size corresponding to the peak on the size distribution frequency curves. Using this measure for comparison between different distributions can be disadvantageous, because some distributions may have multiple peaks (referred to as multi-model distributions). However, for distribution of similar shape the mode is a preliminary indicative measure of where most of the mass (or volume) of the sample is, with respect to a volume distribution.

- Median

The median is defined as the particle diameter where half of the population resides below this point, and half reside above. For a volume distribution the median is denoted as Dv50. The median can easily be determined from a cumulative undersize curves. This value is one of the easier statistics to understand and is also the most meaningful in describing the average particle size of a polydispered population of particles.

- Mean

Expressing the particle size of a sample in terms of a single linear length measure is required, in the sense that it can be uniquely define for sphere (*i.e.* the diameter) describing the particles area and volume. For all other shapes, more than one measurement is required and their size must be defined clearly. In practice, derived diameters (means) are determined by measuring a size dependent property of a population (e.g. surface or volume distribution) and relating it to a single linear measure. The most common of these are the equivalent spherical diameter.

An equivalent diameter of a particle is usually defined in relation to a specific sizing method, developed on the basis of a certain equivalency criteria. Thus a mean size will describe only one particular characteristic of the particle poplulation and it is therefore important to decide what that characteristic should be (Richardson *et al.*, 2002).

The volume diameter of a particle may be useful in applications where equivalent volume is of primary interest, such as in the estimation of solids holdup in a fluidized bed or in the calculation of buoyancy forces of the particles (Fan & Zhu, 1998). By comparison the area diameter, specifically Sauter's diameter, is widely used in the field of reacting fluid-solid or mass transfer processes, where the specific surface area is of most interest. Considering sphalerite oxidation mechanisms (chapter 4) the equivalent surface-mean diameter is of most importance.

In the following discussion the particle size will be defined in such a way that either the volume (mass) or surface is characterised by the mean value of all the particles in the sample.

Equivalent volume-mean diameter (De Brouckere mean diameter, D[4,3])

Considering a particle size distribution based on volume (if the density is constant across the size fractions), *e.g.*, obtained through laser diffraction particle size analysis, the D[4,3] mean indicates around which diameter the frequency of the volume would be centred (Rawle, 2003).

$$D[4,3] = \frac{\int_0^1 x \; df_v}{\int_0^1 df_v} = \int_0^1 x \, df_v \qquad 6.1$$

where x is the diameter of the particle and f_v the volume (mass) frequency distribution. Equation 6.2 expresses the integral form in its finite difference from, that can be applied to a fixed step size distribution.

$$D[4,3] = \frac{\sum x_i f_{vi}}{\sum f_{vi}} = \sum_{i=x_0}^{x_{max}} x_i f_{vi} \qquad 6.2$$

Equivalent surface-mean diameter (Sauter mean diameter, D[3,2])

D[3,2] indicates around which diameter the frequency of the surface area distribution would be centred (Rawle, 2003). The mean diameter would have the same ratio of external surface to volume as the whole population of particles (*i.e.* equivalent specific surface in mass).

$$D[3,2] = \frac{\int_0^1 x \, df_s}{\int_0^1 x \, df_s} = \int_0^1 x \, df_s \qquad 6.3$$

In equation 6.3 the surface frequency distribution function is denoted as f_s. Expressing this relation in the volume distribution and finite difference form, then (Richardson *et al.*, 2002):

$$D[3,2] = \frac{1}{\sum_{i=x_0}^{x_{max}} \frac{f_{vi}}{x_i}} \qquad 6.4$$

The equivalent surface-mean and volume-mean diameters are analogous to moments of inertia, and are the two most important diameters used in practice. From a statistical point of view, if the volume distribution is measured (*i.e.* by laser diffraction) it will be subject to an error, ε. In the case of D[4,3] and D[3,2] the mean diameters will relate linearly with the error.

- Percentiles

A common approach to define a distribution width is citing the 10% passing (Dv10) and 90% passing (Dv90) values of the cumulative volume distribution. Similar to the Dv50, the Dv90 diameter is defined as the diameter where 90 percent of the distribution lies below this value, and 10 percent of the population lies below the Dv10 value.

- Span

Another common approach is to relate D_v50, D_v10 and D_v90 values into a single comparable value that captures the width of the distribution, called the span. The span is calculated as follows:

$$Span = \frac{D_v90 - D_v10}{D_v50} \times 100 \qquad 6.5$$

Particle porosity and angularity analysis

The surface area of porous particles is an important parameter in characterising the oxidation behaviour involving sphalerite particles. For a transport phenomenon of interest, a specified effective surface area is defined, implying that for surface chemical reaction (or adsorption/desorption processes), the internal surface area provided by the interior pores of the particle may determine the overall reaction rate. Diffusion limited reactions on the other hand are dependent on the effective external surface area to determine the rate of reaction.

The internal surface area of each size fraction is analysed by the principle of gas adsorption, using the Brunauer-Emmett-Teller (BET) method. When a solid surface is exposed to a gaseous atmosphere, gas molecules impinge on the surface and a certain percentage is adsorbed. The equilibrium amount of adsorbed gas (moles/g) as a function of relative pressure (*i.e.* P/P_o the saturation vapour pressure over the standard pressure), at standard pressure and constant temperature, is called an adsorption isotherm (Pabst & Gregorova, 2007). Thus, the adsorption isotherm represents a dynamic equilibrium between adsorption onto and desorption from the solid surface.

According to the IUPAC pore size classification standards, pores are divided into micro-pores (< 2 nm), meso-pores (2 – 50 nm) and macro-pores (> 50 nm). In particles containing micro- and meso-pores, the absorbed gas could attain a liquid-like state (capillary condensation). Gas

molecules apparently adsorbed would then greatly exceed the required monolayer adoption, resulting in unrealistically high surface area values (Pabst & Gregorova, 2007).

The BET method measures the surface area per gram of mass (m^2/g). A comparison test between the BET surface area and equivalent spherical surface area, S_A (m^2/g), will reveal a quantitative measure of the particles angularity and porosity. In order to compare these measures a mean particle diameter of the particle size distribution needs to be converted to similar units. Calculating the equivalent spherical specific surface area from the Sauter's mean diameter (equivalent surface-mean diameter, D[3,2]) was performed as follows:

$$S_A = \frac{A_p}{M_p} = \frac{A_p}{\rho_p \cdot V_p} = \frac{\phi_A}{\phi_V} \cdot \frac{1}{\rho_p \cdot x_p} = \frac{6}{\rho_p \cdot x_p} \qquad 6.6$$

where A_p and V_p is the area and volume of a spherical particle, ρ_p is the particle density and x_p the diameter of the particle. Furthermore, the ratio of area to volume shape factor, ϕ_A/ϕ_V, for a sphere is 6. Substituting D[3,2] for the particle diameter, x_p, the equivalent smooth specific surface area can be calculated. Equation 6.6 requires the density to be known of each size fraction.

The particle size analysis methodology to address the characteristics of the distribution in term of the (1) form of the particle size distribution, the (2) measures of a particle size distribution, and the (3) particle angularity and porosity will give sufficient evidence on whether or not a particle population can be assumed to be mono-sized.

6.3.3 Results

With the particle size analyses background in mind from the previous section, the distribution results are analysed. The three feed concentrate particle size distributions (Fc1, Fc2 and Fc3) were analysed by laser diffraction to obtain their respective volume (mass) distributions. The frequency distributions (in semi-log scale) at various particle sizes are presented in Figure 6.3a, while Figure 6.3b presents the cumulative particle size distribution of the feed concentrates.

Size fractions (Sf1 to Sf7) that were prepared for the batch tests are presented in Figure 6.4. Figure 6.4a present the frequency distribution and Figure 6.4b the cumulative frequency distribution in semi-log scale.

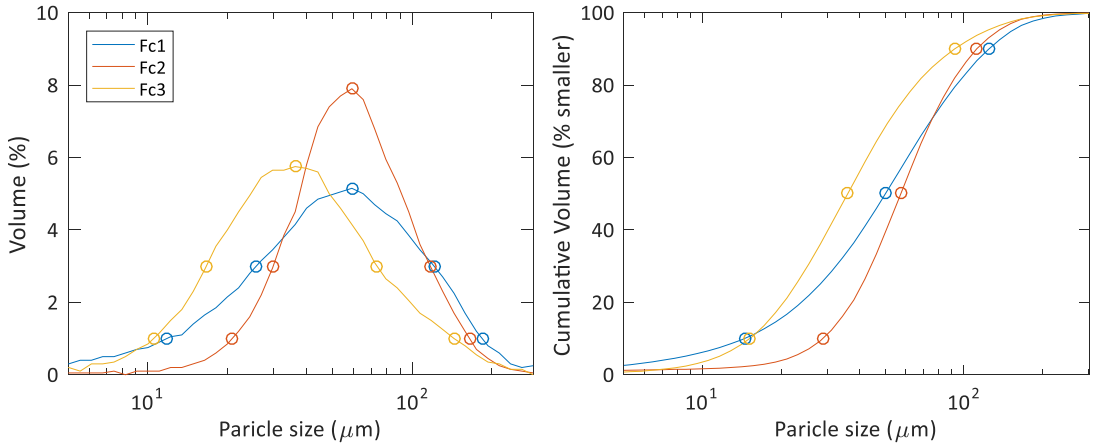

Figure 6.3: Particle size distributions by (a) Frequency and by (b) Cumulative passing of the feed stock concentrates

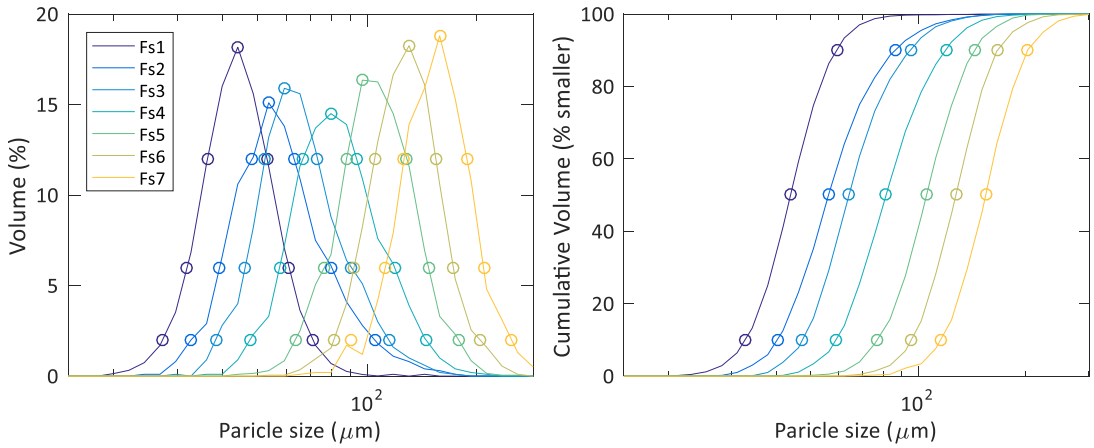

Figure 6.4: Particle size distributions by (a) Frequency and by (b) Cumulative passing of the feed stock concentrates

Milling of the 2 tons of sphalerite concentrate, in a ball mill operation, produced very fine particles (< 10 µm), which is expected from a ball mill operational design, creating tailed distributions (Figure 6.3, see also Appendix H.1). The resulting particle size distributions display a bell-shaped (Gaussian) from in the semi-log scale (*i.e.* lognormal distribution).

The seven size fractions used in the experimental program (Figure 6.4) exhibit also a symmetrical bell-shaped (Gaussian) volume distribution form in the lognormal abscissa. Hence, the distribution form gives an indication that each sample has approximately the same shape in area and volume (Zender, 2015), but will be quantified by the distribution measures.

To validate the lognormal distributions' form quantitatively, statistical parameters in Table 6.2 were computed from the PSD data (Appendix H.1). The results are given in Table 6.3.

Table 6.3: The lognormal distribution form statistics

Fraction	Average	Sorting		Skewness		Kurtosis	
		Value	Result	Value	Result	Value	Result
Fc1	44.7	2.45	Moderate	-0.99	Left	4.73	Leptokurtic
Fc2	54.9	1.95	Moderate	-2.18	Left	14.18	Leptokurtic
Fc3	36.1	2.05	Moderate	-0.20	Symmetrical	3.70	Mesokurtic
Sf1	44.1	1.27	Very Well	0.16	Symmetrical	3.95	Mesokurtic
Sf2	57.8	1.35	Well	0.50	Right	3.44	Mesokurtic
Sf3	65.7	1.31	Well	0.43	Symmetrical	3.24	Mesokurtic
Sf4	82.6	1.31	Well	0.23	Symmetrical	2.98	Mesokurtic
Sf5	105.7	1.28	Well	-0.04	Symmetrical	3.14	Mesokurtic
Sf6	127.2	1.25	Very Well	-0.04	Symmetrical	3.26	Mesokurtic
Sf7	153.9	1.25	Very Well	-0.15	Symmetrical	3.35	Mesokurtic

The distribution shape statistics indicate that the experimental size fractions are well sorted around the mean diameter and that the PSD's are symmetrical. The peakedness of the distributions are all mesokurtic (*i.e.* whose kurtosis is similar to the kurtosis of the normally distributed data set).

The measures of a particle size distribution were also calculated and compared in Table 6.4.

Table 6.4: Comparison of various equivalent-sphere measures for the sphalerite concentrate samples used in the batch experimental testwork

Test Number	Average Screen aperture (µm)	Dv50 (µm)	Mode (µm)	D[4,3] (µm)	D[3,2] (µm)	Dv10 (µm)	Dv90 (µm)	Span (%)
Fc1	-	50.1	59.2	61.9	25.4	14.5	124.4	219.4
Fc2	-	57.4	59.2	65.3	33.7	28.9	111.9	144.7
Fc3	-	36.0	36.1	47.0	27.0	15.2	92.1	214.0
Sf1	29.0	43.9	44.0	45.3	42.8	33.0	59.3	59.9
Sf2	41.5	56.1	53.6	60.6	55.1	40.6	85.9	80.7
Sf3	49.0	63.9	59.2	68.2	63.3	47.8	94.6	73.3
Sf4	64.0	81.4	79.5	85.8	79.4	59.4	118.9	73.1
Sf5	82.5	105.3	107.0	108.8	99.4	76.9	142.5	62.3
Sf6	98.0	127.3	130.5	130.5	121.7	96.2	167.0	55.6
Sf7	128.0	154.3	158.5	158.0	148.1	116.4	203.2	56.3

The most prominent feature from the particle size measures in Table 6.3, is the similarity of the median (Dv50) to the mode (most frequent size), the equivalent surface-mean diameter, D[3,2], and the equivalent volume-mean diameter, D[4,3]. Thus, supporting the assumption of symmetry in the lognormal scale. D[4,3] and D[3,2] are almost equal, indicating that each size fraction has approximately the same shape in area and mass distribution. A distribution with a relatively small span (as seen for Sf1, Sf6 and Sf7) indicates a closer tendency towards a central particle size and carries more significance to the mono-sized assumption.

There is a relatively large discrepancy between the measured equivalent-median diameters and the mean screen aperture for the screened fractions (Sf1 to Sf7). This may be ascribed to the irregular shape of the particles; see the secondary electron image (SEI) of the grain-mounted particles showing typical particle geometries (Figure 6.5), images were taken by Steyl (1996). The measured distribution may have corresponded better with the screen apertures, if the particles had been more spherical. The elaborate long screening procedure allowed larger particles to pass through the sieve.

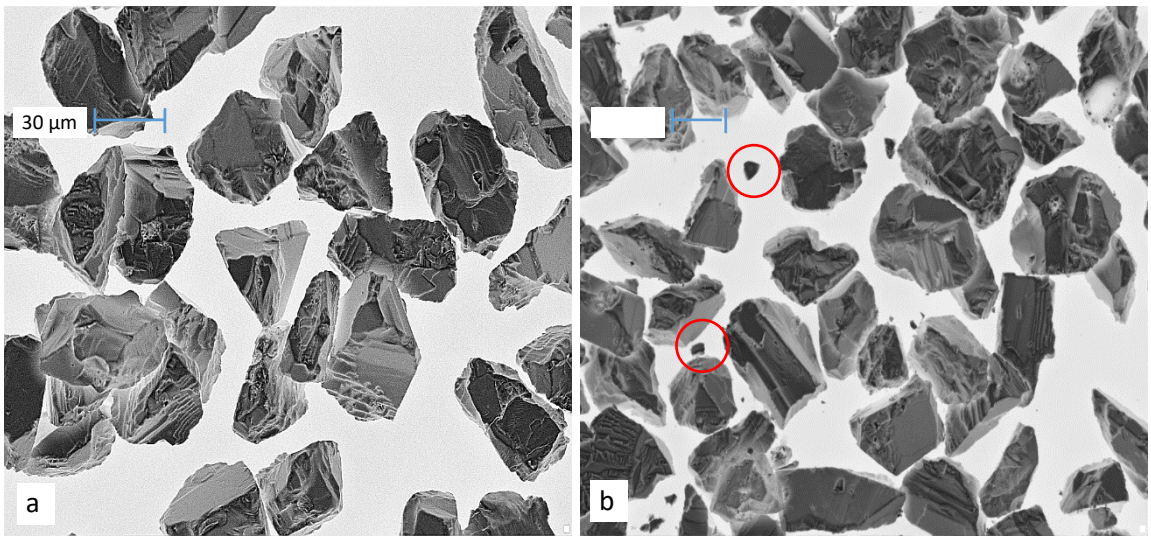

Figure 6.5: SEI of feed size fraction Sf1 (25-38 µm) used in the sphalerite leaching testwork (a) exhibiting no ultrafine particles; (b) some ultrafine particles (ultrafine particles circled in red)

Almost no ultrafine particles were observed to be attached to the surfaces of larger particles in most of the SEI (Figure 6.5a), while in some other images the occurrence of ultrafine particles is clear (Figure 6.5b). Cleaning of the size fractions (by ultrasonic means) was successful. Ultrafine particles would result in undesirable higher initial reaction rates, due to the increased initial surface area. Furthermore, particles of irregular shapes are prominent in the feedstock, which would also enhance the initial rate (ref. irregular particle shapes have low sphericity and very high angularity, see (Rawle, 2003)). It is thus expected that the leaching batch experimental test would demonstrate enhanced initial leaching rates.

To confirm the previous observation, claiming the feed particles actual surface area is greater than that of the equivalent spherical surface area (*i.e.* calculated from the measured particle size distribution), the particle surface area is measured by gas adsorption (*i.e.* BET metod). Table 6.5 summarises the estimated specific surface areas and densities of each particle size fraction.

Table 6.5: Size fraction densities, BET specific surface areas (S_A) and equivalent spherical specific surface area (Steyl, 1996)

Size fraction	< 20 µm	Sf1	Sf2	Sf3	Sf4	Sf5	Sf6	Sf7
Density (kg/l)	4.01	4.02	4.02	4.01	4.01	4.01	3.99	3.98
BET S_A (m^2/g)	—	0.24	0.22	0.19	0.17	0.14	0.14	0.12
[a]Spherical S_A (m^2/g)	—	0.035	0.027	0.024	0.019	0.015	0.012	0.010

[a]*Calculated using the equivalent surface area mean diameter (D[3,2]) and Equation* 6.6*.*

The density evidently does not vary with any significance between the different size fractions. A sphalerite concentrate density of 4.01 kg/l is assumed throughout this project.

A considerable increase in specific surface area, approximately 7 to 12 times larger, is observed for the BET surface area compared to the equivalent specific surface area. Indicating the large effects that either the high angularity, macro-pores or ultrafine particles have on the total area of the concentrate. To confirm that the large surface areas are not due to micro-pores, the adsorption isotherm is presented in the following figure for Sf1.

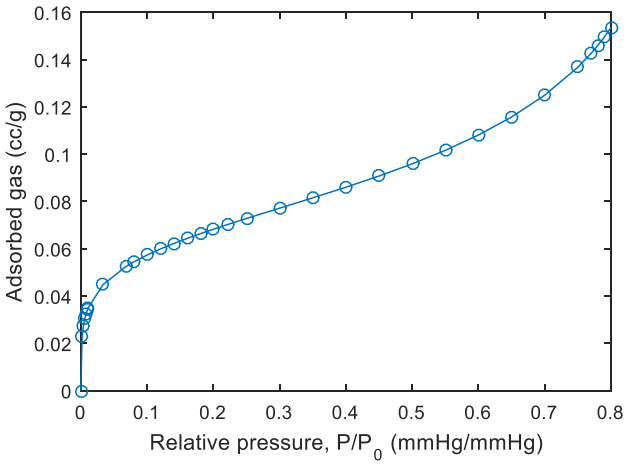

Figure 6.6: Adsorption isotherm for size fraction Sf1 (20-38µm), Steyl (1996)

The shape of the above isotherm (Figure 6.6) is a clear indication that the small pores or cracks do not contribute much to the total surface area (see Gregg and Sing, 1982). The angularity of the particles may therefore be more likely to be the reason for the large initial surface area and could result in higher initial rates.

6.3.4 Conclusions

The main objective of analysing the particles was to confirm whether or not the median diameters of each distribution can be used as approximation of the average particle size. This objective was addressed by analysing three characteristics of the feed particles, namely the form of the particle size distribution, the measures of a particle size distribution, and by analysing the particle angularity and porosity.

The feed concentrates (Fc1 to Fc3) displayed similar characteristics as a lognormal distribution, but the statistical results have shown that there was not sufficient proof to assume that they follow such a distribution. Size fractions (Sf1 to Sf7) used as feed concentrate for the batch experiments were found to have the form of a lognormal distribution, and supported with sufficient enough evidence.

During comparison of the particle distributions' measures (Table 6.4) it was found that the feed size fractions (Sf1 to Sf7) each have approximately the same shape in area and volume (*i.e.* the shape of the particles is consistent between particle sizes). Having the same shape in area and volume is an important factor for the mono-sized particle assumption, since a change in particle size due to a reaction occurring would manifest in the same change in area and volume throughout the whole distribution of particle. The mode, median, equivalent volume and area diameters are also similar. Therefore, the median diameters of each size fraction are a good approximation of the average particle size and assumed to be so, presented below:

Table 6.6: Average particle sizes used throughout this project

Size fraction	Fc1	Fc2	Fc3	Sf1	Sf2	Sf3	Sf4	Sf5	Sf6	Sf7
Size (µm)	50.1	57.4	36	43.9	56.1	63.9	81.4	105.3	127.3	154.3

The particles also have very irregular shapes and the area determined by BET analysis (*i.e.* surface area with high angularity, macro-pores and ultrafine particles) was much higher compared to the surface area determined by the equivalent mean surface area diameter, which was calculated from the PSD obtained from the laser diffraction analysis.

The feed particle size fractions (Sf1 to Sf7) was found to be mono-sized. The feed (head) concentrates (Fc1 to Fc3) could not be assumed to be mono-sized, because the spread of the distribution and measures did not match up.

6.4 Particle composition analysis

6.4.1 Objective

The different sulphide phases react differently in aqueous sulphuric acid solutions. Impurities like iron and copper are present in some leachable phases and contribute to the solution tenor. Leaching of impurities could contribute to changes in the reagent concentration in solution. Both these factors may alter the kinetics of sphalerite dissolution. In order to model the batch and continuous reactors, it is therefore important to know which elements are present in what phases and in what quantities. The distribution of the different elements and phases varies between particle size fractions and must also be quantified to accurately model the leaching process for a feed consisting of polydispersed particles.

6.4.2 Methodology

The quantification process of the particle composition involved two analyses, *viz.* chemical analysis and mineralogical analysis. A brief discussion of analysis techniques used for these two analyses are presented in this section (Steyl, 1999).

Chemical analysis was done by Inductive Coupled Plasma Optical Emission Spectroscopy (ICP-OES) to determine the elemental composition of the different size fractions. In Inductively Coupled Plasma (ICP) based analytical techniques, a sample is nebulized into the core of an inductively coupled argon plasma, where temperatures of approximately 9000 K are attained. At such high temperatures the species are atomized, ionized and thermally excited. The species can then be detected and quantified with an optical emission spectrometer (OES).

Mineralogical analysis involved four techniques in order to quantify the mineral phases and elemental composition of the different phases. X-ray powder diffraction (XRD) was first used to identify the most prominent phases present in the different size fractions. Secondly, backscattered-electron images produced on a scanning-electron microscope (SEM) are visually investigated to determine the degree of liberation. Thirdly, the bulk modal composition of the feed size fraction was determined in order to quantify the relative amounts of gangue and base metal sulphides (BMS). In addition, the BMS phase is analysed by SEM-based image analysis to determine the minerals present in each size fraction. The fourth and final mineralogical analysis technique involves an electron microprobe analysis to determine the stoichiometric composition of the sphalerite, pyrite, chalcopyrite and pyrrhotite phases. From the quantitative results of these four mineralogical analysis techniques, the elemental composition and leachable amounts are determined.

6.4.3 Chemical analysis results

All of the size fractions were analysed by ICP-OES, as mentioned above, and the results are given in Table 6.7. It was found that total sulphur (S_0) and sulphide (S^{2-}) were approximately equivalent, and thus all sulphur reported are in sulphide form. Results in Table 6.7 of the feed material are presented as an average of 10 analyses, conducted over the course of Steyl's (1999) research campaign. Elemental distributions were reproducible validating the accuracy.

Table 6.7: Chemical analysis of the feed size fractions of the head, Steyl (1996)

Size Fraction (µm)	Zn (%)*	Fe (%)*	Cu (%)*	S^{2-} (%)*	Si (%)*	Al (%)*	Ca (%)*	Pb (%)*	Mg (%)*	Mn (%)*	Sum (%)*
< 20	56.6	9.0	0.3	33.8	0.1	< 0.05	< 0.1	< 0.01	< 0.05	< 0.05	99.8
+20-38	57.0	8.7	0.2	33.9	0.1	< 0.05	< 0.1	< 0.01	< 0.05	< 0.05	99.9
+38-45	56.1	9.2	0.4	33.8	0.2	< 0.05	< 0.1	< 0.01	< 0.05	< 0.05	99.7
+45-53	54.9	9.7	0.6	33.7	0.4	< 0.05	< 0.1	< 0.01	< 0.05	< 0.05	99.3
+53-75	53.5	9.8	1.0	33.8	0.8	< 0.05	< 0.1	< 0.01	< 0.05	< 0.05	98.9
+75-90	52.9	9.9	1.4	33.6	1.0	< 0.05	< 0.1	< 0.01	< 0.05	< 0.05	98.8
+90-106	50.5	10.3	2.1	33.4	1.7	< 0.05	< 0.1	< 0.01	< 0.05	< 0.05	98.0
+106-150	49.1	10.8	2.5	33.0	2.1	< 0.05	0.1	0.01	< 0.05	< 0.05	97.6

*mass %

Only Zn, Fe, Cu and Si were found in any significant amount. The remaining metals are present in trace amounts. Zinc content appears to decrease with increasing particle size, while iron copper and silicon appears to increase. With the present composition knowledge, it is unclear as to why the increases and decreases are observed, but this may be the result of variation in hardness of the mineral phases or presence of gangue material (discussed in the next section).

As indicated, not all of the material is accounted for, especially in the larger size fractions. The sum of all the element percentages should add up to 100% if all these individual elements could be analysed to a very low concentration range. The observation may be due to the presence of more gangue material (e.g. SiO_2) in the larger particle size fractions. Carbon, nitrogen, hydrogen, oxygen and halogens cannot be quantified by ICP-OES analysis. A significant portion of the difference is expected to be ascribed to the presence of oxygen (associated with quartz and calcite mineral). However, this is only an assumption and will be validated in the next section, by inspection of the mineral phases present in each size fraction.

6.4.4 Mineralogical analysis results

In order to assess the distribution of the elements, detected during the chemical analysis, the following mineralogical analyses were performed. X-ray powder diffraction (XRD) was used as a first qualitative approximation to identify the most prominent mineral phases present in each feed size fraction. The detailed XRD results are shown in Table 6.8, below.

Table 6.8: X-ray power diffraction (XRD) analysis of feed size fractions (Steyl, 1996)

Size Fraction (µm)	Major (20-100 mass%)	Minor (5-20 mass%)	Trace (< 5 mass%)
< 20	Sphalerite	-	Pyrite Chalcopyrite Pyrrhotite Fe-oxide (magnetite) Quartz
+20-38	Sphalerite	-	Pyrite Chalcopyrite Pyrrhotite Fe-oxide (magnetite) Quartz
+38-45	Sphalerite	-	Pyrite Chalcopyrite Pyrrhotite Fe-oxide (magnetite) Quartz
+45-53	Sphalerite	-	Pyrite Chalcopyrite Pyrrhotite Fe-oxide (magnetite) Quartz
+53-75	Sphalerite	Pyrite	Chalcopyrite Pyrrhotite Fe-oxide (magnetite) Quartz
+75-90	Sphalerite	Pyrite	Chalcopyrite Pyrrhotite Fe-oxide (magnetite) Quartz
+90-106	Sphalerite	Pyrite Chalcopyrite	Pyrrhotite Fe-oxide (magnetite) Quartz
+106-150	Sphalerite	Pyrite Chalcopyrite	Pyrrhotite Fe-oxide (magnetite) Quartz

Sphalerite (ZnS), pyrite (FeS_2), chalcopyrite ($CuFeS_2$), pyrrhotite ($Fe_{1-x}S$), magnetite (Fe_3O_4) and quartz (SiO_2)

Sphalerite, (Zn,Fe)S, constitutes the major phase in all the size fractions as expected. Pyrite, FeS_2, was found only in trace amounts in the smaller size fractions, and from fraction Sf4 (+53-70 µm) and larger to be present as a minor phase. Chalcopyrite, $CuFeS_2$, only constitutes as a minor phase in the two largest fractions, *i.e.* Sf6 (+90-106 µm) and Sf7(+106-150 µm). The remaining impurity phases, found in trace amounts, consisted of pyrrhotite, $Fe_{1-x}S$, an iron-oxide, which is assumed to be magnetite, Fe_3O_4, and quartz, SiO_2.

A significant increase in impurity phases is observed (Table 6.8) as the particle size increased, which supports the element distribution result from the chemical analysis (section 6.4.3) of increasing iron and copper impurities as the size fraction increased. The hardness, based on Mohs' relative hardness scale, of the prominent mineral phases in ascending order is: *sphalerite, 3.5-4 ≤ chalcopyrite, 3.5-4 ≤ pyrite, 6-6.5* (Barthelmy, 1997; Friedman, 1996; The Hudson Institute of Mineralogy, 1993). It is therefore possible that milling has concentrated the sphalerite in the finer fractions with respect to pyrite, due to its lower hardness. Mineral hardness, however, does not explain the chalcopyrite (copper) distribution between the size fractions. Increasing copper content with increasing particle size may be the result of copper being an impurity within the sphalerite and pyrite mineral phases. Optical microscope work is, further, required to assist in evaluating the liberation of the feed size fractions.

Backscattered-electron images of two polisections of the largest and smallest particle size fractions were produced on the scanning-electron microscope (SEM). These images are present in Figure 6.7 and Figure 6.8 for the size fraction Sf1 (+20-38 µm) and Sf6 (+90-106 µm), respectively, on the following page.

The SEM images confirm the increased presence of impurity phases in the large size fraction. There are also other phases present in the coarser sample that was not detected by the XRD analysis, mainly because of their low levels. Phases like calcite, dolomite, mica (K, Fe, Mg, Al, Si), and an unknown clay material (Mg, Fe, Al, Si) were identified.

Increased contact and/or entanglement of pyrite and chalcopyrite phases with the sphalerite phase in the coarser fraction is observed in the images, as opposed to the free sulphide particles in the finer size fractions. It can therefore be concluded that the milling of the head (feed) concentrate had successfully liberated the minerals, with the degree of liberation in the smaller size fraction being much better. The electrochemical contact between sulphide phases (*i.e.* sphalerite and pyrite or chalcopyrite) may result in galvanic interactions which will alter the leaching kinetics compared to pure (liberated) sphalerite.

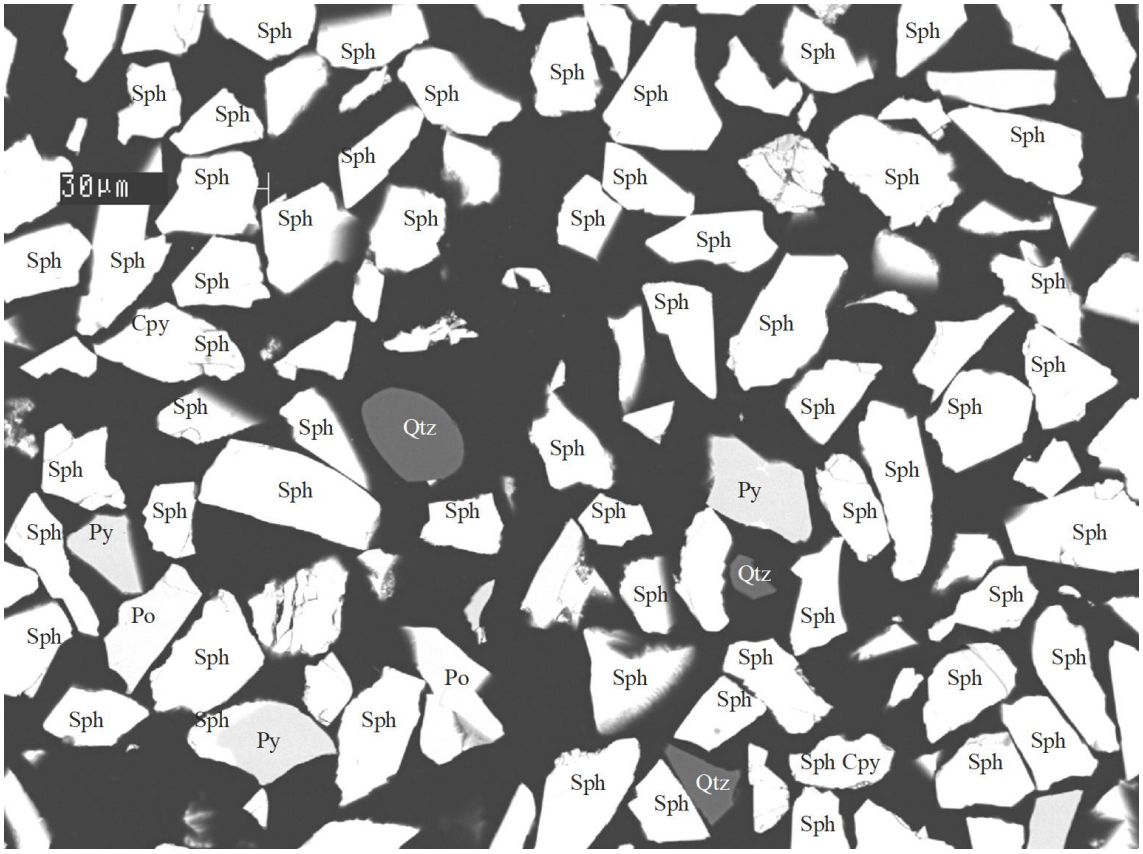

Figure 6.7: SEM photomicrograph of size fraction Sf1 (+20-38 µm) head (feed) concentrate, Steyl

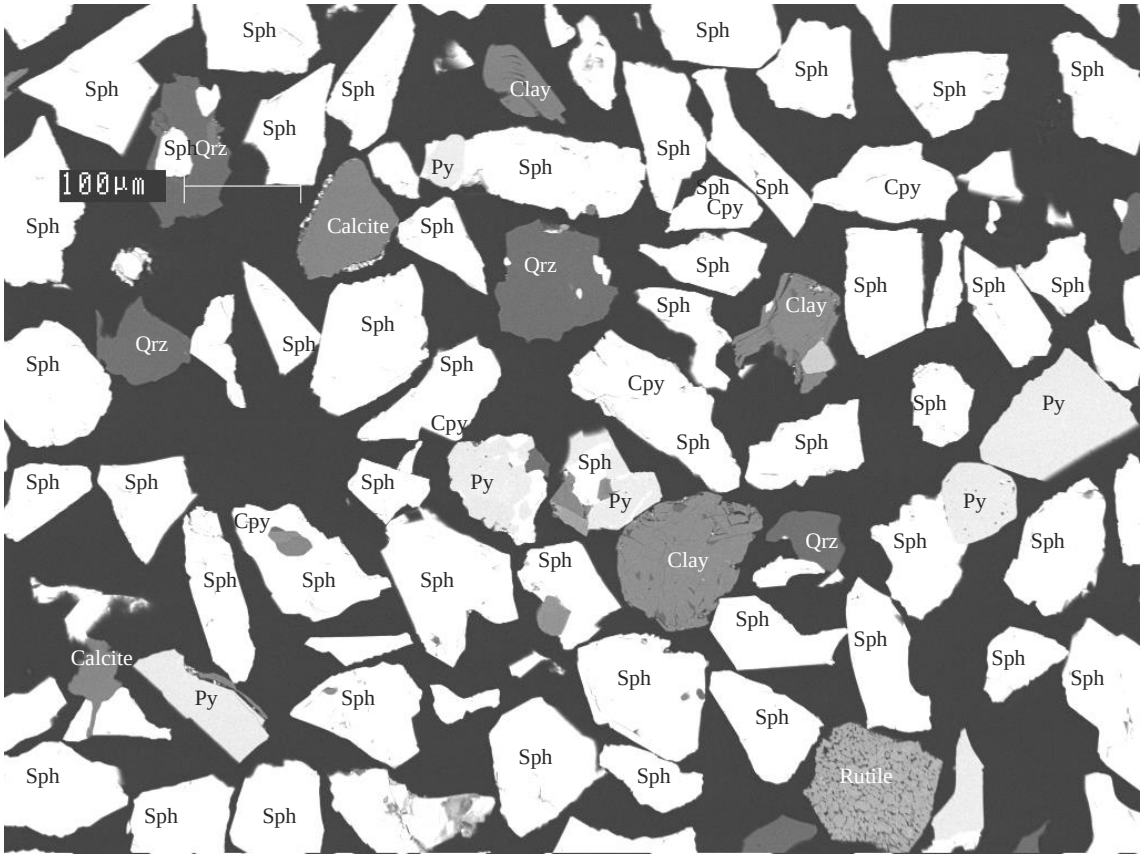

Figure 6.8: SEM photomicrograph of size fraction Sf6 (+90-106 µm) head (feed) concentrate, Steyl

Symbols: Sph: Sphalerite; Py: Pyrite; Cpy: Chalcopyrite; Po: pyrrhotite; Qtz: quartz

The mineralogical (bulk modal) composition was quantified with a scanning electron microscope (SEM) based image analyser. A breakdown of the concentrate in base metal sulphides (BMS), *i.e.* sulphide minerals, and gangue material (other phases) is presented in Table 6.9.

Table 6.9: Scanning electron microscope (SEM) based image analysis results of the mineral phases present in the head concentrates (Steyl, 1996)

Mineral		Sf1	Sf2	Sf3	Sf4	Sf5	Sf6	Sf7
	< 20	+20-38	+38-45	+45-53	+53-75	+75-90	+90-106	+106-150
BM	97.21	97.91	97.78	96.41	96.35	94.93	93.53	91.50
Gangue	2.79	2.09	2.22	3.59	3.65	5.07	6.47	8.50
[a]Sphalerite	95.24	95.70	93.58	93.35	90.91	90.47	88.18	87.43
[a]Pyrite	0.97	1.02	1.58	2.34	4.02	3.57	4.16	4.83
[a]Chalcopyrite	0.83	0.73	1.36	1.09	2.81	3.47	6.05	6.35
[a]Pyrrhotite	2.07	1.99	2.90	2.98	1.91	1.89	1.11	0.91
[a]Magnetite	0.43	0.32	0.10	0.12	0.01	0.30	0.10	0.26
[a]Other	0.46	0.24	0.48	0.12	0.34	0.30	0.40	0.22

[a]*Percentage of the total BMS phase*

The mineralogical breakdown confirms the increase in gangue content as the particle size increases. The majority of the BMS consists of a sphalerite phase, while pyrite and chalcopyrite content increases with particle size (which is in agreement with XRD and BSE image results). The pyrrhotite phase varied more or less proportionally to the sphalerite phase, *i.e.* a general decrease as the particle size increases. Very little to no zinc oxide was detected. The gangue material that is present in the head concentrate, consisted of unidentified metal sulphates, metal oxides (MeO) and/or clay material (Mg, Fe, Al, Si). It is assumed the gangue material is inert during the experimental batch tests.

The next step in the bulk modal analysis is to convert the volume percentages from the SEM results to mass percentages. In order to convert the volume percentages, the density of each phase is required. The gangue material was not quantitatively measured, but is assumed to consist of mainly quartz, SiO_2 (see SEM image Figure 6.8, XRD results and silicon abundance from the chemical analysis result). Within the larger particle size fractions dolomite (≈ 2.84 g/cm^3), calcite (≈ 2.71 g/cm^3), mica (≈ 2.8 g/cm^3) and clay were present as gangue material, but have similar densities to that of quartz (≈ 2.66 g/cm^3). It is therefore assumed that the density of quartz represents the gangue phase as a whole. The density of the base metal sulphide was

calculated from its constituting mineral phases. The other sulphide phases, which are undefined, were assumed to have the same density as the whole BMS phase. Mineral densities obtained from the literature are summarised in Table 6.10 and the calculated and measured concentrate densities are compared in Table 6.11.

Table 6.10: Densities of mineral phases (Barthelmy, 1997; Friedman, 1996; The Hudson Institute of Mineralogy, 1993)

Mineral Phase	Density (g/cm^3)
Sphalerite	4.00
Pyrite	5.02
Chalcopyrite	4.20
Pyrrhotite	4.62
Magnetite	5.18
Quartz	2.66

Table 6.11: Measured and calculated particle densities of the head concentrates (Steyl, 1996)

Size fraction (µm)	Particle ρ Measured (g/cm^3)	Particle ρ Calculated (g/cm^3)	BMS ρ Calculated (g/cm^3)
< 20	4.01	3.99	4.05
Sf1 (+20-38)	4.02	4.00	4.04
Sf2 (+38-45)	4.02	4.01	4.06
Sf3 (+45-53)	4.01	4.02	4.07
Sf4 (+53-75)	4.01	3.99	4.06
Sf5 (+75-90)	4.01	3.98	4.06
Sf6 (+90-106)	3.99	3.95	4.07
Sf7 (+106-150)	3.98	3.91	4.07

The measured and calculated densities are shown to be very close. There is a slight decrease of the particle density with increasing size, because of the increased less dense gangue phase present in the larger size fractions. The base metal sulphide phase has shown an increase in density with increasing size fraction due to the higher content of pyrite in the large size fractions. The densities in Table 6.10 and Table 6.11 were used to calculate the mass percentage of every phase in each size fraction, which is shown in Table 6.12.

Table 6.12: Detailed mineralogical abundance (bulk modal) analyses of head concentrate samples used in the experimental campaign (in mass percentage), Steyl (1996)

Size fraction micron	Sphalerite (%)	Pyrite (%)	Chalcopyrite (%)	Pyrrhotite (%)	Magnetite (%)	Other (%)	Gangue (%)
< 20	92.78	1.19	0.85	2.33	0.54	0.45	1.86
Sf1 (+20-38)	93.71	1.25	0.75	2.25	0.41	0.24	1.39
Sf2 (+38-45)	91.33	1.94	1.39	3.27	0.13	0.47	1.47
Sf3 (+45-53)	90.08	2.83	1.10	3.32	0.15	0.12	2.40
Sf4 (+53-75)	87.42	4.85	2.84	2.12	0.01	0.34	2.42
Sf5 (+75-90)	86.14	4.27	3.47	2.08	0.37	0.29	3.38
Sf6 (+90-106)	83.05	4.92	5.98	1.21	0.12	0.39	4.33
Sf7 (+106-150)	80.99	5.62	6.18	0.97	0.31	0.21	5.72

The total sulphide material content was around 94 to 98 weight percent for the above samples. The narrow sized fractions (Sf1 to Sf7) were thus upgraded (in terms of sulphide mineral content) by successive washing and ultrasonic 'cleaning'. Mineral mass distribution trends obtained in Table 6.12 are similar to those previously discussed.

Optical microscopy of sphalerite frequently showed internal reflections, which indicated the presence of some iron in the sphalerite structure. The stoichiometric composition of the sphalerite, pyrite, chalcopyrite and pyrrhotite phases was determined in detail by an electron microprobe analysis. Table 6.13 gives the average mass percentages (raw data) of the phases. The phase composition (except for pyrrhotite) did not vary to any significant extent ($AARD_{sphalerite} = 6.1\ \%, AARD_{pyrite} = 4.8\ \%$) between different particle size fractions.

Table 6.13: Average composition over 15 detections per phase of sphalerite, pyrite and pyrrhotite

Phase	Zn (%)	Fe (%)	Cu (%)	S^T (%)	Sum (%)
Sphalerite	58.87	6.53	0.09	34.00	99.49
Pyrite	0.90	45.65	0.00	53.45	100.00
Pyrrhotite	1.10	59.74	0.09	38.76	99.69

S^T – total sulphide

The raw data, in mass percentages, is not ideal for the comparison to ideal stoichiometries and must be converted to mole fractions. The molecular weight of each element is required for the conversion, however, the total mass of sphalerite and pyrrhotite does not add up to 100%. The

residual amounts were found to consist of varying amounts of Ni, Co and Mn. The symbol Im was used to combine the effect of these impurities. Furthermore, the mole fraction of every constituent was calculated and then normalised to a total metal mole fraction of one.

Table 6.14: Stoichiometric composition of the sphalerite, pyrite and pyrrhotite phase (Steyl, 1996)

Mineral phase	Zn (mol)	Fe (mol)	Cu (mol)	[a]Im (mol)	Sum (mol)	S^{2-} (mol)	$M_{w,calc}$ (kg/mol)
Sphalerite	0.8765	0.1138	0.0014	0.0083	1	1.0324	97.345
Pyrite	0.0166	0.9834	-	-	1	2.0058	120.311
Pyrrhotite	0.0154	0.9786	0.0013	0.0047	1	1.1060	91.482

[a]Im is the total base metal impurities, assumed to have an average M_w = 60 kg/mol (quartz)

Pyrite, FeS_2, compares to its ideal phase stoichiometric composition, while sphalerite, ZnS, and pyrrhotite, $Fe_{1-x}S$ varies quite significantly. Most importantly, the iron content within the sphalerite phase is about 11.38 mole%, which enforces the incorporation of the electrochemical mechanism as presented by Crundwell (1988c), see section 5.43 for description. Allthough not shown in Table 6.4, the chalcopyrite phase was consistently found to be very close to its ideal stoichiometry ($CuFeS_2$) and impurity levels were below the detection limit of the electron microprobe.

6.4.5 Mineralogical inspection of the unreacted core of partially leached particles

Polished sections of leaching residue samples were viewed under and optical microscope (backscattered-electron imaging) in reflected light. Mineralogical inspection of partially leached solids was important, because it indicated the topochemical kinetics of sphalerite dissolution, and it gave an indication of the relative reactivity of the different mineral phases as well as the general form of partially leached particles. However, polished sections may give a false impression of the surface reactivity. Nevertheless, images from optical microscopy gave some indication of the reactivity, especially if the particle sizes are compared and the thickness of the product layer is taken into account. The sulphur product layer is clearly visible and distinct from the unreacted core. Optical microscopy also revealed that galvanic interactions may occur between different mineral phases, due the close proximities and sulphide product density.

The following micrographs clearly show the topochemcial characteristics of the shrinking sphalerite particles and the surrounding porous product layer of elemental sulphur.

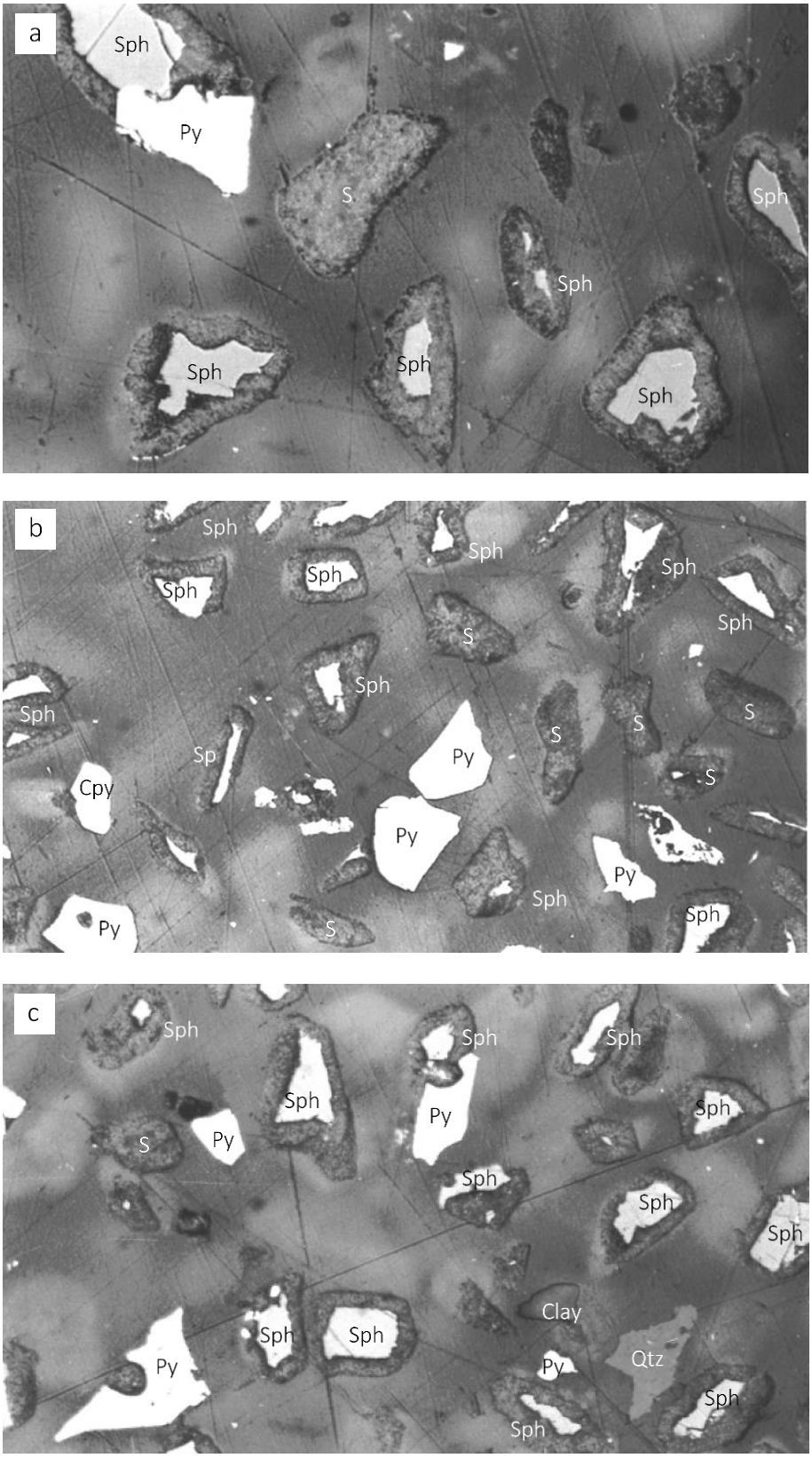

Figure 6.9: Partially leached (180 minutes) size fraction Sf3 (+45-53 µm) in 0.414 M H_2SO_4, 0.126 M $Fe_2(SO_4)_3$, 0.11 M $FeSO_4$ and 0.01 g/l lignosulphonate at 80 °C (experiment Db3). Symbols: Sph: Sphalerite, Py: Pyrite, Cpy: Chalcopyrite, Qtz: quartz, S: sulphur. SEM images taken by Steyl (1996)

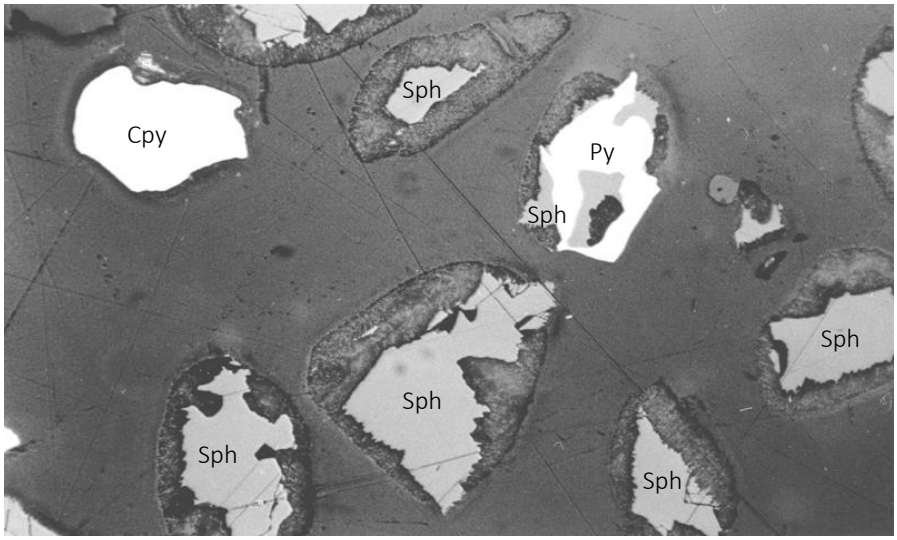

Figure 6.10: Partially leached (180 minutes) size fraction Sf7 (+106-150 µm) in 0.143 M $Fe_2(SO_4)_3$, 0.455M H_2SO_4 and 0.1 g/l lignosulphonate at 80 °C and 500 kPa O2 overpressure. Symbols: Sph: Sphalerite, Py: Pyrite, Cpy: Chalcopyrite. SEM image taken by Steyl (1996).

In the top right of Figure 6.10 and top left corner of Figure 6.9a is sphalerite phases that were in electrochemical contact with a pyrite phase. No major acceleration of the sphalerite dissolution rate seemed to occur due to galvanic interactions.

There were some particles that were completely leached, while most other particles only leached to a certain extent (Figures 6.9 and 6.10). This phenomenon was observed in many micrographs taken of the residues in this study. One of the most prominent features was the varying reactivity on different surfaces, even within a particle, and deviated from topochemical kinetics. Most of the sphalerite particles in the micrographs show rough edges between unreacted sphalerite and sulphur product layers and is most likely due to the formation of hillocks (see discussion of section 5.4.3.1). Crundwell (1988c) also observed the formation of hillocks in partially leached particles in ferric medium.

None (or very little) of the pyrite and chalcopyrite particles leached to any significant extend in the above micrographs, while sphalerite was very reactive. Very little or no pyrrhotite was found in most residues which suggests that its leaching rate was much faster than that of sphalerite. A residue image was also taken for a sample leached under severe leaching conditions, *i.e.* 95 °C, 0.24M $Fe_2(SO_4)_3$, 0.022 M $FeSO_4$ and 1.3 M H_2SO_4. From Figure 6.11 most of the sphalerite particles had leached completely, and that quartz and even the chalcopyrite particles appeared to be stable. There was some degree of leaching of the pyrite particles, although this phenomenon is not expected under the milder conditions encountered during the high-solids density batch tests (especially with regard to the acid concentration).

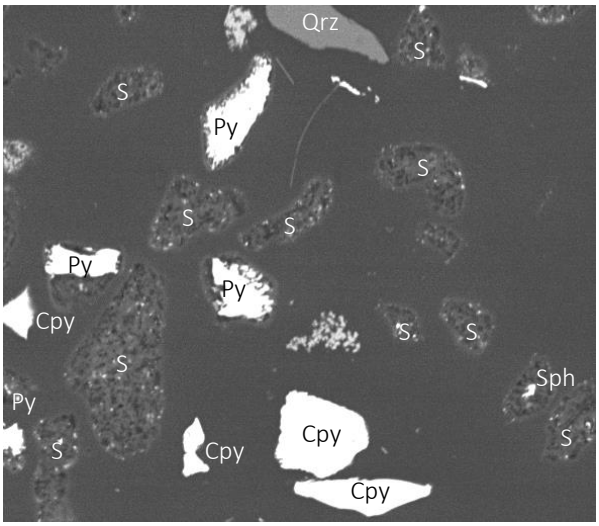

Figure 6.11: Nearly completely leached particles (90 minutes) of size fraction Sf3 (+45-53 µm) in 0.24 M $Fe_2(SO_4)_3$, 0.022 M $FeSO_4$, 1.3 M H_2SO_4 and 0.1 g/l lignosulphonate at 95 °C (test Fd3). Steyl (1996)

Pyrite and chalcopyrite are assumed to be inert during the batch experiments and sphalerite dissolution rate (zinc concentration change) is independent of the presence of these phases, while pyrrhotite is assumed to leach at the same rate as sphalerite. Xu et al. (2013) observed similar results under the atmospheric oxygen-rich direct leaching conditions.

In order to model the leaching process, it is assumed that the cleaved particle surfaces are approximately randomly distributed. It is assumed that the deviation from topochemical particle shrinkage (as illustrated in Figures 6.9 and 6.10) plays an insignificant role in the overall dissolution kinetics.

In conclusion to the mineralogical analysis of partially leached particles, Figure 6.12 below, illustrates the porous product layer of a partially leached particle. The micrograph shows the variation in sulphur porosity on a particle, most likely due to surfaces with hillocks, while dense sulphur forms on homogeneous-flat surfaces.

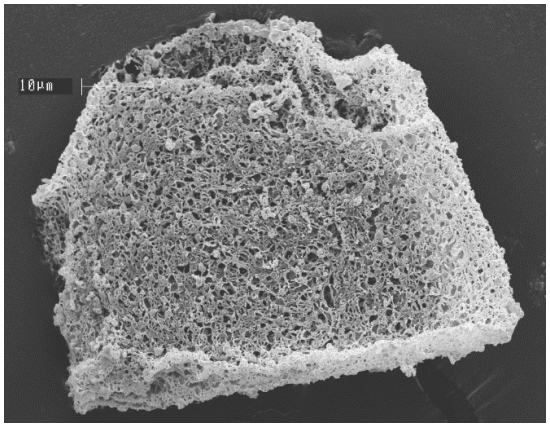

Figure 6.12: Completely leached particle (300 minutes) of size fraction (+45-53 µm) in 0.1 M $Fe_2(SO_4)_3$, 0.07M H_2SO_4 and 0.001 g/l lignosulphonate at 90 °C (test Ed1). (Steyl, 1996)

6.4.6 Conclusions

The main objective of the particle composition analysis was to quantify the distribution of different elements and phases between particle size fractions. The objective was addressed by first quantifying the distribution of elements by chemical analysis, then to determine the mineral phase distribution through a mineralogical analysis and finally to qualitatively determine the reactivity of the different mineral phases during leaching of the concentrate. The chemical analysis results are compared, in Table 6.15, to the mineralogical determined elemental composition (from Table 6.12 and Table 6.14) as reported earlier.

Table 6.15: Chemical and mineralogical analysis comparison (mass percentage), Steyl (1996)

Size fraction (µm)	Element	Chemical Analysis (%)	Mineralogical Analysis (%)	Mineralogical Leachable[a] (%)
Sf1 (+20-38)	Zn	57.0	55.20	55.19
	Fe	8.7	8.56	7.46
	Cu	0.2	0.35	0.09
	S^{2-}	33.9	33.67	32.73
Sf2 (+38-45)	Zn	56.1	53.82	53.80
	Fe	9.2	9.32	7.92
	Cu	0.4	0.57	0.09
	S^{2-}	33.8	33.84	32.32
Sf3 (+45-53)	Zn	54.9	53.09	53.07
	Fe	9.7	9.60	7.87
	Cu	0.5	0.47	0.08
	S^{2-}	33.7	33.82	31.92
Sf4 (+53-75)	Zn	53.5	51.53	51.49
	Fe	9.8	10.06	6.98
	Cu	1.0	1.06	0.08
	S^{2-}	33.8	34.13	30.55
Sf5 (+75-90)	Zn	52.9	50.77	50.74
	Fe	9.9	10.14	6.87
	Cu	1.4	1.28	0.08
	S^{2-}	33.6	33.59	30.09
Sf6 (+90-106)	Zn	50.5	48.95	48.91
	Fe	10.3	10.30	6.14
	Cu	2.1	2.15	0.08
	S^{2-}	33.4	33.43	28.71
Sf7 (+106-150)	Zn	49.1	47.74	47.69
	Fe	10.8	10.54	5.87
	Cu	2.5	2.21	0.07
	S^{2-}	33.0	33.07	27.91

[a]Only the sphalerite and pyrrhotite phases were assumed leachable (section 6.4.5)

The element distribution differed slightly between the chemical and mineralogical analysis, especially for the zinc distribution. A plausible explanation may be that the modal analysis was not completely accurate, because only a limited number of particles were considered with this method. As mentioned before, the chemical analysis was reproducible by 10 ICP-OES analyses and assumed to be correct.

The results of these analyses are now combined to calculate the leachable amount of each element in each size fraction, under oxidative and non-oxidative conditions. The chemical analysis of Zn, Fe, Cu and S^{2-} were therefore used, but taken proportional to the mineralogically determined leachable amount given in Table 6.15 (see equation 6.7 for calculation). These calculated values are given in Table 6.16.

$$\%\ Leachable|_{CA} = \frac{\%\ Leachable|_{MA}}{\%\ Element|_{MA}} \times \%\ Element|_{CA} \qquad 6.7$$

where CA denotes chemical analysis and MA denotes mineralogical analysis

Table 6.16: Final leachable amount of elements in the sphalerite concentrate used for this project

Size fraction (μm)	Zn (%)	Fe (%)	Cu (%)	S^{2-} (%)
Sf1 (+20-38)	57.0	7.6	0.05	33.0
Sf2 (+38-45)	56.1	7.8	0.06	32.3
Sf3 (+45-53)	54.9	7.9	0.09	31.8
Sf4 (+53-75)	53.5	6.8	0.08	30.3
Sf5 (+75-90)	52.9	6.7	0.09	30.1
Sf6 (+90-106)	50.5	6.1	0.07	28.7
Sf7 (+106-150)	49.0	6.0	0.08	27.9

As mentioned before, the impurities that represent base metals or oxide form (Mn, Ni and Co sulphides or oxides) were present in very small quantities in the concentrate. An average molecular weight of 60 kg/mol (*i.e.* quartz) was assumed for these metals, because their relative amounts were unknown. Furthermore, the pyrite and chalcopyrite phases were assumed to be stable (inert) and the sphalerite and pyrrhotite phases were considered to leach at the same rate.

Chapter 7 Sphalerite Reaction Modelling

7.1 Objective

The essential understandings of some of the processes proposed to treat sphalerite concentrates under various conditions are summarised in chapter 1, while focussing on the atmospheric direct leaching route. Detailed aspects of the atmospheric direct leaching process are described by patent publication ("Albion Process | Glencore Technology", 2016; and "Atmospheric Direct Leaching | Outotec", 2016). The key aspects of direct leaching include fine grinding of the concentrate (80 % passing 20 µm), temperature of the reactor vessel (typically between 90-100 °C) and the sulphate medium background concentrations of acid, ferric and ferrous as well as zinc. Therefore, the atmospheric direct leaching process relies on a combination of these parameters to increase the rate of sphalerite oxidation, and thus this chapter should be regarded within this context.

The literature review (Chapter 2) outlined basic methods to develop kinetic rate expressions from experimental batch data. Chapter 3 presented a summary of the methodologies for the characterisation of the kinetic expressions, including the experimental procedures and a thermodynamic framework for the $ZnSO_4$-$Fe_2(SO_4)_3$-$FeSO_4$-H_2SO_4-H_2O system. A detailed review of the phenomenological nature of sphalerite was presented in Chapter 4 and simplified mechanistic views with the corresponding intrinsic oxidation rate expressions were derived. Chapter 5 characterised the sphalerite concentrated regarding the particle distribution and composition. The true value of these investigations can now be obtained by combining them in a consistent reaction model of the system, such that the rate for sphalerite leach can be predicted.

The overall objective of this research is to establish rate equations for the leaching of the sphalerite concentrate. This chapter focuses on resolving this objective and quantifying the rate expressions on a phenomenological level, based on the batch experimental results and insights from the previous chapters. In order to quantify sphalerites kinetic expressions, the relevant reaction regimes should be identified with sphalerites response to bulk property changes on a phenomenological level, and by validating the mechanisms and proposed mechanism.

7.2 Reaction model equations

7.2.1 Rate limiting models

The complexation reactions of the solution species are an order of magnitude faster than the proposed mechanism rate limiting reaction detailed in section 5.5, even in the reactive system at lower temperatures, < 95 °C (Biley, 2015). Assuming conventional limits for the activation energies, these faster complexation rates facilitate a simplification of the kinetic model equations, since the observed rate will only be a function of the proposed rate limiting step. Hence, a pseudo-equilibrium is reached instantaneously and may be combined with the batch reactor model through a rate-limiting approach.

The first electron or proton transfer step was also assumed to be the rate-limiting step of the non-oxidative (reaction 5.47) and oxidative (reaction 5.46) mechanism, while the subsequent transformation or protonation reactions are expected to be comparatively fast. This assumption was made from the basis of the electrochemical nature of hole formations in the lattice and ion mitigation over the Helmholtz-layer. However, the assumed rate limiting reactions are indeed still ambiguous and therefore needs to be validated by examining the ability of the derived rate expressions to predict the experimental data which will show the accuracy of this assumption.

In order to regress the electrochemical rate parameters, it is important to mathematically relate the dynamic behaviour of the batch experiments into a viable solution. The shrinking core model (SCM) is a well-defined method to quantify a non-catalytic reaction of particles with surrounding fluid in a batch reactor experiment (section 2.4.2). The fundamental batch reactor model of the leaching kinetics, under approximately constant reaction conditions, is as follows:

$$1-(1-X)^{\frac{1}{3}}=k_s t \tag{7.1}$$

where X is the fraction of sphalerite leaching after time t and k_s is the overall observed leaching rate constant, which is shown to be (see appendix B.1 for derivation):

$$k_s=-\frac{v_i}{|v_{sph}|}\cdot\frac{M_{w_{sph}}}{\rho_{sph}}\cdot\frac{\Phi_a}{\Phi_v}\cdot\frac{(r_{sph})}{r_0} \tag{7.2}$$

This overall rate constants (k_s) is a function of the reaction stoichiometric coefficients (v_i), the overall reaction stoichiometric coefficient ($v_{sph}=1$), the sphalerite mineral density and molecular weight (ρ_{sph} & $M_{w_{sph}}$, respectively), the area and volume shape factors (Φ_a &Φ_v, respectively), the intrinsic reaction rate (r_{sph}) and initial particle size (r_0).

If the left-hand side ($1-(1-X)^{1/3}$, conversion term) of the SCM is plotted against time and a straight line is obtained, it can be assumed that the system operates under a surface reaction controlled regime. By using the shrinking core model, unknown oxidation effects are averaged over the total particle surface area thus simplifying the modelling approach. When the major parameters (*e.g.* temperature and concentration of the solution species), as discussed previously, are kept approximately constant the rate parameters (k_i) can easily be regressed from the observed linear rate constants. Leaching tests were therefore performed at low solids content (low pulp density). Also, implicit within the SCM approach to parameter optimisation is the requirement for the particles to be screened to a narrow size (mono-sized).

Instead of using the integrated form of the time differential (*i.e.* the SCM, equation 7.1), the batch model solution could be kept in its differential form. The derivation of the batch reactor model is presented in Appendix B, which entailed substitution of equation 2.38 and any of the proposed rates (*i.e.* equation 5.54, 5.63, 5.64, 5.70 or 5.71) and also assuming spherical particles. While the typical concentration-time differential (dC/dt) in the conventional approach to solve reactor models is appropriate, it is more convenient to relate it to the fractional conversion-time differential, in the instance of particle kinetics. This simplification eliminates the requirement of an additional particle size differential (dr_p/dt) to obtain the area and eliminating unnecessary constants, thus creating a better optimisable model. The following sphalerite dissolution model for a batch reactor is obtained:

$$\frac{dX}{dt} = \frac{3 \cdot M_{w_{sph}}}{(1000)\rho_{sph} \cdot r_0} \cdot (1-X)^{\frac{2}{3}} \cdot \left(r_{sph}\right) \tag{7.3}$$

With the constants having units of $M_{w_{sph}}$ in $\frac{g}{mol}$, ρ_{sph} in $\frac{kg}{m^3}$, r_0 in m and r_{sph} in $\frac{mol}{m^2 \cdot min}$. The fraction mineral leached (X) can be used to calculate the extent of reaction and subsequently the concentration of all the species can be determined by using suitable mass balances. Additionally, by taking the variation of initial particle size (r_0) into account the following differential were obtained:

$$\frac{dX}{dt} = \frac{3 \cdot M_{w_{sph}}}{(1000)\rho_{sph}} \cdot (1-X)^{\frac{2}{3}} \cdot \left(r_{sph}\right) \cdot \sum_{n=0}^{r_{0,max}} \frac{1}{r_{0,n}} \cdot W_{f,n} \tag{7.4}$$

where $W_{f,n} = W_f(r_{o,n})$ is the weight fraction of the original feed particle size in size class n. The differential equation is solved numerically using the functionalities in MATLAB and Simulink (R2016a). The methodology of parameter regression by experimental data follows.

7.2.2 Parameter optimisation methodology

To quantify the rate parameters a twofold strategy is followed (as explained in section 3.4). The first method is by using the *curve-fitting: linear regression* technique to estimate an initial value for each rate parameter at a fixed temperature. A constant solution composition is required for this regression technique during each batch test, however the zinc concentration will change as sphalerite dissolve. The leaching rate is dependent on the concentration of zinc and, hence, would result in non-optimal (errors) in the rate parameters. Yet, using this technique at the corresponding average solution composition (over the linear region) and mean particle size, would give a good first approximate of the value of each rate parameter that could be used to initiate parameter regression of the second *curve-fitting: non-linear regression* technique. Parameter optimisation would follow a non-linear regression (curve-fitting) approach. This is done by solving the extent-differential over time to fit the experimental data by minimizing the error. Each regression technique is explained below.

- **Curve-Fitting: Linear Regression**

Assuming a form of the rate expression and after appropriate mathematical manipulation and analytical integration of the conservation balance (appendix B.1), a linearized expression (equation 7.1) was obtained. This linearized SCM and overall observed leaching rate constant, k_s, can now be fitted to the observed reaction extent curves that were obtained from the experimental data. Hence, obtaining each batch experiment's k_s value. The experimental rate constants (k_l) acquired from the linearized plots are used in the error function below, to optimize the rate parameters.

$$\min E_f = \sum_i E_i = \sum_i \left| k_s^{calculated\ i} / k_s^{experiment\ i} - 1 \right| \qquad 7.5$$

The error function, E_f, is defined as the calculated k_s value from equation 7.2 divided by the measured overall rate constant for batch test i. The optimisation routines (*Matlab*, R2016a) minimise the root mean square difference, in its defined optimisation algorithm, by varying the intrinsic rate parameters (*i.e.* k_1, k_2 and k_3) of r_{sph}.

- **Curve-Fitting: Non-Linear Regression**

Once good initial estimates of the rate parameters are obtained from the linear regression technique, all tests were included in the objective function for the final non-linear optimisation. A dynamic simulation of the batch reactor was built in Simulink (R2016a). The ode45 (Dormand-Prince) solver was selected to obtain a numerical solution of the differential equation 7.3. The relative and absolution tolerances for the solver were selected to be 1×10^{-10}, well below a 1

ppm zinc concentration (<$1 \times 10^{-5} \frac{mol}{kg}$). Furthermore, the solver was allowed to take variable step sizes in time, but restricted to a maximum step size of 1 minute. These settings were selected to give the most accurate and optimal numerical solution algorithm.

After obtaining the fractional conversion results from the simulation, the sum-of-squared error (SSE) is calculated to measure the total deviation from the experimental results as follows:

$$SSE_i = \sum_{t=0}^{t_{max}} \left(X_t^{exp\ i} - X_t^{calc\ i}\right)^2 \tag{7.6}$$

where $X_t^{exp\ i}$ and $X_t^{calc\ i}$ is the conversion values at experimental sampling time t for batch test i of the experiment and simulation. The sum-of-squared error is denoted as SSE_i. This measure of total deviation is for a batch test and, hence, should be summed over all the experiments. The total sum-of-squared error (TSSE) was taken as the overall objective function for the non-linear regression algorithm, per equation 7.7 below:

$$\min TSSE = \sum_{i}^{N} SSE_i = \sum_{i}^{N} \sum_{t=0}^{t_{max}} \left(X_t^{exp\ i} - X_t^{calc\ i}\right)^2 \tag{7.7}$$

The TSSE was minimised by optimising the intrinsic rate parameters (*i.e.* k_1, k_2 and k_3) in a suitable optimisation algorithm. Both the *generic algorithm (ga)* and *fsolve* optimisation functions were used to solve the set of non-linear equations as explained in the methodology.

7.2.3 Reaction heat effects

As discussed in sections 2.1.1, 5.5.2 and 5.5.3 the rate constant is a function of temperature and is assumed to conform to the Arrhenius relationship. This assumption of Arrhenius behaviour is based on inner-sphere electron transfer and is in accordance with Marcus' theory of electron transfer (Marcus, 1964). However, the frequency factor (k_0, in equation 2.30) is typically found to be extremely large or small and generally does not have any significant meaning. It was therefore chosen to relate the rate constant to a reference rate constant (*i.e.* at a reference temperature) by taking the ratio of the Arrhenius relationship, and after rearrangement gives:

$$k_T = k_{T_{ref}} \exp\left(-\frac{E_a}{R}\left(\frac{1}{T} - \frac{1}{T_{ref}}\right)\right) \tag{7.8}$$

Since most of the experiments are conducted at 95 °C and is the normal operating temperature in practice, it was selected to be the reference temperature (*i.e.* 368.15 K).

7.3 Verification of experimental results

To instil confidence in the experimental results, a few aspects concerning the validity of the proposed regime and precision of the data are evaluated. Problems are also identified, specifically with regards to areas where there is a lack of information to make decisive conclusions.

Three experiments were repeated to validate the precision of the obtained results. These include experiments from series C, D and F (see Appendix C, D, and F for details on experimental conditions). The initial and repeated tests were conducted at separate times, which validates their independence.

Figure 7.1 compares the repeated experiments and graphically illustrates the calculated error. The student's t statistical procedure was applied to estimate the uncertainty of the measured conversion error (see Appendix G.2 for error calculations).

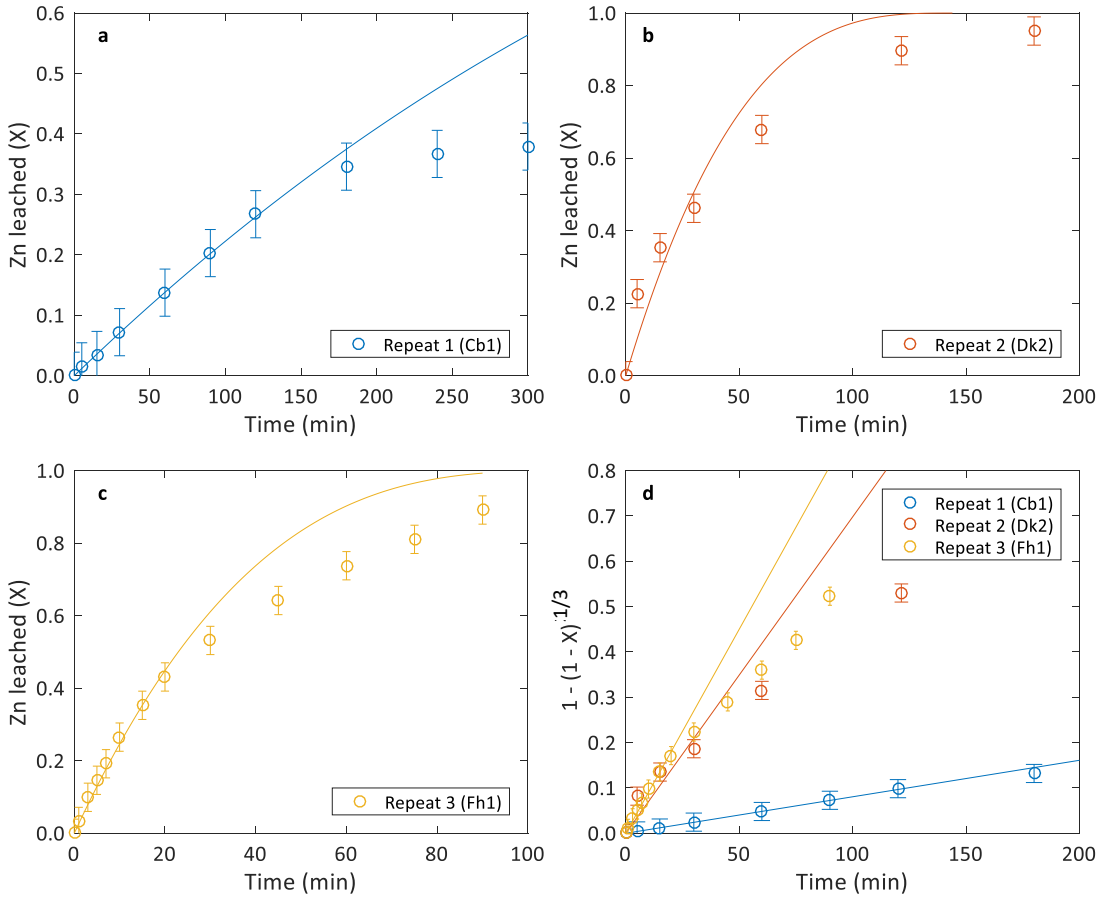

Figure 7.1: Repeated experiment results, showing initial experiments (a) Cb1, (b) Dk2 and (c) Fh1 with error bars indicating the calculated error and (d) the shrinking core model plot under reaction controlled regime (line represents best fit as determined in appendix C, D and F)

The error bar limits are defined as the average error plus uncertainty in the error (as summarised in Table 7.1, also see Appendix G.2 for calculations). Error propagation to the shrinking core model was also determined and shown in Table 7.1d. An increase in spread (or region of uncertainty) is expected at higher leaching extents, this is due to the cubic nature of the SCM (equation 7.1). The statistical analysis results of the error are summaries in Table 7.1, below.

Table 7.1: Residual analysis results of the repeated experiments

Repeat	Average (%)	Standard Deviation (%)	MAE (%)	AARD (%)	X Error (%)	SCM Error
1	0.07	2.08	1.60	9.97	1.55	0.0052
2	4.39	1.27	3.29	11.72	7.31	0.0249
3	1.44	2.29	1.93	9.74	2.83	0.0095
Average	1.97	1.88	2.27	10.48	**3.90**	**0.0132**

MAE – mean absolue error, SCM Error – shrinking core model data points error

A high error of 7.3 percent extraction of zinc from sphalerite was obtained for the second repeated experiments (of series D), while in comparison the first and third repeated experiments produced much lower errors of 1.55 % and 2.83 %, respectively. The data are consistent enough to safely assume a 5 % accuracy during all the experimental tests within this research. However, this uncertainty represents a biased estimate of the accuracy since sample dilution, titration, analysis methods and equipment calibration etc. could have introduced measurement errors. Unfortunately, such errors could not be quantified due to the lack of information. Therefore, the uncertainty should be viewed as a qualitative and not a quantitative measure.

The qualitative nature of the uncertainty is reflected in determining whether or not sphalerite dissolution is under a surface reaction controlled mechanism. A larger uncertainty is expected for the shrinking core model at higher conversions, due to the cubic nature of the conversion formula (equation 7.1). This could result in a significant loss in accurcy during regression of the overall rate constant.

During the SCM analysis it is assumed that when the data points deviate from a linear trend, the kinetics is no longer controlled by a surface reaction controling mechanism. Deviation from linear behaviour could indicate that other rate controlling mechanisms are limiting or the solution properties (i.e. concentration, temperature etc.) are not kept constant. A clear deviation from linearity is oberved at higher reaction extents (> 0.3), which reflects the tendency of kinetics to deviate from the shrinking core reaction model either by solution property changes or the formation of a sulphur product layer. If the SCM line resides within the uncertainty region,

the rate is assumed to be surface controlling. Howerver, once the linear line extends beyond the error boundaries a significant enough change is observed to conclude that the reaction regime changed from surface reaction rate controlling to diffusion limiting.

The linear trend hypothesis in combination with the error region were used to regress the initial kinetic rate constants (k_s) of each batch experiment, so that the linear kinetics reside within all of the initial data point error bounds up-to the last data point where deviation behond this boundary was obtained. The regression results are presented in appendix C, D, E and F.

Next the initial rate (< 10 min) is discussed to analyse weather or not the start-up effects have any significant influence on the kinect behaviour of sphalerite leaching. Figures 7.2 and 7.3 illustrate these start-up effects over the initial period of leaching under non-oxidative and oxidative conditions, respectively. Start-up effects of the non-oxidative leaching are first analysed, followed by the oxidative leaching.

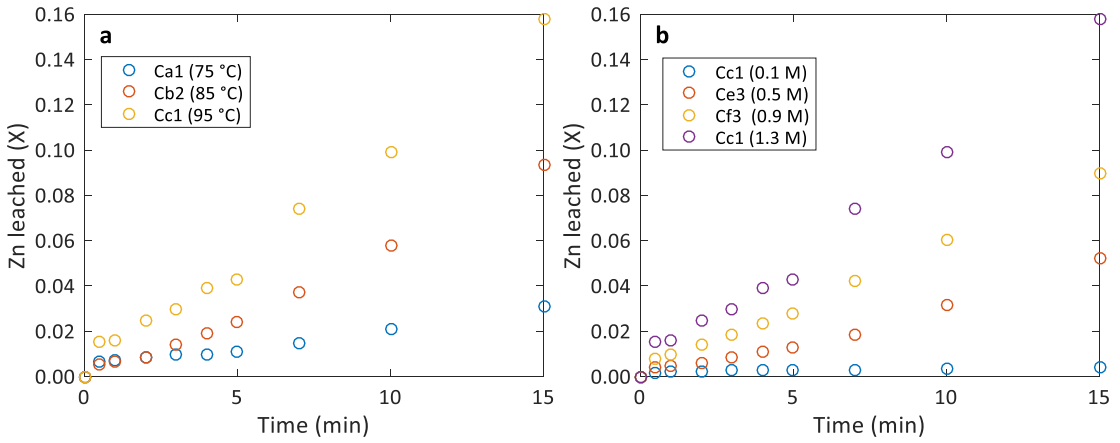

Figure 7.2: Initial non-oxidative leaching kinetics (Series C) at 0.03 g/L Sf3 concentrate: a) various temperatures and b) initial acid molar concentrations

A clear initial (< 1 min) "jump" in zinc extraction is observed, followed by a slow propagation into the linear shrinking core kinetic phenomena. The apparent rapid initial dissolution rate may be the result of either the faster leaching kinetics of ultrafine particles or unquantified reactive surface layers (*i.e.* high angularity of the particles, see section 6.3.3) or higher initial acid concentration (see Figure 7.2b).

Furthermore, the slow kinetics after the rapid leach shows the significant effect of the activation of the particle surface by acid (reaction activation). The slower initial kinetic region might be due to diffusion of acid to the particle surface (*i.e.* film diffusion), but this is unlikely since a proton (acid) has very high mobility in aqueous solutions (see also section 7.4.1 for details of the effect

of agitation). Reaction activation is highly dependent on the temperature as observed in Figure 7.2a (refer to appendix C.2 for more results).

Overall the start-up effects have a significant effect on the initial leaching rate of sphalerite under non-oxidative conditions. Initial extraction data points are therefore neglected and only the linear region was used during regression of the kinetic constants, to ensure a higher accuracy of capturing the phenomenological intrinsic rate of reaction.

Contrary to non-oxidative kinetics, the initial zinc extraction response under oxidative conditions is far less disturbed by start-up effects. Figure 7.3 presents the initial rate of sphalerite under various oxidative conditions, as well as comparing it to the non-oxidative rate.

Data used to develop the kinetic expressions are limited to start at a 5 % extraction for non-oxidative experiments, *i.e.*, approximately up to 10 minutes.

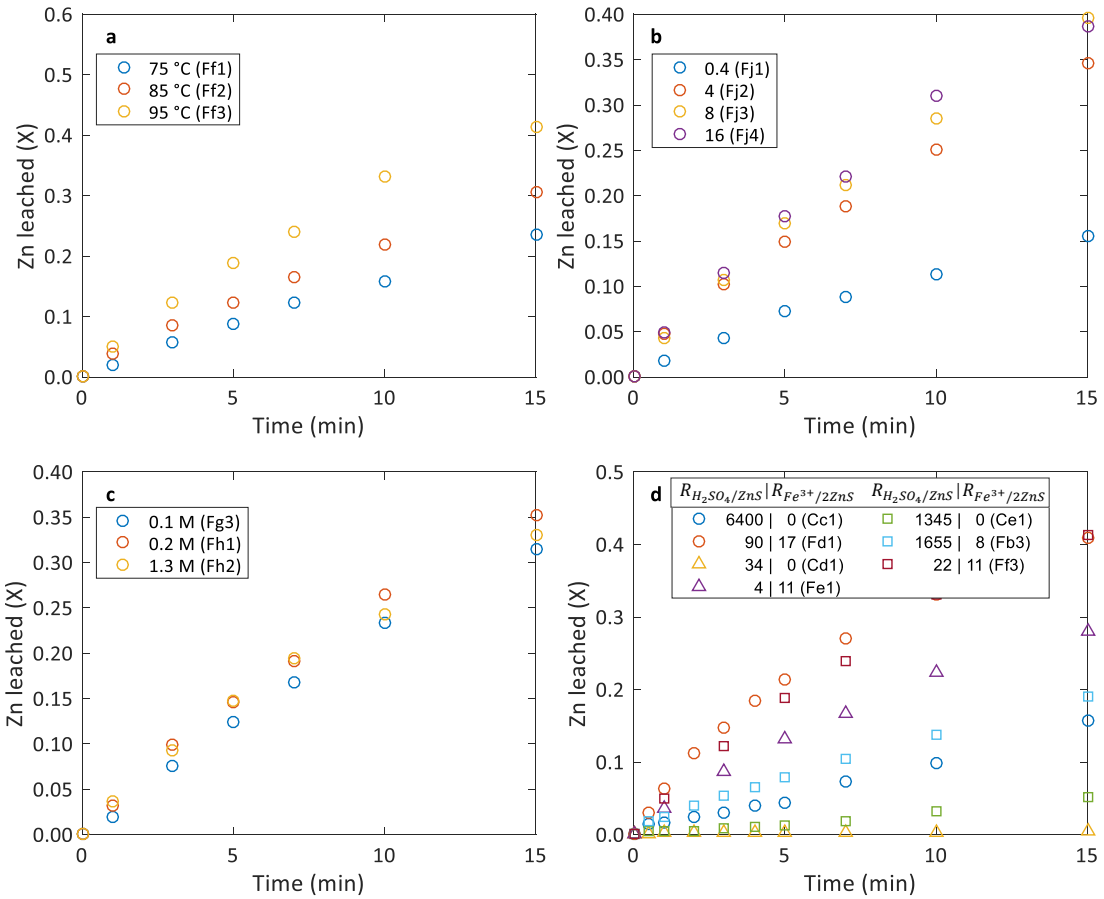

Figure 7.3: Initial oxidative leaching kinetics (Series F). Showing the effect of a) temperature, b) stoichiometric initial ferric to sphalerite ratios, c) acid concentration and d) various combinations of initial acid and ferric ratios, with ○: 1.3 M, Δ: 0.1 M and □: 0.5 M initial H_2SO_4

Neither a fast initial (< 1 min) jump in the rate nor a slow propagation (activation) into the linear kinetic reaction regime is observed for oxidative kinetics. Non-oxidative kinetics are relatively slow (Figure 7.3d), thus causing start-up variations to have a pronounced effect. The much faster oxidative kinetics encapsulate small deviations caused by the start-up procedure. This is evident from the reaction extent after 15 minutes of leaching, where oxidative experiments are much greater than 16 % extraction and non-oxidative experiments are all less than 16 % extraction.

A most interesting result of sphalerite dissolution is the considerable rate increase (Figure 7.3d) by the addition of a small amount of ferric to the solution. Even at a high acid concentration (1.3 M) the oxidative leaching rate is much faster, with the ratio of acid to sphalerite being much higher for the non-oxidative experiment.

Figure 7.3 also indicates that none of the solution properties (*i.e.* temperature, ferric or acid concentration) caused the start-up procedure to have any significant effect on the rate. Within the scope of this project the oxidative batch test start-up effects are assumed to be negligible.

Since it was practically difficult to obtain true rate data over the first few minutes, the linear regression is forced through the origin. Thus, averaging any start-up effects over the full regression. This also provides the ability to observe any sudden deviations from linear kinetics, because the reference point is always fixed at zero. Nevertheless, the start-up effects are within the 5 % uncertainty range assumed for the project.

Particle size influence on the rate is now addressed, to validate the mono-sized particle assumption. Higher leaching rates at smaller particle size fraction are expected, since smaller particle sizes have more area per gram concentrate. This point is illustrated in Figure 7.4, which represents the extent and SCM plots for the six narrow-size fractions.

Deviation of linearity for the finer size fractions (a high zinc extraction), shown in Figure 7.4, could be the result of highly irregular particle shapes. This is especially apparent at smaller particle sizes and would have greater effect on leaching rate as explained in section 6.4.5. Deviation from the expected dissolution rate may also have been result of the formation of hillocks and less reactive surfaces (refer to the discussion in section 5.4.3.1). The distribution of different particles sizes (PSD width), albeit narrow, may be another reason for deviation from linearity (section 6.33). The true nature of deviation of the smaller particle sizes could be a function of all the above-mentioned effects.

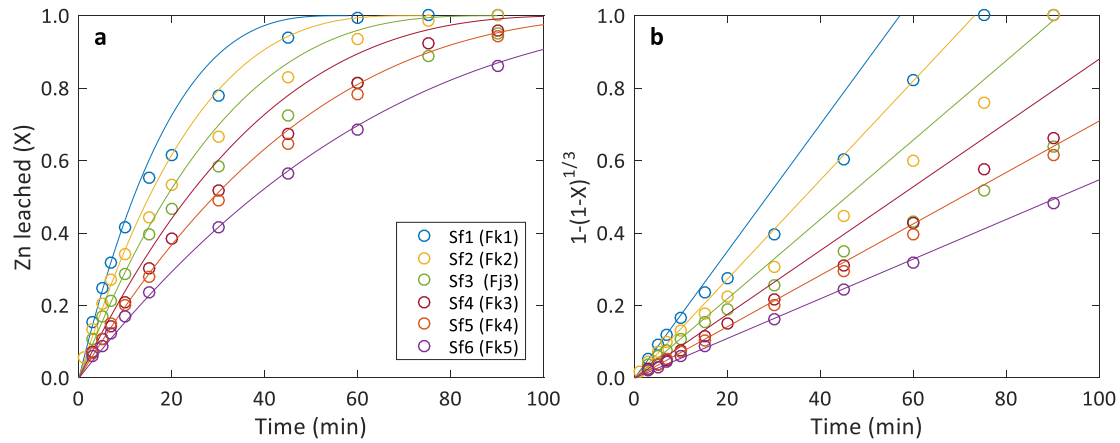

Figure 7.4: The influence of particle size on the extent of zinc dissolution, starting with 2.678 g/L concentrate, 49 g/L H_2SO_4, 0.35 M Fe^{3+}, 0 M Fe^{2+} and 0.01 g/L LS: a) Zn leaching extent and b) SCM plot for surface reaction control (line represents best fit; see appendix F for details).

Table 7.2 compares the calculated linear rate constants (k_l), while Figure 7.5 compares the initial overall observed leaching rate constant (k_s) against the inverse of the initial mean particle size.

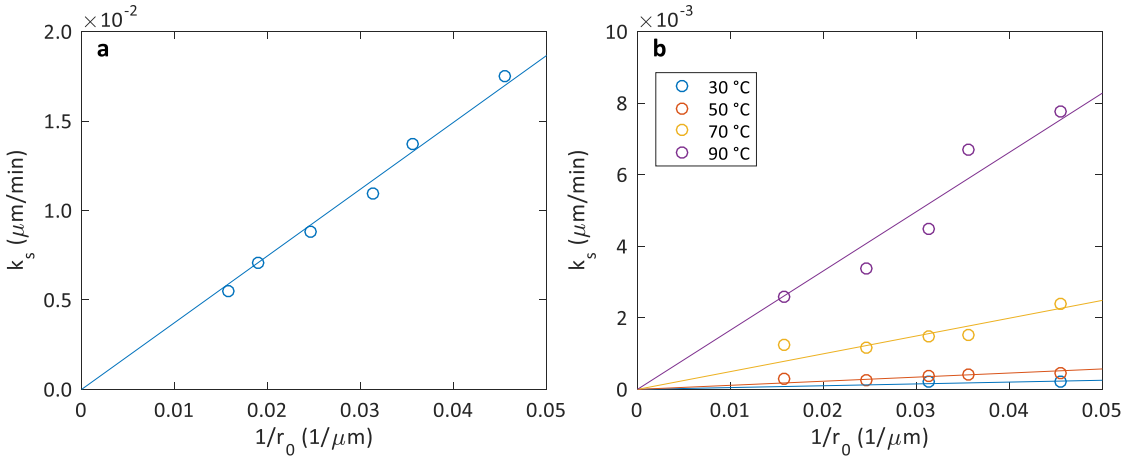

Figure 7.5: Initial overall rate constant vs. inverse of the mean particle size. a) Starting with 2.678 g/L concentrate, 0.5 M H_2SO_4, 0.35 M Fe^{3+}, 0 M Fe^{2+} and 0.01 g/L LS and; b) 0.1 g/L concentrate, 40 g/L H_2SO_4, 0.2 M Fe^{3+}, 0.1 M Fe^{2+} and 0.001 g/L LS.

Table 7.2: Experimental intrinsic linear rate constants (k_l) calculated from the mean particle size (r_0) and regressed overall rate constants from Figure 7.4b, by equation 2.43.

Size Fraction	Sf1	Sf2	Sf3	Sf4	Sf5	Sf6
k_l (µm/min)	0.385	0.384	0.351	0.359	0.374	0.387
Average k_l	0.373	Standard Deviation		0.015	Δu_{k_l}	0.016

The calculated intrinsic linear rate constants compare well to each other, with a small standard deviation and uncertainty. The linear relationship follows directly from equation 2.43, expressing the inverse relationship between k_s and r_0, which must be obeyed if linear shrinking with the surface reaction controlling the rate is true. Figure 7.5a was composed from the rate

constants obtained in Figure 7.4b and Figure 7.5b was produced from batch experiments Dp1 to Dt3 (appendix D). Each data point represents an overall rate constant of a batch test performed using a specific size fraction.

The fitted lines in Figure 7.5 were fixed through the origin to be consistent and no significant change from ideal behaviour was observed. All the batch tests conform to the inverse relationship. The shrinking core model under a surface reaction control mechanism is valid and could therefore be used to model the initial dissolution rate of sphalerite, that is under predominantly oxidative conditions

An interesting aspect concerning the fractional conversion-time differential (equation 7.4, see derivation in appendix B) was the summation term of the initial weight fraction divided by initial particle size ($i.e.\ \sum_{n=0}^{r_{0,max}} \frac{1}{r_{0,n}} \cdot W_{f,n}$) over the whole PSD. This term is also known as the harmonic mean (or the Sauter mean diameter, refer to section 6.3.2). Since the particle size distributions have the same shape in area and measure (*i.e.* equivalent mean diameters) as well as the fact that the distributions were very narrow to start off with, the mean diameter was an excellent approximation for the SCM analysis and is reflected by the linear relationship of the obtained initial rates shown in Figure 7.5.

Investigating the effect of higher oxygen concentration during sphalerite leaching is essential for the phenomenological understanding of sphalerite leaching and possible reaction mechanisms. Figure 7.6 presents the effect of oxygen partial pressure on the leaching extents with and without ferric present in solution.

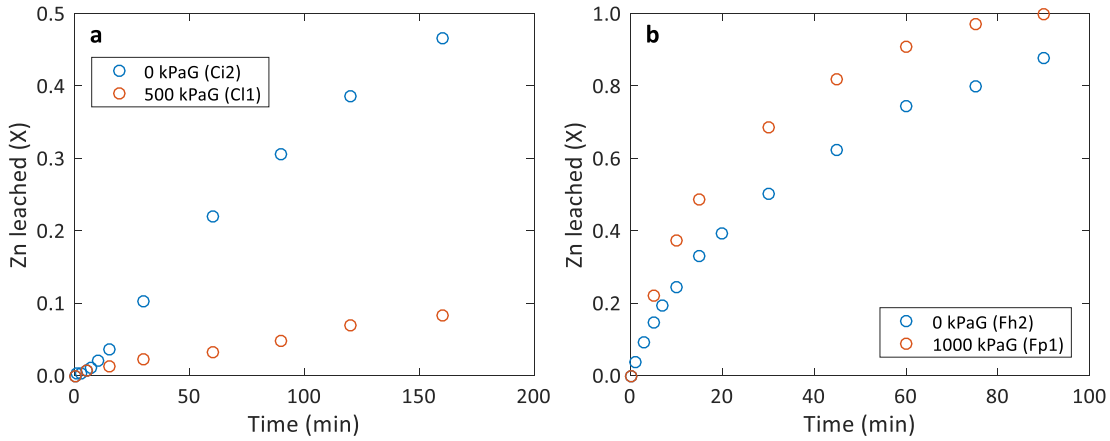

Figure 7.6: Effect of oxygen partial pressure in the a) absence of ferric (non-oxidative) and in the b) presence of ferric (oxidative) in solution.

A significant decrease in the rate of non-oxidative leaching was obtained by changing the process from atmospheric to pressurised oxygen leaching, while a significant increase in rate for

oxidative leaching was observed, as shown in Figure 7.6. The reason for a decrease in leaching rate under non-oxidative conditions may be due to the polarization of sphalerite surface to less reductive states by oxygen. Contrary, the increase in reaction rate under oxidative conditions may be the result of the regeneration of ferric (Fe^{3+}) from ferrous (Fe^{2+}) by the reduction of oxygen. The leaching rate and extent of dissolution of sphalerite is dependent on the oxygen content, however it is not investigated further since it is not the focus of this study.

The overall reaction stoichiometry of Fe^{3+} reduction on sphalerite was investigated to determine if reaction 7.9 is applicable. This can be partially confirmed from the data in Figure 7.7, which compares the experimentally determined zinc produced with the equivalent concentrations of ferric consumed and ferrous produced by the reaction, *i.e.*, $[M^{n+}]_t - [M^{n+}]_0$. All the oxidative experimental data (appendix D, E, and F) were used during the stoichiometric analysis.

$$ZnS + 2Fe^{2+}_{(aq)} \rightarrow Zn^{2+}_{(aq)} + 2Fe^{3+}_{(aq)} + S^{0}_{(s)} \qquad 7.9$$

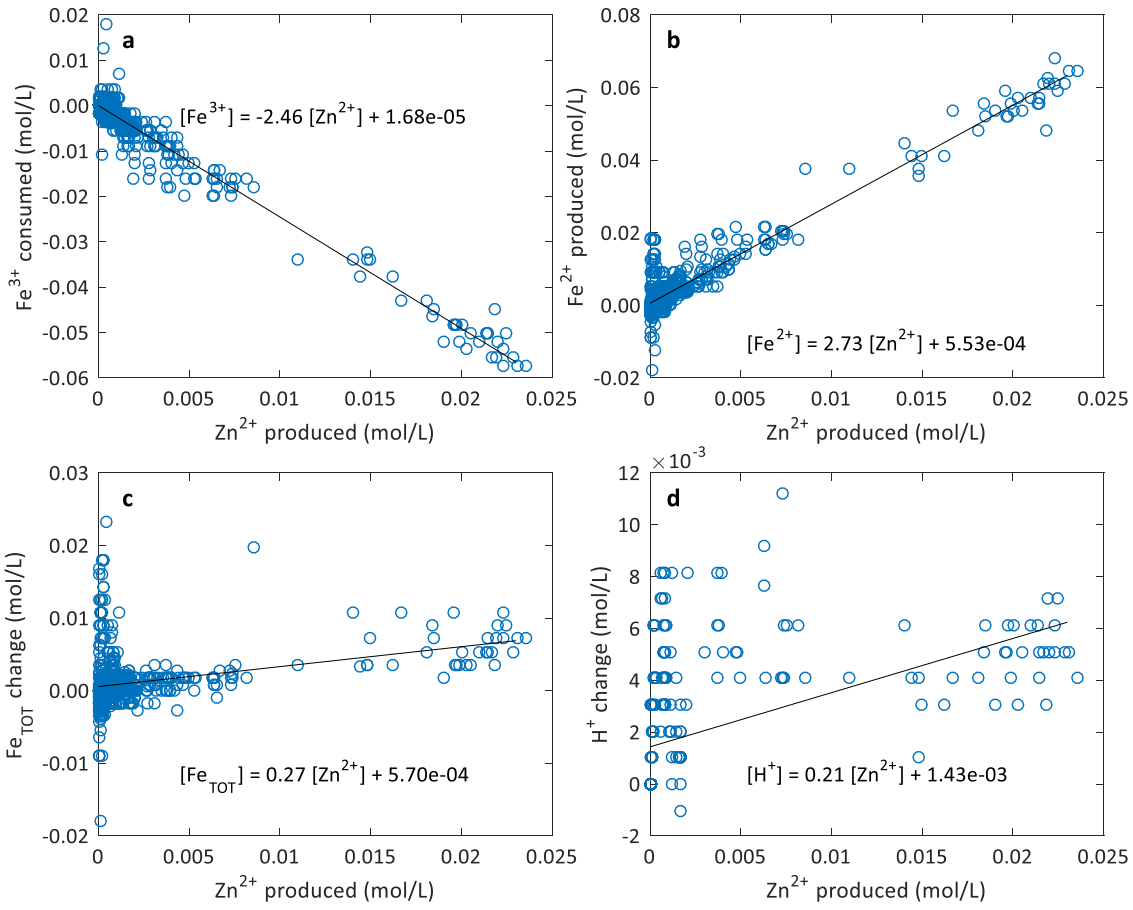

Figure 7.7: Relationship between zinc produced and a) ferric consumed, b) ferrous produced, c) total iron change and d) acid change in order to test the oxidative reaction stoichiometry. The fitted lines are linear robust fits of the data with equations shown on each graph.

For these batch tests performed with low pulp densities, in which bulk solution concentrations where considerably greater compared to the molar change of the species, the reaction

stoichiometry was calculated as -2.46 mole Fe^{3+} per mole Zn^{2+} and 2.73 mole Fe^{2+} per mole Zn^{2+}. A considerable spread at very low concentration changes are the result of measurement error, especially with the ferrous analysis. The higher ferrous production per mole of zinc is the result of iron dissolution in the concentrate and not the cause ferric reduction, which is confirmed by the total iron change in Figure 7.7c. Despite the large scatter, these data do suggest that reaction stoichiometry is representative of the overall reaction under the conditions of these tests.

Figure 7.7d also suggests that 0.2 mole H^+ per mole of Zn^{2+} is produced. A maximum H^+ change of 11.2×10^{-3} mole was observed, with the bulk H_2SO_4 concentration being between 0.1 and 1.3 mol/L (mostly 0.5 mol/L) which is 1 to 2 orders greater than the H^+ change. The H^+ change is also not consistent and the data have a large spread, as seen on Figure 7.7d. Therefore, the bulk acid concentration remained approximately constant during oxidative leaching, providing confidence in the reaction stoichiometry.

A deficiency with regards to these experimental results is that the solid phase product was not analysed. No conclusive deductions could be made on the sulphur product formation or phases. That is to say S^{2-} oxidation to elemental sulphur or polysulphides or sulphates. No conclusions of the collection of unreacted sulphur conglomerates could be made as well (*i.e.* the why sulphur disperse after some reaction time). Since the solid product composition is unknown, only the solution concentrations could be used to model the rate and deduct possible mechanistic paths.

No chemical detector was used to determine the presence of H_2S during the experiments. Only the odour was noted during experimentation in terms of a faint, moderate or strong H_2S smell. Thus, being dependent on the observer senses, to conclude the extent of H_2S production during test work.

7.4 Non-oxidative model evaluation

This section details the non-oxidative reaction regime and conceptualises the reaction mechanism. The reaction model of the non-oxidative leaching system is then quantified. Kinetic constants were calibrated using all available data and validated against an independent test set, presented in appendix C.

7.4.1 Reaction regime

This section elaborates on the different reaction regimes present during protonation of the sphalerite concentrate with respect to bulk property changes. The previous section highlighted the apparent deviation from shrinking core (linear) behaviour, near complete conversion, for

the monosized samples. Possible reasons included the formation of product layers on the particle surface, film diffusion could have become prominent as the particles shrink to smaller sizes or the distribution of initial particle sizes could have influenced the observed rate trends. Hence, this section addresses the relative importance of film diffusion, initial surfactant dosage and the retardation of the non-oxidative rate due to ferrous concentration.

Quantification of mass transfer limitations is essential in laboratory experiments to ensure that no physical limitations are present during reaction, so that the observed rate is a true representation of the chemical reaction rate. A set of experiments aims to determine whether a changing the mixing rate (impeller speed) would result in a change in the reaction rate. Changing the agitation rate would manifest in a rate change if film diffusion is prominent. However, an absence of agitation speed effects does not necessarily prove that no internal mass transfer limitations exist (Steyl, 2015).

In order to highlight mass transfer limitation, two batch experiments in a 0.5 M H_2SO_4 solution were conducted at 85 °C with decreased agitation speeds of 200 and 400 rpm. The measured rates of these experiments were compared to the 650 rpm series in Figure 7.8.

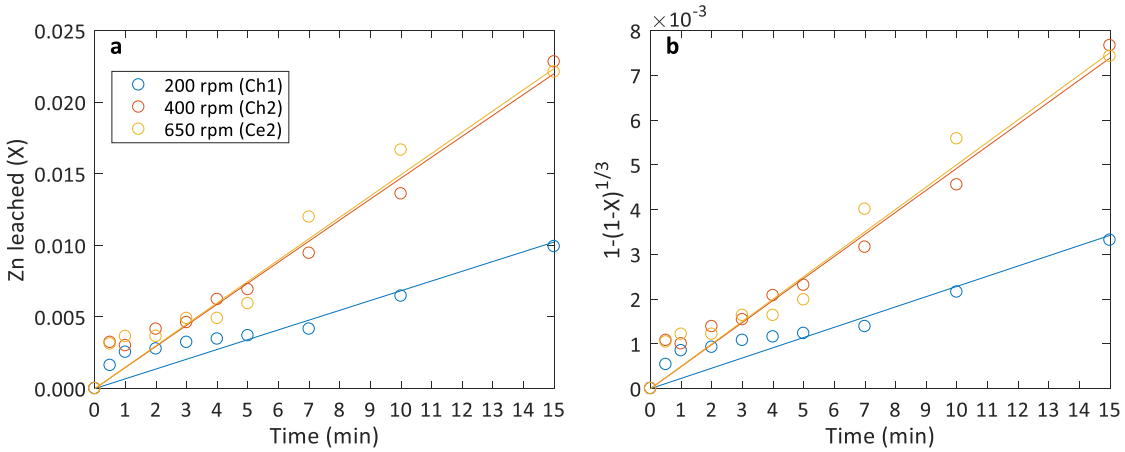

Figure 7.8: Effect of agitation speed on initial sphalerite leaching rate (using feed concentrate Sf3 with 48.7 g/L H_2SO_4 at 85 °C). a) Zn leaching extent; b) SCM plot for surface reaction control (line represents best SCM fit, 0 – 15 min)

It is apparent that higher agitation rates increased the rate of Zn dissolution, suggesting that mass transfer limitations are present at lower (< 400 rpm) agitation rates. Zinc leaching rate may be considered independent of agitation speed at higher (> ≈400 rpm) rates. This does not prove that no intra-particle mass transfer limitations exist, especially since the results are over the initial period of 15 minutes. The fact that the measured zinc extraction rate follows SCM behaviour (chemical reaction controlled) over the initial period (Figure 7.8 b), provides

additional proof that no mass transfer limitations were initially present at higher agitation rates. All experimental tests were conducted at 650 rpm.

Another important aspect of varying the agitation rate, was to inspect the effect thereof on the initial retardation (*i.e.* start-up effects) observed for non-oxidative kinetic test as shown during the previous section. The initial "jump" (< 1 min) remained relatively unchanged (Figure 7.8 a). Albeit, the time it took for the slower initial propagation zone to change into linear SCM behaviour decreased slightly (*i.e.* from 7 min in experiment Ch1 to 3 min in experiment Ce1). The slower initial kinetic region might be due to diffusion of acid to the particle surface (*i.e.* film diffusion) and the effect decreases as the agitation rate increases. Overall, these effects have negligible influence on the overall reaction, because after 15 minutes of leaching zinc extraction is less than 2.5 % and falls well within the experimental uncertainty (± 5 %).

In an attempt to establish the relative importance of initial dosage of lignosulphonate (LS) on the observed kinetics, whether the addition would result in an extension or shortening of the linear region of the SCM (*i.e.* the region of the chemical reaction controlling mechanism). Several experiments were conducted varying with surfactant concentrations (0 – 1 g/L) and a pulp concentration of 0.025 g/L Sf3, while keeping the acid concentration (1.3 M) and temperature (95 °C) constant. The patent of Kawulka et al. (1975), from Gordon Sherritt Mines Limited, shows that a calcium lignosulphonate dosage of 0.5 kg/t of sphalerite concentrate improved zinc extraction from 63 % to 96 %, with a solution composition of 50 g/L Zn, 150 g/L H_2SO_4 and an oxygen partial pressure of 200 kPa at 150 °C. Typically, industrial autoclaves operate using surfactant concentrations of 0.5 – 1.5 kg/t (Owusu, 1993).

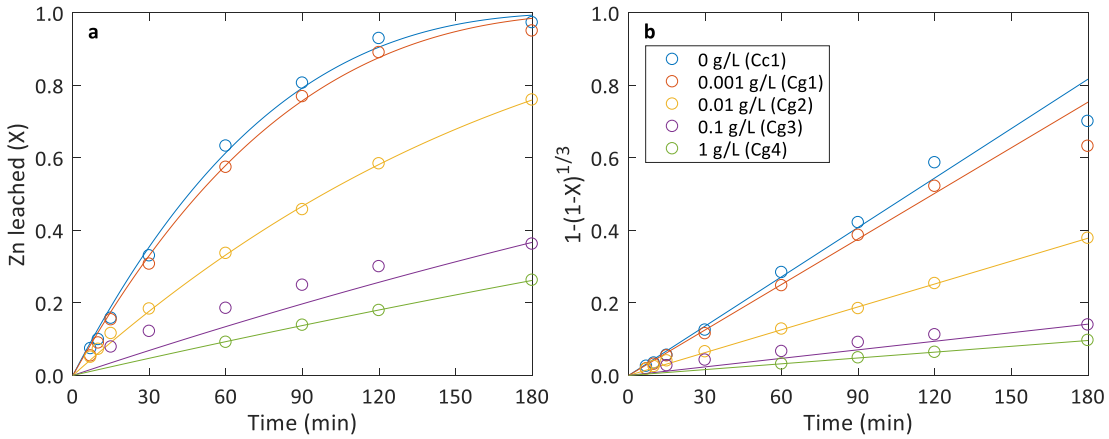

Figure 7.9: Effect of surfactant (lignosulphonate) concentration on sphalerites' leaching kinetics, starting with 0.025 g/L of Sf3 concentrate and 1.3 M H_2SO_4 solution. a) Zn leaching extent; b) SCM plot for surface reaction control (line represents best SCM fit, 0 – 120 min)

In light of being comprehensive from a purely academic standpoint, these results are included in this discussion. The extraction trends in Figure 7.9 indicate a decrease in the fraction zinc extracted with increasing surfactant concentration. Passivation of the non-oxidative leaching rate is most probably the result of the over-dosage of lignosulphonate, which prohibited (or changed) the surface from reacting with acid. Although the SCM plot (Figure 7.9b) still shows linear behaviour even at the highest surfactant concentration (1 g/L), which is counter intuitive to the expected diffusion behaviour.

Lignosulphonate's chemical function is to disperse sulphide that has formed during leaching, reducing diffusion effects and polarisation of the particle surface, and in effect would increase the rate of reaction.

The primary conclusion from these trends is that the surfactant is ineffective or more so inhibited the extraction of zinc from sphalerite under non-oxidative conditions. This conclusion may not be true in lower surfactant to concentrate ratios and could be the same as typically observed in surfactant studies (Owusu, 1993). Fortunately, the non-oxidative kinetic batch experiments (series C) were all conducted with no added surfactant and could be used for the calibration of the rate parameters.

Lastly, the effect of ferrous (Fe^{2+}) concentration on the non-oxidative zinc extraction rate was considered. Chapter 6 has shown the sphalerite concentrate contains a large amount of iron impurity (*i.e.* 6 – 8 % Fe leachable, where the sphalerite phase contains approximately 6.5 % iron), and when leached releases iron (as ferrous) into the solution. The contribution of ferrous to the solution tenor influences the non-oxidative reaction mechanism as seen in Figure 7.10.

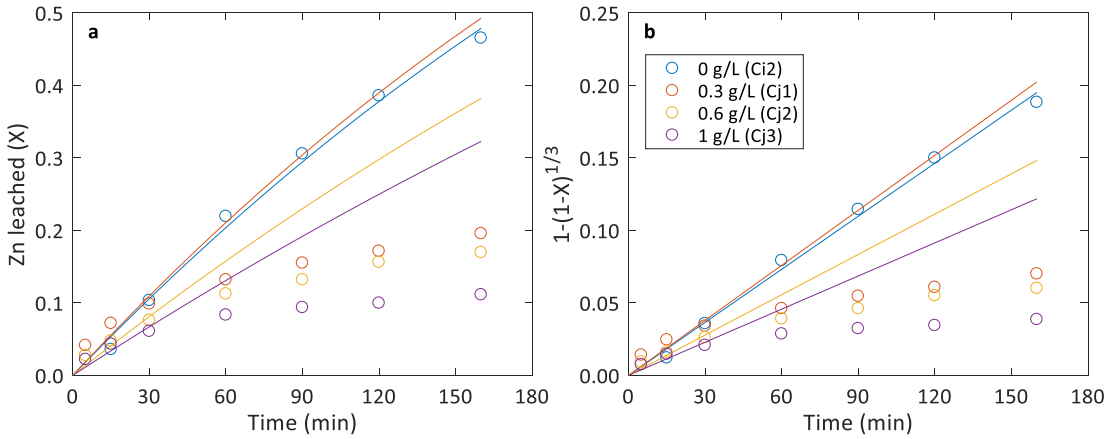

Figure 7.10: Effect of ferrous (Fe^{2+}) on the reaction extents, starting with 1.5 g/L Sf3 concentrate and 0.9 M H_2SO_4 a) Zn leaching extent; b) SCM plot for surface reaction control (lines represent best fit, 0 – 30 min).

A significant decline in the overall rate is observed with increasing ferrous concentration. The initial rate on the other hand displays very similar behaviour between these experiments. This similar initial rate (< 30 min) but decreased rate at longer reaction times might reflect the interaction of ferrous on sphalerite particle surface to form surface layers (*e.g.* jarosites or ferrous oxides or sulphides). The formation of surface layers could change the oxidation rate completely by the change of the reaction mechanism (pathway). Albeit, surface layer formation was not conclusively proven. Crundwell (1988) observed a decrease in sphalerites' oxidation rate due to the formation of a film of insoluble lead sulphate ($PbSO_4$) in concentrates with a high galena content, while Steyl (2012) observed copper sulphate and covellite rims around chalcopyrite (through a detailed analysis) during oxidation test work. The decreased reaction rate due to increased ferrous (Fe^{2+}) concentration is most probably the result of a change in surface polarisation of the solid particles, that decreased the movement of electrons over the charge barrier. More importantly, this result emphasises the use of initial rates to calibrate the kinetic model parameters, since the ferrous concentration will increase during the process of zinc leaching.

7.4.2 Validating the chemistry and proposed mechanism on a phenomenological level

Very little information on the non-oxidative mechanism and kinetic rate was available from the literature. This section attempts to reveal insights into the mechanism of oxidation and corresponding reaction rate from the phenomenological nature of the batch experiments.

The importance of the proton (acid) is revealed in the following discussion, with respect to low pulp density experiments. Experiment Series C represents all tests (including repeats) performed under non-oxidative conditions in appendix C. These results are illustrated below, after recombining the experiment orders to illustrate the relevant bulk solution properties effect on the rate. The concentrate sample Sf3 (+45-53 µm) was leached at 0.5, 0.9 and 1.3 M acid concentrations and temperatures of 75, 85 and 95 °C (Figure 7.11), respectively.

As expected, the basic trend of increasing reaction rate with increasing acid concentration and increasing rate with increasing temperature was obtained from the experiments (Figure 7.11). A most interesting result was the consistent reaction order of approximately 1.7 for acid at the respective temperatures. The consistency validates the accuracy of these tests. Albeit, the reaction order is higher than those obtained from the literature (Crundwell & Verbaan, 1987).

An unexpected contradiction arises from the experimentally obtained reaction order to that of the derived kinetic expression in Chapter 5 (reaction 5.63). The derived kinetic expression would result in reaction orders between 0.5 and 1 for acid, according to the proposed mechanism, yet the obtained reaction order is much higher than one. This means that the kinetic rate expression 5.63, would not be able to predict the leaching behaviour in varying acid concentration.

The assumption of first protonation reaction 5.47 to be the rate-limiting reaction step was most probably incorrect, while the second protonation reaction 5.49 was assumed to be comparatively fast. These assumptions were made based on the insights from the literature. Hence, the reaction mechanism or rate limiting step must be redefined in order to derive a rate expression that can predict the observed kinetic behaviour, but first the effects of pulp density and hydrogen sulphide (H_2S) concentration on sphalerite's leaching kinetics are examined.

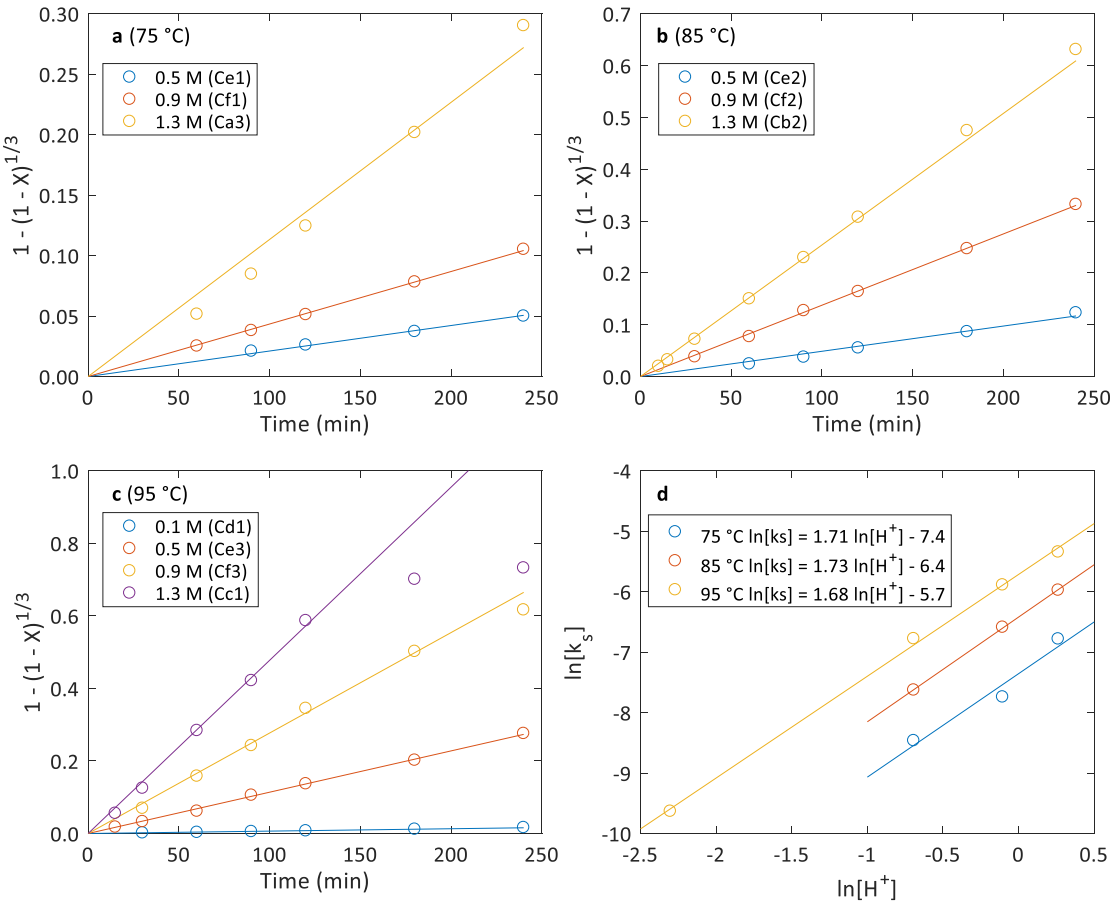

Figure 7.11: Effect of initial acid concentration on the reaction extents, using sample Sf3 as the feed concentrate: SCM plot for surface reaction control at a) 75 °C, b) 85 °C and c) 95 °C (lines represent best fits). The logarithmic plot d) of the overall rate constant as a function of the acid concentration.

Section 7.2.1 highlighted the importance of performing the batch experiments at low solids content. The main reasoning for keeping the pulp density low was to ensure that the solution composition remains approximately constant during each batch experiment. However, accuracy is sacrificed when measuring components produced against high electrolyte concentrations of the same species.

The effects of pulp density on reaction extents are shown in Figure 7.12.

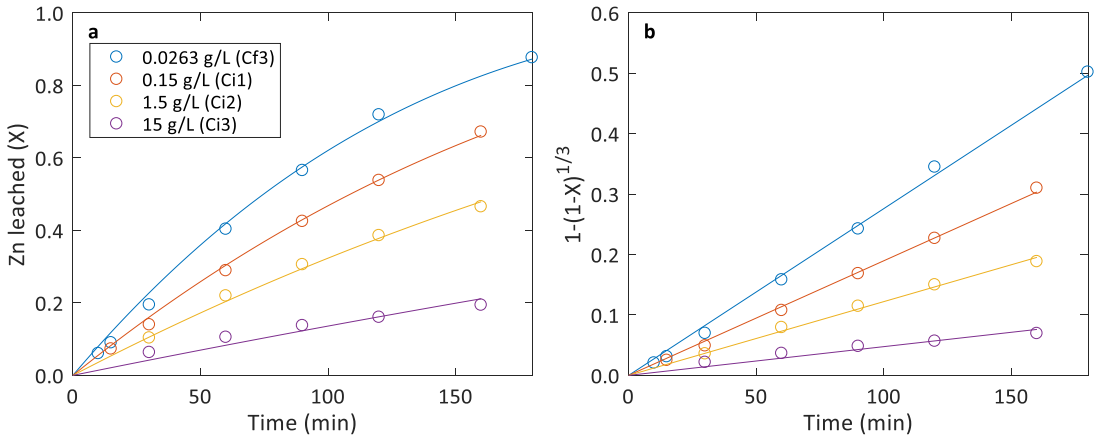

Figure 7.12: Effect of pulp density on reaction extents, using Sf3 as feed concentrate at 95 °C and starting with an initial H_2SO_4 concentration of 0.9 M (lines represent best fit, 0 - 160 min).

Clearly, there is a significant decrease in the rate with an increase in solids content (within the range of experimental error shown in Figure 7.12), suggesting the reaction mechanism is severely affected by pulp-density changes in these lower ranges. The formation of Zn^{2+} and H_2S products might be the primary reason for the dramatic rate change, since the acid (reagent) concentration remained approximately constant during each batch test (because of the high initial acid concentration of 0.9 M, see Table C.2).

To confirm whether the change in rate was established from reaction products, several batch experiments were conducted at various H_2S gas phase concentrations (i.e. partial pressures, while keeping the overall pressure at atmospheric pressure see Figure 7.13) and a test was also performed having an initial $ZnSO_4$ concentrator of 0.1 g/L (see Figure 7.14). The similar sphalerite rate constants in Figure 7.13d indicate that the non-oxidative rate is independent of the H_2S concentration under atmospheric conditions. Noting that these experiments were conducted in an open system configuration (exposed to the atmosphere), thus $H_2S_{(g)}$ evaporated into the atmosphere and therefore no equilibrium is reached (open system configuration, pseudo-equilibrium).

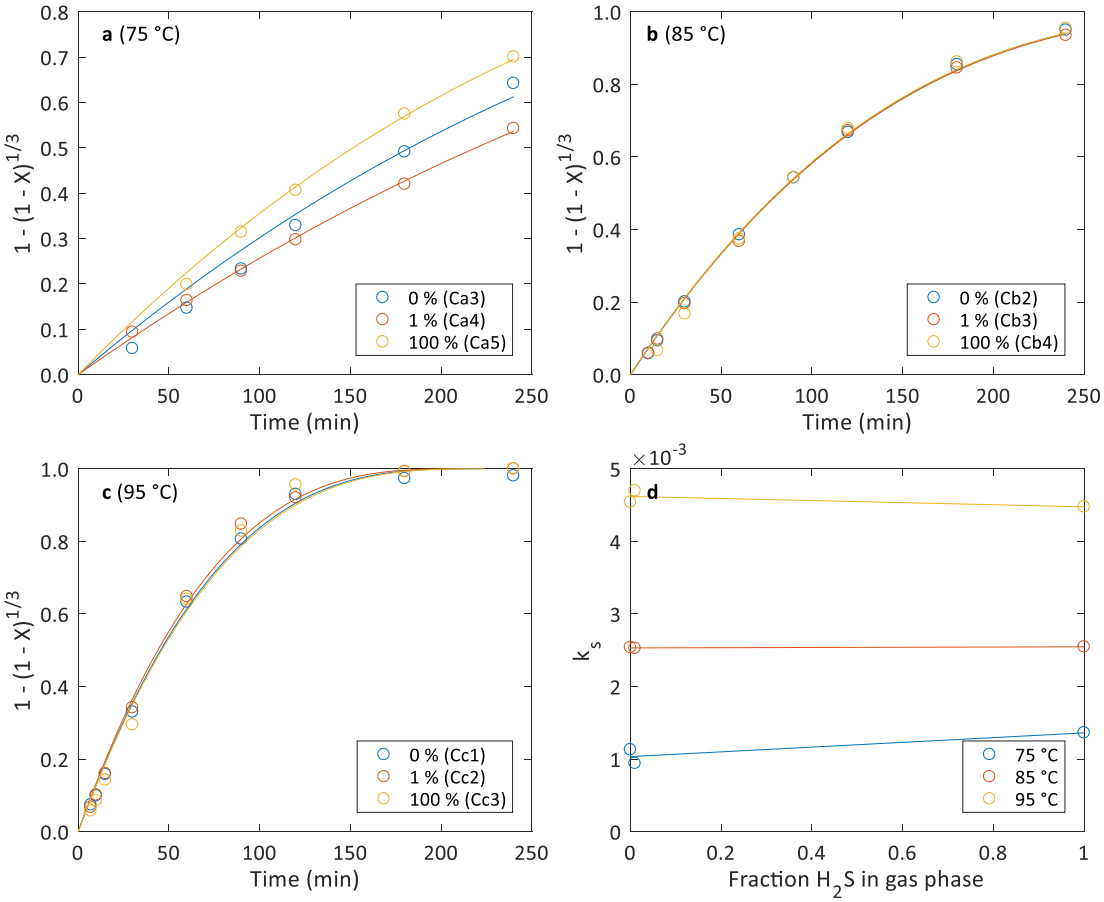

Figure 7.13: Effect of hydrogen sulphide (H_2S) on the reaction extent, under atmospheric pressure and using sample Sf3 as the feed concentrate: SCM plot for surface reaction control at a) 75 °C, b) 85 °C and c) 95 °C (lines represent best fits). d) The regressed overall rate constants versus the fraction of hydrogen sulphide in the gas phase sparged through the reactor.

With a 0 % H_2S in the gas phase sparged through the reactor vessel, evaporation would occur and keep the hydrogen sulphide concentration very close to zero. While for the 1 % and 100 % H_2S gas phase concentrations, the hydrogen sulphide concentration is assumed to remain near the corresponding equilibrium concentration with the excess hydrogen sulphide produced by the reaction evaporating to the atmosphere. It is furthermore assumed that the rate of evaporation would be faster than the H_2S production rate, thus quasi-equilibrium would be established. Regrettably, these assumptions were not validated by mass-transfer measurements, *i.e.* determining the overall mass transfer coefficient (k_La).

To give some indication of the concentration of hydrogen sulphide in an aqueous environment data from Wright and Maass (1932) are given in Table 7.3, and was also validated against equilibrium calculations from the HSC (2006) database. A decrease in H_2S solubility at higher temperatures is observed as the result of the higher volatility of H_2S. The maximum (or equilibrium) concentration of H_2S with a partial pressure of 1 atmosphere at 75 °C is 0.042

mol/kg, which is relativity low in comparison to the acid concentration (H_2SO_4) 1.3 mol/kg. Not excluding the fact that the H_2S produced at 100 % sphalerite leached is $4.64 \cdot 10^{-4}$ mol per kg of water (if no H_2S evaporates into the atmosphere), which is much lower than the equilibrium values. Also, acid stabilises H_2S in water (Kertes *et al.*, 1988), that would result in higher $H_2S_{(aq)}$ concentrations.

Table 7.3: Equilibrium liquid-gas H_2S concentrations in water (Wright & Maass, 1932)

H_2S Partial Pressure	Equilibrium concentration of H_2S (mol/kg)		
(bar)	75 °C	85 °C	95 °C
0	0	0	0
0.01	0.000421	0.000378	0.000346
1.01325	0.0421	0.0378	0.0346

All these factors indicate the insignificant effect of H_2S on the rate of sphalerite dissolution under atmospheric pressure in an open system configuration (within the scope of this study). Yet, it does not mean that hydrogen sulphide do not participate or influence the rate of sphalerite dissolution under non-oxidative conditions and this result should not be generalised to all systems and pressures. It only means the effect of H_2S under these conditions is negligible. For example, the study of Verbaan (1977) undoubtedly indicated the rate of sphalerite dissolution being dependent on H_2S partial pressure, however, his experiments were performed in a sealed reactor (closed system) and equilibrium could have been reached. Whereas the reactor within this study was exposed to the atmosphere and while $H_2S_{(g)}$ was sparged through the reactor, only pseudo-equilibrium would have been established.

The considerable drop of the non-oxidative leaching rate due to denser pulp concentrations (Figure 7.12) was not a result of the formation of H_2S (or more correctly; had a negligible effect on the rate). An investigation into the rate change behaviour due to Zn^{2+} ionic content was further undertaken to explain the possible pulp density-rate change result.

A batch experiment was conducted starting with a slightly higher Zn^{2+} (*i.e.* 100 ppm $ZnSO_4$, or measured as $7.34 \cdot 10^{-4}$ mole Zn^{2+} per kg water) concentration and a pulp density of 0.15 g/L Sf3, as shown in Figure 7.14. The reaction kinetics was found to be strongly dependent on the background zinc sulphate salt concentration observed in Figure 7.14. With only a slight increase of 0 to 0.1 g/L $ZnSO_4$, a decrease of 51 % in the overall rate constant (k_s) was attained. Hence, the decrease of the non-oxidative reaction rate with increasing pulp density (Figure 7.12) was the result of the formation of Zn^{2+} during leaching.

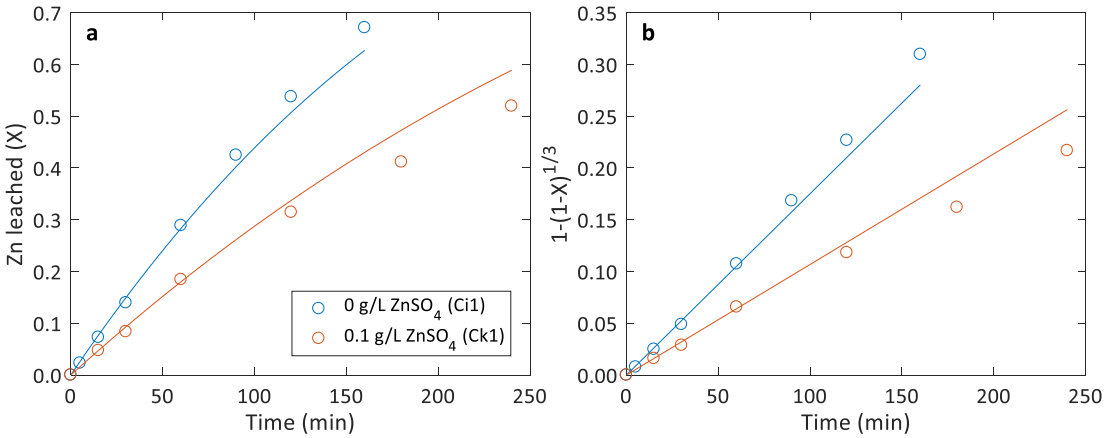

Figure 7.14: The effect of higher zinc concentration on the extent of sphalerite leached. a) Zn leaching extent, b) SCM plot of surface reaction control (line represents best SCM fit, 0 – 180 min)

The non-oxidative rate behaviour due to bulk property changes are summarised as follows:

- Faster kinetics at higher temperatures.
- An acid concentration dependency having a reaction order of 1.7.
- The reaction rate remained unchanged at various H_2S partial pressures from 0 – 100 % (*i.e.* at all possible concentrations of H_2S in the aqueous phase under atmospheric pressure and solution composition of this study).
- A strong dependency on the Zn^{2+} (*i.e.* initial $ZnSO_4$) concentration.

The rate dependency on the H_2S and Zn^{2+} concentrations reflects the behaviour of the proposed intrinsic non-oxidative mechanism (*i.e.* mechanism 2 proposed in Chapter 5). However, the acid concentration reaction order obtained from the experimental results cannot be obtained by the associate intrinsic rate model (equation 5.63). Since the non-oxidative rate is primarily a function of the acid concentration, it is desired to derive a kinetic expression which will be able to capture the kinetic behaviour even if it is based on a semi-empirical (or semi-fundamental) approach. Crundwell (2014) proposed a general mechanism of non-oxidative dissolution of minerals in acidic solutions. Although the mechanism was generalised (*i.e.* can be considered empirical in nature), the proposed dissolution mechanism attempts to comprehend the following two aspects (Crundwell, 2014a):

- The mechanism must illustrate the rate changes as a function of the composition of the solution, specifically it must be able to portray the observed orders of reaction
- The mechanism must account for changes in the rate of dissolution as a function of the composition of the solid, *e.g.* ZnS, ZnO, CuS, CuO, NiO etc. the effects of substitution in solid solutions.

The second aspect is redundant, because minerals differ fundamentally in their nature (*i.e.* crystalline structure, orbital bonding orientation and strengths, impurities *etc.* and will be dependent on the origin of the ore). Nevertheless, the first aspect is inevitable and the mechanism must be able to describe the dissolution rate from a phenomenological perspective. Revised half-reactions, *viz.* anodic (reaction 7.10) and cathodic (reaction 7.11), are proposed with the main difference being the simultaneous participation of two protons (*i.e.* the combined first and second protonation reactions) during the dissolution of sulphide atoms from the lattice.

$$Zn^{2+}_{|lat} + wH_2O + 2h^+ \rightleftharpoons Zn(H_2O)^{2+}_w \quad 7.10$$

$$S^{2-}_{|lat} + 2H^+ \rightleftharpoons H_2S^* + 2h^+ \quad 7.11$$

Utilising the Butler-Volmer equation and mixed potential theory as well as incorporating the effects of the bulk properties on the dissolution rate as observed from the batch experiments, a new rate expression is derived (the derivation is shown in Appendix B.2):

$$r_{sph} = \frac{k_1 \cdot [H^+]^2}{([H^+]^2 + k_2 \cdot [Zn^{2+}])^{0.5}} \quad 7.12$$

The concentrations in equation 7.12 take the units of molality ($\frac{mol}{kg\ Water}$), while k_1 and k_2 is equivalent to $\frac{(kg\ Water)^2}{m^2.min}$ and $\frac{mol}{kg\ Water}$, respectively.

7.4.3 Quantification (regression) and verification of the non-oxidative rate model

Optimisation routines using Matlab, 2016b was applied on the error functions derived in section 7.2.2, to suit the specific mathematical routine that optimises rate constants of equation 7.12. Four rate parameters (i.e. $k^1_{95°C}$, E^1_a, $k^2_{95°C}$, E^2_a) were tuned during the non-oxidative tuning campaign. The rate parameters originated from the reaction heat equations of the rate constants k_1 and k_2, as shown in equations 7.13 and 7.14.

$$k_1 = k^1_{95\,°C} \cdot \mathrm{e}^{-\frac{\mathrm{E}^1_a}{R}\left(\frac{1}{T}-\frac{1}{368.15}\right)} \quad 7.13$$

$$k_2 = k^2_{95\,°C} \cdot \mathrm{e}^{-\frac{\mathrm{E}^2_a}{R}\left(\frac{1}{T}-\frac{1}{368.15}\right)} \quad 7.14$$

The first approach to regress the rate parameters was performed using the shrinking core model linear rate constant, $k_{l,sph}$, outlined in section 7.2.2. By using the SCM regression results as first approximation during the non-linear (dynamic) fundamental model regression, the optimised

rate parameters for the intrinsic non-oxidative rate model were quantified. The following sets of experiments were used as testing and training data to identify and verify the rate model.

Table 7.4: Training & testing experimental series

Type	Experiments
Training	Ca3, Cb2, Cc1, Ce1, Ce2, Ce3, Cf1, Cf2, Cf3, Ci1, Ci2, Ci3
Testing	Cd1, Ck1

Because the rate parameters obtained from the SCM are based upon the averaged reaction rate and solution composition within the evaluation range (*see* Table C.2), the solution speciation is assumed to be at the corresponding saturation concentration at these conditions. The actual free hydrogen (H^+) and zinc ion (Zn^{2+}) concentration at reactor temperature and solution vapour pressure of the electrolyte solution are obtained from the thermodynamic model developed in Chapter 4. These average saturation concentrations, presented in Table C.2, and calculated rate constants were used to determine the average rate of sphalerite dissolution, r_{sph}^{ave}, and used in the SCM equation 7.2 to model the extent of reaction.

The equivalent $k_{l,sph}$ were compared to the experimental linear rate constant (equation 2.42), and the error (E_f) minimised through the Matlab optimisation algorithm. The error results are shown in Figure 7.15, while the optimised rate constants are presented in Table 7.5.

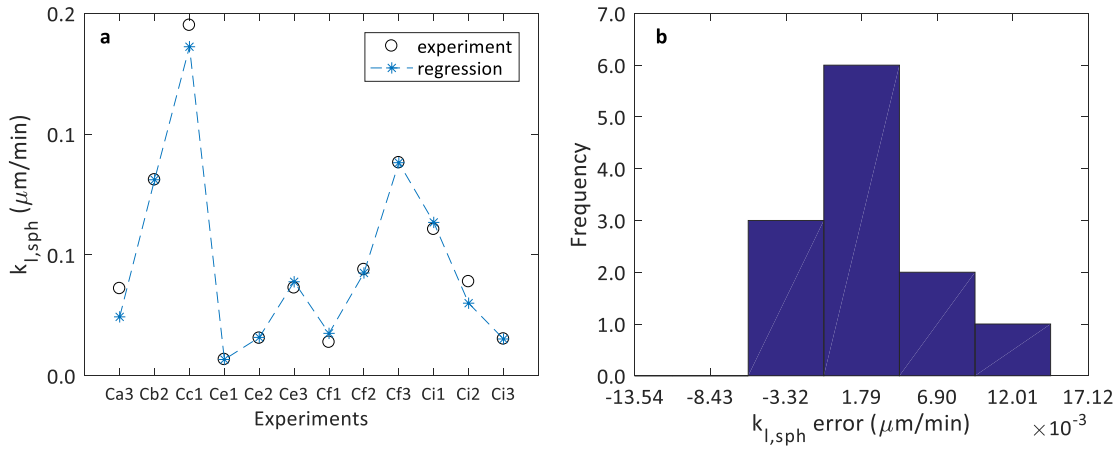

Figure 7.15: Comparison between measured & regressed values of the initial linear rate constant, $k_{l,sph}$, for the sphalerite concentrate. AARD = 8.75 %, where $AARD = \frac{100}{N_i} \cdot \sum E_i$, & an average error of 0.001787 µm/min.

The predicted linear rate constants compare well to that of the experimentally calculated rate constants. As stated previously the resulting rate parameters from the SCM optimisation is used as initial values for the non-linear regression model. Table 7.5 summarises these optimised

parameters, while Table 7.6 compares the AARD of each training batch experiment values with corresponding (modelled) rate data from the optimised rate parameters. The error introduced by using the model ($\approx$ 15 %) is of the same order of magnitude as the experimental error.

Table 7.5: Optimized rate constant parameters for the intrinsic non-oxidative reaction rate

Optimisation (regression) method	$k^1_{95\,°C}$ (kg/m^2.min)	E^1_a (J/mol)	$k^2_{95\,°C}$ (mol/kg)	E^2_a (J/mol)	[a]AARD %
SCM	0.00463358	18734	2769	-249483	17.78
Non-Linear	0.00356719	19484	2656	-259763	13.72
Final	0.004	20000	2700	-250000	13.75

[a]Averaged absolute relative error of the experiments

Table 7.6: Experimental test AARD resulting from the optimised rate parameters

Experiment	SCM	Non-Linear	Final (SCM)	Final (Non-Linear)
Ca3	31.36	19.12	32.56	24.94
Cb2	16.24	8.93	18.89	8.90
Cc1	8.47	12.88	8.49	7.41
Ce1	7.12	4.71	8.24	17.68
Ce2	20.97	12.80	22.87	6.25
Ce3	9.52	7.79	12.68	6.04
Cf1	22.14	28.37	35.59	9.83
Cf2	13.02	3.79	14.64	12.55
Cf3	11.73	15.35	12.63	10.40
Ci1	31.41	10.00	32.06	5.55
Ci2	31.41	21.15	32.06	26.29
Ci3	9.93	19.75	8.16	29.21
Average	17.78	13.72	19.91	13.75
Standard Dev.	9.43	7.33	10.65	8.59

While realising that the obtained AARD are quite high for the individual experiments, one should take into account that AARD is very sensitive to smaller values (*i.e.* < 10 % extraction). That is to say that the high AARD values originate from data at initial leaching times, where a small deviation from experimental value will result in a large AARD value. Hence, these results should be regarded in this light and must also be viewed through visual inspection of the trends as shown in Figure 7.16.

The average AARD dropped by 4 % using the non-linear model. While the optimized rate parameters gave good accuracy in modelling the leaching behaviour of sphalerite, these values

are somewhat abstract and meaningless to include all the significant figures. Therefore, by visual inspection and rounding, the rate parameters were adjusted to give final selected rate parameter value as result for this work. The models were then recalculated using the final rate parameters and the AARD calculated. There was only a decrease of 0.03 % in the AARD for the training data and 1 % standard deviation. Hence, very little accuracy is lost by selecting these rate parameters as final values for this work and are coherent as seen from an engineering perspective.

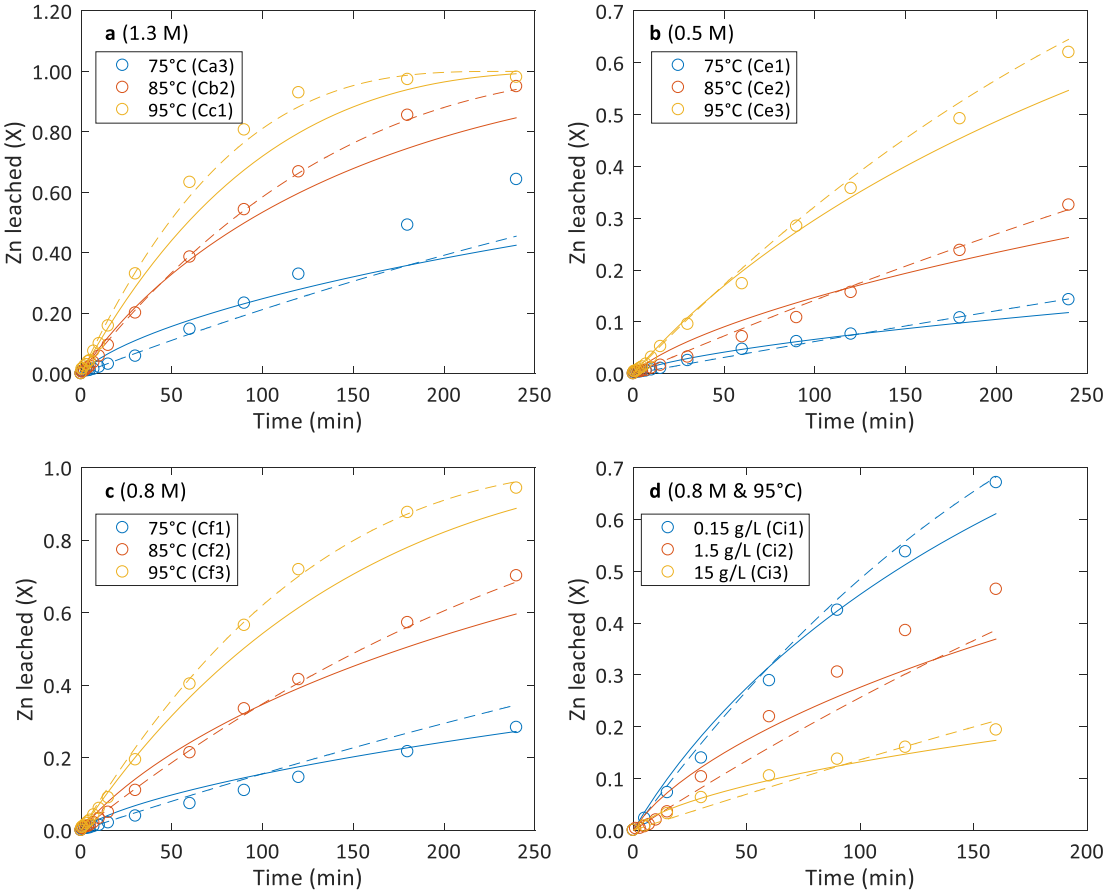

Figure 7.16: Training data comparison to modelling results, where solid lines (-) represent the shrinking core model and the striped lines (--) represent the non-linear model. a) compares temperature variation at 1.3 M acid concentration, b) compares temperature variation at 0.5 M acid concentration, c) compares temperature variation at 0.8 M acid concentration and d) compares different solid concentrations at 0.8 M and 95 °C.

To verify the ability to reproduce the extent of sphalerite dissolution the model was compared to testing data. Two tests were used as reference, 1) one experiment which was conducted at a lower acid concentration (0.1 M) compared to the experiments upon which the model was optimised (experiment Cd1) and one experiment which was conducted starting with a higher initial $ZnSO_4$ concentration while all the training experiments had no initial $ZnSO_4$ present

(experiment Ck1). The model's ability to predict unseen data is show in Figure 7.17. As seen the model did predict the leaching behaviour of sphalerite under almost similar conditions very well. The rate model and parameters are a "well-enough" predictive method to characterise and describe the leaching behaviour of sphalerite under non-oxidative atmospheric conditions.

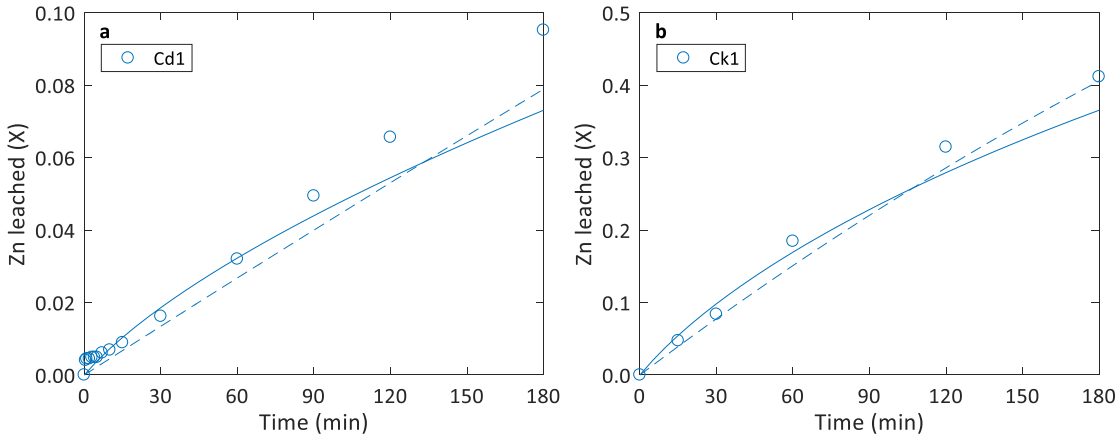

Figure 7.17: Testing data comparison to modelling results, where solid lines (-) represent the shrinking core model and the striped lines (--) represent the non-linear model. a) is an experiment done in a very low acid concentration of 0.1 M, and b) is an experiment done starting with an $ZnSO_4$ concentration of 100 ppm $ZnSO_4$.

7.5 Oxidative model evaluation

The oxidative reaction characteristics and conceptualised mechanism are evaluated in this section. Thereafter the oxidative kinetic rate parameters were quantified. Kinetic constants were calibrated using all available data and validated against independent tests, presented in appendix D, E & F.

7.5.1 Reaction regime

An approximately constant initial sphalerite leaching rate was observed for all the oxidative experiments, see appendices. Occasionally the experimental data deviated from ideal linear SCM behaviour at longer reaction times (> 0.4 – 0.5 fractional dissolution of sphalerite). Deviation may be due to diffusion through the solid sulphur formation. It can also be observed from the figures that at low Fe^{3+}/Fe^{2+} ratios, Fe^{3+} becomes diffusion limited.

The data followed the logic of the mechanism discussed in Chapter 5, and the model is limited to the following conditions:

0.01 – 0.7 M Fe^{3+}, 0 – 0.75 M Fe^{2+} and 0.1 – 1.3 M H_2SO_4

7.5.2 Quantification (regression) and verification of the oxidative rate model

Optimisation methods, similar to non-oxidative methods, were used to regress the rate constants of the oxidative model. The kinetic rate model (equation 5.69) was mathematically related within the differential equation 7.3, forming the reactor model. By first approximation there are six rate parameters to optimize, namely $k^1_{95°C}$, E^1_a, $k^2_{95°C}$, E^2_a, $k^3_{95°C}$ & E^3_a. After evaluation of the data and preliminary regression it was found that rate constant k_2 is independent of temperature, *i.e.* 75 °C to 95 °C. The rate constant equations are as follows:

$$k_1 = k^1_{95\,°C} \cdot \mathrm{e}^{-\frac{\mathrm{E}^1_a}{R}\left(\frac{1}{T}-\frac{1}{368.15}\right)} \quad 7.15$$

$$k_2 = k^2_{95\,°C} \quad 7.16$$

$$k_3 = k^3_{95\,°C} \cdot \mathrm{e}^{-\frac{\mathrm{E}^3_a}{R}\left(\frac{1}{T}-\frac{1}{368.15}\right)} \quad 7.17$$

The batch experiments were divided into two categories, *viz.* training data and testing data. Training data were used to train the rate model, while testing data were used to validate the model output results. Table 7.7 shows the respective category for each test.

Table 7.7: Training and testing categories

Type	Experiments
Training	Fd2, Fe2, Ff1, Ff2, Ff3, Fg1, Fg2, Fg3, Fh1, Fh2, Fi1, Fj1, Fj2, Fj3, Fj4, Fk1, Fk2, Fk3, Fk4, Fk5, Fl1, Fl2, Fl3, Fm1, Fm2, Fm3, Fm4, Fn1, Fn2, Fn3, Fn4, Fo1, Fo2, Fo3, Fo4, Db3, Df1, Dj3, Dk3, Dl3
Testing	Fb1, Fj1, Fi1, Dh1, Dh2, Dh3, Dp3, Dq2, Dr3, Ds2, Dt2, Dp4, Dq3, Dr4, Ds3, Dt3, Dj1, Dk1, Dl1, Dj2, Dk2, Dl2, Eb1, Eb2, Eb3, Eb4, Ec2, Ed1, Ed2, Fp2

By first approximation the parameters were evaluated from the SCM linear rate constant, $k_{l,sph}$, regression method. From Figure 7.18a it is clear that the optimal model parameters gave linear rate constants comparable to those obtained from the experiments, albeit not very accurate. An average absolute relative error, AARD, of 17.7 % for $k_{l,sph}$ compared to the experiments. Although this is quite a large error, the loss in experimental error, *i.e.* leaching extents of each batch experiment, did not suffer such a significant loss in accuracy. The experimental error modelled by $k^{exp}_{l,sph}$ gives an AARD of 17.5 %, while modelled by the rate equation $k^{scm}_{l,sph}$ gave an AARD of 19.6%. With only a 2.1 % loss in accuracy through the modelling of $k_{l,sph}$ by the intrinsic kinetic model, the insensitivity of the linear rate constant and SCM is highlighted. Any error in

$k_{l,sph}$ would result in a $\frac{1}{3}$ order error in the leaching extent, due to the cubic nature of the SCM, taking the AARD of 17.7 % in $k_{l,sph}$ modelled and calculating the exponent value results in an 2.6 % loss in leaching extent accuracy. The average error of $k_{l,sph}$ is $8.6 \times 10^{-4} \mu m/min$, which compared to the absolute linear rate constant values is much lower. The error is also normally distributed around the mean, as shown in Figure 7.18b. Hence, the SCM gave sound results and can be considered as a good first approximation. The shrinking core model results are presented in Figure 7.19 (training) and Figure 7.20 (testing).

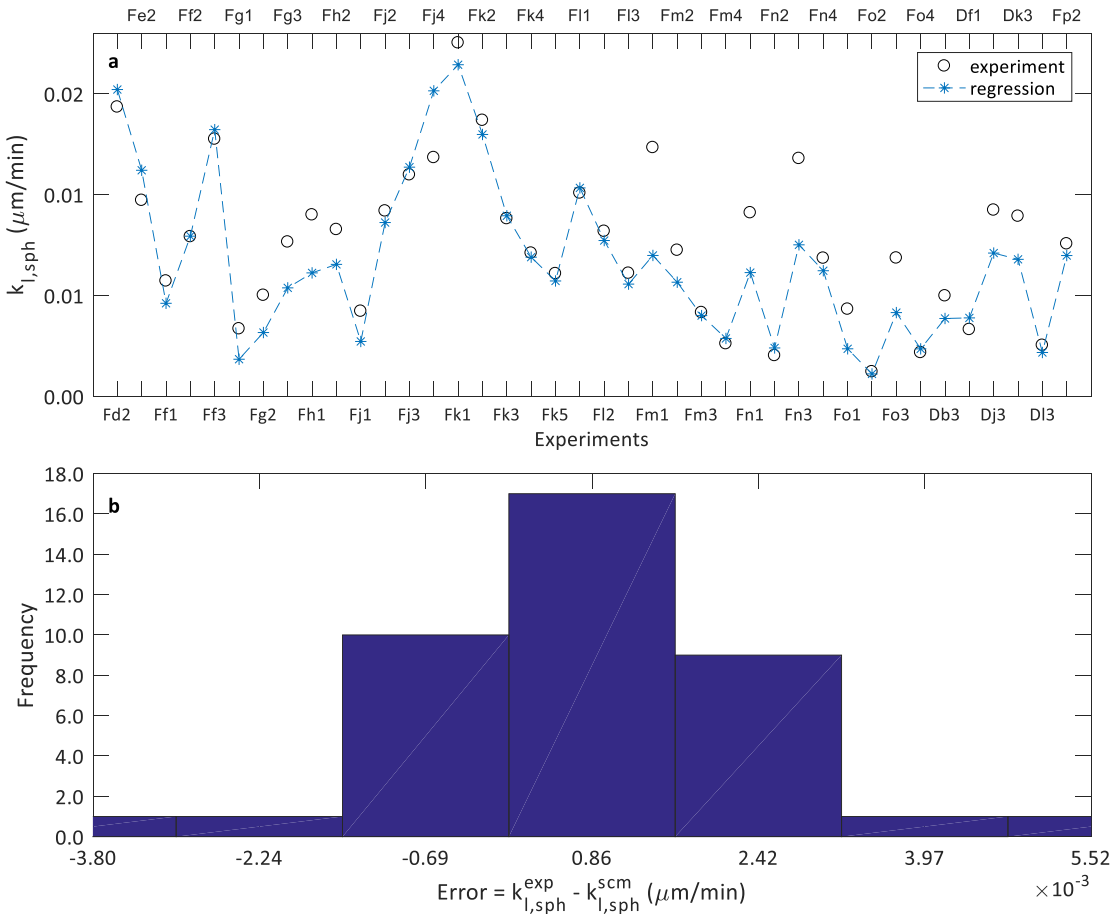

Figure 7.18: Comparison between measured & regressed values of the initial linear rate constant, $k_{l,sph}$, for the sphalerite concentrate. AARD = 17.7 %, where $AARD = \frac{100}{N_i} \cdot \sum E_i$, & an average error of 0.000863 µm/min. a) optimisation results, b) error histogram.

The optimized rate parameters are presented in Table 7.8. The approach to solving the rate parameters differed slightly with regards to the non-linear model. Instead of finding the optimal value for all five rate parameters, the three reference constants were solved independently from the two activation energy parameters. By using all the experiments conducted at 95 °C these three reference constants were optimised to get the minimum error, while all other experiments not performed at 95 °C were used to optimize the activation energies. This ensured that the

optimal values for each of these constants were obtained. Limiting error propagation of the lower temperature experiments into the reference constants.

Table 7.8: Optimized rate constant parameters for the intrinsic oxidative reaction rate

Optimisation (regression) method	$k^1_{95\,^\circ C}$ $\frac{(mol.kg)^{0.5}}{m^2.min}$	E^1_a $\frac{J}{mol}$	$k^2_{95\,^\circ C}$ $-$	$k^3_{95\,^\circ C}$ $\frac{kg}{mol}$	E^3_a $\frac{J}{mol}$	[a]AARD %
Linear	0.02980	57758	0.15128	0.02270	-226413	17.7
Non-Linear	0.03114	33187	0.18438	0.07047	-262213	14.3
Final	0.03	35000	0.2	0.07	-250000	14.8

[a]Averaged absolute relative error of the experiments

The optimized parameters of the linear and non-linear regression methods are comparable and follow sound logic comparable to the rate model derived in section 5.5.3. The activation energy for rate constant k_3 is negative, which might seem wrong. However, $k_3 = k_{a_2}/k_{a_1}$ as derived from the intrinsic mechanism, which is obtained by the deviation of the anodic rate constants from the Butler-Volmer equation as derived in equation 5.67. Thus, one can relate the following expression from the Arrhenius relationship:

$$E^3_a = E_{a2} - E_{a1} \tag{7.18}$$

Therefore, the anodic reaction activation energy of the first electron transfer step from the dissolution of zinc, E_{a1}, is larger than the activation energy for the anodic electron transfer of ferrous to ferric, E_{a2}. This would then result in a negative activation energy. It would also indicate that the effect of ferrous retardation on the overall reaction rate decreases with an increase in temperature. Hence, the negative activation energy is an acceptable result.

To account for engineering sensibility, the optimised parameters were rounded to normal values and presented as the result for this dissertation. The final values, in Table 7.8, resulted in a negligible loss in accuracy ($\approx 0.5\%$). The well-defined kinetic model gave superior results in modelling the leaching behaviour of sphalerite.

Training data modelling results are presented in the graphs of Figure 7.19, while the models accuracy to predict unseen data is presented in the graphs of Figure 7.20. Experimental tests were performed at slurry densities of 2.7 g/L and below. While this is good for developing the intrinsic rate, leaching at higher densities could result in a different leaching behaviour. Another experimental result is also show in Figure 7.21, with an experiment conducted at 15 g/L.

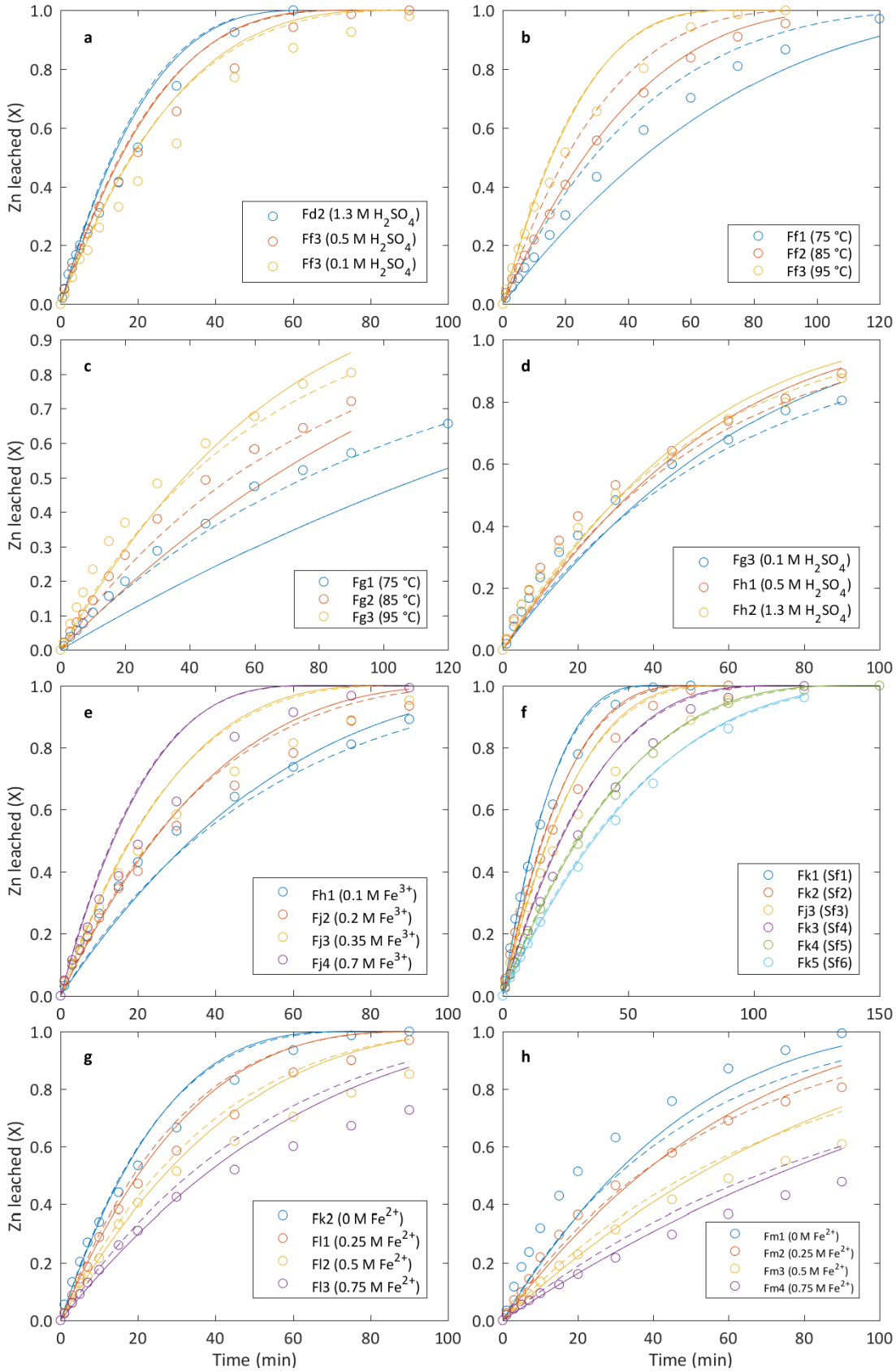

Figure 7.19: Training data compared to model results, where solid lines (-) represent the shrinking core model and the striped lines (--) represent the non-linear model (continue on next page)

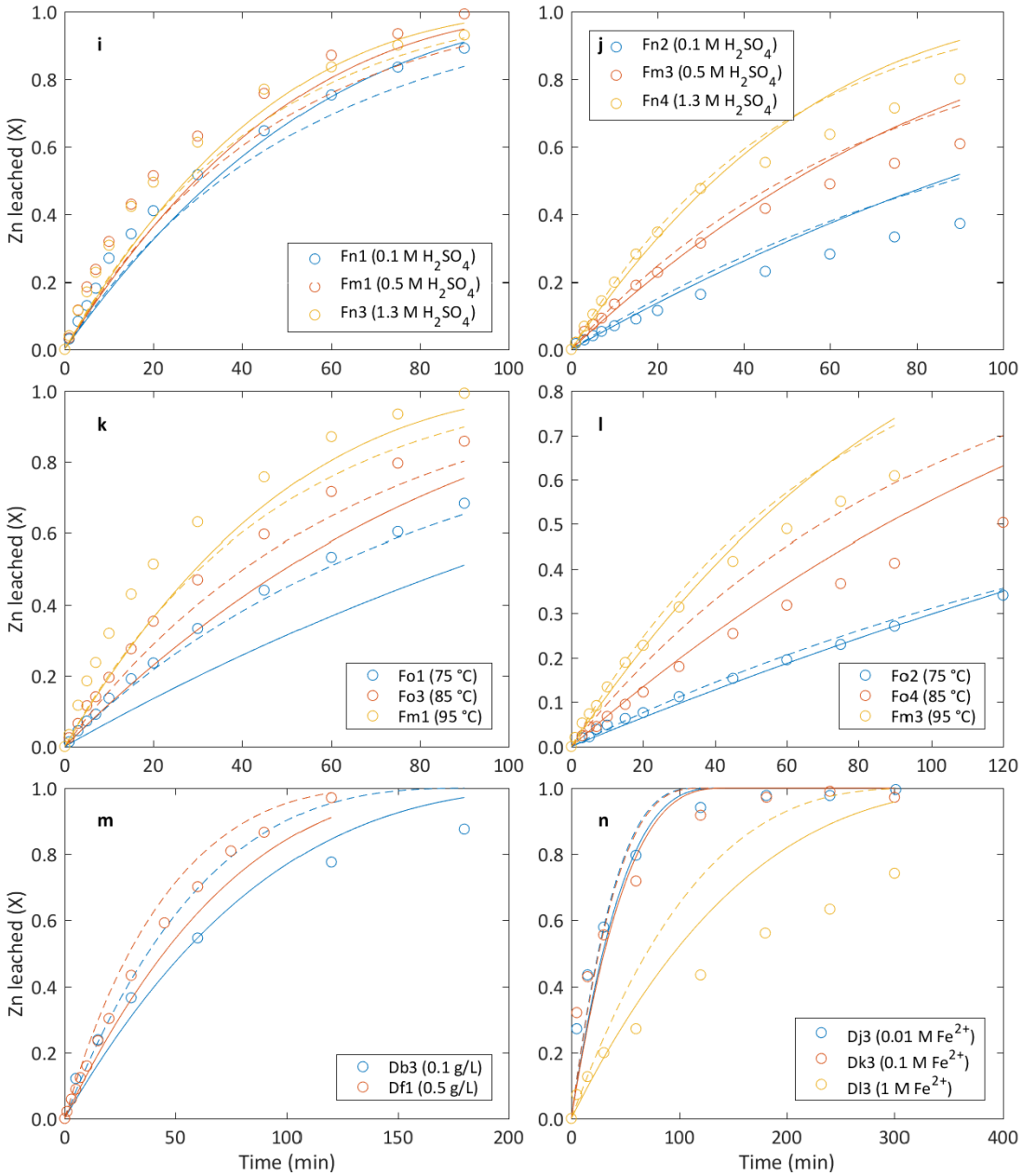

Figure 7.19: Training data compared to model results, where solid lines (-) represent the shrinking core model and the striped lines (--) represent the non-linear model

From graphs a to n in Figure 7.19 the modelled results compared well to the data, especially at lower ferrous concentrations. The leaching behaviour of sphalerite at 1 M Fe^{2+} as seen from graph n was not captured at all. Hence, the rate model is limited to a 0.7 M Fe^{2+} concentration. The effect of speciation to a change in acid concentration was also captured in the model, which emphasises the importance of the formation of contact ion pares. Overall the initial rate was modelled well, while at higher leaching extents the error became larger. Nonetheless, the optimal result is quite good, specifically because the rate model was not built from the experimental data (as common practice found in the literature), but rather from first principles.

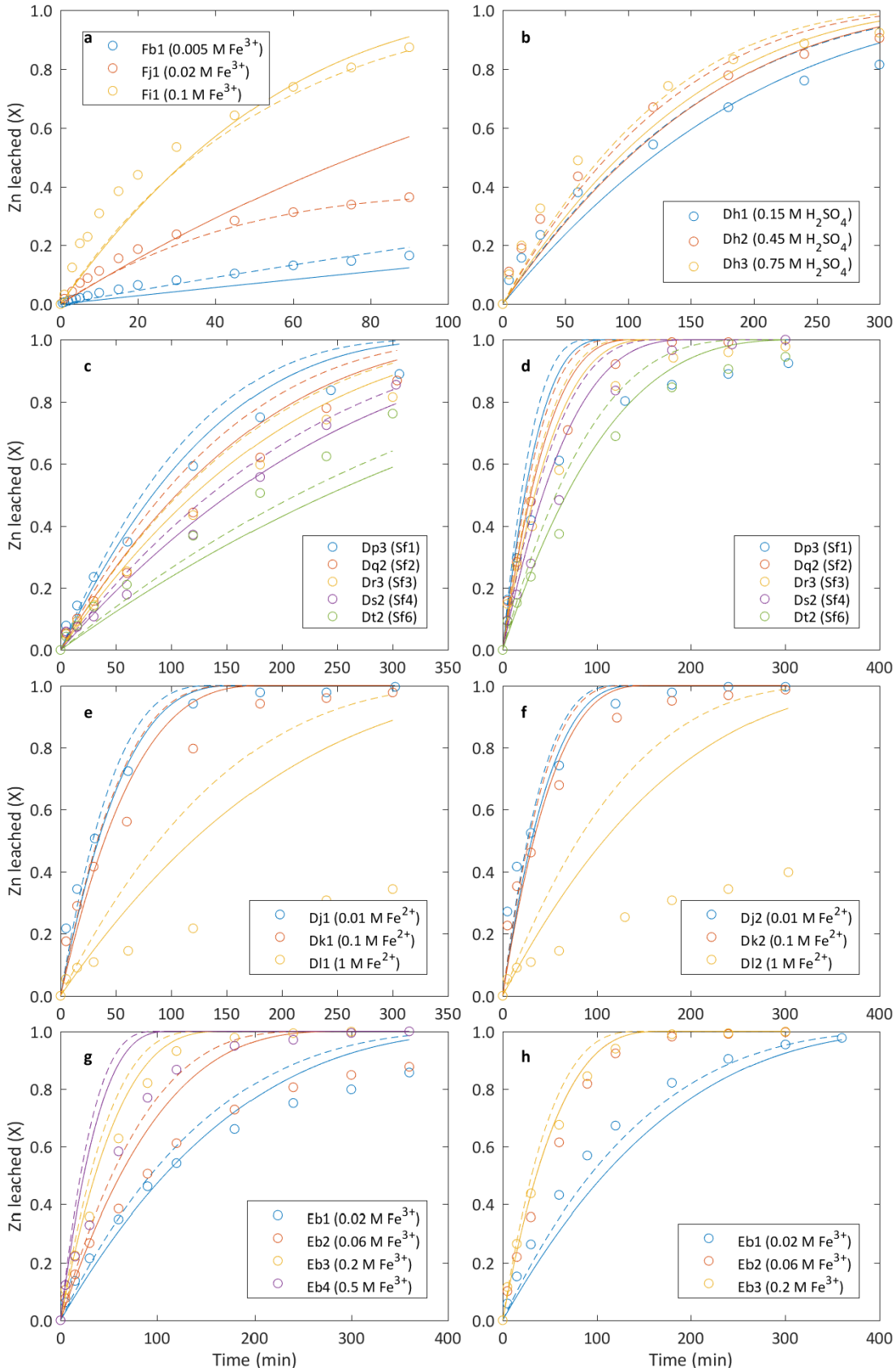

Figure 7.20: Testing data compared to model results, where solid lines (-) represent the shrinking core model and the striped lines (--) represent the non-linear model

The kinetic model could predict unseen data (testing) data from other batch experimentation, albeit there is some loss in accuracy. Graphs c to h, show data from the experimental series D and E. Although these data sets were selected for testing, they do not always fall within the range of conditions whereupon the kinetic parameters were trained, hence these graphs should be viewed in light as if they are extrapolated. From this viewpoint, the model performed well since it could predict leaching behaviour beyond its bound of training. The model could however not predict the leaching behaviour of sphalerite at high Fe^{2+} concentrations, as seen from Figure 7.20e and f.

Validating the kinetic rate at higher pulp densities experiment Fp2 was modelled. Figure 4.21 clearly shows the ability of the kinetic expression to predict the dissolution of sphalerite and solution composition in almost free copper solutions.

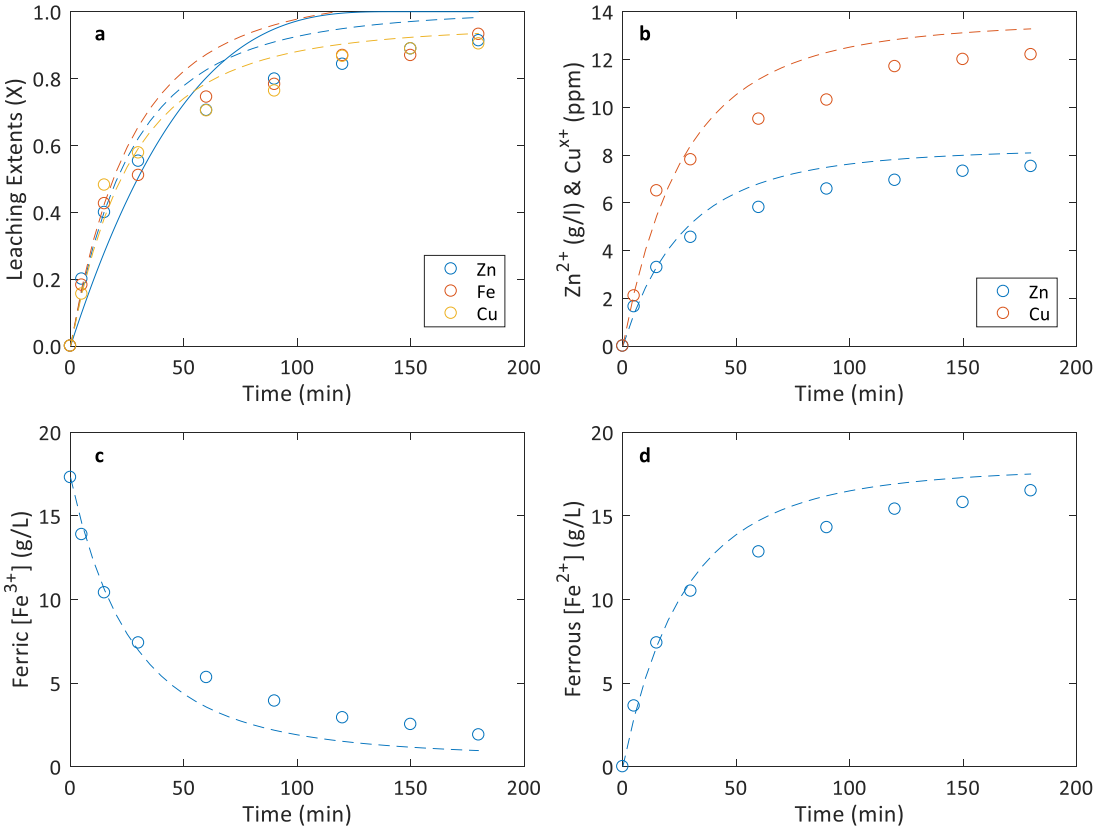

Figure 7.21: Model compared to unseen data from experiment Fp2, performed under 15 g/L solid concentration at 95 °C and 0.1 g/L lignosulphonate.

7.6 Conclusions

The objective of this chapter was to obtain the kinetic model parameters from the phenomenological batch experiments. This objective was achieved, and the kinetic model was defined within the defined mathematical framework and scope.

The intrinsic mechanisms developed in Chapter 5 were investigated. It was found that the non-oxidative model derived in Chapter 5 was not able to predict the behaviour of sphalerite leaching by acid. The mechanism was revisited and it was decided to include both hydrogen ions moving through the polarized (charge) barrier (Crundwell, 2014a), within the activation-polarisation relationship used in the mixed potential theory to derive a new rate equation. Equation 7.12 captured the non-oxidative dissolution accurately. The oxidation mechanism developed in Chapter 5 could, however, explain the leaching behaviour of sphalerite under oxidative conditions. The kinetic expression 5.69 accurately captured the oxidative leaching of sphalerite.

The batch experimental results were verified. It was found to have a repeatability error of 5 %. The initial rate of non-oxidative leaching showed odd retarded behaviour, but the initial rate was excluded from modelling due to the slow leaching kinetics and reaction activation. On the other hand, oxidative leaching show fast initial rates that was all linear and could be used during kinetic model evaluation. Particle size distribution and mean diameters followed the expected linear shrinking core model behaviour, that validated the use of the SCM. Lastly, the overall reaction stoichiometry compared to the experimental stoichiometry.

The batch experiments were used to confirm the reaction regimes. It was found that all the experiments used in training and testing the rate model, were occurring *via* surface reaction controlled mechanisms. Exception did occur, usually after 40 to 50 % of zinc leached, when the mechanism may have changed to diffusion controlled due to passivating layers. However, this was very rare, since the surfactant (lignosulphonate) dispersed the formed sulphur layers and promoted diffusion.

In conclusion, quantification of the kinetic expressions for non-oxidative and oxidative leaching of sphalerite was performed, and obtained kinetic constants with acceptable accuracies.

Chapter 8 Study Overview and Conclusions

8.1 Overview of the contributions of this work

The focus of this work has been a kinetic study of the non-oxidative and oxidative leaching behaviour of sphalerite, under various operating conditions with the addition of a surfactant. The major advantage of operating sphalerite leaching at elevated temperatures (85 – 95 °C) and atmospheric pressure is the reduced energy input in processing sphalerite (as compared to medium temperature/high pressure autoclave operations), with notable fast leaching kinetics accompanied by elemental sulphur yields. On the other hand, atmospheric leaching requires ultra-fine grinding and higher acid concentration, which may lead to high energy inputs. The stifling effect of solid elemental sulphur is highly dependent on the effectiveness of the surfactant and places strict requirements on the top size (coarse) particle fraction during atmospheric sphalerite leaching. Figure 8.1 shows an overview of contributions.

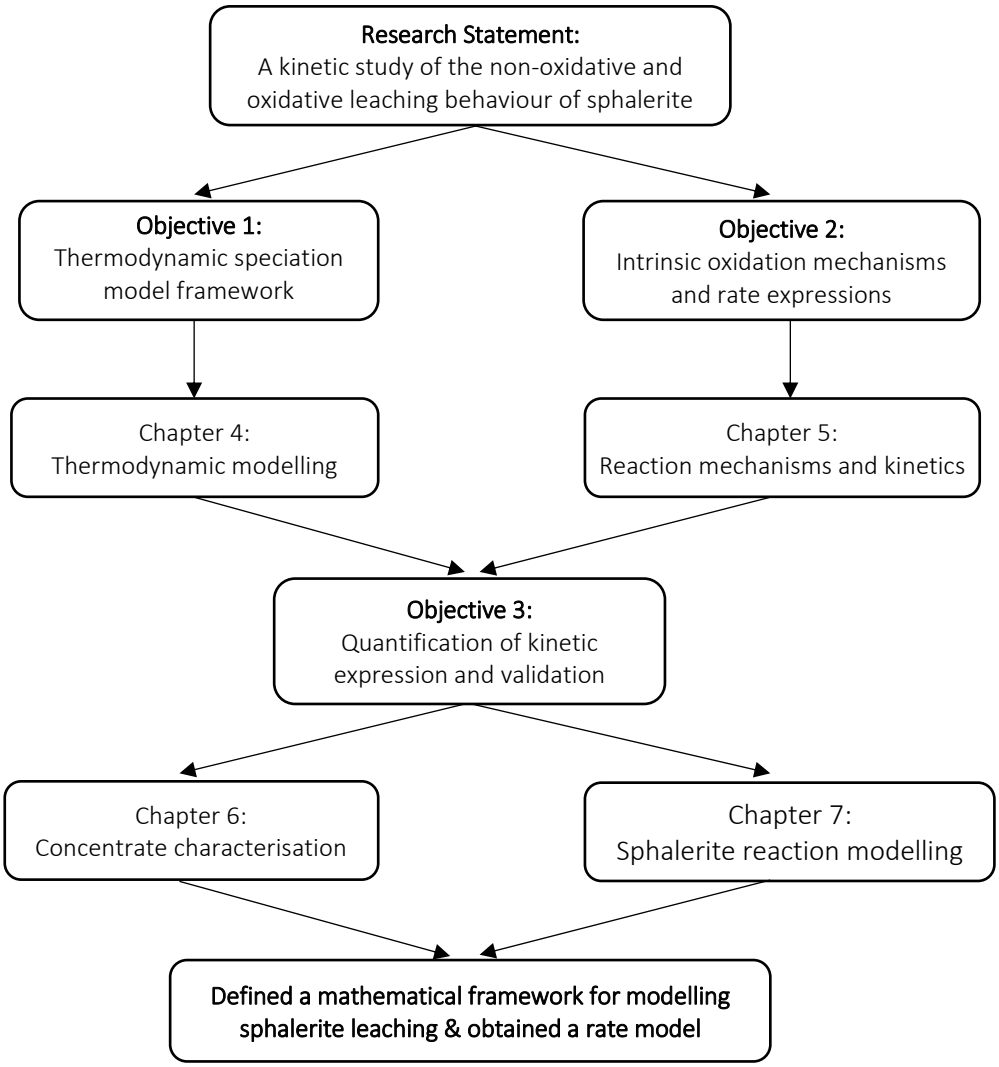

Figure 8.1: Overview of the structure and contributions of this work

8.2 Conclusions on objectives

Conclusions are made in terms of the objectives specified in the introduction of this study (Chapter 1). The research statement reads:

A kinetic study of the non-oxidative and oxidative leaching behaviour of sphalerite, under various operating conditions with the addition of a surfactant.

The objectives of this thesis were:

1. To develop a self-consistent thermodynamic solution modelling framework of the various sub-systems applicable to the $ZnSO_4$ – $Fe_2(SO_4)_3$ – $FeSO_4$ – H_2SO_4 – H_2O reactive system on which the kinetics of sphalerite leaching with Fe^{3+} and H^+ can be interpreted.
2. To derive intrinsic oxidation mechanism and rate expressions for the non-oxidative and oxidative leaching of sphalerite.
3. To verify the rate expressions for the leaching of the sphalerite concentrate and to quantify the rate parameters on a phenomenological level.

The **first objective** was to develop a thermodynamic speciation model from which the solution phase behaviour could be predicted. In chapters 2 and 4 the detailed development and optimisation of such a self-consistent minimum parameter thermodynamic model was discussed, in order to describe the $ZnSO_4$ – $FeSO_4$ – $Fe_2(SO_4)_3$ – H_2SO_4 – H_2O system over a temperature range of 75 – 95 °C. After considering various literature sources it was decided to use the Pitzer model as the framework upon which the solution species activities were modelled.

The Pitzer model was calibrated by a systematic approach of considering the binary and ternary systems individually and forms the basis from which the overall higher order systems were predicted. Calibration was done by using thermodynamic data from various sources, while the primary (initial) model parameters and speciation data came from studies of Steyl (2009) and Biley (2015). The solution model is accurate up to concentrations of 1.5 M $ZnSO_4$, 1.5 M $FeSO_4$, 1.5 M $Fe_2(SO_4)_3$ and 2 M H_2SO_4. A focus was to capture speciation of the ions in solution (*i.e.* Fe^{3+}, $FeSO_4^+$, Zn^{2+}, $ZnSO_4^0$, etc.), that is distinguishing between inner- and outer-sphere complexes and was achieved through the inclusion of Raman spectroscopic stability constants. Contact ion pair (CIP) formation was therefore predicted by the Pitzer model and has shown superior results in the modelling of the ionic aqueous solution relevant to this metallurgical kinetic study.

The **second objective** was to derive intrinsic oxidation rate expressions for the non-oxidative and oxidative leaching of sphalerite, based on insights from the literature. Chapter 5 condensed the relevant mechanisms of zinc sulphide mineral oxidation in context of the sphalerite leaching process at elevated temperatures and atmospheric pressure. It should be emphasized that it is unlikely that a single proposed mechanism would be sufficient to describe sphalerite leaching and that multiple mechanistic schemes may be proposed depending on the crystal face and oxidising conditions at the reactive surface. The proposed mechanistic views were therefore viewed in light of the scope of this work, comparable to conditions found in industrial processes.

Sulphide oxidation paths are embedded within the electrochemical nature of the mineral surface and bonding electrons of the metal-sulphide atoms. Each distinct crystalline face of natural sphalerite (under ideal conditions) has its own particular surface atom bonding strengths and packing, and thus will react in a unique fashion to a solution which it is in contact with. It was found that the expected reactivity of the different faces in order is (100) < (110) < (111), and was confirmed by scanning-electron microscope images by the formation of hillocks of partially leached particles. Since it is unnecessary (difficult) to model individual reactive surfaces it was assumed that the cleaved particle surfaces are randomly distrusted and assumed to have a constant average role in the overall dissolution kinetics. Deviation would only be reflected close to the point of complete dissolution.

Sphalerite is an extreme case of a semiconductor by having a wide band gap, in the range of 3.6 to 3.9 eV, and low rest potential, approximately 0.264 V, at standard temperature and pressure (STP) conditions (Crundwell, 1988b). Making it, in its purest form, a very stable compound; not easily leachable. The ability to leach sphalerite is therefore embedded within the electrochemical nature of the mineral. From the electron band theory, iron atoms create an impurity band within the band gap of zinc sulphide. This impurity band corresponds to redox potentials of oxidizing agents, *i.e.* ferric and oxygen. Although, direct oxidation of sphalerite by oxygen reduction corresponds well with the electron band theory, experiments conducted with a low iron head grade and overall iron content showed remarkably slower dissolution kinetics than that observed for sphalerite concentrates containing high iron content. It was concluded from literature studies that the surface binding energy of oxygen shows unfavourable adsorption characteristics on sphalerite. Oxygen reduction also involves a series of one electron transfer steps and from a thermodynamic perspective oxygen would be an ineffective oxidising agent, due to this mismatch of energy levels. It is concluded that the anodic dissolution reaction of sphalerite is coupled with the cathodic ferric redox reaction.

Sphalerite leaching is proposed to occur by either one the three first electron or proton transfer reaction (mechanisms), presented in Table 8.1.

Table 8.1: The first electron or proton transfer reaction of the sphalerite dissolution mechanisms

Mechanism	Reaction	Reference
1: Oxidative	$ZnS_{(s)} + 2h^{+} \Rightarrow Zn^{2+}_{(aq)} + \cdot S^{*}$	Gerischer and Mindt (1968)
2: Non-oxidative	$ZnS_{(s)} + H^{+} \Rightarrow Zn^{2+}_{(aq)} + HS^{-*}$	Crundwell (1988c, 2014a)
3: Oxidative	$ZnS_{(s)} + H^{+} + h^{+} \Rightarrow Zn^{2+}_{(aq)} + HS\cdot^{*}$	Steyl (2012)

*Where * denotes a site on the surface*

For mechanism 1 to occur, it is assumed that there is an excess supply of holes injected by ferric without the presence of an intermediary hydrogen ion interaction with sulphide, as illustrated by mechanism 3 in Table 5.3. Albeit, this is a superficial and vague assumption; and cannot be proven or explained by normal batch experiments. The strong interaction of the hydrogen ion and sulphide is illustrate (qualitatively) by the binding energies from literature (Steyl, 2012). Mechanism 3 can be seen as an intermediary mechanism as oxidative dissolution transforms to non-oxidative dissolution, and the first electron transfer step may become rate limiting. For the purpose of simplicity and difficulty associated with defining the region of this possible intermediary mechanism, the extreme limiting non-oxidative and oxidative cases are assumed to capture the pronounced sphalerite leaching behaviour.

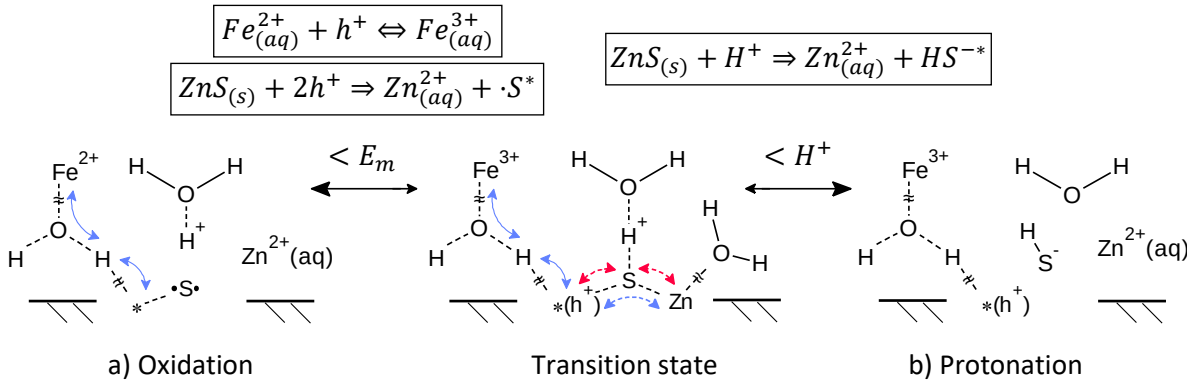

Figure 8.2: Schematic diagram of sphalerite leaching: a) oxidative & b) non-oxidative dissolution

Sphalerite dissolution within the scope of this study is divided into two mechanistic pathways termed *non-oxidative* and *oxidative*. Non-oxidative sphalerite leaching refers to the direct reaction with acid (protons), while oxidative leaching refers to sphalerite oxidation by ferric ions. These two reaction paths will capture the prominent characteristics of sphalerite leaching. Figure 8.2 depicts the oxidative and non-oxidative mechanism, with the first electron or proton

transfer step assumed to be the rate-limiting step. This model also assumes that the hydrogen ion prevents the direct adsorption of Fe^{3+} species on sulphide sites and presumes that electron transfer may occur *via* the relatively slow Grotthuss-type conduction mechanism at a high redox potential. Whilst at high acid concentrations the sulphide will undergo a protonation reaction.

The basic application of the mixed potential (MP) theory of metallic corrosion was then used to derive the intrinsic rate expression for the non-oxidative and oxidative dissolution of sphalerite, based on the assumption that the first electron transfer step is rate limiting. These rate expressions were then used to model the leaching behaviour of sphalerite.

The **third object** was to verify the rate expressions for the leaching of the sphalerite concentrate and to obtain the kinetic model parameters from the phenomenological batch experiments (performed by Dr Johan Steyl) by the way of regression. This objective was achieved, and the kinetic model was defined within the defined mathematical framework and scope of conditions.

The intrinsic mechanisms developed in Chapter 5 were investigated. It was found that the kinetic model (*i.e.* equation 5.63) derived in Chapter 5 was not be able to predict the behaviour of sphalerite leaching by acid. It was found that the reaction order with respect to acid (*i.e.* the hydrogen/proton) concentration is of the order 1.7, while the derived kinetic expression 5.63 could only attain a maximum reaction order of 1, with respect to the acid concentration. The mechanism was revised and it was concluded that the mechanism should include both hydrogen ions participating within the non-oxidative reaction. The revised mechanism followed that of the study of Crundwell (2014a,b), which resulted in the rate expression 7.12. This new rate model could accurately capture the leaching behaviour of sphalerite under non-oxidative conditions.

The oxidative mechanism and rate expression developed in Chapter 5 (*i.e.* equation 5.69) predicted the behaviour of sphalerite leaching under oxidative conditions. Oxidative leaching under surface reaction rate controlling regime have been accurately described/predicted by the rate model developed.

The experimental results were verified. It was found to have a repeatability error of 5 %. Initial rates of non-oxidative leaching showed retarded behaviour, which may have been the result of reaction activation, incomplete mixing, fine particles or diffusion limitations during those initial periods. Nevertheless, the initial data points were excluded from modelling due to the extensively slower kinetics and falling within the error bounds.

Oxidative leaching, however, had very fast initial rates which overshadowed the initial rate effects as observed during non-oxidative leaching. The initial rates were also linear and was used during kinetic modelling.

Particle size distribution and mean diameters followed the expected linear shrinking core model behaviour, that validated the use of the SCM. Lastly, the overall reaction stoichiometry as developed from the second objective compared to the experimental stoichiometry's obtained.

The batch experiments were used to confirm the reaction regimes. It was found that all the training and testing experiments used to develop the rate model, was controlled by the surface reaction mechanism. With the exceptions after usually 40 to 50 % of zinc leached, when the mechanism changed may have change to diffusion controlled due to passivating sulphur layers. However, this was limited by the surfactant (lignosulphonate) that dispersed the formed sulphur layers and prolonged the surface rate controlling regime.

In conclusion, quantification of the kinetic expressions for non-oxidative and oxidative leaching of sphalerite was performed. Kinetic constants were obtained, having acceptable accuracies. The overall reactions, kinetic model and rate constants are summarised below:

Non-Oxidative (protonation/acid attack) rate of sphalerite dissolution ($\frac{mol}{m^2 \cdot min}$):

Reaction $$ZnS + 2H^+_{(aq)} \Rightarrow Zn^{2+}_{(aq)} + H_2S$$

Rate $$r_{sph} = \frac{k_1 \cdot [H^+]^2}{([H^+]^2 + k_2 \cdot [Zn^{2+}])^{0.5}}$$

Constants $$k_1 = 0.004 \cdot \mathrm{e}^{-\frac{20000}{R_g}\left(\frac{1}{T}-\frac{1}{368.15}\right)} \qquad k_2 = 2700 \cdot \mathrm{e}^{-\frac{250000}{R_g}\left(\frac{1}{T}-\frac{1}{368.15}\right)}$$

Oxidative (by ferric) rate of sphalerite dissolution ($\frac{mol}{m^2 \cdot min}$):

Reaction $$ZnS + 2Fe^{3+}_{(aq)} \Rightarrow Zn^{2+}_{(aq)} + 2Fe^{2+}_{(aq)} + S^0_{(s)}$$

Rate $$r_{sph} = k_1 \left(\frac{[Fe^{3+}] + k_2[Zn^{2+}]}{1 + k_3[Fe^{2+}]}\right)^{0.5} - k_1 k_2 [Zn^{2+}] \left(\frac{[Fe^{3+}] + k_2[Zn^{2+}]}{1 + k_3[Fe^{2+}]}\right)^{-0.5}$$

Constants $$k_1 = 0.03 \cdot \mathrm{e}^{-\frac{50\,000}{R_g}\left(\frac{1}{T}-\frac{1}{368.15}\right)} \qquad k_2 = 0.2 \qquad k_2 = 0.07 \cdot \mathrm{e}^{\frac{250\,000}{R_g}\left(\frac{1}{T}-\frac{1}{368.15}\right)}$$

8.2.1 Kinetic Model Assumption Fault

It should be noted by all readers of the thesis that there was an assumption made during the derivation of the oxidative kinetic model which is wrong. It was assumed that the reverse oxidative reaction of Zn^{2+} reacting with S^0 to form ZnS (of equation 5.46) occurred. This is, however, not thermodynamically possible. Unfortunately, the reverse reaction was included in the activation polarisation equation 5.65, and hence lead to the derivation of a kinetic model which is not fundamentally sound and correct. Therefore, it is recommended to derive a new kinetic model excluding the reverse reaction.

8.3 Recommendations

From the results and conclusions, application of the proposed reaction mechanism and kinetic model for the leaching of sphalerite in iron-containing acidic solutions at atmospheric pressure and elevated temperatures (75 – 95 °C) is recommended as a model to predict the rate and extent of sphalerite dissolution. The accuracy of the model is limited to the same type of concentrate used and operation under surface reaction controlling regimes.

System thermodynamics

It should be highlighted that, despite the numerous studies and industrial application of iron-containing systems, there is a general poor understanding of the thermodynamics of these type of acid systems. The lack chemical data of ferric-ferrous acid solutions limits the extent to which predictive models can by developed and applied for industrial use. Even though it was attempted to include a speciation model, it is emphasized that this model is not very accurate and still lacks good predictive capabilities. To this end, it is recommended that further studies be conducted in extending the currently available thermodynamic data for the $Fe_2(SO_4)_3 – FeSO_4 – H_2SO_4 – H_2O$ system through experimental measurements.

Within this study precipitation of soluble metallic ions was not considered in detail. I would be advantageous to investigate the behaviour of soluble ferric/ferrous precipitation of a range of iron products under leaching conditions.

Mechanisms and kinetics

It was concluded from the mechanistic investigation that there may exist three first electron rate limiting steps and hence three mechanistic pathways. However, mechanism 3 was excluded from this research due to lack of information and nature of the batch experiments. It is recommended that further studies should give more detail on this mechanistic pathway, to

define the range of conditions under which this mechanism would be most prominent, as well as to develop a rate model and define the kinetic parameters. This would add to sphalerite leaching knowledge, rather than to assume only the non-oxidative and oxidative reaction mechanisms occurring as done in this study. As well as to perform a study where it is not assumed that non-oxidative and oxidative leaching occur independently, but to combine them into one model and develop one model for the leaching of sphalerite.

It is also recommended to investigate the sulphur products formed, under the different operating conditions. This would lead to further insights into the mechanistic of sphalerite.

References

Ahmed, M.M. & Ahmed, S.S. 2008. A Comparison Study to Determine the Mean of Particle Size Distribution for Truthful Characterization of Environmental Data (Part 1). *J. Eng. Sci., Assiut University*. 36(1):147–166.

Albion Process | Glencore Technology. 2016. [Online], Available: http://www.albionprocess.com [2016, September 08].

Albright, J.G., Rard, J.A., Serna, S., Summers, E.E. & Yang, M.C. 2000. Isopiestic determination of the osmotic and activity coefficients ofZnSO4(aq) atT = 298.15 K, and the standard potential of the electrochemical cell ZnHgx(two phase)| ZnSO4(aq)| PbSO4(s)| PbHgx(two phase). *The Journal of Chemical Thermodynamics*. 32(11):1447–1487.

Anderson, G.M., Castet, S., Schott, J. & Mesmer, R.E. 1991. The density model for estimation of thermodynamic parameters of reactions at high temperatures and pressures. *Geochimica et Cosmochimica Acta*. 55(7):1769–1779.

Archer, D.G. & Rard, J.A. 1998. Isopiestic Investigation of the Osmotic and Activity Coefficients of Aqueous MgSO4 and the Solubility of MgSO4·7H2O(cr) at 298.15 K: Thermodynamic Properties of the MgSO4 + H2O System to 440 K. *Journal of Chemical & Engineering Data*. 43(5):791–806.

Atkins, P. & Paula, J. de. 2013. *Elements of Physical Chemistry*. Oxford University Press.

Atmospheric Direct Leaching | Outotec. 2016. [Online], Available: http://www.outotec.com/en/About-us/Our-technologies/Leaching/Zinc-leaching/Application/Atmospheric-Direct-Leaching/ [2016, September 08].

Baes, C.F., Reardon, E.J. & Moyer, B.A. 1993. Ion interaction model applied to the cupric sulfate-sulfuric acid-water system at 25.degree.C. *The Journal of Physical Chemistry*. 97(47):12343–12348.

Baláž, P. 2000. *Extractive Metallurgy of Activated Minerals*. Elsevier.

Baláž, P. & Ebert, I. 1991. Oxidative leaching of mechanically activated sphalerite. *Hydrometallurgy*. 27(2):141–150.

Barthelmy, D. 1997. *Mineralogy Database*. [Online], Available: http://webmineral.com/ [2016, August 14].

Bea, S.A., Carrera, J., Ayora, C. & Batlle, F. 2010. Modeling of concentrated aqueous solutions: Efficient implementation of Pitzer equations in geochemical and reactive transport models. *Computers & Geosciences*. 36(4):526–538.

Bender, E.A. 2012. *An Introduction to Mathematical Modeling*. Courier Corporation.

Biegler, T. 1976. Oxygen reduction on sulphide minerals. *Journal of Electroanalytical Chemistry and Interfacial Electrochemistry*. 70(3):265–275.

Biley, C. 2015. Thermodynamic and kinetic modelling of iron (III) reduction with sulfur dioxide gas. PhD Dissertation. Stellenbosch University. [Online], Available: http://scholar.sun.ac.za/handle/10019.1/97120 [2016, August 01].

Blott, S.J. & Pye, K. 2001. GRADISTAT: a grain size distribution and statistics package for the analysis of unconsolidated sediments. *Earth Surface Processes and Landforms*. 26(11):1237–1248.

Bockris, J.O., Reddy, A.K.N., Gamboa-Aldeco, M. & Gamboa-Aldeco, M.E. 2000. *Modern Electrochemistry*. Springer Science & Business Media.

Bockris, J.O., Reddy, A.K.N. & Gamboa-Aldeco, M.E. 2001. *Modern Electrochemistry 2A: Fundamentals of Electrodics*. Springer Science & Business Media.

Bradley, D.J. & Pitzer, K.S. 1979. Thermodynamics of electrolytes. 12. Dielectric properties of water and Debye-Hueckel parameters to 350.degree.C and 1 kbar. *The Journal of Physical Chemistry*. 83(12):1599–1603.

Burkin, A.R. 2001. *Chemical hydrometallurgy: theory and principles*. London; River Edge, NJ: Imperial College Press; Distributed by World Scientific Pub. Co.

Chen, J. & Chen, Y. 2010. A first-principle study of the effect of vacancy defects and impurities on the adsorption of O2 on sphalerite surfaces. *Colloids and Surfaces A: Physicochemical and Engineering Aspects*. 363(1–3):56–63.

Clegg, S.L. & Brimblecombe, P. 1995. Application of a Multicomponent Thermodynamic Model to Activities and Thermal Properties of 0-40 mol kg-1 Aqueous Sulfuric Acid from <200 to 328 K. *Journal of Chemical & Engineering Data*. 40(1):43–64.

Clegg, S.L., Rard, J.A. & Pitzer, K.S. 1994. Thermodynamic properties of 0–6 mol kg–1 aqueous sulfuric acid from 273.15 to 328.15 K. *Journal of the Chemical Society, Faraday Transactions*. 90(13):1875–1894.

Crundwell, F.K. 1985. Kinetics of the leaching of sphalerite in acidic ferric sulphate media in the presence and absence of oxygen. Masters Degree. Witwatersrand.

Crundwell, F.K. 1988a. Effect of iron impurity in zinc sulfide concentrates on the rate of dissolution. *AIChE Journal*. 34(7):1128–1134.

Crundwell, F.K. 1988b. The influence of the electronic structure of solids on the anodic dissolution and leaching of semiconducting sulphide minerals. *Hydrometallurgy*. 21(2):155–190.

Crundwell, F.K. 1988c. The role of charge-transfer mechanisms in the oxidative and non-oxidative dissolution of Sphalerite. Thesis. University of the Witwatersrand.

Crundwell, F.K. 2014a. The mechanism of dissolution of minerals in acidic and alkaline solutions: Part I — A new theory of non-oxidation dissolution. *Hydrometallurgy*. 149:252–264.

Crundwell, F.K. 2014b. The mechanism of dissolution of minerals in acidic and alkaline solutions: Part III. Application to oxide, hydroxide and sulfide minerals. *Hydrometallurgy*. 149:71–81.

Crundwell, F.K. 2015. The mechanism of dissolution of minerals in acidic and alkaline solutions: Part IV equilibrium and near-equilibrium behaviour. *Hydrometallurgy*. 153:46–57.

Crundwell, F.K. & Verbaan, B. 1987. Kinetics and mechanisms of the non-oxidative dissolution of sphalerite (zinc sulphide). *Hydrometallurgy*. 17(3):369–384.

Dickson, A.G., Wesolowski, D.J., Palmer, D.A. & Mesmer, R.E. 1990. Dissociation constant of bisulfate ion in aqueous sodium chloride solutions to 250.degree.C. *The Journal of Physical Chemistry*. 94(20):7978–7985.

Diéguez, O. & Marzari, N. 2009. A first-principles characterization of the structure and electronic structure of alpha-S and Rh-S chalcogenides. *Physical Review B*. 80(21).

Dutrizac, J. e. 2010. Dissolution of Low Iron Sphalerite in Ferric Sulphate-Sulphuric Acid Media. *Canadian Metallurgical Quarterly*. 49(1):9–19.

Dutrizac, J.E. 2006. The dissolution of sphalerite in ferric sulfate media. *Metallurgical and Materials Transactions B*. 37(2):161–171.

Eigen, M. & Tamm, K. 1962a. Sound absorption in electrolyte solutions as a result of chemical relaxation I. Relaxationstheorie of multistage dissociation. *Zeitschrift für Elektrochemie, Berichte der Bunsengesellschaft für physikalische Chemie*. 66(2):93–107.

Eigen, M. & Tamm, U.K. 1962b. Sound absorption in electrolyte solutions as a result of chemical relaxation II. Measurements and relaxation mechanisms for 2-2 -valent electrolytes. *Zeitschrift für Elektrochemie, Berichte der Bunsengesellschaft für physikalische Chemie*. 66(2):107–121.

Epstein, B. 1947. The mathematical description of certain breakage mechanisms leading to the logarithmico-normal distribution. *Journal of the Franklin Institute*. 244(6):471–477.

European Commission. 2014. *Best Available Techniques (BAT) Reference Document for the Non-Ferrous Metal Industries*. (Draft 3). Joint research centre Institute for Prospective Technological Studies, Sustainable Production and Consuption Unit and the European IPPC Bureau.

Fan, L.-S. & Zhu, C. 1998. Size and Properties of Particles. In (Cambridge Series in Chemical Engineering). Cambridge University Press *Principles of Gas and Solid Flows*.

Farnsworth, M. & Kline, C.H. 1973. *Zinc Chemicals*. 1st edition ed. Zinc Institute.

Fogler, H.S. 2001. *Elements of Chemical Reaction Engineering Third (3rd) Edition*. CD NOT INCLUDED edition ed. Prentice Hall.

Friedman, H. 1996. *The Mineral and Gemstone Kingdom: Home*. [Online], Available: http://www.minerals.net/ [2016, August 14].

Fuls, H.F. & Petersen, J. 2013. Evaluation of processing options for the treatment of zinc sulphide concentrates at Skorpion Zinc. *Journal of the Southern African Institute of Mining and Metallurgy*. 113(5).

Gardner, P.J. & Pang, P. 1988. Thermodynamics of the zinc sulphide transformation, sphalerite → wurtzite, by modified entrainment. *Journal of the Chemical Society, Faraday Transactions 1: Physical Chemistry in Condensed Phases*. 84(6):1879–1887.

Gatos, H.C. 1960. *The Surface Chemistry of Metals and Semiconductors*. John Wiley & Sons.

Gerischer, H. & Mindt, W. 1968. The mechanisms of the decomposition of semiconductors by electrochemical oxidation and reduction. *Electrochimica Acta*. 13(6):1329–1341.

Gilat, A. & Subramaniam, V. 2011. *Numerical Methods with MATLAB*. Wiley.

Guendouzi, M.E., Mounir, A. & Dinane, A. 2003. Water activity, osmotic and activity coefficients of aqueous solutions of Li2SO4, Na2SO4, K2SO4, (NH4)2SO4, MgSO4, MnSO4, NiSO4, CuSO4, and ZnSO4 at T=298.15 K. *The Journal of Chemical Thermodynamics*. 35(2):209–220.

Guerra, E. & Bestetti, M. 2006. Physicochemical Properties of ZnSO4−H2SO4−H2O Electrolytes of Relevance to Zinc Electrowinning. *Journal of Chemical & Engineering Data*. 51(5):1491–1497.

Harmer, S.L., Thomas, J.E., Fornasiero, D. & Gerson, A.R. 2006. The evolution of surface layers formed during chalcopyrite leaching. *Geochimica et Cosmochimica Acta*. 70(17):4392–4402.

Harvey, D. 2015. *13B: Chemical Kinetics*. [Online], Available: http://chemwiki.ucdavis.edu/Analytical_Chemistry/Analytical_Chemistry_2.0/13_Kinetic_Methods/13B%3A_Chemical_Kinetics [2015, May 06].

Havlík, T. 2008. *Hydrometallurgy: principles and applications*. Cambridge; Boca Raton, FL: Cambridge International Science Pub. : Woodhead Pub.; CRC Press.

Hefter, G. 2006. When spectroscopy fails: The measurement of ion pairing. *Pure and Applied Chemistry*. 78(8):1571–1586.

Holmes, H.F. & Mesmer, R.E. 1983. Isopiestic studies of aqueous solutions at elevated temperatures VII. MgSO4 and NiSO4. *The Journal of Chemical Thermodynamics*. 15(8):709–719.

Holmes, H.F. & Mesmer, R.E. 1992. Isopiestic studies of H2SO4(aq) at elevated temperatures. *The Journal of Chemical Thermodynamics*. 24(3):317–328.

Holmes, P.R. & Crundwell, F.K. 2000. The kinetics of the oxidation of pyrite by ferric ions and dissolved oxygen: an electrochemical study. *Geochimica et Cosmochimica Acta*. 64(2):263–274.

Horne, R.A. & Axelrod, E.H. 1964. Proton Mobility and Electron Exchange in Aqueous Media. *The Journal of Chemical Physics*. 40(6):1518–1522.

Horváth, A.L. 1985. *Handbook of aqueous electrolyte solutions: physical properties, estimation, and correlation methods*. Ellis Horwood.

Hovey, J.K., Pitzer, K.S. & Rard, J.A. 1993. Thermodynamics of Na2SO4(aq) at temperatures T from 273 K to 373 K and of {(1-y)H2SO4+yNa2SO4}(aq) at T = 298.15 K. *The Journal of Chemical Thermodynamics*. 25(1):173–192.

International Zinc Association. 2011. *Zinc Production - From Ore to Metal*. [Online], Available: http://www.zinc.org/basics/zinc_production.

Jin, Z.-M., Warren, G.W. & Henein, H. 1985. Reaction mechanism for the ferric chloride leaching of sphalerite. *Metallurgical Transactions B*. 16(4):715–724.

Kammel, R., Pawlek, F., Simon, M. & Li, X.-M. 1987. Oxidizing leaching of sphalerite under atmospheric pressure. *Metall*. 41(2):158–161.

Kawulka, P., Haffenden, W.J. & Mackiw, V.N. 1975. *Patent No. US3867268 A*. [Online], Available: http://www.google.com/patents/US3867268 [2016, November 02].

Kertes, A.S., Fogg, P.G.T. & Young, C.L. 1988. Hydrogen sulfide in aqueous solvents. *IUPAC-NIST Solubility Data Series*. 32:25.

Klauber, C. 2008. A critical review of the surface chemistry of acidic ferric sulphate dissolution of chalcopyrite with regards to hindered dissolution. *International Journal of Mineral Processing*. 86(1–4):1–17.

Koryta, J., Dvorak, J. & Kavan, L. 1993. *Principles of Electrochemistry*. 2 edition ed. Chichester: Wiley.

Laidler, K.J. & King, M.C. 1983. Development of transition-state theory. *The Journal of Physical Chemistry*. 87(15):2657–2664.

Levenspiel, O. 1999. *Chemical reaction engineering*. Wiley.

Li, G., Zhang, Y., Asselin, E. & Li, Z. 2014. Vapor–Liquid Equilibria for the ZnSO4–H2SO4–H2O and MgSO4–H2SO4–H2O Systems at (30, 60, 90, and 101.3) kPa. *Journal of Chemical & Engineering Data*. 59(11):3449–3460.

Li, J., Zhong, T.-K. & Wadsworth, M.E. 1992. Application of mixed potential theory in hydrometallurgy. *Hydrometallurgy*. 29(1):47–60.

Liu, H. & Papangelakis, V.G. 2005a. Chemical modeling of high temperature aqueous processes. *Hydrometallurgy*. 79(1–2):48–61.

Liu, H. & Papangelakis, V.G. 2005b. Thermodynamic equilibrium of the O2–ZnSO4–H2SO4–H2O system from 25 to 250 °C. *Fluid Phase Equilibria*. 234(1–2):122–130.

Liu, H., Papangelakis, V. g., Alam, M. s. & Singh, G. 2003. Solubility of Hematite in H2SO4 Solutions at 230-270 °c. *Canadian Metallurgical Quarterly*. 42(2):199–207.

Lotens, J.P. & Wesker, E. 1987. The behaviour of sulphur in the oxidative leaching of sulphidic minerals. *Hydrometallurgy*. 18(1):39–54.

Marcus, R.A. 1964. Chemical and Electrochemical Electron-Transfer Theory. *Annual Review of Physical Chemistry*. 15(1):155–196.

Markus, H., Fugleberg, S., Valtakari, D., Salmi, T., Murzin, D.Y. & Lahtinen, M. 2004a. Kinetic modelling of a solid–liquid reaction: reduction of ferric iron to ferrous iron with zinc sulphide. *Chemical Engineering Science*. 59(4):919–930.

Markus, H., Fugleberg, S., Valtakari, D., Salmi, T., Murzin, D.Y. & Lahtinen, M. 2004b. Reduction of ferric to ferrous with sphalerite concentrate, kinetic modelling. *Hydrometallurgy*. 73(3–4):269–282.

Meyer, B. 1976. Elemental sulfur. *Chemical Reviews*. 76(3):367–388.

Miladinović, J., Todorović, M. & Ninković, R. 2002. Osmotic coefficient of the ZnSO4(aq) at T=298.15 K. *The Journal of Chemical Thermodynamics*. 34(11):1769–1776.

Missen, R.W., Missen, R.W., Mims, C.A. & Saville, B.A. 1999. *Introduction to chemical reaction engineering and kinetics*. Wiley.

Mottola, H.A. 1993. Kinetic determinations of reactants utilizing uncatalyzed reactions. *Analytica Chimica Acta*. 280(2):279–287.

Newman, J.S. & Thomas-Alyea, K.E. 2004. *Electrochemical systems*. Hoboken, N.J.: J. Wiley.

Norgate, T.E. & Rankin, W.J. 2002. An environmental assessment of lead and zinc production processes. In *Green Processing*. 177–184. [Online], Available: http://www.minerals.csiro.au/sd/CSIRO_Paper_LCA_PbZn.pdf.

Nørskov, J.K., Rossmeisl, J., Logadottir, A., Lindqvist, L., Kitchin, J.R., Bligaard, T. & Jónsson, H. 2004. Origin of the Overpotential for Oxygen Reduction at a Fuel-Cell Cathode. *The Journal of Physical Chemistry B*. 108(46):17886–17892.

Osseo-Asare, K. 1992. Semiconductor electrochemistry and hydrometallurgical dissolution processes. *Hydrometallurgy*. 29(1):61–90.

Owusu, G. 1993. The role of surfactants in the leaching of zinc sulphide minerals at temperatures above the melting point of sulphur. The university of British Columbia.

Pabst, W. & Gregorova, E. 2007. Characterization of particles and particle systems. *ICT Prague*. 2007.

Pardue, H.L. 1989. Kinetic aspects of analytical chemistry. *Analytica Chimica Acta*. 216:69–107.

Perez, I.P. & Dutrizac, J.E. 1991. The effect of the iron content of sphalerite on its rate of dissolution in ferric sulphate and ferric chloride media. *Hydrometallurgy*. 26(2):211–232.

Pitzer, K.S. Ed. 1991. *Activity coefficients in electrolyte solutions*. 2nd ed ed. Boca Raton: CRC Press.

Pitzer, K.S. 1972. Thermodynamic properties of aqueous solutions of bivalent sulphates. *Journal of the Chemical Society, Faraday Transactions 2: Molecular and Chemical Physics*. 68(0):101–113.

Pitzer, K.S. 1973. Thermodynamics of electrolytes. I. Theoretical basis and general equations. *The Journal of Physical Chemistry*. 77(2):268–277.

Pitzer, K.S., Roy, R.N. & Silvester, L.F. 1977. Thermodynamics of electrolytes. 7. Sulfuric acid. *Journal of the American Chemical Society*. 99(15):4930–4936.

Rard, J.A. 1997. Isopiestic determination of the osmotic and activity coefficients of {zH2SO4+(1−z) MgSO4}(aq) at the temperatureT=298.15 K. I. Results forz=(0.85811, 0.71539, and 0.57353). *The Journal of Chemical Thermodynamics*. 29(5):533–555.

Rard, J.A. & Clegg, S.L. 1999. Isopiestic determination of the osmotic and activity coefficients of {zH2SO4+ (1−z)MgSO4}(aq) atT= 298.15 K. II. Results forz= (0.43040, 0.28758, and 0.14399) and analysis with Pitzer's model. *The Journal of Chemical Thermodynamics*. 31(3):399–429.

Rawle, A. 2003. Basic of principles of particle-size analysis. *Surface coatings international journal*. 86(2):58–65.

Reardon, E.J. & Beckie, R.D. 1987. Modelling chemical equilibria of acid mine-drainage: The FeSO4-H2SO4-H2O system. *Geochimica et Cosmochimica Acta*. 51(9):2355–2368.

Rice, J.A. 2006. *Mathematical Statistics and Data Analysis*. Cengage Learning.

Richardson, J.F., Harker, J.H. & Backhurst, J.R. 2002. *Chemical Engineering Vol. 2*. 5th ed. Vol. 2. Estados Unidos: Butterworth-Heinemann.

Robinson, R.A. & Jones, R.S. 1936. The Activity Coefficients of Some Bivalent Metal Sulfates in Aqueous Solution from Vapor Pressure Measurements. *Journal of the American Chemical Society*. 58(6):959–961.

Robinson, R.A. & Stokes, R.H. 1959. *Electrolyte Solutions: The Measurement and Interpretation of Conductance, Chemical Potential and Diffusion in Solutions of Simple Electrolytes*. Butterworths Scientific Publications.

Romankiw, L.T. (Lubomyr T. 1962. Kinetics of dissolution of zinc sulfide in aqueous sulfuric acid. Thesis. Massachusetts Institute of Technology. [Online], Available: http://dspace.mit.edu/handle/1721.1/11442 [2016, May 13].

Rudolph, W.W. & Pye, C.C. 1999. Zinc(II) Hydration in Aqueous Solution: A Raman Spectroscopic Investigation and An ab initio Molecular Orbital Study of Zinc(II) Water Clusters. *Journal of Solution Chemistry*. 28(9):1045–1070.

Rudolph, W., Brooker, M.H. & Tremaine, P.R. 1997. Raman spectroscopic investigation of aqueous FeSO4 in neutral and acidic solutions from 25‡C to 303‡C: inner- and outer-sphere complexes. *Journal of Solution Chemistry*. 26(8):757–777.

Rudolph, W.W., Brooker, M.H. & Tremaine, P. 1999a. Raman- and Infrared Spectroscopic Investigation of Aqueous ZnSO4 Solutions from 8°C to 165°C: Inner- and Outer-Sphere Complexes. *Zeitschrift für Physikalische Chemie*. 209(Part_2):181–207.

Rudolph, W.W., Brooker, M.H. & Tremaine, P.R. 1999b. Raman Spectroscopy of Aqueous ZnSO4 Solutions under Hydrothermal Conditions: Solubility, Hydrolysis, and Sulfate Ion Pairing. *Journal of Solution Chemistry*. 28(5):621–630.

Rumpf, H. 2012. *Particle Technology*. Springer Science & Business Media.

Rumyantsev, A.V., Hagemann, S. & Moog, H.C. 2004. Isopiestic Investigation of the Systems Fe2(SO4)3–H2SO4–H2O, FeCl3–H2O, and Fe(III)–(Na, K, Mg, Ca)Cln–H2O at 298.15 K. *Zeitschrift für Physikalische Chemie/International journal of research in physical chemistry and chemical physics*. 218(9/2004):1089–1127.

Scatchard, G., Hamer, W.J. & Wood, S.E. 1938. Isotonic Solutions. I. The Chemical Potential of Water in Aqueous Solutions of Sodium Chloride, Potassium Chloride, Sulfuric Acid, Sucrose, Urea and Glycerol at 25°1. *Journal of the American Chemical Society*. 60(12):3061–3070.

Seidell, A. & Linke, W.F. 1940. *Solubilities of inorganic and metal organic compounds; a compilation of quantitative solubility data from the periodical literature,*. New York: D. Van Nostrand Company, Inc.

Shi, Z., Zhang, J., Liu, Z.-S., Wang, H. & Wilkinson, D.P. 2006. Current status of ab initio quantum chemistry study for oxygen electroreduction on fuel cell catalysts. *Electrochimica Acta*. 51(10):1905–1916.

Shock, E.L. & Helgeson, H.C. 1988. Calculation of the thermodynamic and transport properties of aqueous species at high pressures and temperatures: Correlation algorithms for ionic species and equation of state predictions to 5 kb and 1000°C. *Geochimica et Cosmochimica Acta*. 52(8):2009–2036.

Smith, F.G. 1955. Struckture of zinc sulphide minerals. *American Mineralogist*. 40:658–675.

Smith, J.M., Van Ness, H.C. & Abbott, M.M. 2005. *Introduction to chemical engineering thermodynamics*. 7th ed. McGraw-Hill international edition.

Snipes, H.P., Manly, C. & Ensor, D.D. 1975. Heats of dilution of aqueous electrolytes. Temperature dependence. *Journal of Chemical & Engineering Data*. 20(3):287–291.

Sobron, P., Rull, F., Sobron, F., Sanz, A., Medina, J. & Nielsen, C.J. 2007. Modeling the physico-chemistry of acid sulfate waters through Raman spectroscopy of the system FeSO4□H2SO4□H2O. *Journal of Raman Spectroscopy*. 38(9):1127–1132.

Steyl, J.D.T. 2009. Kinetic modelling of chemical processes in acid solution at t ≤ 200 C.(i) thermodynamics and speciation in H2SO4–Metal (II) SO4–H2O system. In *Hydrometallurgy Conference 2009*. 401–443. [Online], Available: http://www.saimm.co.za/Conferences/Hydro2009/401-444_Steyl.pdf [2016, July 31].

Steyl, J.D.T. 2012. Simulating the medium temperature chalcopyrite oxidation system in batch and continuous autoclaves. PhD Dissertation. Stellenbosch University. [Online], Available: http://oatd.org/oatd/record?record=handle%5C%3A10019.1%5C%2F71978 [2015, April 20].

Tartar, H.V., Newschwander, W.W. & Ness, A.T. 1941. 3A Thermodynamic Study of the System Zinc Sulfate—Sulfuric Acid—Water at 25°. *Journal of the American Chemical Society*. 63(1):28–36.

The Hudson Institute of Mineralogy. 1993. *Mineralogy Database - Mineral Collecting, Localities, Mineral Photos and Data*. [Online], Available: http://www.mindat.org/ [2016, August 14].

Tosca, N.J., Smirnov, A. & McLennan, S.M. 2007. Application of the Pitzer ion interaction model to isopiestic data for the Fe2(SO4)3–H2SO4–H2O system at 298.15 and 323.15 K. *Geochimica et Cosmochimica Acta*. 71(11):2680–2698.

Velázquez-Rivera, M., Palmer, D.A. & Kettler, R.M. 2006. Isopiestic Measurement of the Osmotic Coefficients of Aqueous {xH2SO4+ (1−x)Fe2(SO4)3} Solutions at 298.15 and 323.15 K. *Journal of Solution Chemistry*. 35(12):1699–1730.

Verbaan, B. 1977. A kinetic study of the dissolution of natural and synthetic sphalerite in aqueous sulphuric acid and in acidic ferric suplhate media. Thesis. [Online], Available: http://researchspace.ukzn.ac.za/xmlui/handle/10413/8658 [2015, August 19].

Vignes, A. 2011. *Extractive metallurgy*. London; Hoboken, N.J.: ISTE ; Wiley.

Wagman, D.D., Evans, W.H., Parker, V.B., Schumm, R.H., Halow, I., Balley, S.M., Churney, K.L. & Nuttal, R.L. 1982. *NBS Tables of Chemical Thermodynamic Properties: Selected Values for Inorganic and C1 and C2 Organic Substances in SI Units*. Washington, D.C.: American Chemical Society.

Wang, P., Springer, R.D., Anderko, A. & Young, R.D. 2004. Modeling phase equilibria and speciation in mixed-solvent electrolyte systems. *Fluid Phase Equilibria*. 222–223:11–17.

Wasserman, G. 2002. *Reliability Verification, Testing, and Analysis in Engineering Design*. CRC Press.

Weisener, C.G., Smart, R.S.C. & Gerson, A.R. 2004. A comparison of the kinetics and mechanism of acid leaching of sphalerite containing low and high concentrations of iron. *International Journal of Mineral Processing*. 74(1–4):239–249.

Wright, R.H. & Maass, O. 1932. The Solubility of Hydrogen Sulphide in Water from the Vapor Pressures of the Solutions. *Canadian Journal of Research*. 6(1):94–101.

Xie, K., YANG, X., WANG, J., YAN, J. & SHEN, Q. 2007. Kinetic study on pressure leaching of high iron sphalerite concentrate. *Transactions of Nonferrous Metals Society of China*. 17(1):187–194.

XU, Z., JIANG, Q. & WANG, C. 2013. Atmospheric oxygen-rich direct leaching behavior of zinc sulphide concentrate. *Transactions of Nonferrous Metals Society of China*. 23(12):3780–3787.

Yang, H., Zeng, D., Voigt, W., Hefter, G., Liu, S. & Chen, Q. 2014. Isopiestic Measurements on Aqueous Solutions of Heavy Metal Sulfates: MSO4 + H2O (M = Mn, Co, Ni, Cu, Zn). 1. T = 323.15 K. *Journal of Chemical & Engineering Data*. 59(1):97–102.

Yang, H., Zeng, D., Voigt, W., Chen, Y. & Zhou, Q. 2016. Isopiestic Measurements on Aqueous Solutions of Heavy Metal Sulfates: MSO4 + H2O (M = Mn, Co, Ni, Cu, Zn). 2. T = 373.15 K. *Journal of Chemical & Engineering Data*. 61(10):3406–3412.

Zemaitis, J.F., Clark, D.M., Rafal, M. & Scrivner, N.C. 1986. Activity Coefficients of Weak Electrolytes and Molecular Species. In John Wiley & Sons, Inc. *Handbook of Aqueous Electrolyte Thermodynamics*. 481–549. [Online], Available: http://onlinelibrary.wiley.com/doi/10.1002/9780470938416.ch7/summary [2016, June 05].

Zender, C. 2015. *Particle size distributions: Theory and Application to Aerosols, Clouds and Soils*. University of California, Irvine.

Software References:

Matlab Student version 9.0.0.341360. (Matlab, R2016a). The MathWorks Inc., Natick, MA.

Simulink Student version 8.7. (Simulink, R2016a). The MathWorks Inc., Natick, MA.

HSC Chemistry (*HSC*, 2006) Chemical Reaction and Equilibrium Software with Thermochemical Database, Outokumpu Research, Pori, Finland, Release 6.0.

Jmol: an open-source Java viewer for chemical structures in 3D. (*Jmol*, 2016). [Online], Available: http://www.jmol.org [2016, August 31].

Appendices

Appendix A Thermodynamics

A.1 Standard thermodynamic values

Table A.1 contains a list of standard heats of formation for the solution species applicable to this study. These values are standardized by the convention where the hydrated proton at infinite dilution has zero values and a total ionic concentration of 1 mol/L in the aqueous solution. Many of the values have significant variation in their reported values, which emphasizes the difficulties in measuring such quantities. Since the thermodynamic model used in this theses was primarily developed by Biley (2015), the literature data reported by him was selected for this study based on its ability to characterise the stability constants of interest and produce the best results under extrapolation.

Table A.1: Standard aqueous species heats of formation

Species	ΔG_f^0 (kJ/mol)	ΔH_f^0 (kJ/mol)	S^0 (J/mol.K)	C_p^0 (J/mol.K)	Reference
H^+	0	0	0	0	
Fe^{2+}	-78.9	-89.1	-137.7	0	Wagman et al. (1982)
Fe^{3+}	-17.23	-49.5	-277.4	-142.67	Liu et al. (2003)
$Fe(OH)_2^+$	-452.29	-559.78	2.4	-155.3	Liu et al. (2003)
$FeSO_4^+$	-785.44	-932.86	-91.2	41.75	Liu et al. (2003)
$Fe(SO_4)_2^-$	-1537.3	-1829.5	-4.57	0	Liu et al. (2003)
$FeSO_4^0$	-823.43	-998.3	-117.6	0	Wagman et al. (1982)
$H_2SO_4^0$	-683.07	-815.66	127.99	-279.9	Liu et al. (2003)
H_2O	-237.18	-285.85	69.96	75.35	Liu et al. (2003)
HSO_4^-	-755.76	-889.1	125.52	22.18	Liu et al. (2003); Shock and Helgeson (1988)
SO_4^{2-}	-744.46	-909.6	18.83	-269.37	Liu et al. (2003); Shock and Helgeson (1988)
Zn^{2+}	-147.25	-153.39	-109.62	-25.64	Wagman et al. (1982); Shock and Helgeson (1988)
$ZnSO_4^0$	-904.9	-1047.7	5	0	Wagman et al. (1982)
ZnS	-201.29	-205.98	57.7	46	Wagman et al. (1982)

A.2 Temperature extrapolation of complex stability constants

The standard thermodynamic properties of an equilibrium reaction are constituted from the sum of the primary components taking part in the reaction. Often, the partial molar properties of a species are known only at the reference temperature (T_r, usually 25 °C). The equilibrium constant can be calculated if the partial molar enthalpy of formation of the constituent species, or the standard molar enthalpy of the reaction is known as a function of temperature (or at the required temperature). The most basic relationship is known as the Van't Hoff equiation (Smith *et al.*, 2005), which is derived from classical thermodynamics:

$$\frac{d(\ln K)}{dT} = \frac{\Delta H^0}{RT^2} \qquad \text{A.1}$$

Usually assumptions are made to simplify Equation A.1 and would give only an estimate over a very short temperature range. Predictive methods have been developed to estimate the average heat capacity between T and T_r. Anderson et al. (1991) developed a significantly simpler model termed the *density function*, based on the apparent almost linear relationship between $\ln K$ and $\ln \rho$. The density function is remarkably accurate in estimating dissociation constants of reactions at higher temperatures when the molal heat of formation and heat capacity value is known at a reference temperature and adopts the following form:

$$\ln \beta_i\,(T) = \ln \beta_i\,(T_r) - \frac{\Delta H_i^0}{R}\left(\frac{1}{T} - \frac{T}{T_r}\right) + \frac{\Delta C_p^0}{RT_r\left(\frac{\partial \alpha_w}{\partial T}\right)_{P_r}}\left(\frac{1}{T}\ln\frac{\rho_{w,r}}{\rho_w} - \frac{\alpha_r}{T}(T - T_r)\right) \qquad \text{A.2}$$

The density (ρ_w) and coefficient of thermal expansion (α_w) of water are well documented, *e.g.* study of Anderson et al. (1991). In this study, water density function is adopted from Biley (2015) modelled from 25 °C up to 150 °C:

$$\rho_w = \frac{\Big(\Big(\big((p_1T + p_2)T + p_3\big)T + p_4\Big)T + p_5\Big)T + p_6}{1 + p_7T} \qquad \text{A.3}$$

where p_i = $[-2.8054253\text{x}10^{-10};\ 1.0556302\text{x}10^{-7};\ -4.6170461\text{x}10^{-5};\ -0.0079870401;\ 16.945176;\ 999.83952;\ 0.01687985]$ and T is in degrees Celsius. The thermal expansion of water, and its derivative, were calculated by a polynomial expansion fitted to the measured data of Anderson et al. (1991):

$$\alpha_w = 1.713185\text{x}10^{-10}\text{T}^3 - 5.528825\text{x}10^{-8}\text{T}^2 + 1.120729\text{x}10^{-5}\text{T} + 1.163333\text{x}10^{-5} \qquad \text{A.4}$$

$$\left(\frac{\partial \alpha_w}{\partial T}\right)_{P_r=1\ atm} = 5.986\text{x}10^{-10}\text{T}^2 - 1.300\text{x}10^{-7}\text{T} + 1.220\text{x}10^{-5} \qquad \text{A.5}$$

where T is in degrees Celsius. The goodness of fit over the range 25 – 150 °C of these polynomials is presented in Figure A.1.

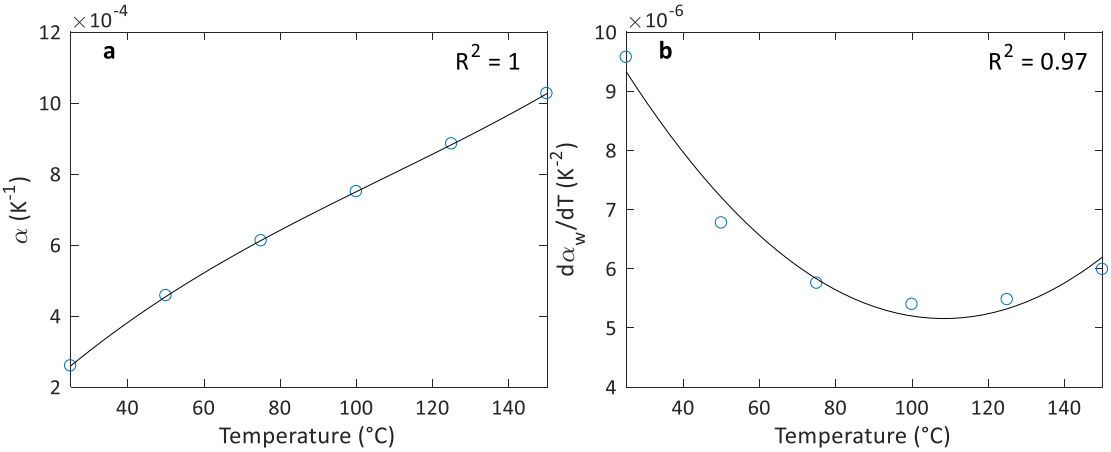

Figure A.1: Thermal expansion of water and its temperature derivative over 25 °C – 150 °C. Data points from Anderson et al. (1991), polynomial fit from equations A.4 and A.5 (black line).

The density function is coded in MATLAB named densityFunction.m, which receives the equilibrium constant, molal heat of formation and heat capacity as input and calculates the equilibrium (dissociation) constant at the desired temperature (< 100 °C).

A.3 Speciation model computational details, parameters and structure

A.3.1 Reaction extent (speciation) model computational methodology

The calculation of solution speciation per each species thermodynamic equilibrium constant (or stability constants) and activity involves a set of non-linear mass action equations (reactions). The following procedure was developed, from the basis of Smith et al. (2005, chap. 13), to solve the solution speciation equations (*i.e.* chemical reaction equilibria). This procedure is summaries in Figure A.2. From the definition of minimisation of Gibbs-free energy change the equilibrium constant of an aqueous reactions adopts the following form:

$$K_j\ (or\ \beta_j) = \prod_{i=1}^{n} a_i^{v_{ij}} = \prod_{i=1}^{n} m_i^{v_{ij}} \gamma_i^{v_{ij}} \qquad \text{A.6}$$

where j refers to the specific reaction with the equilibrium constant K_j and i refers to a species within the system with activity (a_i), molality (m_i) and activity coefficient (γ_i). The stoichiometric coefficient, v_{ij}, refers to the stoichiometry of reaction j of species i. When the equilibrium state in a reacting system depends on two or more independent chemical reactions, the equilibrium

composition can be found by a defining an extent (ξ_j) of each reaction and extending the equilibrium calculation method of a single reaction to the set of reactions. Firstly, the equilibrium (or intermediate) molality of a species is calculated as follows:

$$m_i = m_i^0 + \sum_{n=1}^{N} v_{in}\xi_n \qquad \text{A.7}$$

The initial molal concentration of species i is denoted as m_i^0 and the molality of each specie (m_i) is calculated from the sum of the change over all reactions (N). Now, for reaction j with equilibrium constant K_j, the extent can be excluded from the summation and a new fractional molality ($\tilde{m}_i$) defined as:

$$m_i = m_i^0 + \sum_{n=1,\ n\neq j}^{N} v_{in}\xi_n + v_{ij}\xi_j = \tilde{m}_i + v_{ij}\xi_j \qquad \text{A.8}$$

$$\tilde{m}_i = m_i^0 + \sum_{n=1,\ n\neq j}^{N} v_{in}\xi_n \qquad \text{A.9}$$

Substituting equation A.8 into equation A.6 and be rearrange to give:

$$\prod_{i=1}^{n}\left(\tilde{m}_i + v_{ij}\xi_j\right)^{v_{ij}} = \frac{K_j}{\Gamma_j} \qquad \text{A.10}$$

Here, Γ_j is the product of activity coefficients of reaction j, obtained from the Pitzer model that is a function of all species' molalities and temperature (see appendix A.4.1):

$$\Gamma_j = \prod_{i=1}^{n} \gamma_i^{v_{ij}} \qquad \text{A.11}$$

$$\gamma_i = f^{pitzer}(m_i, T) \qquad \text{A.12}$$

With all the other reaction extents values being ξ_n, a new extent for reaction j can be calculate by expanding equation A.10 into a polynomial and solving for the roots, to equate the equilibria of reaction j having a constant K_j. The *roots* function in MATLAB (2016b) was used to calculate the roots of each reactions polynomial expansion. Each root of a polynomial expansion must be validated by removing roots that has imaginary parts or when substituted back into equation A.7 make a concentration value less than zero (which against conservation principles).

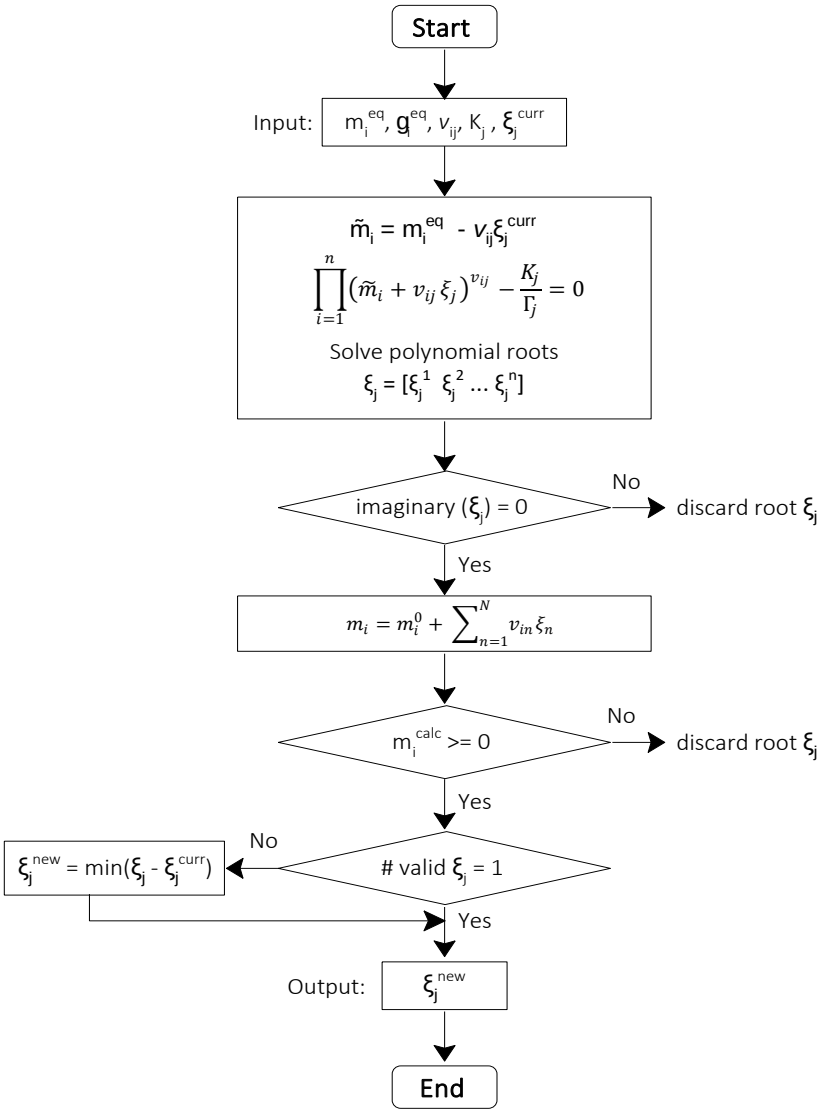

Figure A.2: Extent function calculation methodology flow diagram

A.3.2 Thermodynamic values of the speciation reactions

The thermodynamic data presented in this section is gathered from Biley (2015), to model the complex CIP equilibrium formations. Table A.2 provides each speciation reaction considered within this research and its corresponding thermodynamic model and parameters.

Table A.2: Speciation reactions equilibrium constant model and parameter values

Equilibria 1					
Reaction	$H^+ + SO_4^{2-} \rightleftharpoons HSO_4^-$				
Equilibrium Equation	$\log_{10} K = p_1 + \frac{p_2}{T} + p_3 lnT + p_4 T + p_5 T^2$				
	p_1	p_2	p_3	p_4	p_5
	562.7097	-13273.75	-102.5154	0.2477538	-1.117033E-04

Table A.2: Speciation reactions equilibrium constant model and parameter values (continue)

Equilibria 2			
Reaction	$Zn^{2+} + SO_4^{2-} \rightleftharpoons ZnSO_4^0$		
Equilibrium Equation	$K = densityFunction(\log_{10}\beta^0, \Delta H^0, \Delta C_p^0)$		
	$\log_{10}\beta^0$	ΔH^0	ΔC_p^0
	1.5	10000	250
Equilibria 3			
Reaction	$Fe^{2+} + SO_4^{2-} \rightleftharpoons FeSO_4^0$		
Equilibrium Equation	$K = densityFunction(\log_{10}\beta^0, \Delta H^0, \Delta C_p^0)$		
	$\log_{10}\beta^0$	ΔH^0	ΔC_p^0
	1.5	15000	376.58
Equilibria 4			
Reaction	$Fe^{3+} + SO_4^{2-} \rightleftharpoons FeSO_4^+$		
Equilibrium Equation	$K = densityFunction(\log_{10}\beta^0, \Delta H^0, \Delta C_p^0)$		
	$\log_{10}\beta^0$	ΔH^0	ΔC_p^0
	4.04	26110	394.4
Equilibria 5			
Reaction	$Fe^{3+} + 2SO_4^{2-} \rightleftharpoons Fe(SO_4)_2^-$		
Equilibrium Equation	$K = densityFunction(\log_{10}\beta^0, \Delta H^0, \Delta C_p^0)$		
	$\log_{10}\beta^0$	ΔH^0	ΔC_p^0
	5.38	38872	781.625
Equilibria 6			
Reaction	$Fe^{3+} + 2H_2O \rightleftharpoons Fe(OH)_2^+ + 2H^+$		
Equilibrium Equation	$K = densityFunction(\log_{10}\beta^0, \Delta H^0, \Delta C_p^0)$		
	$\log_{10}\beta^0$	ΔH^0	ΔC_p^0
	-1.23669	15325.8	0

A.4 Pitzer's Model

A.4.1 Pitzer model equations

In a series of papers, Pitzer extended electrolyte theory by combining insights from fundamental theory with a clear focus on model simplicity and empirical effectiveness. The Pitzer model is a flexible, semi-empirical model which could be applied to systems having a wide range of species, concentrations and temperatures. However, the model can become very complex with increasing systems and sub-systems included into the model. A significant advantage of the Pitzer mode over other simpler models is the direct calculation of the osmotic coefficient and hence water activity from the model parameters. The model has become a standard means of correlating experimental data and has been applied to systems to characterise speciation. The standard Pitzer ion-interaction model is based on an expression for the excess Gibbs energy of the solution, which consists of an extended Debye-Hückel (DH) term and virial expansion terms (see equation 2.18). This sections aim to describe the Pitzer model equations to calculate the activity and osmotic coefficients directly by substitution of the virial expansion terms and model parameters (equation 2.18) into the definition of the osmotic (equation 2.16) and activity (equation 2.17) coefficients. Only the virial expansion terms applicable to this study (*i.e.* the binary (B_{ca}) and ternary (C_{ca}) virial coefficients) are given. The single-ion activity coefficient of a cation (M), anion (X) and neutral ion (N) may respectively be represented as:

$$\ln \gamma_M = z_M^2 F + \sum_a m_a (2B_{Ma} + ZC_{Ma}) + z_M \sum_c \sum_a m_c m_a C_{ac} + 2 \sum_n m_n \lambda_{Mn} \qquad \text{A.13}$$

$$\ln \gamma_X = z_X^2 F + \sum_c m_c (2B_{cX} + ZC_{cX}) + |z_X| \sum_c \sum_a m_c m_a C_{ac} + 2 \sum_n m_n \lambda_{Xn} \qquad \text{A.14}$$

$$\ln \gamma_N = 2 \sum_c m_c \lambda_{Nc} + 2 \sum_a m_a \lambda_{Na} \qquad \text{A.15}$$

The osmotic coefficient, also a function of the water activity equation 2.15, may be written as:

$$\phi - 1 = \frac{2}{\sum_i m_i} [f^\phi I + \sum_c \sum_a m_c m_a \left(B_{ca}^\phi + ZC_{Ma}\right) + \sum_n \sum_c m_n m_c \lambda_{nc} + \sum_n \sum_a m_n m_a \lambda_{na} \qquad \text{A.16}$$

The subscript i covers all species in the solution, while a, c and n refers to the anodic, cathodic and neutral species, respectively, and refers to summation over all distinguishable ion pairs. The ancillary functions are defined in equation A.17.

$$F = f^{\gamma} + \sum_{c}\sum_{a} m_c m_a B'_{ca} \qquad \text{A.17}$$

The ionic strength (I) dependence of the DH terms may be represented as follows:

$$I = 0.5\sum_{i} m_i z_i^2 \qquad \text{A.18}$$

$$f^{\phi} = -\frac{A_{\phi} I^{\frac{1}{2}}}{1 + bI^{\frac{1}{2}}} = f^{\gamma} + \left(\frac{2A_{\phi}}{b}\right)\ln\left(1 + bI^{\frac{3}{2}}\right) \qquad \text{A.19}$$

where z_i is the charge of ion i and the empirical parameter b is equal to 1.2 (kg/mol)$^{1/2}$. A_{ϕ} is the usual Debye-Hückel parameter (0.39145 kg$^{0.5}$.mol$^{-0.5}$ at 25 °C and standard conditions) for the osmotic coefficient and was calculated from a simplified fitted equation to the dielectric properties of pure water reported by Bradley & Pitzer (1979):

$$A_{\phi} = 5.81758 \times 10^{-10}T^3 + 4.22852 \times 10^{-6}T^2 + 5.071328 \times 10^{-4}\mathrm{T} + 0.37638 \qquad \text{A.20}$$

where T is in °C. The binary (B_{ca}), the binary derivative (B'_{ca}) and ternary (C_{ca}) virial coefficients are expressed in terms of their respective interactions parameters, *i.e.* β_{ca} and C^{ϕ}_{ca}, and ionic strength functions:

$$B_{ac} = \beta^{(0)}_{ca} + \beta^{(1)}_{ca} \cdot g\left(\alpha_1 I^{\frac{1}{2}}\right) + \beta^{(2)}_{ca} \cdot g\left(\alpha_2 I^{\frac{1}{2}}\right) \qquad \text{A.21}$$

$$B'_{ac} = \left[\beta^{(1)}_{ca} \cdot g'\left(\alpha_1 I^{\frac{1}{2}}\right) + \beta^{(2)}_{ca} \cdot g'\left(\alpha_2 I^{\frac{1}{2}}\right)\right]/I \qquad \text{A.22}$$

$$B^{\phi}_{ac} = \beta^{(0)}_{ca} + \beta^{(1)}_{ca} \cdot \exp\left(-\alpha_1 I^{\frac{1}{2}}\right) + \beta^{(2)}_{ca} \cdot \exp\left(-\alpha_2 I^{\frac{1}{2}}\right) \qquad \text{A.23}$$

$$C_{ca} = \frac{C^{\phi}_{ca}}{2|z_c z_a|^{\frac{1}{2}}} \qquad \text{A.24}$$

The values of parameters α_1 and α_2 are usually set to 1.4 and 12 (kg/mol)$^{1/2}$, respectively, for 2-2 electrolytes, however for all other types of interactions the values are set to 2 and 0 (Pitzer, 1973, 1991). The $g(x)$ and $g'(x)$ functions may be represented as follows:

$$g(x) = 2[1 - (1 + x)\exp(-x)]/x^2 \qquad \text{A.25}$$

$$g'(x) = -2[1 - (1 + x + x^2/2\,)\exp(-x)]/x^2 \quad \text{A.26}$$

The mean activity coefficient and ionic strength (Z) are calculated as follows:

$$\gamma_{\pm} = (\gamma_M^{v+} \cdot \gamma_X^{v-})^{\frac{1}{v+ + v-}} \quad \text{A.27}$$

$$Z = 0.5 \sum_i m_i |z_i| \quad \text{A.28}$$

A.4.2 Pitzer model parameters

Optimised speciation model parameters as detailed in Chapter 4.

Table A.3: Pizter model cation-anion interaction parameters

Parameter	p_0			$10^3 \cdot p_1$		
Species	SO_4^{2-}	HSO_4^-	$Fe(SO_4)_2^-$	SO_4^{2-}	HSO_4^-	$Fe(SO_4)_2^-$
			$\beta_{ca}^{(0)}$			
H^+	0.028578	0.22109	0	-1.0244	-0.30535	0
Zn^{2+}	0.25383	0.2606	0	1.9	0.121	0
Fe^{2+}	0.18995	0.269	0	-2.8774	0	0
Fe^{3+}	1.0962	0.43885	1.23151	4.0438	0.25266	9.2555
			$\beta_{ca}^{(1)}$			
H^+	0.20502	0.48515	0	-8.0561	-1.7541	0
Zn^{2+}	2.19312	2.0949	0	4.558	13.823	0
Fe^{2+}	3.4302	0.98649	0	24.564	0	0
Fe^{3+}	6.2122	0	0	-6.3897	0	0
			$\beta_{ca}^{(2)}$			
H^+	0	0	0	0	0	0
Zn^{2+}	-29.2634	0	0	-73.2641	0	0
Fe^{2+}	-32	0	0	0	0	0
Fe^{3+}	0	0	0	0	0	0
			C_{ca}^{ϕ}			
H^+	0	0	0	0	0	0
Zn^{2+}	0	0.27526	0	0	0	0
Fe^{2+}	0.075016	0.27526	0	1.4889	0	0
Fe^{3+}	-0.18496	0	0	1.7195	0	0

Table A.3: Pitzer model normal-anion and normal-cation species interaction parameters

Parameter	p_0		$10^3 \cdot p_1$	
Species	ZnSO4	FeSO4	ZnSO4	FeSO4
		λ_{na}		
SO_4^{2-}	-0.10795	0	-4.88	0
HSO_4^-	0	0	0	0
$Fe(SO_4)_2^-$	0	0	0	0
		λ_{nc}		
H^+	-0.04248	-0.04249	0	0
Zn^{2+}	0.035811	0	-1.3943	0
Fe^{2+}	0	0.035811	0	-0.17928
Fe^{3+}	0	0	0	0

Appendix B Model Derivations

B.1 Derivation of the batch reactor model

Discussions within this thesis imply that a sulphide mineral particle shrinks as a result of the electrochemical oxidation reaction. The unreacted shrinking core model dictates that a boundary at the surface of the uncreated core forms and moves towards the centre of a particle as zinc gets extracted and a layer of impervious product (*i.e.* elemental sulphur) forms on the unreacted core. Details on the shrinking core model are presented in section 2.4.2. These models rely on the assumption that the oxidation reaction occurs at a sharp interface between the surface of the unreacted sulphide mineral and the solution. This is known as topochemical kinetics and is in line with the above discussions, which assume that the charge transfer reaction occurs across the Helmholtz double layer.

This section focusses on deriving a differential for the batch reactor behaviour. Attention is first given to the leaching behaviour of an individual sulphide mineral particle, without recognition of the solution phase. If no mass transfer effect of the reagent or products is present, the following description of the kinetics may be performed. The rate of leaching (mol/min) of a sulphide mineral particle is defined as:

$$-\frac{dn_{sph}}{dt} = R_{sph} = A_p\left(r_{sph}\right) \tag{B.1}$$

In equation B.1, n_{sph} is the amount of moles of sphalerite in the particle, t is the time, R_{sph} is the rate of sphalerite dissolution in mol/min, A_p is the area a particle and r_{sph} is the intrinsic reaction rate with the units of $\frac{mol}{m^2 \cdot min}$, as derived in Chapter 5. The following two equations give the relationship between the area and particle size, and the volume and particle size of the unreacted sulphide mineral, respectively:

$$A_p = \phi_a \cdot 4\pi(r_t^2) \tag{B.2}$$

$$V_p = \phi_v \cdot \frac{4}{3}\pi(r_t^3) \tag{B.3}$$

where ϕ_a is the area shape factor and ϕ_v is the volume shape factor (*i.e.* for a perfect sphere these parameters would have a value of one), and r_t is the particle's radius at time t. It is customary to assume that these shape factors are independent of the size, *i.e.*, the unreacted particle or particle core maintains its shape as it shrinks.

From equation B.3, it can also be shown that the extent sphalerite leached (X) is related to the initial particle size (r_0) and particle size (r_t) at time t, as follows:

$$\frac{V_{p,t}}{V_{p,0}} = (1 - X_t) = \frac{r_t^3}{r_0^3} \qquad \text{B.4}$$

Combining equations B.1 to B.4, and rearranging, then yields the following relationship:

$$\frac{dX}{dt} = \frac{\phi_a}{\phi_v} \cdot \frac{3M_{w,sph}}{(1000)\rho_{sph} \cdot r_0} \cdot (1 - X)^{\frac{2}{3}} \cdot (r_{sph}) \qquad \text{B.5}$$

Where X is the fractional extent of sphalerite leached from the particle, $M_{w,sph}$ is the molecular weight of sphalerite (g/mol), ρ_{sph} is the density of sphalerite in kg/m^3 and r_0 is the initial particle size. This differential model assumed that the density and molecular weight of the particle remains constant throughout the reaction period.

Integration of equation B.5 leads to the well-known shrink core model equation, as described in the literature (section 2.4.2), and show as follows:

$$1 - (1 - X)^{\frac{1}{3}} = \frac{\phi_a}{\phi_v} \cdot \frac{3M_{w,sph}}{(1000)\rho_{sph} \cdot r_0} \cdot (r_{sph}) \cdot t \qquad \text{B.6}$$

Equation B.6 clearly illustrates that the rate of shrinking of an unreacted sulphide mineral particle under surface controlled regime, *i.e.*, intrinsic kinetics (no diffusion), is dependent on the particles initial size. This expression defines the behaviour of a sphalerite particle leaching. If the shape of the particles is maintained for most of the dissolution process, the linear rate constant (k_l) is defined as:

$$k_l = \frac{\phi_a}{\phi_v} \cdot \frac{3M_{w,sph}}{(1000)\rho_{sph}} \cdot (r_{sph}) \qquad \text{B.7}$$

B.2 Semi-fundamental non-oxidative rate model

After considering the experimental results it was found that assuming the first electron transfer step to be rate limiting, add the derived intrinsic rate model, would not be able to predict the leaching behaviour of sphalerite. The leaching mechanism was therefore re-evaluated and it was decided to include both protons participating during the non-oxidative leaching reaction in the rate limiting step of the mechanism. The reasoning is that both protons, must transfer across the polarized (charge) barrier, and hence both protons would be transfer rate limited over this barrier. Derivation of the new reaction rate is explained in the following section.

Revised half-reactions, *viz.* anodic (reaction B.8) and cathodic (reaction B.10), are proposed with the main difference being the simultaneous participation of two protons (*i.e.* the combined first and second protonation reactions) during the dissolution of sulphide atoms from the lattice. Removal of the zinc atom and formation of the zinc ion is given by the following expression:

$$Zn^{2+}_{|lat} + wH_2O + 2h^+ \rightleftharpoons Zn(H_2O)^x_w \qquad \text{B.8}$$

where $Zn^{2+}_{|lat}$ represents the zinc atom in a lattice position on the surface, w represents the stoichiometric coefficient with respect to water, which holds the zinc ion in solution. The anodic current density, due to direct reaction with the hydrogen ion may be represented as follows:

$$i_A = F \cdot k_{a_1} \cdot [H_2O]^w \cdot \Psi_{Zn^{2+}_{|lat}} \cdot \exp\left(\frac{\beta_A F \Delta\phi}{RT}\right) - F \cdot k_{c1} \cdot [Zn^{2+}] \cdot \exp\left(\frac{-(1-\beta_A) F \Delta\phi}{RT}\right) \qquad \text{B.9}$$

The dissolution of sulphide atoms from the lattice may occur by the reacting with two protons, expressed in the following protonation reaction:

$$S^{2-}_{|lat} + 2H^+ \rightleftharpoons H_2S^* + 2h^+ \qquad \text{B.10}$$

where $S^{2+}_{|lat}$ represents the sulphide atom in a lattice position on the surface. It was observed from batch experimentation that the reaction rate is independent of the H_2S concentration (section 7.4.2), hence the H_2S concentration terms can be excluded from the current density rate model. The cathodic current density, due to the removal of sulphur atom on the surface and the formation of hydrogen sulphide ion, is given by the following rate expression:

$$i_C = -F \cdot k_{c2} \cdot [H^+]^2 \cdot \Psi_{S^{2-}_{|lat}} \cdot \exp\left(\frac{-(1-\beta_C) F \Delta\phi}{RT}\right) \qquad \text{B.11}$$

Application of the mixed potential (MP) theory and using equations B.9 and B.11, similar to the derivation in Section 5.5.2, the

$$R_{sph} = A_p \cdot \frac{k_1 \cdot [H^+]^2}{([H^+]^2 + k_2 \cdot [Zn^{2+}])^{0.5}} \qquad \text{B.12}$$

where $k_1 = \left(k_{a_1} k_{c_2}\right)^{0.5}$, $k_2 = k_{c_1}/k_{c_2}$ and A_p refers to the surface area available for reaction.

Appendix C Non-Oxidative Experimental Results

C.1 Summary of experimental conditions and kinetic constants

Table C.1: Initial conditions of the non-oxidative batch experiments

Experiment	Temperature (°C)	Impeller Speed (rpm)	Slurry Density (g/L)	LS (g/L)	Sparging	$[H_2SO_4]_0$ (g/L)	$[Zn^{2+}]_0$ (g/L)	$[Fe^{2+}]_0$ (g/L)
Ca1	75	650	0.016	0	O_2	127.3	0	0
Ca2	75	650	0.008	0	O_2	127.2	0	0
Ca3	75	650	0.044	0	No	127.1	0	0
Ca4	75	650	0.036	0	1 % H_2S	127.2	0	0
Ca5	75	650	0.024	0	100 % H_2S	127.1	0	0
Cb1	85	650	0.008	0	O_2	127.0	0	0
Cb2	85	650	0.027	0	No	127.2	0	0
Cb3	85	650	0.024	0	1 % H_2S	127.1	0	0
Cb4	85	650	0.024	0	100 % H_2S	127.3	0	0
Cc1	95	650	0.024	0	No	127.2	0	0
Cc2	95	650	0.024	0	1 % H_2S	127.0	0	0
Cc3	95	650	0.024	0	100 % H_2S	127.2	0	0
Cd1	95	650	0.351	0	No	9.7	0	0
Cd2	95	650	0.054	0	1 % H_2S	9.6	0	0
Cd3	95	650	0.045	0	100 % H_2S	9.8	0	0
Ce1	75	650	0.061	0	No	49.3	0	0
Ce2	85	650	0.070	0	No	48.8	0	0
Ce3	95	650	0.044	0	No	48.7	0	0
Cf1	75	650	0.044	0	No	88.1	0	0
Cf2	85	650	0.036	0	No	88.2	0	0
Cf3	95	650	0.026	0	No	88.1	0	0
Cg1	95	650	0.025	0.001	No	127.1	0	0
Cg2	95	650	0.025	0.01	No	127.0	0	0
Cg3	95	650	0.025	0.1	No	127.3	0	0
Cg4	95	650	0.025	1	No	127.4	0	0
Ch1	85	200	0.079	0	No	48.7	0	0
Ch2	85	400	0.079	0	No	48.6	0	0
Ci1	95	650	0.150	0	No	88.0	0	0
Ci2	95	650	1.500	0	No	88.2	0	0
Ci3	95	650	15.000	0	No	88.1	0	0
Cj1	95	650	1.500	0	Slow N_2	88.0	0	16.75
Cj2	95	650	1.500	0	Slow N_2	88.1	0	33.51
Cj3	95	650	1.500	0	Slow N_2	88.1	0	55.85
Ck1	95	650	1.500	0	No	88.1	0.048	0
Cl1	95	500	0.150	0	O_2 (500 kPaG)	88.2	0	0

The batch experiments in Table C.1 where performed with concentrate Sf3 (45-53 µm) as feed concentrate and under atmospheric pressure (except for test Cl1, under 500 kPa gauge).

Table C.2: Experimentally obtained intrinsic rate constants within the respective evaluation ranges and corresponding average solution concentrations

Experiment	Evaluation Range		Intrinsic rate constants		Average Concentrations	
	Extent (fraction)	Time (min)	k_s (1/min)	k_l (µm/min)	[H_2SO_4] (g/L)	[Zn^{2+}] (ppm)
Ca1	0.30	145	8.14E-04	0.0260	127.4	1.21
Ca2	0.30	134	9.18E-04	0.0293	127.4	0.66
Ca3	0.49	180	1.13E-03	0.0361	127.3	5.93
Ca4	0.42	180	9.42E-04	0.0301	127.5	4.16
Ca5	0.57	180	1.36E-03	0.0435	127.4	3.79
Cb1	0.80	157	2.61E-03	0.0835	127.2	1.56
Cb2	0.80	162	2.54E-03	0.0811	127.3	4.96
Cb3	0.80	164	2.53E-03	0.0807	127.4	4.45
Cb4	0.80	160	2.55E-03	0.0814	127.5	4.49
Cc1	0.80	89	4.54E-03	0.1451	127.3	4.19
Cc2	0.80	83	4.70E-03	0.1501	127.2	4.29
Cc3	0.80	85	4.48E-03	0.1430	127.4	4.23
Cd1	0.04	180	6.56E-05	0.0021	9.9	3.38
Cd2	0.03	180	5.40E-05	0.0017	9.9	0.41
Cd3	0.10	180	1.84E-04	0.0059	10.1	1.18
Ce1	0.11	180	2.11E-04	0.0067	49.4	1.82
Ce2	0.24	180	4.87E-04	0.0156	49.0	4.58
Ce3	0.49	180	1.14E-03	0.0364	49.0	5.94
Cf1	0.22	180	4.34E-04	0.0139	88.2	2.62
Cf2	0.57	180	1.38E-03	0.0440	88.3	5.65
Cf3	0.80	151	2.76E-03	0.0882	88.4	5.20
Cg1	0.80	98	4.19E-03	0.1338	127.3	5.29
Cg2	0.80	199	2.10E-03	0.0672	127.3	5.23
Cg3	0.25	91	1.08E-03	0.0344	127.4	1.70
Cg4	0.26	180	5.35E-04	0.0171	127.6	1.81
Ch1	0.01	15	2.28E-04	0.0073	49.0	0.22
Ch2	0.02	15	4.92E-04	0.0157	49.0	0.50
Ci1	0.67	160	1.90E-03	0.0606	88.3	27.65
Ci2	0.47	160	1.22E-03	0.0390	88.5	191.50
Ci3	0.19	160	4.77E-04	0.0152	88.4	797.50
Cj1	0.10	31	1.26E-03	0.0404	88.0	40.50
Cj2	0.10	50	9.26E-04	0.0296	88.2	31.25
Cj3	0.10	42	7.61E-04	0.0243	88.2	25.00
Ck1	0.41	180	9.21E-04	0.0294	88.3	217.50
Cl1	0.08	160	1.86E-04	0.0059	88.3	3.45

C.2 Summary of reaction extents

The figures within this section present the recoveries of zinc from the concentrate of the respective experiments with initial conditions as presented in Table C.1. The solid lines represent the best fit of the shrinking core model (SCM), within the respective evaluation rages and modelled according to the regressed intrinsic rate constants (k_s) as tabulated in Table C.2.

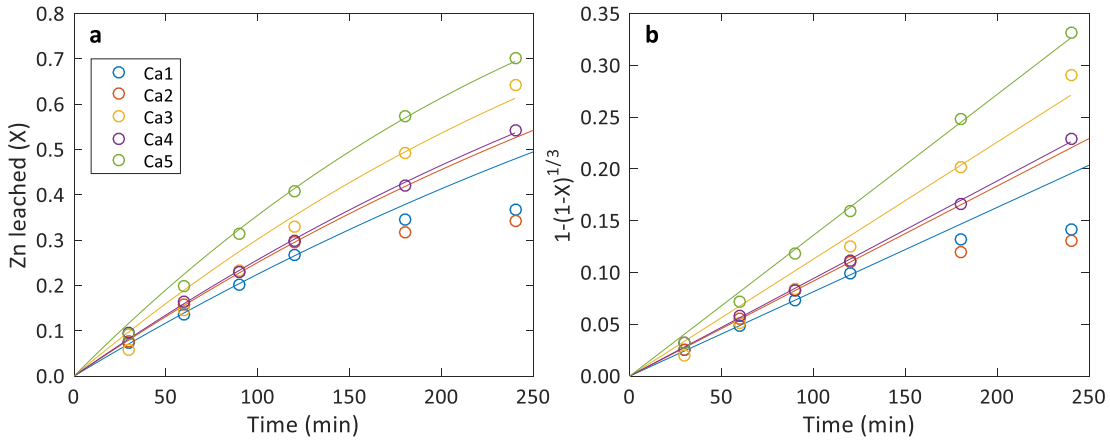

Figure C.1: Effect of gas phase composition at 75 °C a) reaction extent b) shrinking core model

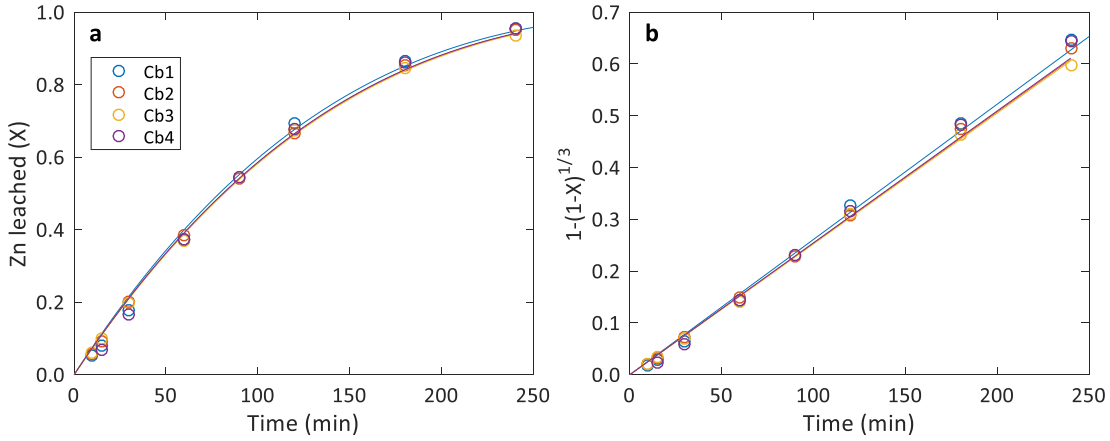

Figure C.2: Effect of gas phase composition at 85 °C a) reaction extent b) shrinking core model

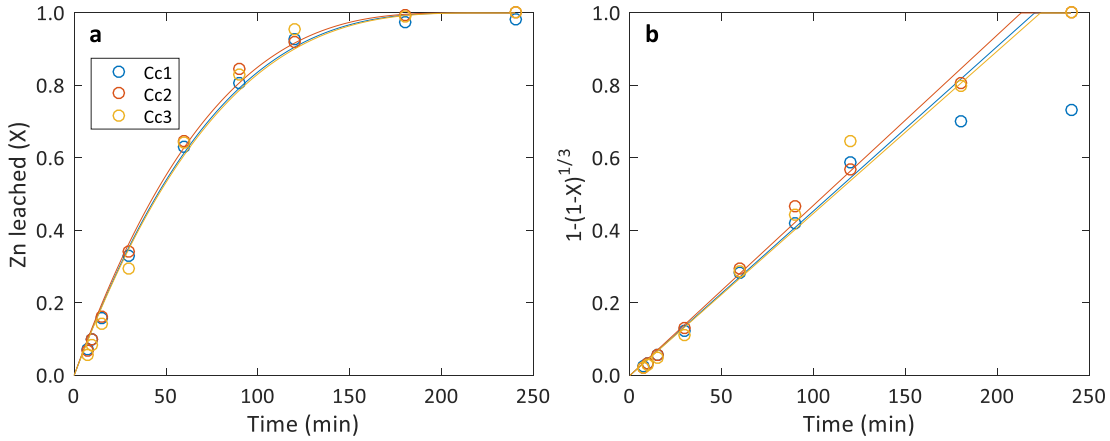

Figure C.3: Effect of gas phase composition at 95 °C a) reaction extent b) shrinking core model

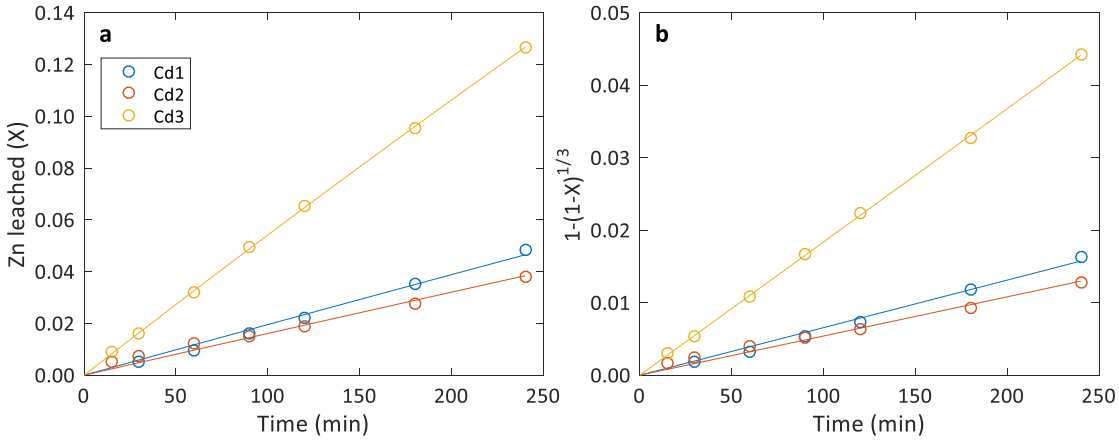

Figure C.4: Effect of gas phase composition a) reaction extent b) shrinking core model

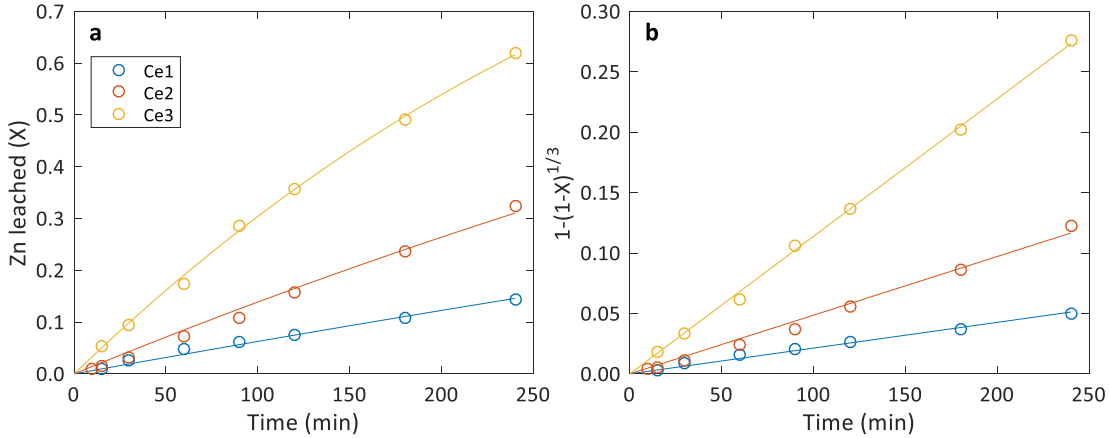

Figure C.5: Effect of temperature at 0.5 M H_2SO_4 a) reaction extent b) shrinking core model

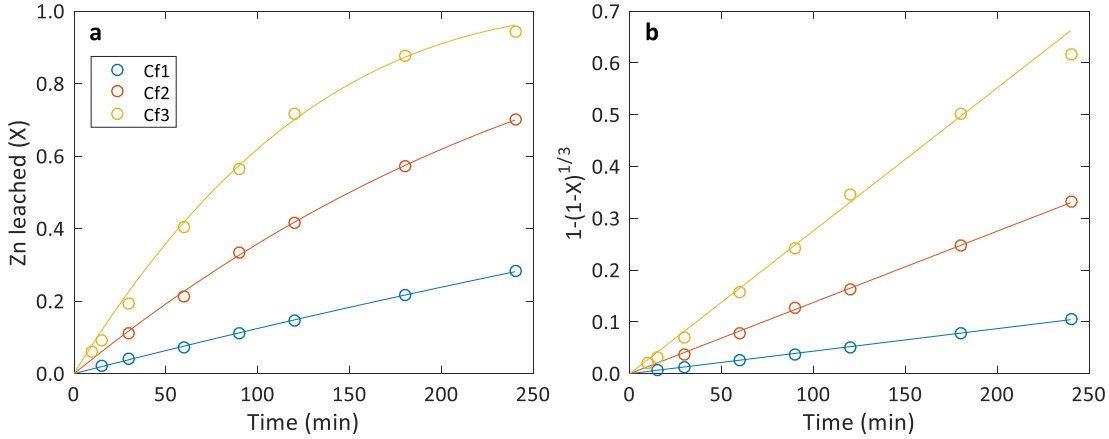

Figure C.6: Effect of temperature at 0.9 M H_2SO_4 a) reaction extent b) shrinking core model

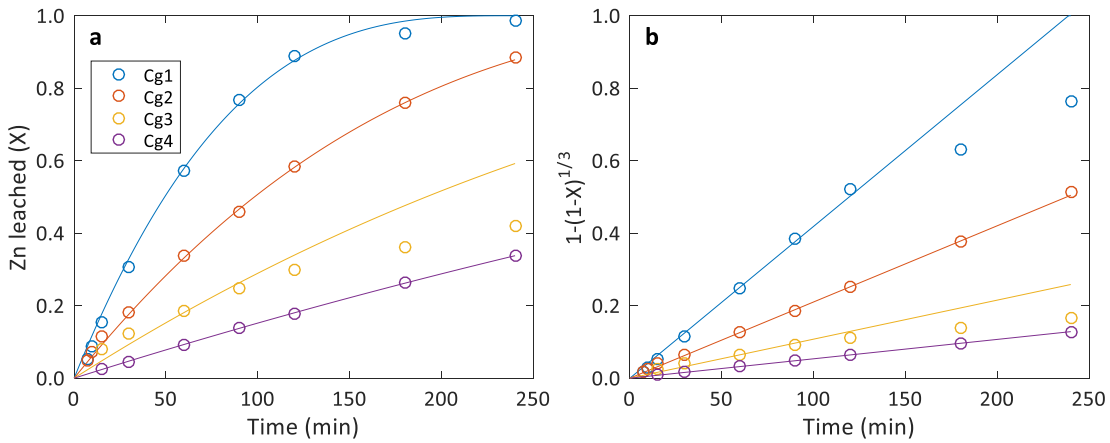

Figure C.7: Effect of surfactant concentration a) reaction extent b) shrinking core model

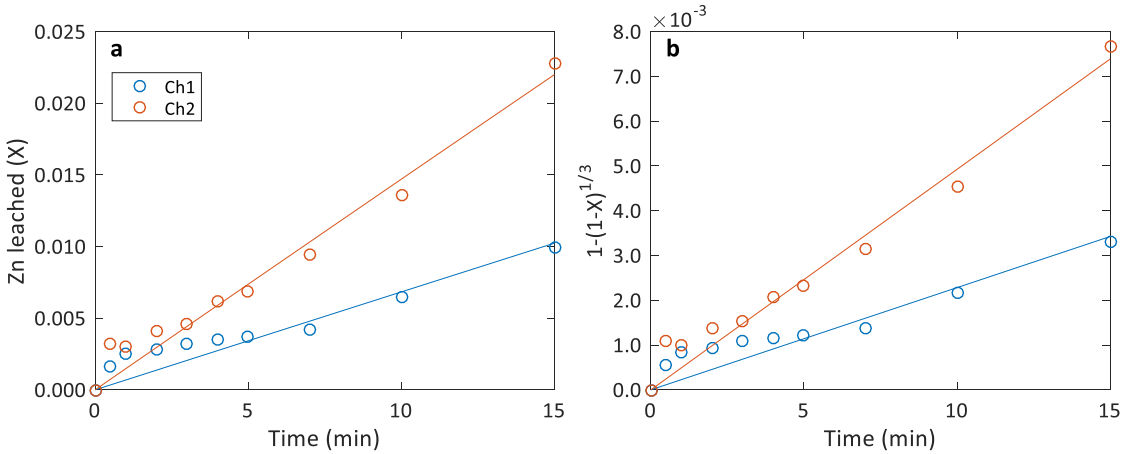

Figure C.8: Effect of impeller speed a) reaction extent b) shrinking core model

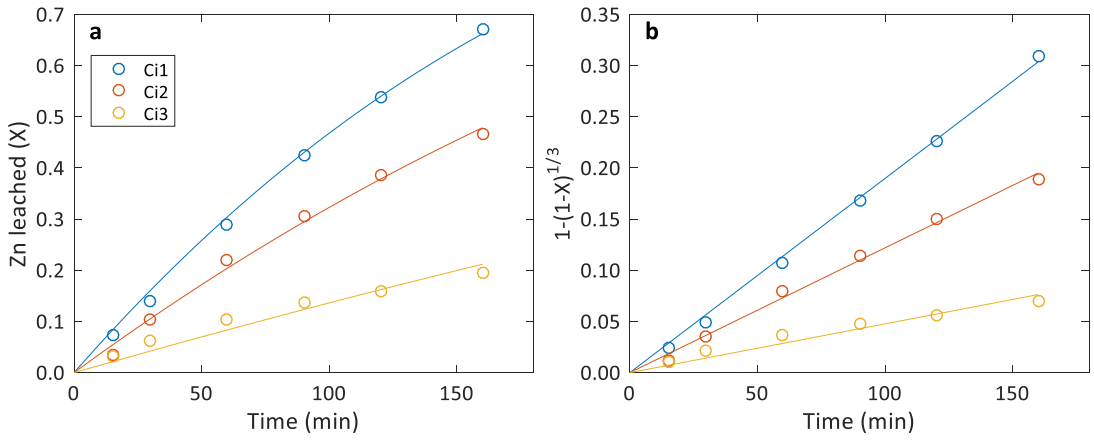

Figure C.9: Effect of pulp density a) reaction extent b) shrinking core model

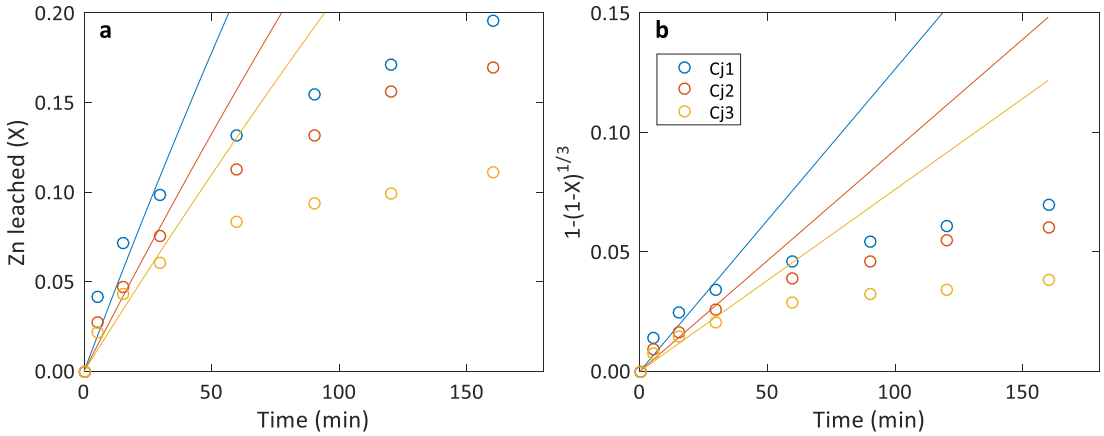

Figure C.10: Effect of ferrous, Fe^{2+} a) reaction extent b) shrinking core model

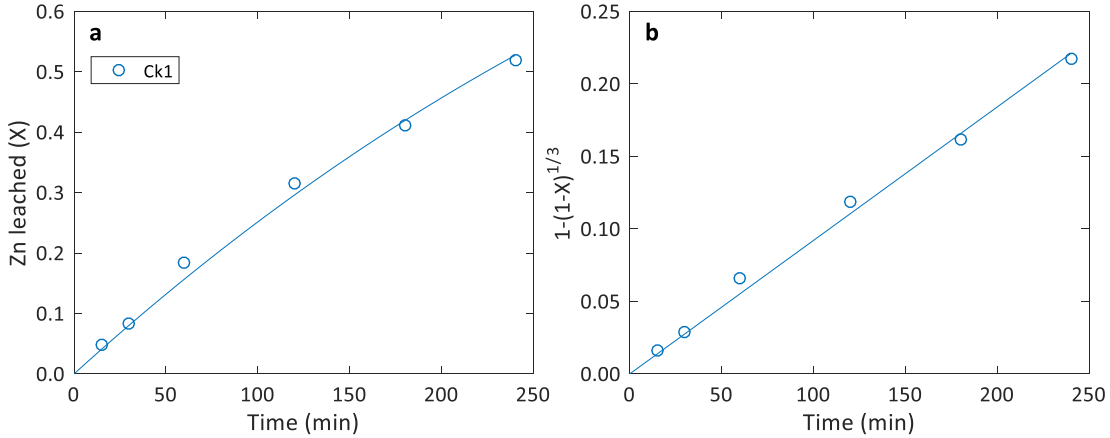

Figure C.11: Non-oxidative leaching at higher initial zinc concentration a) reaction extent b) shrinking core model

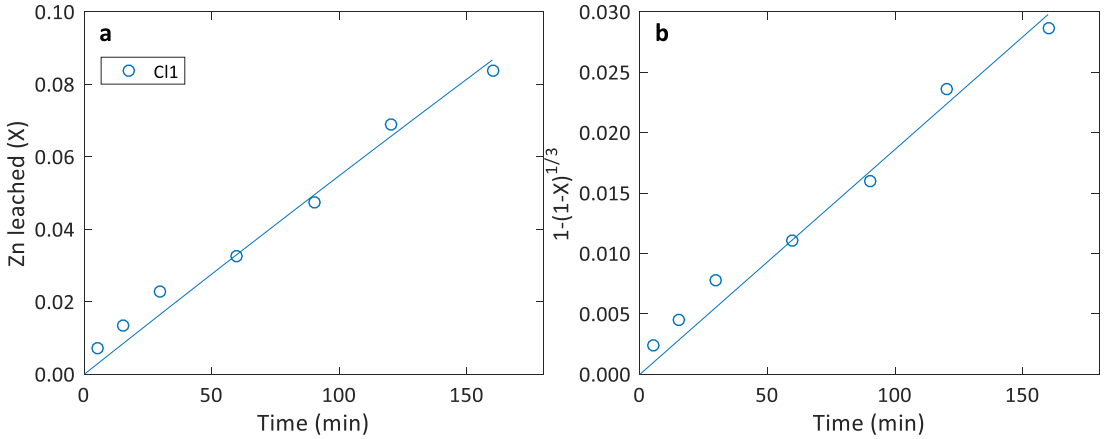

Figure C.12: Non-oxidative leaching at higher pressure of 500 kPa gauge a) reaction extent b) shrinking core model

Appendix D Oxidative Experimental Results (Lower Pulp Densities)

D.1 Summary of experimental conditions and kinetic constants

The initial conditions of oxidative leaching, at lower pulp densities and under atmospheric pressure with no gas sparging, are presented in Table D.1.

Table D.1: Initial conditions of the oxidative batch experiments (at low pulp densities)

Experiment	Temperature	Impeller Speed	Slurry Density	Size fraction	LS	$[H_2SO_4]_0$	$[Fe^{3+}]_0$	$[Fe^{2+}]_0$	$[Zn^{2+}]_0$
	(°C)	(rpm)	(g/L)	(µm)	(g/L)	(g/L)	(g/L)	(g/L)	(ppm)
Da1	80	300	1.006	45-53 (Sf3)	0	39.5	14.5	5.6	2.50
Da2	80	500	1.006	45-53 (Sf3)	0	39.4	14.6	5.6	2.30
Da3	80	700	1.006	45-53 (Sf3)	0	39.8	14.7	5.6	2.00
Db1	80	300	1.006	45-53 (Sf3)	0.01	40.1	14.6	5.7	2.35
Db2	80	500	1.006	45-53 (Sf3)	0.01	40.6	14.6	5.5	2.05
Db3	80	700	1.006	45-53 (Sf3)	0.01	40.3	14.6	5.6	3.20
Dc1	80	300	1.006	45-53 (Sf3)	0.1	40.3	14.5	5.6	2.70
Dc2	80	500	1.006	45-53 (Sf3)	0.1	40.7	14.5	5.7	2.90
Dc3	80	700	1.006	45-53 (Sf3)	0.1	39.5	14.5	5.6	2.30
Dd1	80	300	1.006	45-53 (Sf3)	1	39.7	14.6	5.7	2.50
Dd2	80	500	1.006	45-53 (Sf3)	1	40.2	14.5	5.9	2.90
Dd3	80	700	1.006	45-53 (Sf3)	1	40.7	14.5	6.0	2.60
De1	80	300	1.006	45-53 (Sf3)	10	39.9	14.6	5.6	2.60
De2	80	500	1.006	45-53 (Sf3)	10	40.5	14.5	5.6	2.40
De3	80	700	1.006	45-53 (Sf3)	10	40.7	14.5	5.7	2.80
Df1	80	700	0.483	45-53 (Sf3)	0	39.9	14.6	5.5	2.80
Df2	80	700	0.483	45-53 (Sf3)	0.1	39.5	14.5	5.6	2.20
Df3	80	700	0.483	45-53 (Sf3)	1	39.4	14.5	5.8	2.00
Dg1	90	700	0.101	45-53 (Sf3)	0.001	15.2	1.1	0.6	2.00
Dg2	90	700	0.101	45-53 (Sf3)	0.001	45.6	1.2	0.6	0
Dg3	90	700	0.101	45-53 (Sf3)	0.001	74.5	1.1	0.6	0
Dh1	90	700	0.101	45-53 (Sf3)	0.001	15.1	1.2	5.4	0
Dh2	90	700	0.101	45-53 (Sf3)	0.001	44.3	1.2	5.4	0
Dh3	90	700	0.101	45-53 (Sf3)	0.001	74.8	1.2	5.5	0
Di1	90	700	0.101	45-53 (Sf3)	0.001	15.1	1.1	55.0	9.80
Di2	90	700	0.101	45-53 (Sf3)	0.001	45.6	1.2	55.5	9.90
Di3	90	700	0.101	45-53 (Sf3)	0.001	74.8	1.2	56.0	10.00
Dj1	90	700	0.101	45-53 (Sf3)	0.001	15.1	11.1	0.6	2.00
Dj2	90	700	0.101	45-53 (Sf3)	0.001	44.3	11.2	0.6	0
Dj3	90	700	0.101	45-53 (Sf3)	0.001	74.2	11.1	0.6	0

Table D.1: Initial conditions of the oxidative batch experiments (at low pulp densities), continue

Experiment	Temperature	Impeller Speed	Slurry Density	Size fraction	LS	$[H_2SO_4]_0$	$[Fe^{3+}]_0$	$[Fe^{2+}]_0$	$[Zn^{2+}]_0$
	(°C)	(rpm)	(g/L)	(µm)	(g/L)	(g/L)	(g/L)	(g/L)	(ppm)
Dk1	90	700	0.101	45-53 (Sf3)	0.001	15.3	11.2	5.6	0
Dk2	90	700	0.101	45-53 (Sf3)	0.001	45.1	11.3	5.5	2.50
Dk3	90	700	0.101	45-53 (Sf3)	0.001	75.0	11.2	5.5	2.30
Dl1	90	700	0.101	45-53 (Sf3)	0.001	15.3	11.1	56.0	10
Dl2	90	700	0.101	45-53 (Sf3)	0.001	30.4	11.1	56.0	10
Dl3	90	700	0.101	45-53 (Sf3)	0.001	45.2	11.2	55.5	12
Dm1	90	700	0.101	45-53 (Sf3)	0.001	3.4	55.8	0.6	7
Dm2	90	700	0.101	45-53 (Sf3)	0.001	18.5	55.9	0.6	7
Dm3	90	700	0.101	45-53 (Sf3)	0.001	46.9	55.8	0.6	9
Dn1	90	700	0.101	45-53 (Sf3)	0.001	3.2	55.8	5.6	10
Dn2	90	700	0.101	45-53 (Sf3)	0.001	15.2	55.9	5.6	9
Dn3	90	700	0.101	45-53 (Sf3)	0.001	45.5	55.8	5.6	10
Do1	90	700	0.101	45-53 (Sf3)	0.001	2.9	55.7	56.0	16
Do2	90	700	0.101	45-53 (Sf3)	0.001	15.1	55.7	56.0	16
Do3	90	700	0.101	45-53 (Sf3)	0.001	32.0	55.8	55.7	16
Dp1	30	700	0.101	25-38 (Sf1)	0.001	40.1	11.1	5.6	0
Dp2	50	700	0.101	25-38 (Sf1)	0.001	39.9	11.1	5.6	0
Dp3	70	700	0.101	25-38 (Sf1)	0.001	40.0	11.1	5.6	0
Dp4	90	700	0.101	25-38 (Sf1)	0.001	40.1	11.1	5.6	0
Dq1	50	700	0.101	38-45 (Sf2)	0.001	39.9	11.2	5.6	0
Dq2	70	700	0.101	38-45 (Sf2)	0.001	40.3	11.2	5.6	0
Dq3	90	700	0.101	38-45 (Sf2)	0.001	39.9	11.1	5.7	0
Dr1	30	700	0.101	45-53 (Sf3)	0.001	40.5	11.2	5.5	0
Dr2	50	700	0.101	45-53 (Sf3)	0.001	39.8	11.2	5.6	2
Dr3	70	700	0.101	45-53 (Sf3)	0.001	40.2	11.1	5.7	0
Dr4	90	700	0.101	45-53 (Sf3)	0.001	40.0	11.1	5.7	0
Ds1	50	700	0.101	53-75 (Sf4)	0.001	40.2	11.1	5.6	0
Ds2	70	700	0.101	53-75 (Sf4)	0.001	39.7	11.1	5.7	0
Ds3	90	700	0.101	53-75 (Sf4)	0.001	40.0	11.2	5.5	0
Dt1	50	700	0.101	90-106 (Sf6)	0.001	40.1	11.1	5.7	0
Dt2	70	700	0.101	90-106 (Sf6)	0.001	40.2	11.1	5.7	2
Dt3	90	700	0.101	90-106 (Sf6)	0.001	39.9	11.1	5.7	0

Table D.2: Experimentally obtained intrinsic rate constants within the respective evaluation ranges and corresponding average solution concentrations

Experiment	Evaluation Range		Mean particle size	Intrinsic rate constants		Average Concentrations			
	Extent	Time	d_p	k_s	k_l	$[H_2SO_4]$	$[Fe^{3+}]$	$[Fe^{2+}]$	$[Zn^{2+}]$
	(fraction)	(min)	(µm)	(1/min)	(µm/min)	(g/L)	(g/L)	(g/L)	(g/L)
Da1	0.4	44	63.9	4.16E-03	0.1328	39.57	14.40	5.73	0.08725
Da2	0.4	43	63.9	4.22E-03	0.1349	39.53	14.45	5.72	0.09015
Da3	0.4	42	63.9	4.30E-03	0.1375	39.85	14.45	5.75	0.09100
Db1	0.4	33	63.9	5.20E-03	0.1662	40.14	14.40	5.95	0.10768
Db2	0.4	34	63.9	5.14E-03	0.1642	40.64	14.35	5.78	0.10653
Db3	0.4	36	63.9	4.98E-03	0.1593	40.36	14.40	5.83	0.10410
Dc1	0.4	48	63.9	4.35E-03	0.1389	40.35	14.35	5.75	0.09185
Dc2	0.4	47	63.9	4.43E-03	0.1416	40.75	14.30	5.95	0.09295
Dc3	0.4	50	63.9	4.26E-03	0.1360	39.62	14.35	5.80	0.08965
Dd1	0.3	50	63.9	3.11E-03	0.0993	39.77	14.30	5.98	0.06675
Dd2	0.3	48	63.9	3.04E-03	0.0973	40.27	14.30	6.08	0.06845
Dd3	0.3	42	63.9	3.40E-03	0.1086	40.75	14.30	6.13	0.07330
De1	0.2	48	63.9	1.95E-03	0.0622	39.98	14.30	5.85	0.04530
De2	0.2	46	63.9	2.06E-03	0.0657	40.60	14.30	5.85	0.04670
De3	0.2	41	63.9	2.22E-03	0.0709	40.75	14.35	5.90	0.05090
Df1	0.5	66	63.9	3.31E-03	0.1059	39.95	14.50	5.60	0.06490
Df2	0.5	73	63.9	3.42E-03	0.1093	39.57	14.35	5.70	0.06360
Df3	0.3	45	63.9	3.19E-03	0.1018	39.44	14.45	5.85	0.03450
Dg1	0.5	49	63.9	5.48E-03	0.1751	15.22	1.06	0.59	0.01300
Dg2	0.5	44	63.9	5.35E-03	0.1711	45.62	1.15	0.58	0.01100
Dg3	0.5	37	63.9	6.23E-03	0.1990	74.52	1.05	0.58	0.01250
Dh1	0.5	104	63.9	2.61E-03	0.0833	15.15	1.15	5.45	0.01050
Dh2	0.5	77	63.9	3.12E-03	0.0997	44.36	1.15	5.49	0.01200
Dh3	0.5	63	63.9	3.57E-03	0.1141	74.84	1.20	5.53	0.01350
Di1	0.1	81	63.9	5.87E-04	0.0188	15.14	1.15	55.25	0.01240
Di2	0.1	43	63.9	1.13E-03	0.0362	45.61	1.20	55.50	0.01245
Di3	0.1	38	63.9	1.19E-03	0.0380	74.84	1.15	55.80	0.01250
Dj1	0.6	44	63.9	7.32E-03	0.2340	15.12	11.05	0.59	0.01600
Dj2	0.6	40	63.9	8.31E-03	0.2656	44.33	11.15	0.61	0.01450
Dj3	0.6	33	63.9	9.23E-03	0.2950	74.24	11.05	0.63	0.01600

Table D.2: Experimentally obtained intrinsic rate constants within the respective evaluation ranges and corresponding average solution concentrations, continue

Experiment	Evaluation Range		Mean particle size	Intrinsic rate constants		Average Concentrations			
	Extent (fraction)	Time (min)	d_p (µm)	k_s (1/min)	k_l (µm/min)	$[H_2SO_4]$ (g/L)	$[Fe^{3+}]$ (g/L)	$[Fe^{2+}]$ (g/L)	$[Zn^{2+}]$ (g/L)
Dk1	0.5	47	63.9	5.96E-03	0.1905	15.32	11.15	5.68	0.01150
Dk2	0.5	35	63.9	6.98E-03	0.2230	45.12	11.25	5.56	0.01525
Dk3	0.6	31	63.9	8.93E-03	0.2854	75.03	11.15	5.58	0.01765
Dl1	0.2	106	63.9	9.79E-04	0.0313	15.37	11.10	56.00	0.01400
Dl2	0.2	96	63.9	9.97E-04	0.0319	30.46	11.10	56.00	0.01400
Dl3	0.2	31	63.9	2.53E-03	0.0809	45.24	11.15	56.00	0.01750
Dm1	0.5	115	63.9	2.83E-03	0.0905	3.48	55.80	0.63	0.01740
Dm2	0.5	80	63.9	3.23E-03	0.1032	18.58	55.85	0.60	0.01915
Dm3	0.5	36	63.9	7.46E-03	0.2383	46.94	55.80	0.61	0.02185
Dn1	0.6	94	63.9	3.70E-03	0.1181	3.26	55.80	5.60	0.02275
Dn2	0.6	85	63.9	4.08E-03	0.1303	15.24	55.90	5.59	0.02275
Dn3	0.6	83	63.9	3.94E-03	0.1258	45.57	55.85	5.59	0.02395
Do1	0.2	99	63.9	9.83E-04	0.0314	2.95	55.70	56.35	0.02000
Do2	0.2	91	63.9	1.12E-03	0.0359	15.16	55.65	56.10	0.02050
Do3	0.6	254	63.9	1.09E-03	0.0350	32.34	55.90	55.85	0.03200
Dp1	0.07	180	43.9	1.20E-04	0.0026	40.19	11.05	5.61	0.00205
Dp2	0.21	180	43.9	4.16E-04	0.0091	40.02	11.05	5.68	0.00600
Dp3	0.50	97	43.9	2.39E-03	0.0525	40.05	11.10	5.66	0.01000
Dp4	0.40	43	43.9	7.78E-03	0.1708	40.12	11.10	5.62	0.01200
Dq1	0.15	180	56.1	2.87E-04	0.0080	40.02	11.20	5.58	0.00435
Dq2	0.50	139	56.1	1.51E-03	0.0425	40.37	11.20	5.59	0.01250
Dq3	0.50	34	56.1	6.70E-03	0.1880	39.92	11.10	5.71	0.01350
Dr1	0.06	180	63.9	1.10E-04	0.0035	40.53	11.20	5.49	0.00175
Dr2	0.20	180	63.9	3.65E-04	0.0117	39.92	11.15	5.58	0.00755
Dr3	0.50	144	63.9	1.48E-03	0.0474	40.30	11.10	5.64	0.01200
Dr4	0.60	65	63.9	4.49E-03	0.1435	40.05	11.05	5.75	0.01600
Ds1	0.10	180	81.4	1.88E-04	0.0077	40.23	11.15	5.55	0.00270
Ds2	0.50	161	81.4	1.18E-03	0.0481	39.78	11.15	5.65	0.01000
Ds3	0.50	63	81.4	3.38E-03	0.1376	40.08	11.15	5.57	0.01300
Dt1	0.12	180	127.3	2.13E-04	0.0136	40.13	11.10	5.72	0.00225
Dt2	0.50	177	127.3	1.23E-03	0.0782	40.26	11.05	5.68	0.01165
Dt3	0.50	84	127.3	2.57E-03	0.1636	40.01	11.05	5.79	0.00950

D.2 Summary of reaction extents

The figures within this section shows each batch experiment result, including the fractional recovery of zinc from the concentrate in (a), the shrinking core model based on the fractional recovery in (b), the concentration (g/L) profile of ferric in (c) and the concentration (g/L) profile of ferrous in (d) during the leaching test. The solid lines in (a) and (b) represents the best fit of the shrinking core model (SCM), within the respective evaluation rages and modelled according to the regressed intrinsic rate constants (k_s), as tabulated in Table D.2. While, the solid lines in (c) and (d) are linear connections between consecutive concentration data points, to indicate whether or not the concentration has a trend.

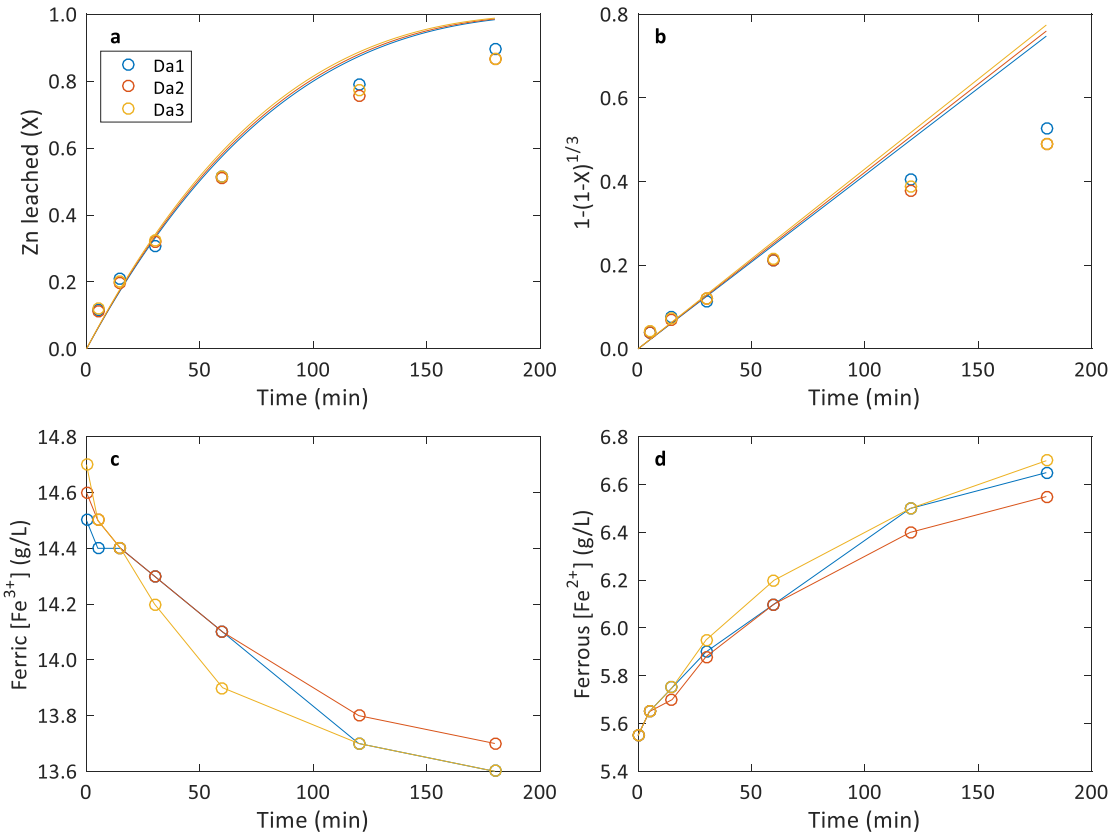

Figure D.1: Effect of impeller speed with 0 g/L LS a) reaction extent b) shrinking core model c) ferric concentration profile and d) ferrous concentration profile

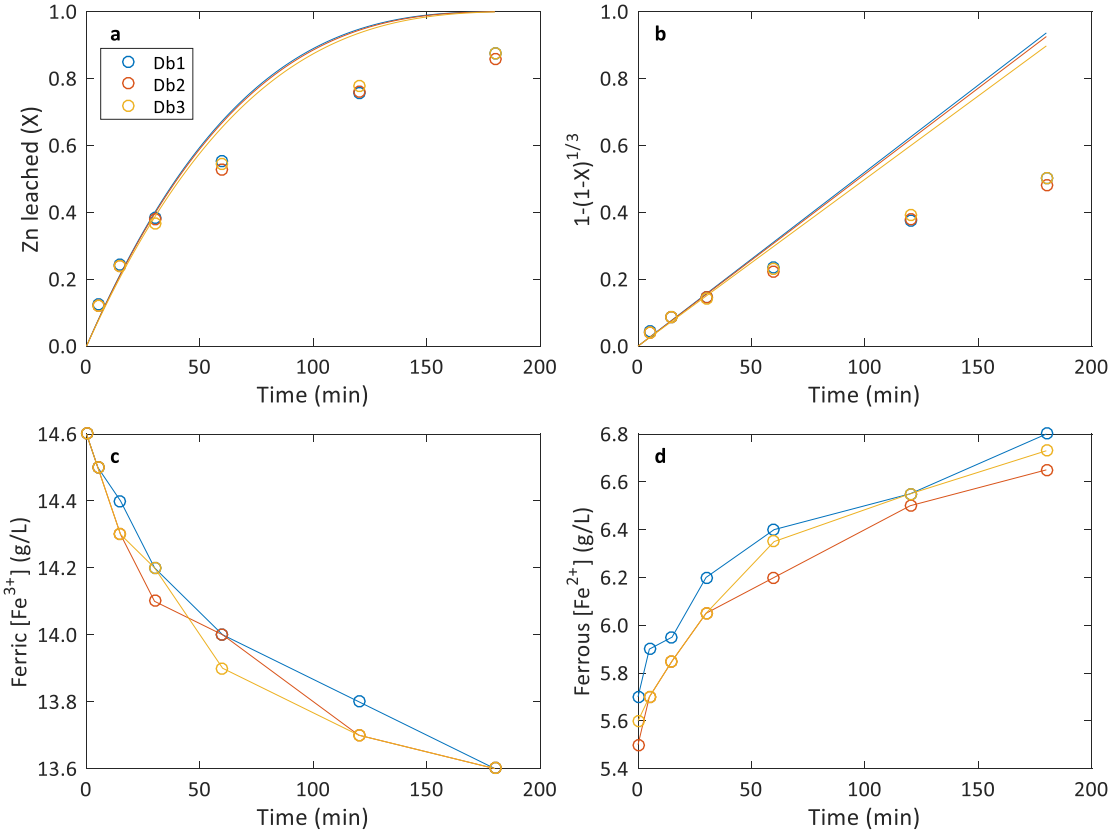

Figure D.2: Effect of impeller speed with 0.01 g/L LS a) reaction extent b) shrinking core model c) ferric concentration profile and d) ferrous concentration profile

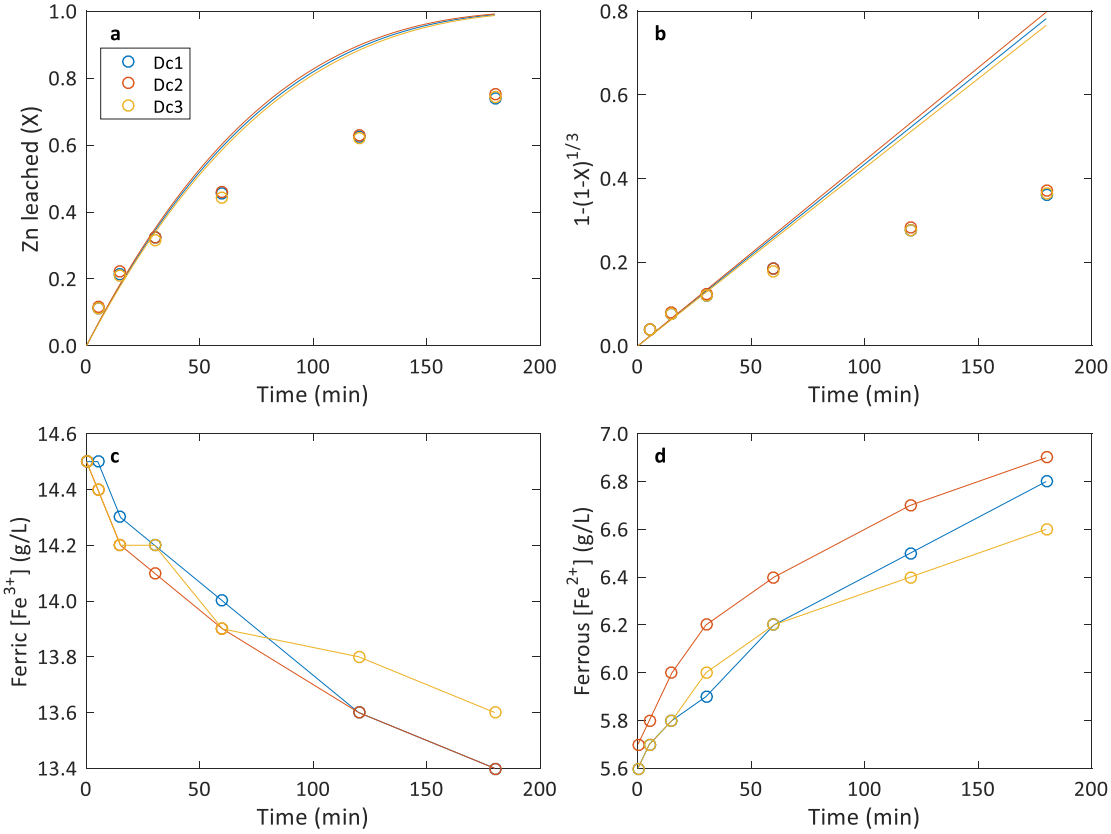

Figure D.3: Effect of impeller speed with 0.1 g/L LS a) reaction extent b) shrinking core model c) ferric concentration profile and d) ferrous concentration profile

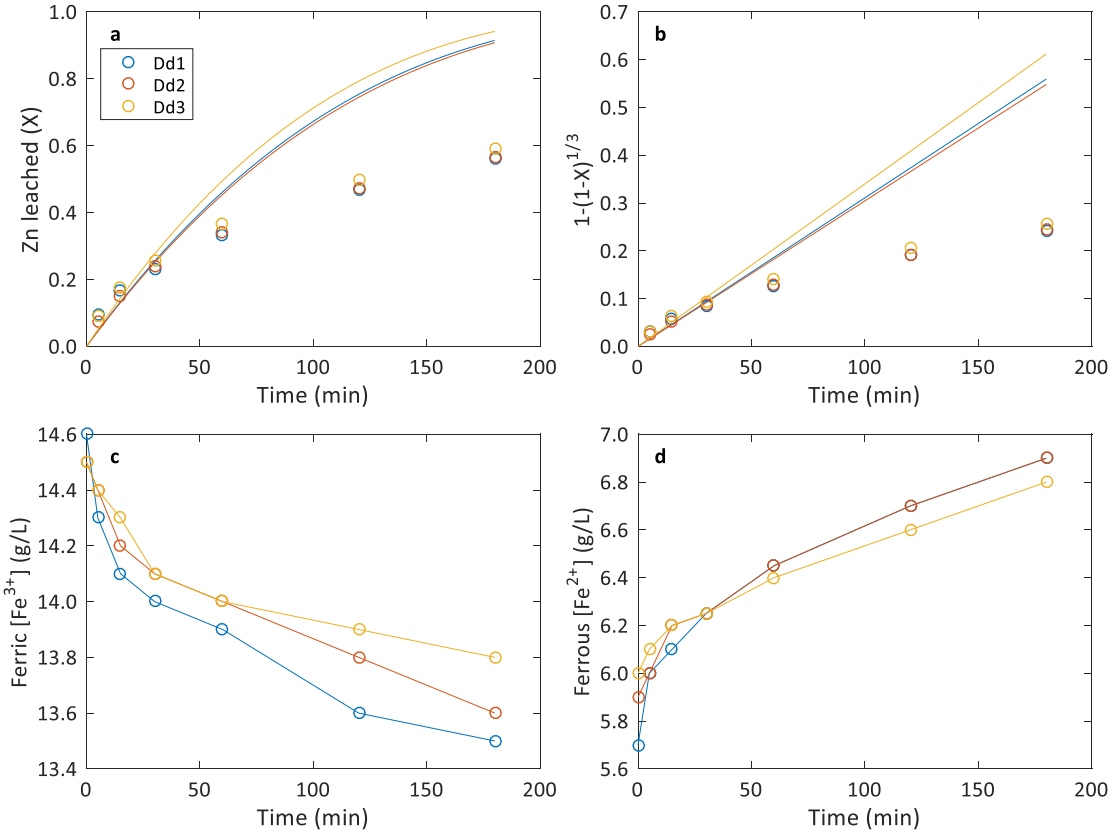

Figure D.4: Effect of impeller speed with 1 g/L LS a) reaction extent b) shrinking core model c) ferric concentration profile and d) ferrous concentration profile

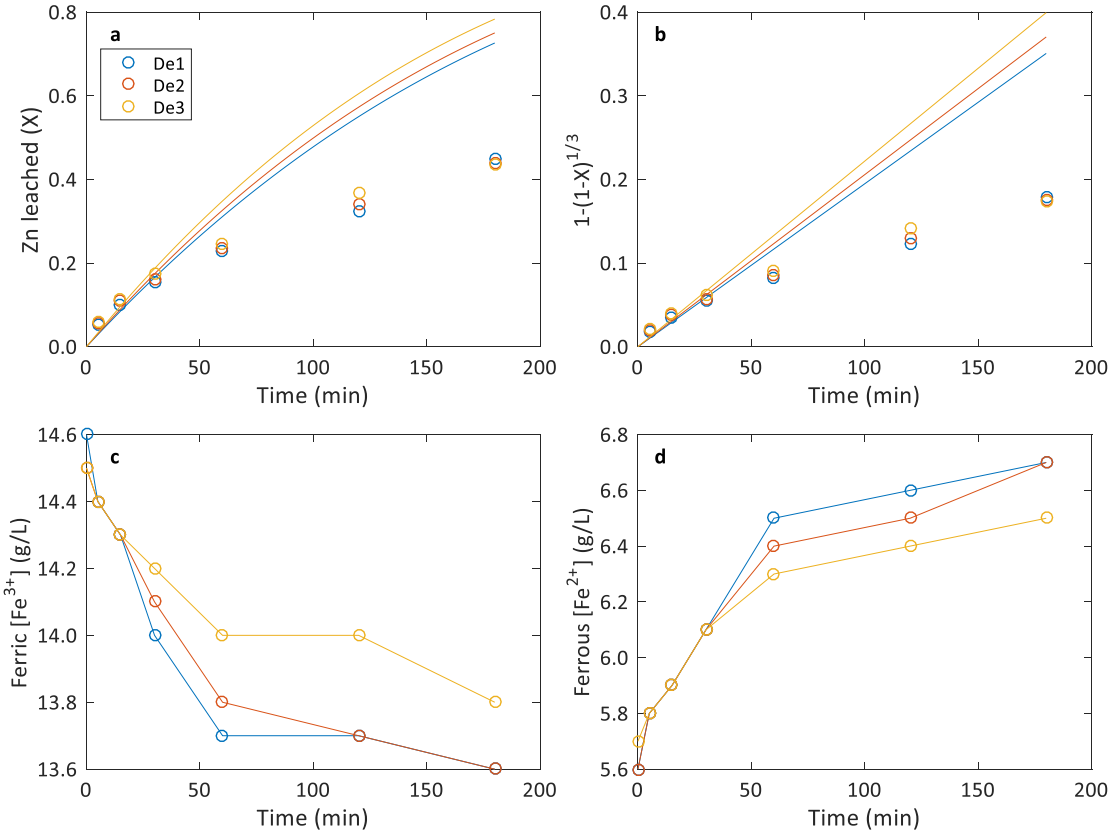

Figure D.5: Effect of impeller speed with 10 g/L LS a) reaction extent b) shrinking core model c) ferric concentration profile and d) ferrous concentration profile

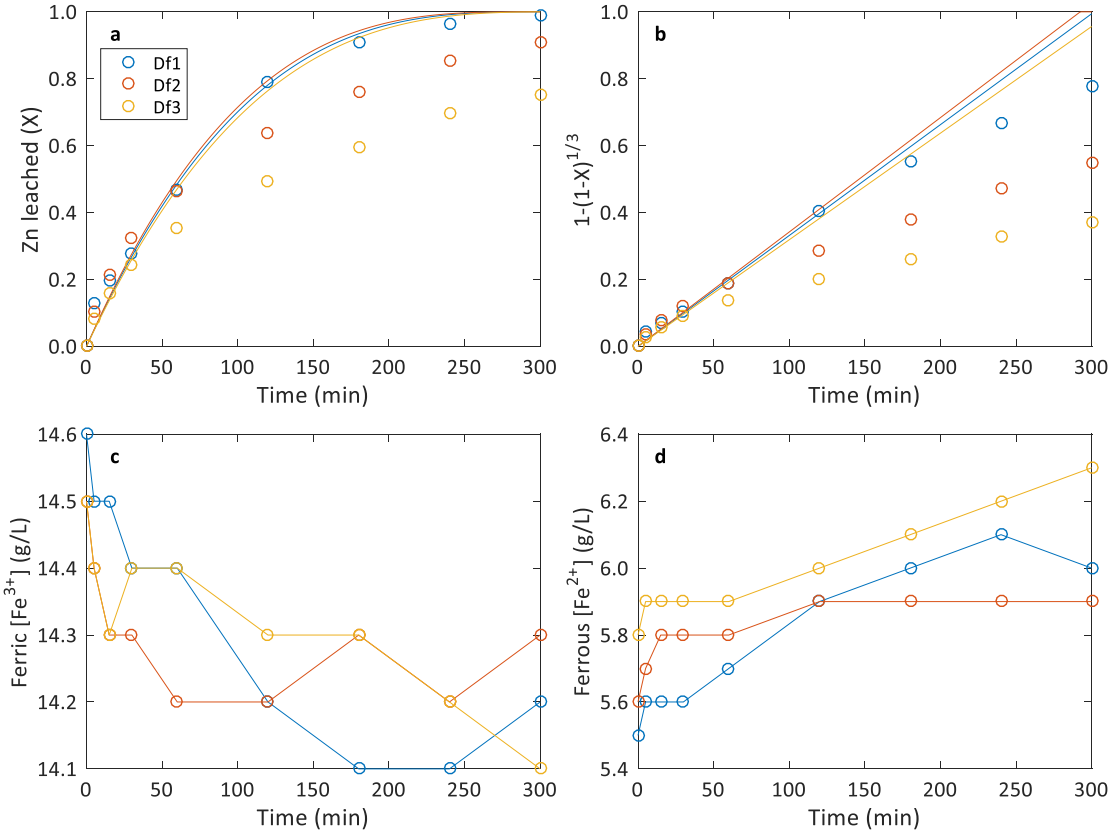

Figure D.6: Effect of surfactant concentration a) reaction extent b) shrinking core model c) ferric concentration profile and d) ferrous concentration profile

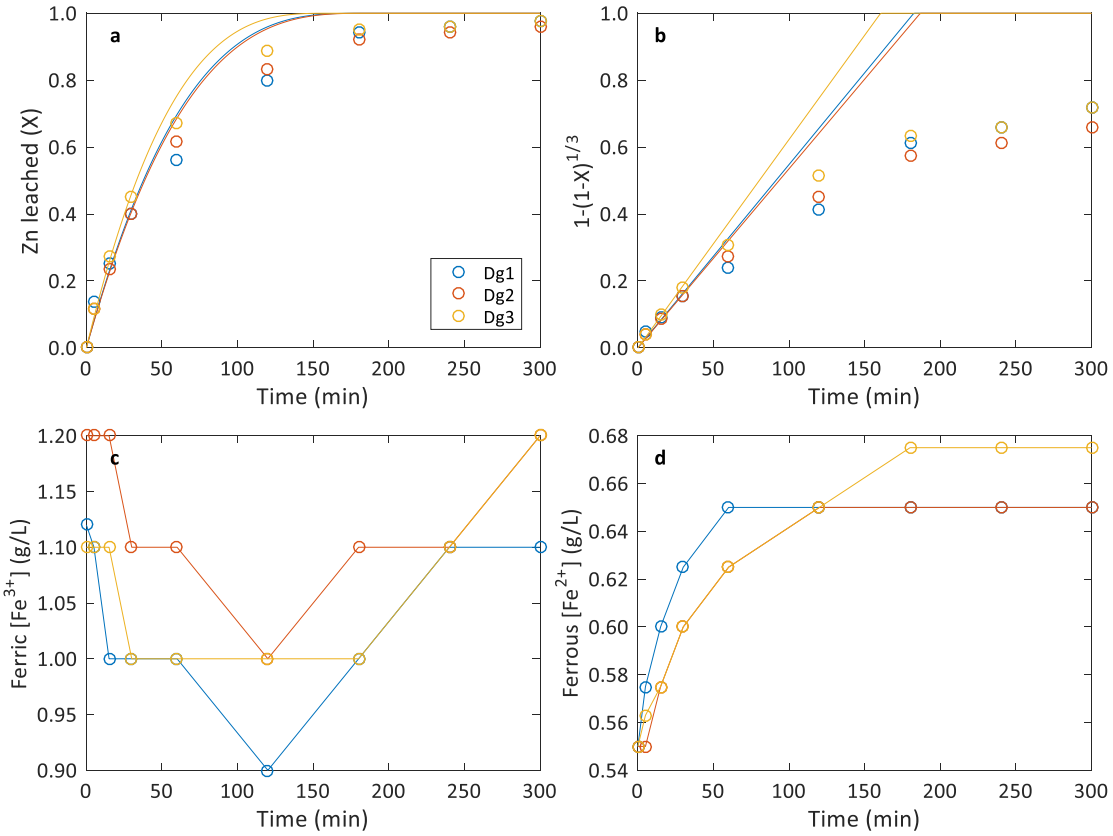

Figure D.7: Effect of acid concentration a) reaction extent b) shrinking core model c) ferric concentration profile and d) ferrous concentration profile

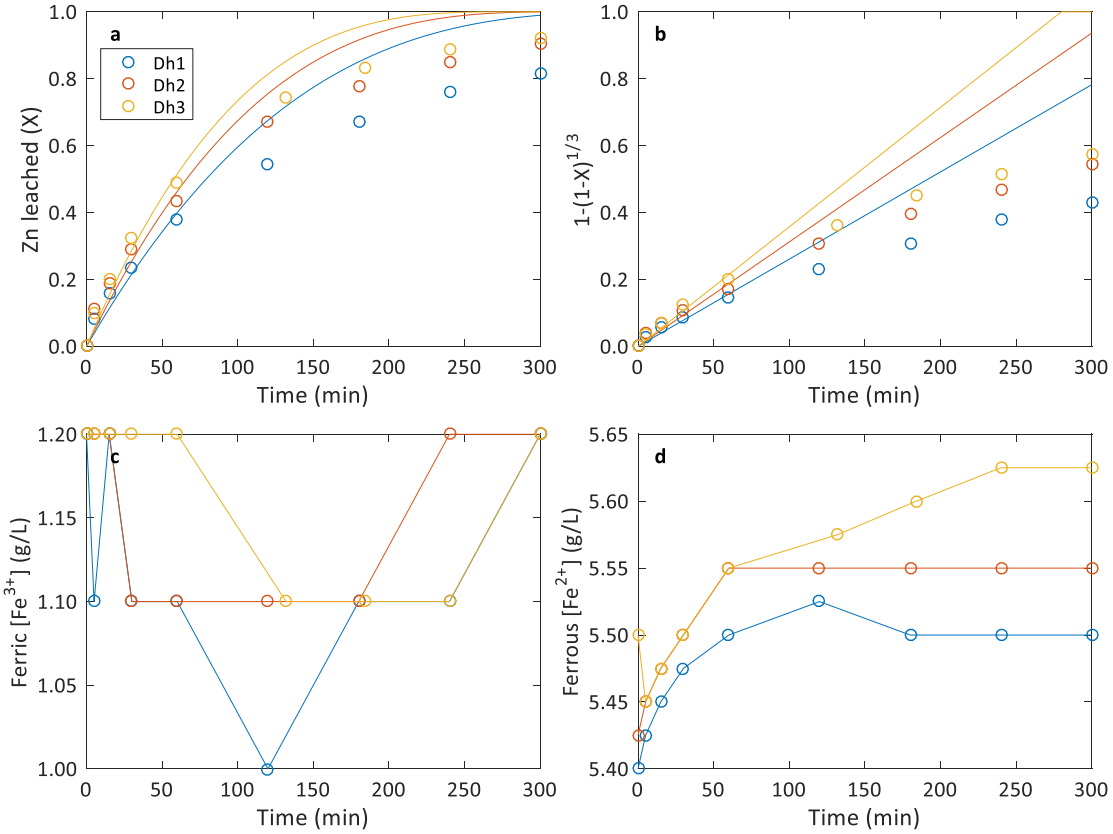

Figure D.8: Effect of acid concentration a) reaction extent b) shrinking core model c) ferric concentration profile and d) ferrous concentration profile

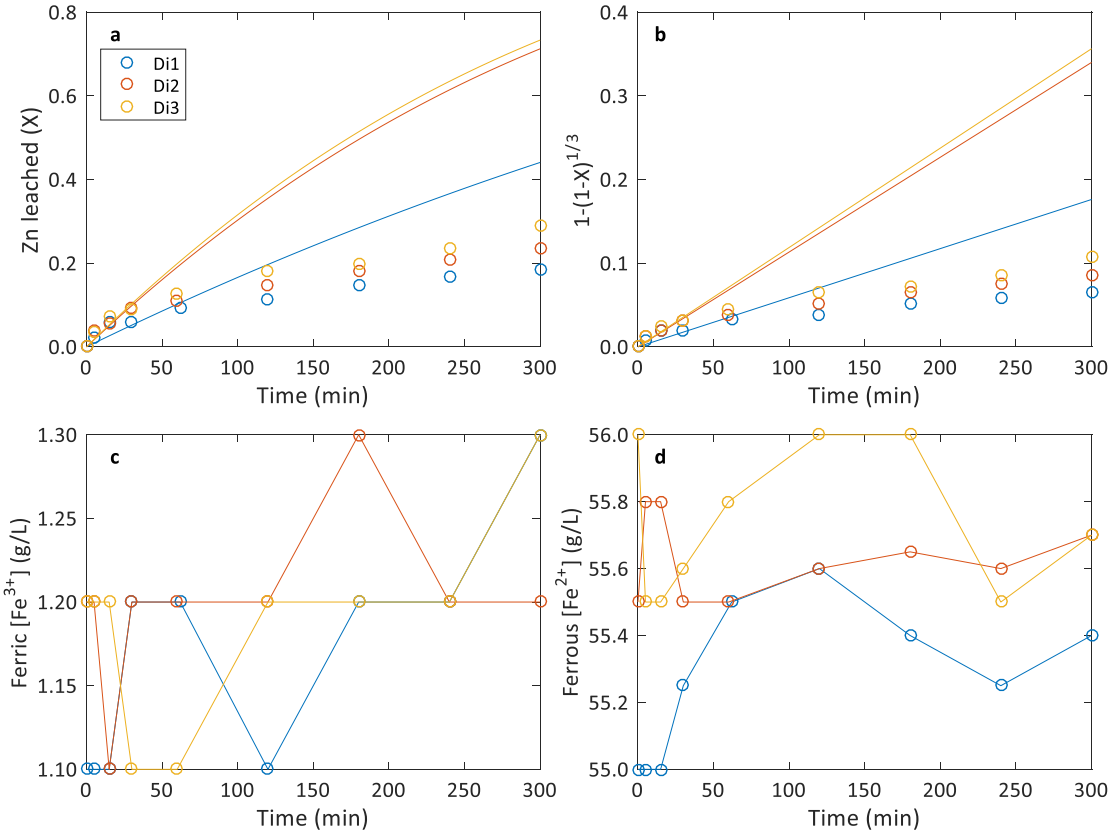

Figure D.9: Effect of acid concentration a) reaction extent b) shrinking core model c) ferric concentration profile and d) ferrous concentration profile

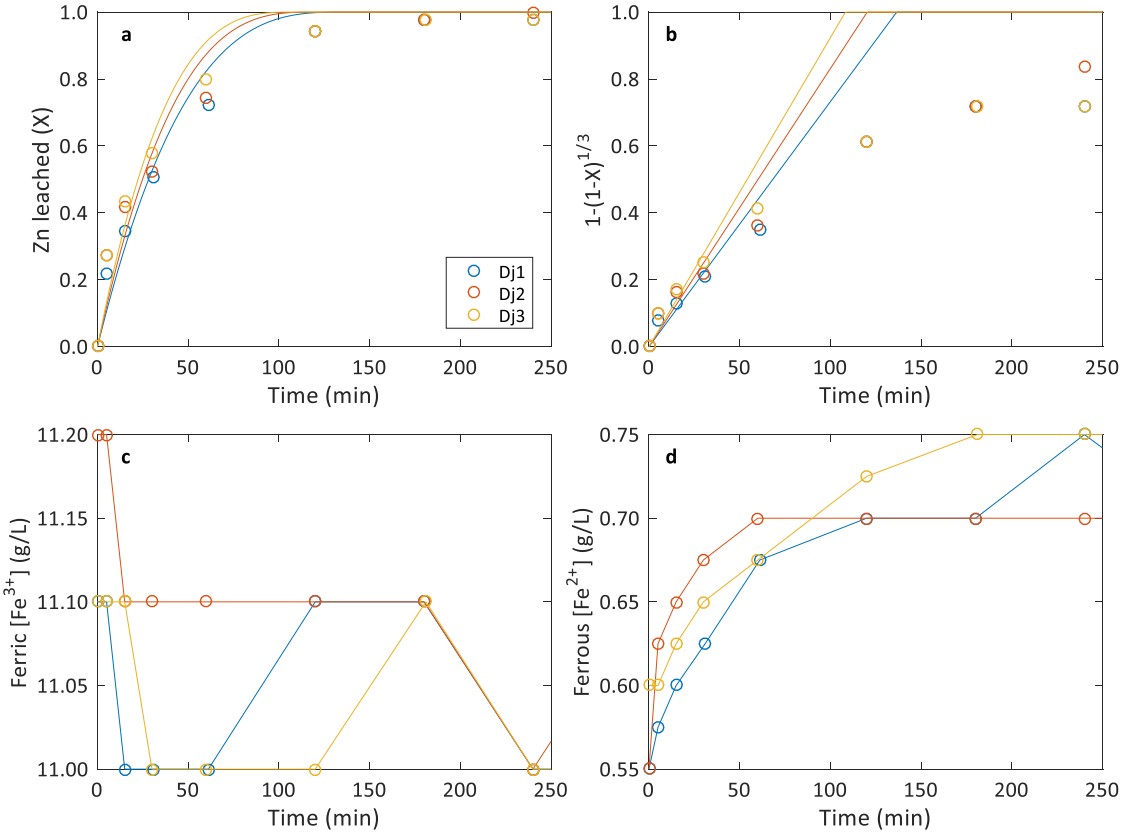

Figure D.10: Effect of acid concentration a) reaction extent b) shrinking core model c) ferric concentration profile and d) ferrous concentration profile

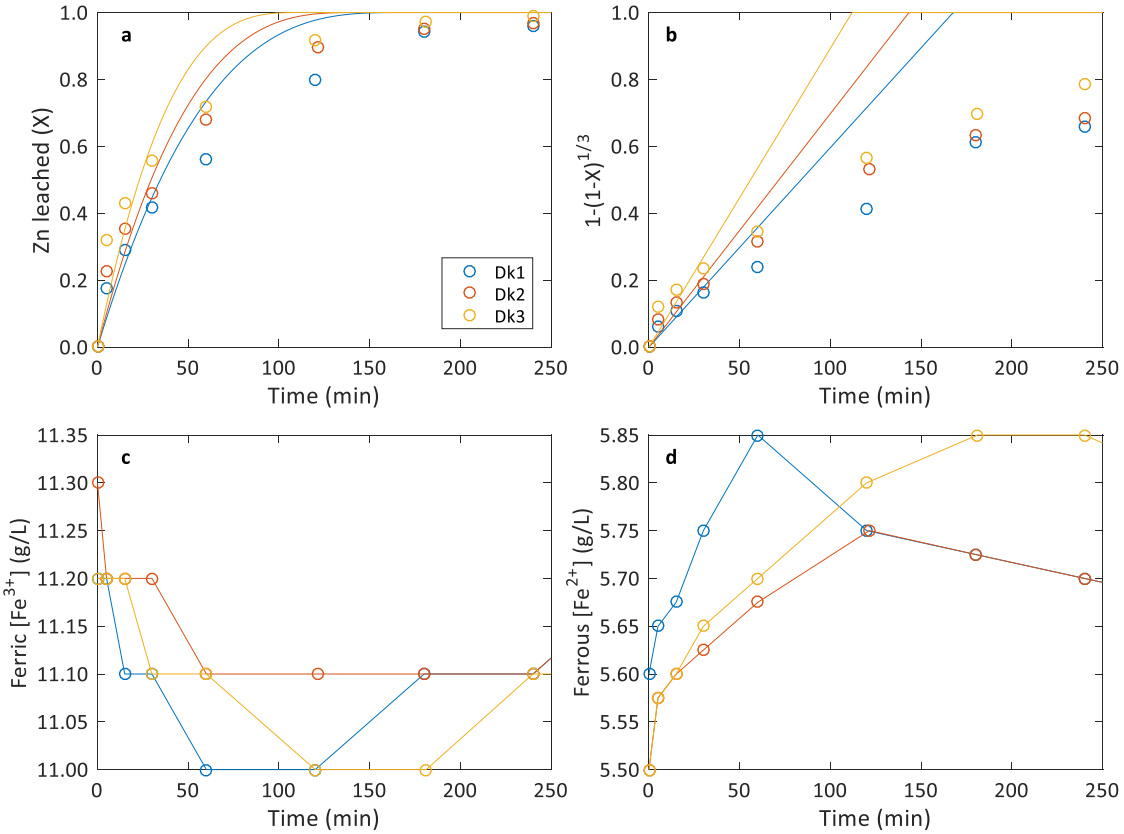

Figure D.11: Effect of acid concentration a) reaction extent b) shrinking core model c) ferric concentration profile and d) ferrous concentration profile

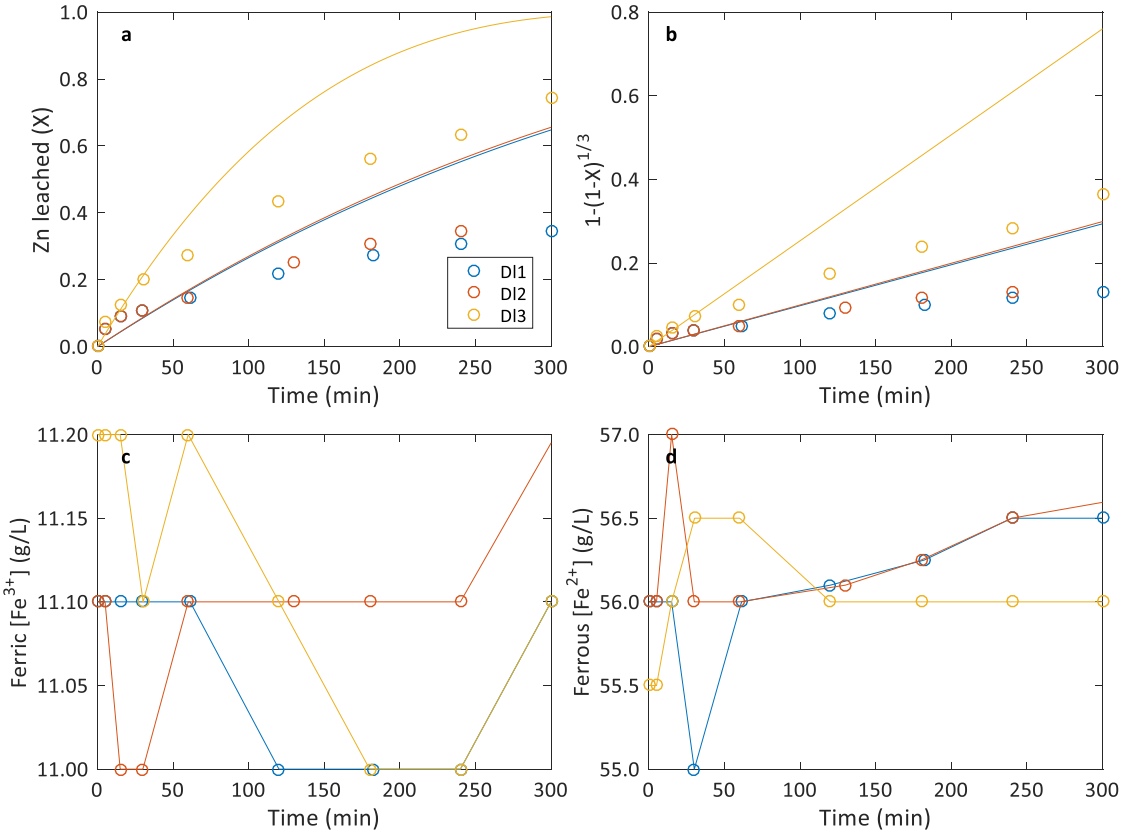

Figure D.12: Effect of acid concentration a) reaction extent b) shrinking core model c) ferric concentration profile and d) ferrous concentration profile

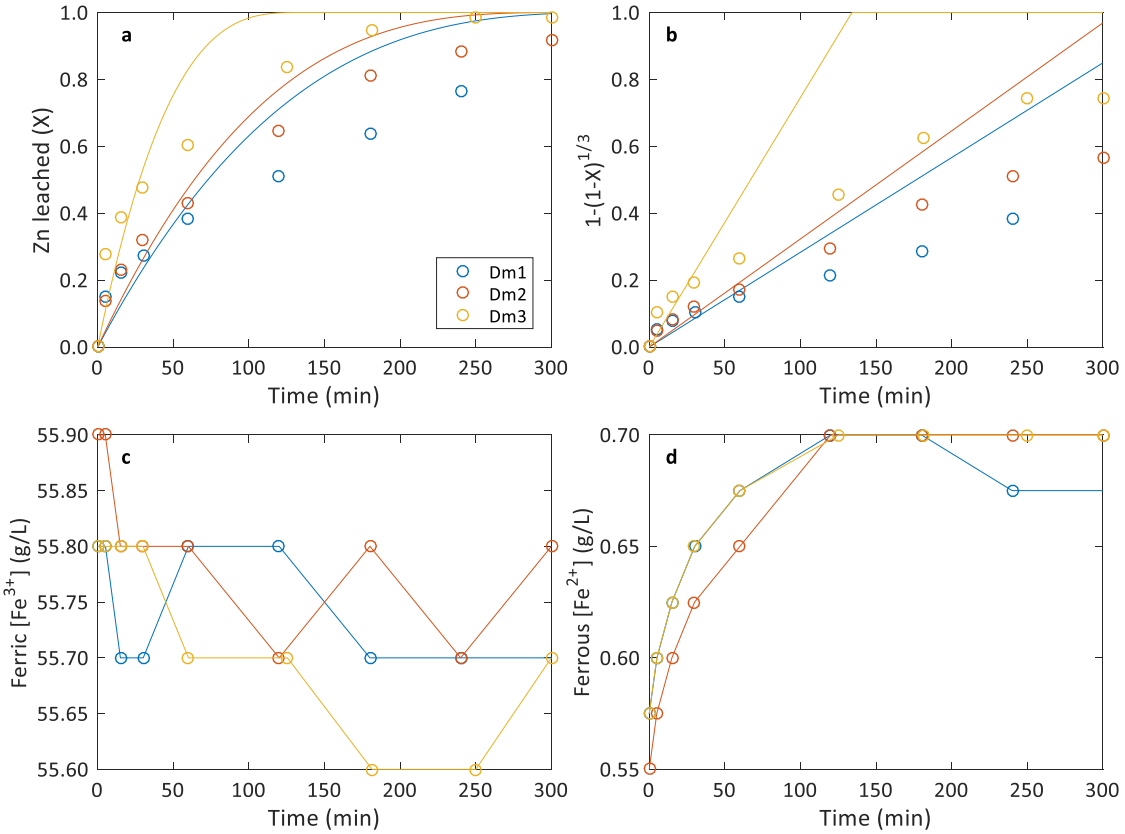

Figure D.13: Effect of acid concentration a) reaction extent b) shrinking core model c) ferric concentration profile and d) ferrous concentration profile

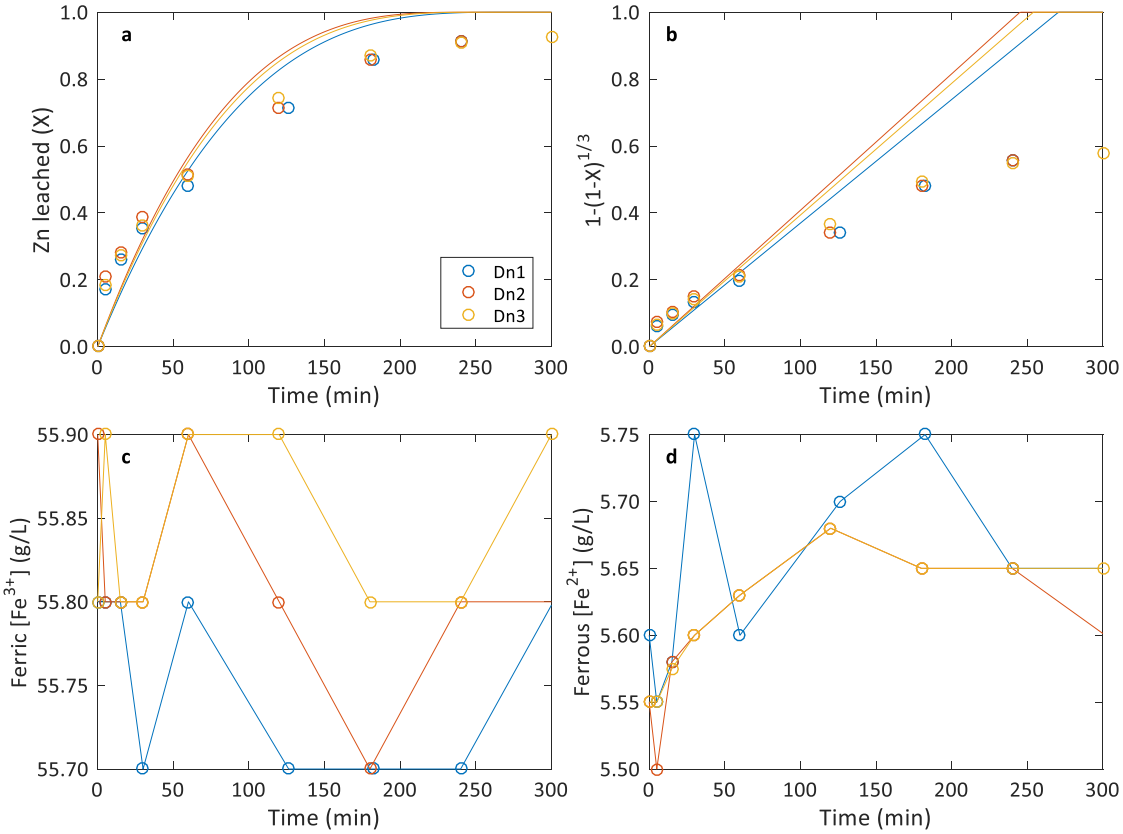

Figure D.14: Effect of acid concentration a) reaction extent b) shrinking core model c) ferric concentration profile and d) ferrous concentration profile

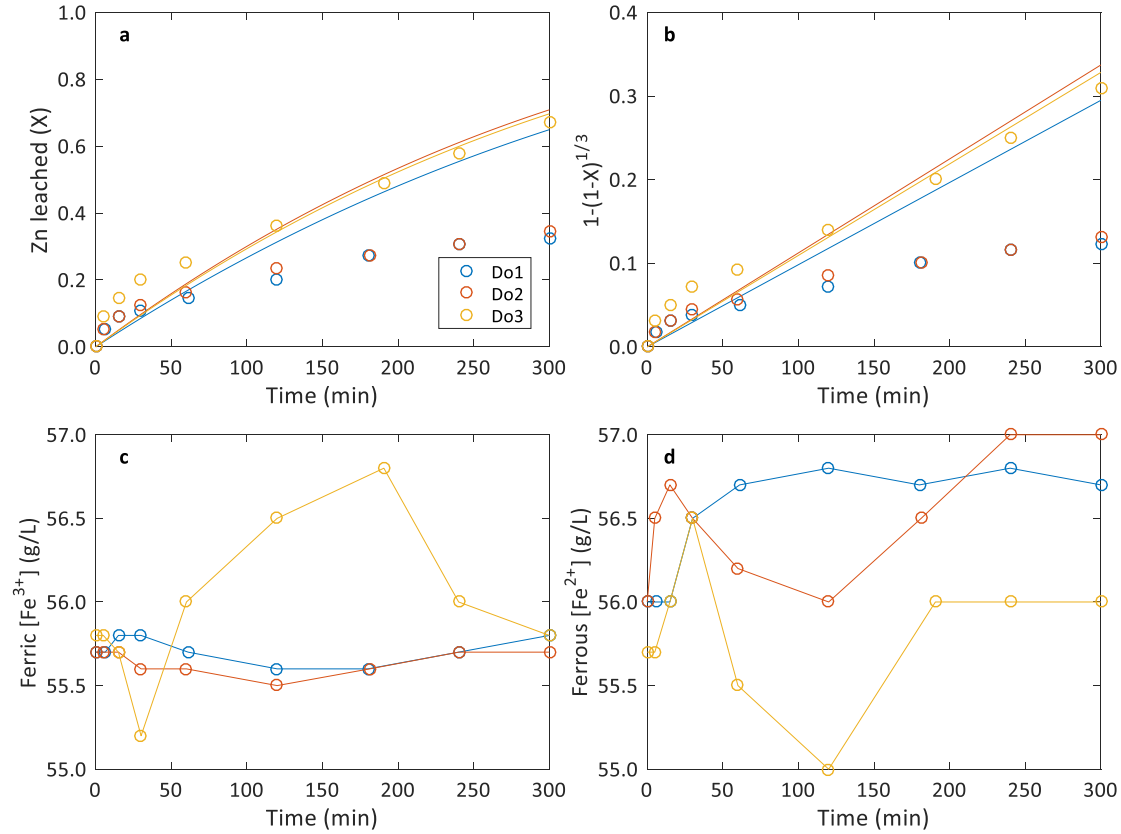

Figure D.15: Effect of acid concentration a) reaction extent b) shrinking core model c) ferric concentration profile and d) ferrous concentration profile

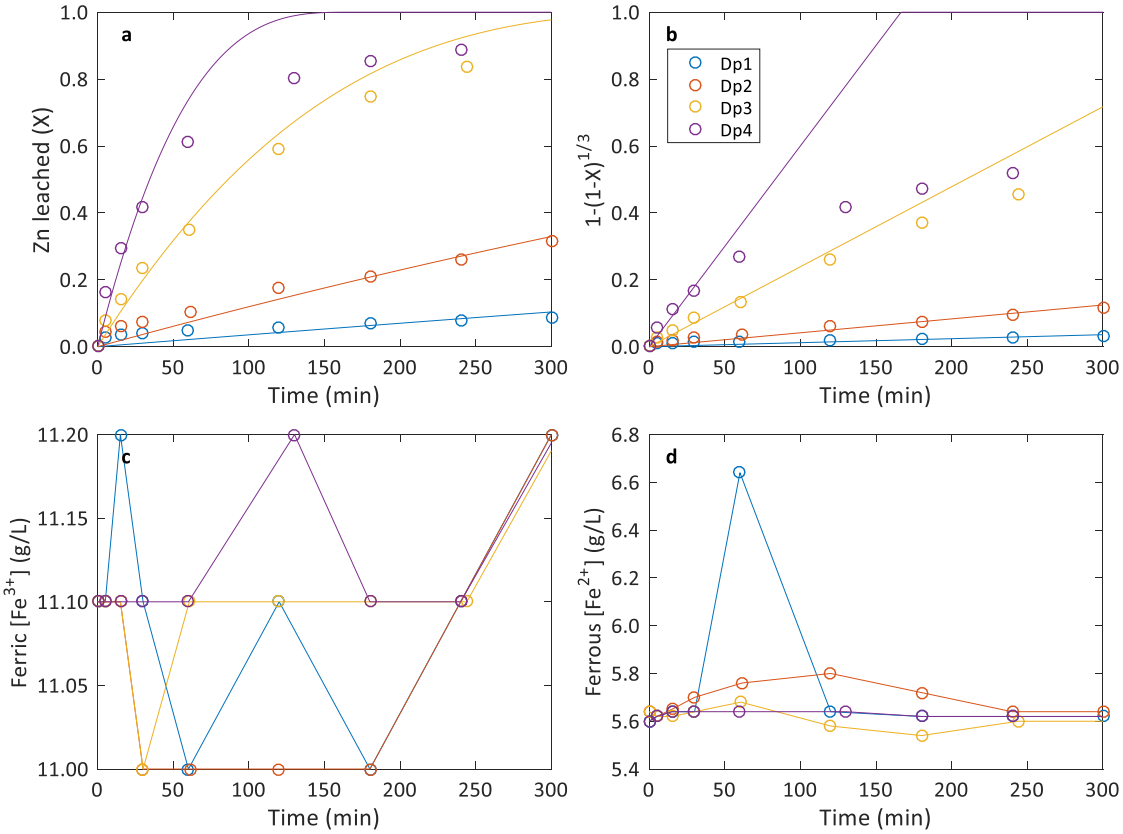

Figure D.16: Effect of temperature on concentrate Sf1 a) reaction extent b) shrinking core model c) ferric concentration profile and d) ferrous concentration profile

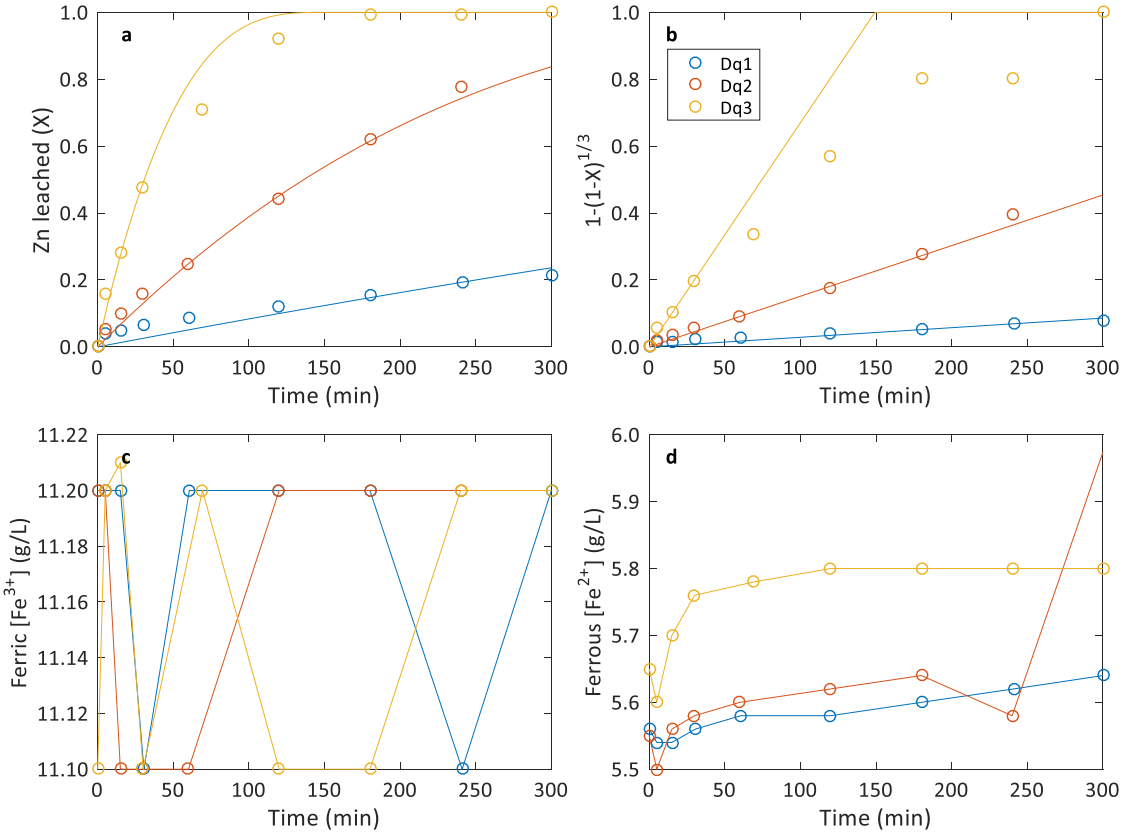

Figure D.17: Effect of temperature on concentrate Sf2 a) reaction extent b) shrinking core model c) ferric concentration profile and d) ferrous concentration profile

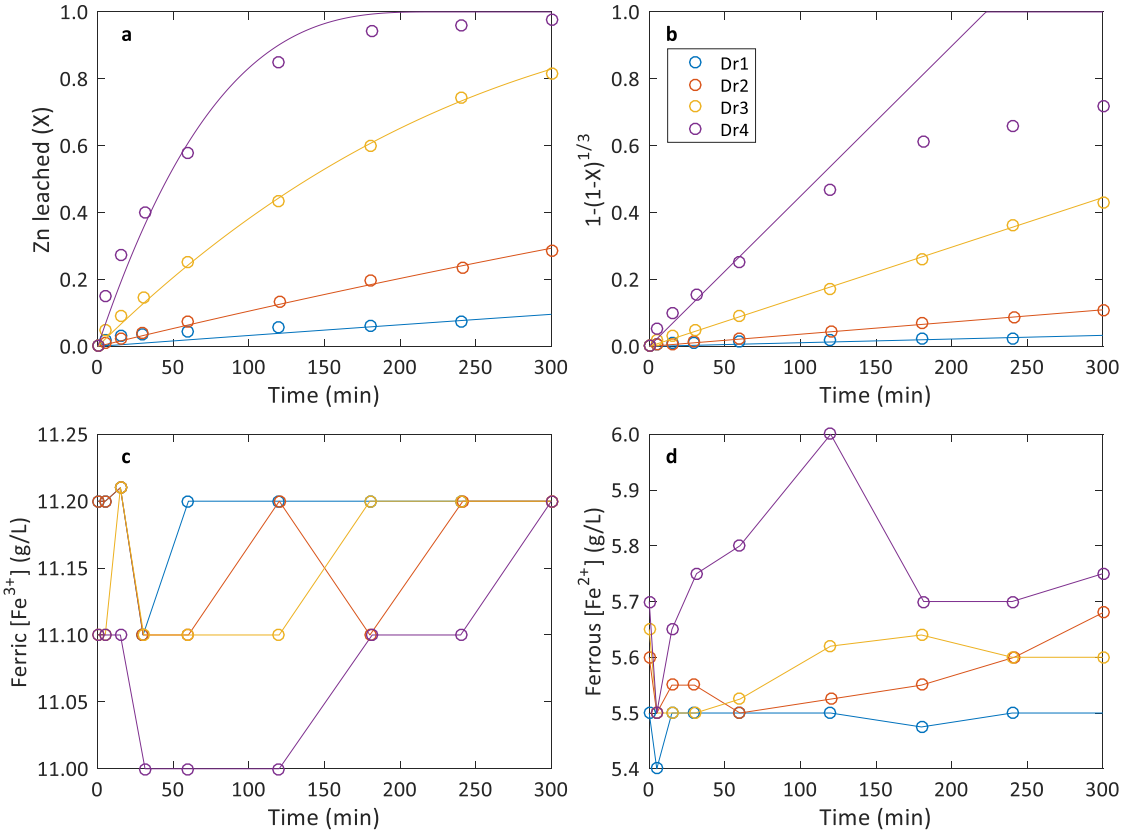

Figure D.18: Effect of temperature on concentrate Sf3 a) reaction extent b) shrinking core model c) ferric concentration profile and d) ferrous concentration profile

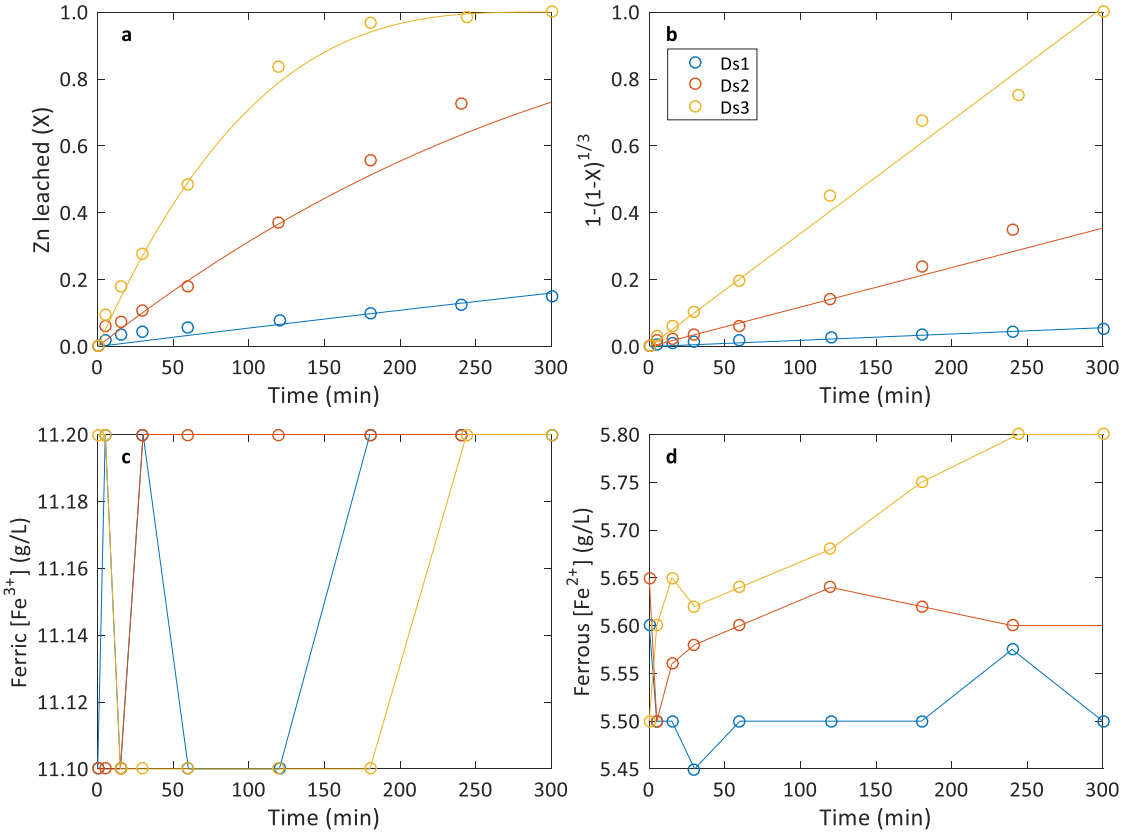

Figure D.19: Effect of temperature on concentrate Sf4 a) reaction extent b) shrinking core model c) ferric concentration profile and d) ferrous concentration profile

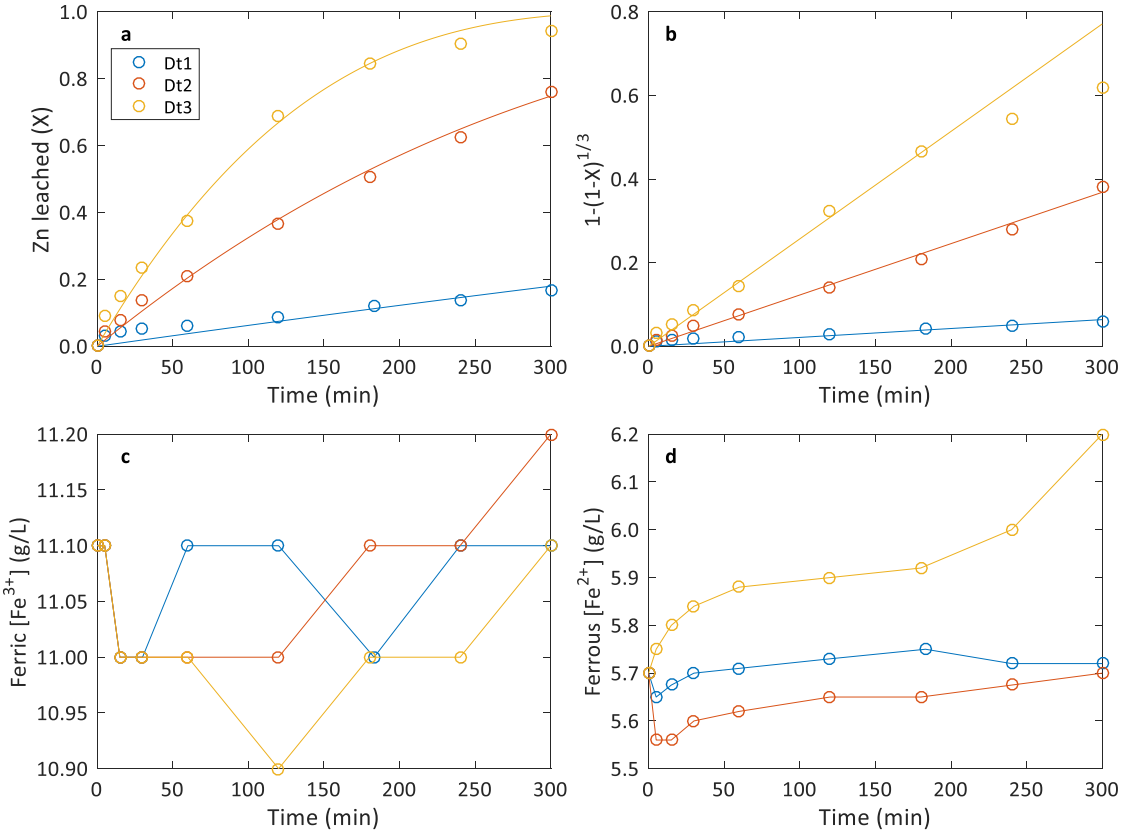

Figure D.20: Effect of temperature on concentrate Sf6 a) reaction extent b) shrinking core model c) ferric concentration profile and d) ferrous concentration profile

Appendix E Oxidative Experimental Results (Low Acid)

E.1 Summary of experimental conditions and kinetic constants

The batch experiments summarised in this section (shown in Table E.1) was performed with a 0.2 g/L of Sf3 (45-53 µm) concentrate solution under atmospheric pressure and a temperature of 90 °C. No ferrous or zinc was added to the initial solution. The solution was stirred at a speed of 650 rpm. The intrinsic rate constants were obtained by linear recreation of the initial rate during each batch experiment and tabulated below.

Table E.1: Initial conditions and experimentally obtained intrinsic rate constants within the respective evaluation ranges and corresponding average solution concentrations

Exp.	Initial conditions			Evaluation Range		Intrinsic rate constants		Average Concentrations			
	LS	$[H_2SO_4]$	$[Fe^{3+}]$	Extent	Time	k_s	k_l	$[H_2SO_4]$	$[Fe^{3+}]$	$[Fe^{2+}]$	$[Zn^{2+}]$
	(g/L)	(g/L)	(g/L)	(-)	(min)	(1/min)	(µm/min)	(g/L)	(g/L)	(g/L)	(g/L)
Ea1	0	2.8	1	0.4	78	2.262E-03	0.1445	2.80	0.95	0.06	0.01865
Ea2	0	2.8	2.2	0.6	82	3.222E-03	0.2059	2.79	2.15	0.05	0.02550
Ea3	0	2.7	3.3	0.6	73	3.727E-03	0.2382	2.71	3.25	0.05	0.02885
Eb1	0	7.1	1.1	0.4	73	2.351E-03	0.1502	7.12	1.05	0.05	0.01920
Eb2	0	7.1	3.41	0.4	64	2.719E-03	0.1738	7.11	3.36	0.06	0.02115
Eb3	0	7.1	11.2	0.4	35	4.803E-03	0.3069	7.11	11.15	0.05	0.01965
Eb4	0	7	27.8	0.4	38	4.485E-03	0.2866	7.02	27.75	0.08	0.01810
Eb5	0	6.9	55.8	0.4	114	1.713E-03	0.1095	6.95	55.75	0.04	0.01930
Ec1	0.001	7.2	1.1	0.5	143	1.607E-03	0.1027	7.22	1.05	0.08	0.02505
Ec2	0.01	7.2	1.1	0.5	75	2.976E-03	0.1901	7.21	1.05	0.08	0.02375
Ec3	0.1	7.1	1.1	0.5	72	3.097E-03	0.1979	7.11	1.00	0.10	0.02460
Ed1	0.001	7.1	11.2	0.5	47	4.757E-03	0.3040	7.11	11.15	0.05	0.01960
Ed2	0.01	7.1	11.2	0.5	38	6.007E-03	0.3838	7.10	11.15	0.08	0.02405
Ed3	0.1	7.1	11.1	0.5	45	5.129E-03	0.3277	7.11	11.05	0.14	0.02115
Ed4	0.5	7.1	10.8	0.5	55	4.425E-03	0.2827	7.11	10.75	0.51	0.01865
Ee1	0.001	7.2	55.8	0.6	93	2.784E-03	0.1779	7.21	55.75	0.09	0.03200
Ee2	0.01	7.1	55.8	0.6	68	3.826E-03	0.2445	7.12	55.75	0.09	0.02905
Ee3	0.1	7.2	55.8	0.6	65	4.337E-03	0.2772	7.21	55.65	0.15	0.03165

E.2 Summary of reaction extents

Figures presented in this section contains the relevant species concentration responses during the respective batch experiment. Each figure contains graphs showing the factional conversion of sphalerite (a), a corresponding shrinking core model plot (b) based on the fractional conversion and the ferric (c) and ferrous (d) concentration (g/L) gradients versus time (min).

The solid lines in (a) and (b) represents the best fit of the shrinking core model (SCM), within the respective evaluation rages and modelled according to the regressed intrinsic rate constants (k_s), as tabulated in Table E.1. While, the solid lines in (c) and (d) are linear connections between consecutive concentration data points, to indicate whether or not the concentration has a trend.

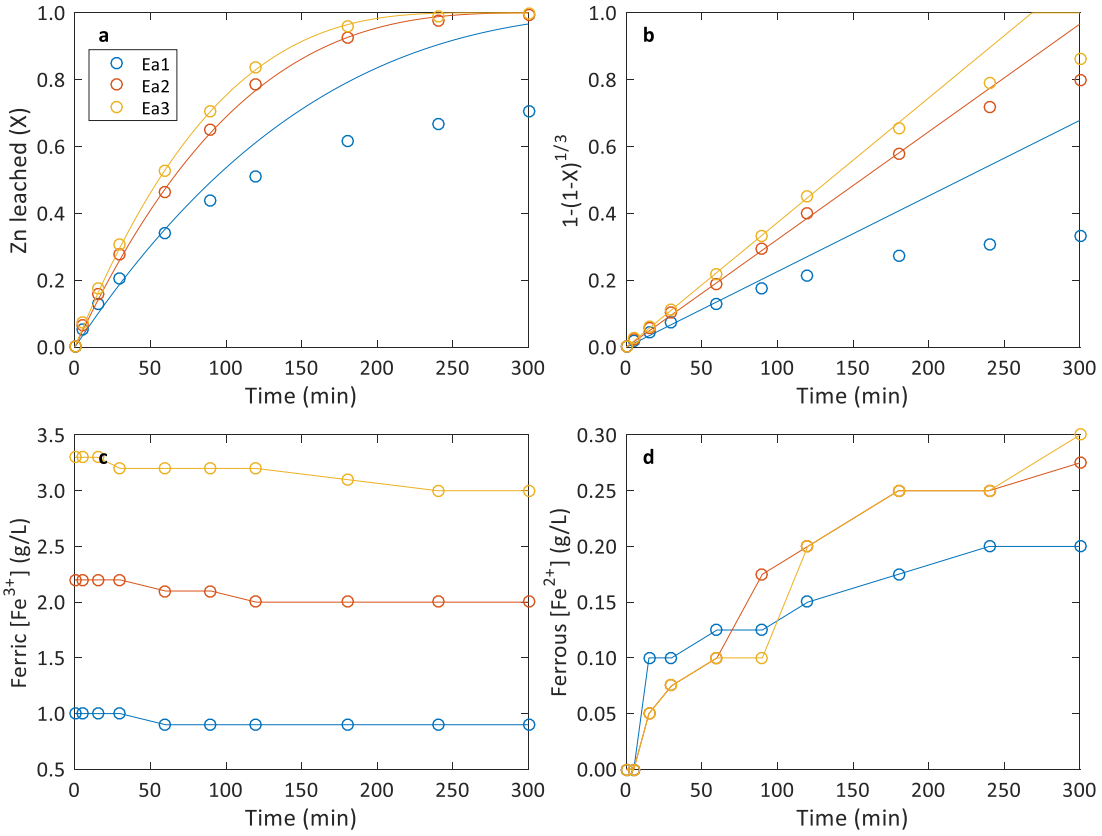

Figure E.1: Effect of ferric concentration at 2.8 g/L H_2SO_4 a) reaction extent b) shrinking core model c) ferric concentration profile and d) ferrous concentration profile

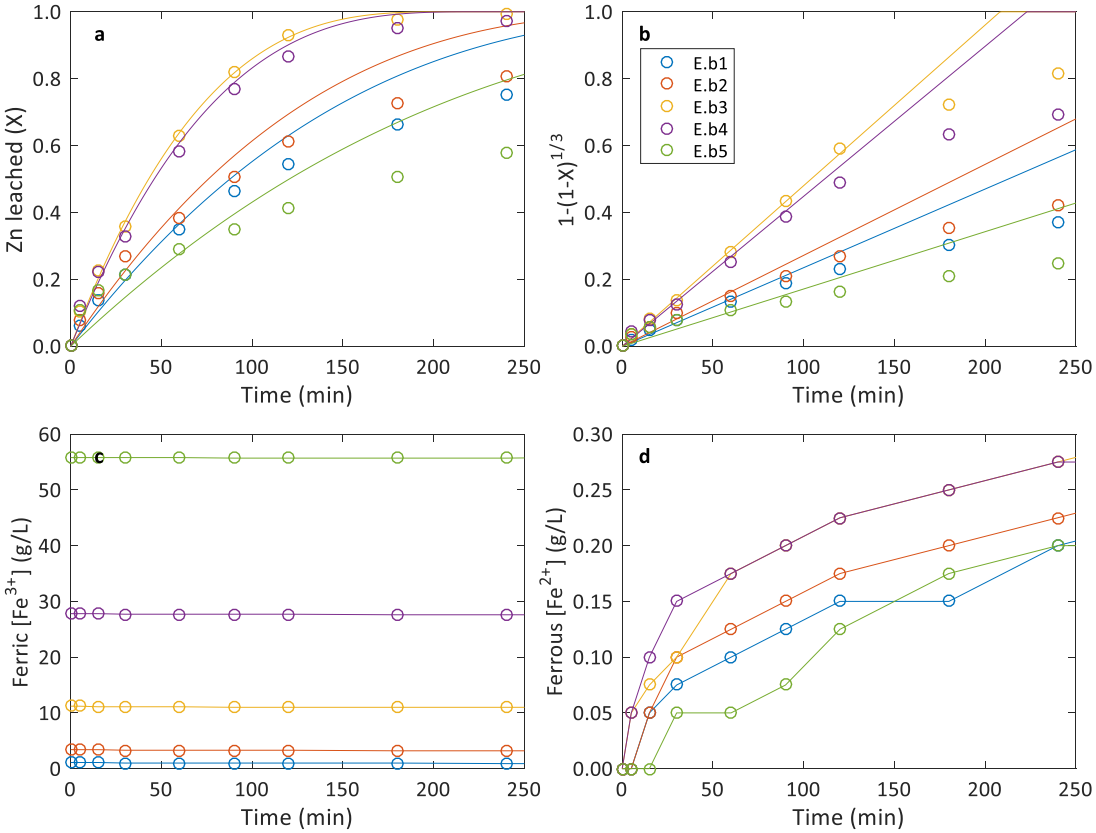

Figure E.2: Effect of ferric concentration at 7.1 g/L H_2SO_4 a) reaction extent b) shrinking core model c) ferric concentration profile and d) ferrous concentration profile

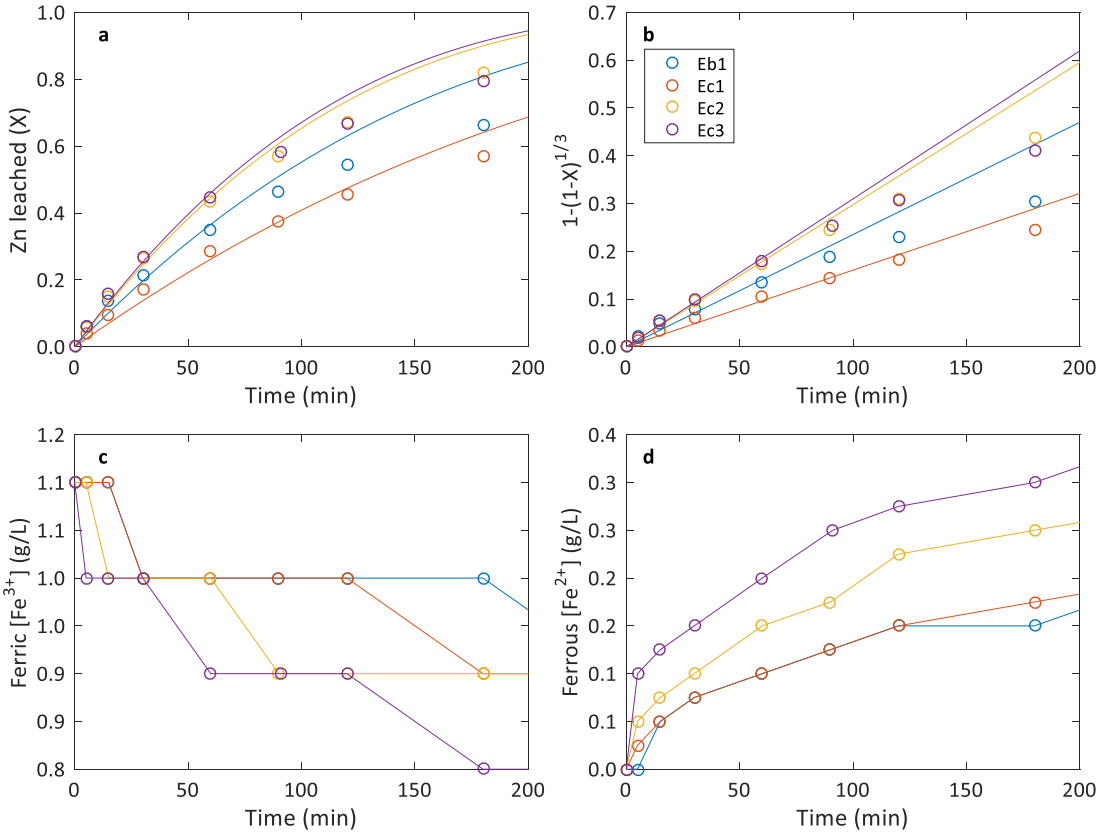

Figure E.3: Effect of surfactant concentration at 1 g/L Fe^{3+} a) reaction extent b) shrinking core model c) ferric concentration profile and d) ferrous concentration profile

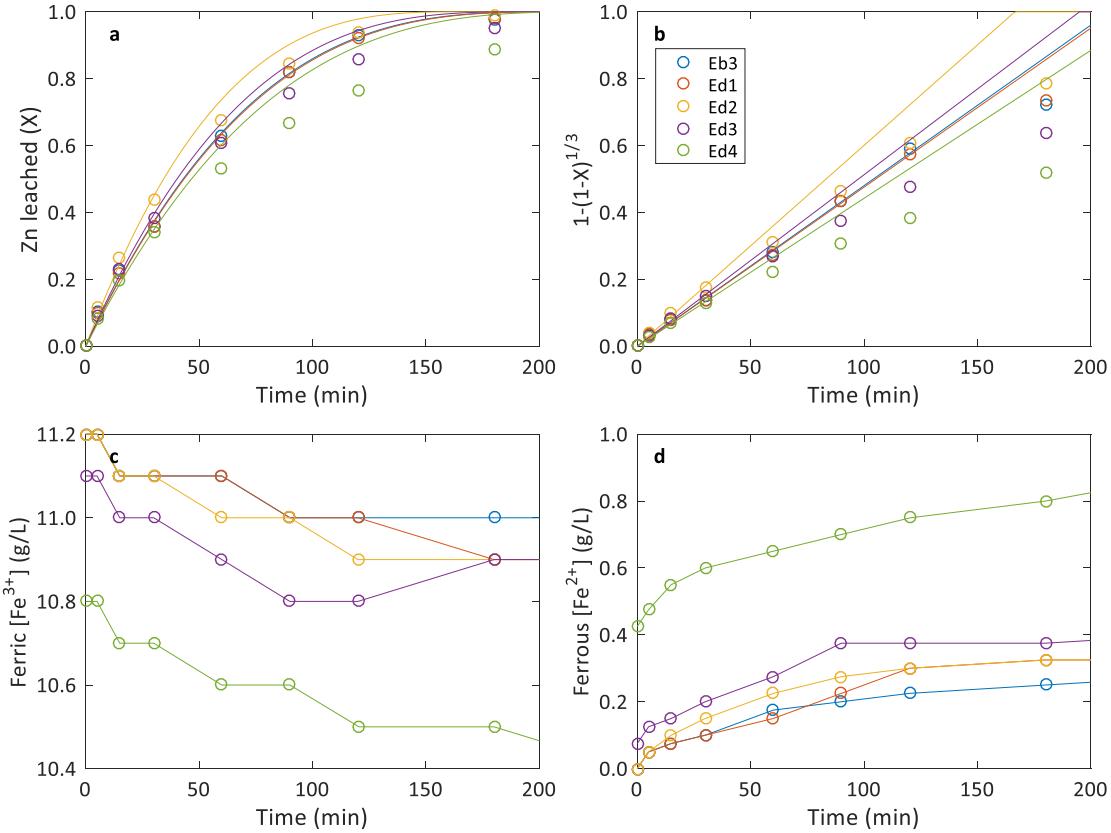

Figure E.4: Effect of surfactant concentration at 11.2 g/L Fe^{3+} a) reaction extent b) shrinking core model c) ferric concentration profile and d) ferrous concentration profile

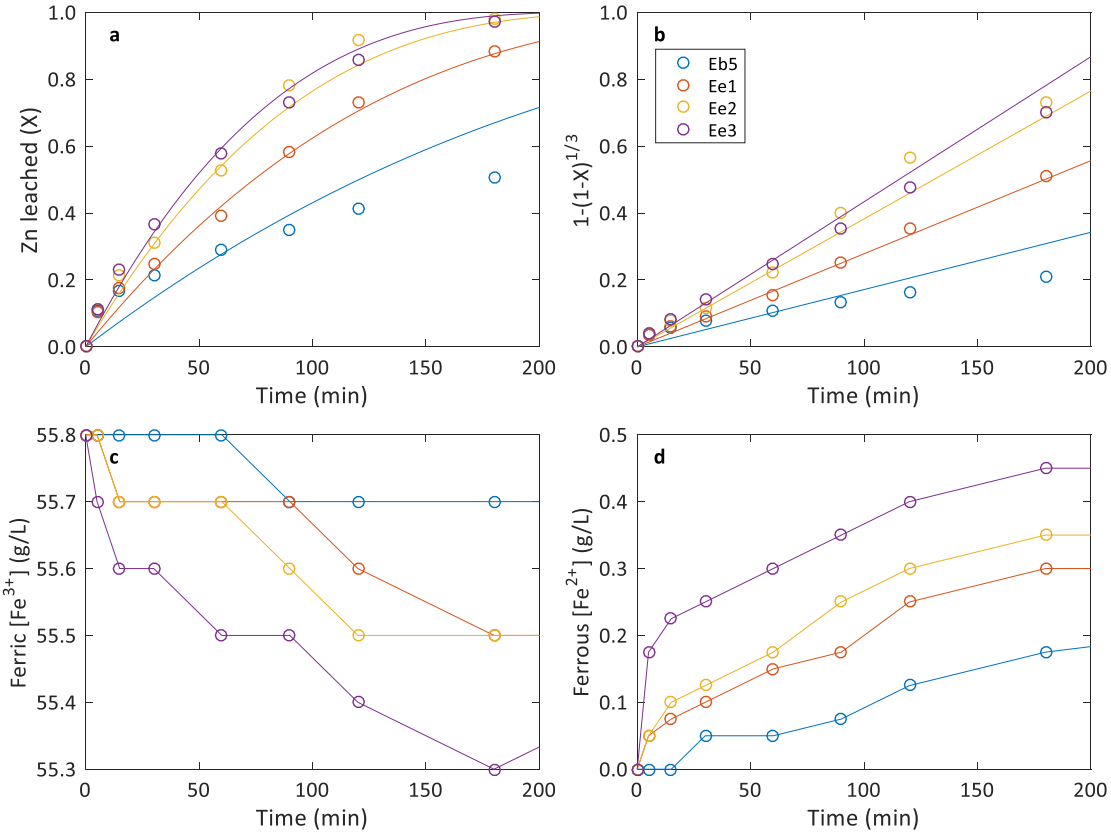

Figure E.5: Effect of surfactant concentration at 55.8 g/L Fe^{3+} a) reaction extent b) shrinking core model c) ferric concentration profile and d) ferrous concentration profile

Appendix F Oxidative Experimental Results (Higher Pulp Density)

F.1 Summary of experimental conditions and kinetic constants

The main oxidative experimental results for this project with their respective initial conditions are summarised in Table F.1. These kinetic batch tests were performed at an impeller speed of 650 rpm and with no added zinc to the initial solution.

Table F.1: Initial conditions of the oxidative batch experiments at higher pulp densities

Experiment	Temperature (°C)	Slurry Density (g/L)	Size fraction (µm)	LS (g/L)	$[H_2SO_4]_0$ (g/L)	$[Fe^{3+}]_0$ (g/L)	$[Fe^{2+}]_0$ (g/L)
Fa1	75	0.1072	45-53 (Sf3)	0	9.7	0.28	0.0
Fa2	85	0.0073	45-53 (Sf3)	0	9.7	0.27	0.0
Fa3	95	0.0357	45-53 (Sf3)	0	9.8	0.26	0.0
Fb1	75	0.1071	45-53 (Sf3)	0.01	49.0	0.26	0.0
Fb2	85	0.0714	45-53 (Sf3)	0.01	48.9	0.27	0.0
Fb3	95	0.0358	45-53 (Sf3)	0.01	48.8	0.27	0.0
Fc1	95	0.0269	45-53 (Sf3)	0.01	9.8	0.26	0.0
Fc2	95	0.0269	45-53 (Sf3)	0.10	9.8	0.22	0.1
Fc3	95	0.0269	45-53 (Sf3)	0.01	127.4	0.27	0.0
Fd1	95	1.7858	45-53 (Sf3)	0.00	127.5	28.00	0.0
Fd2	95	1.7857	45-53 (Sf3)	0.01	127.4	27.90	0.0
Fd3	95	1.7858	45-53 (Sf3)	0.10	127.4	27.90	0.1
Fe1	95	2.6785	45-53 (Sf3)	0.00	9.7	27.90	0.0
Fe2	95	2.6786	45-53 (Sf3)	0.01	9.6	28.00	0.0
Fe3	95	2.6787	45-53 (Sf3)	0.10	9.7	27.80	0.1
Ff1	75	2.6787	45-53 (Sf3)	0.01	49.0	27.90	0.0
Ff2	85	2.6787	45-53 (Sf3)	0.01	49.0	27.90	0.0
Ff3	95	2.6785	45-53 (Sf3)	0.01	48.9	27.90	0.0
Fg1	75	2.6786	45-53 (Sf3)	0.01	9.8	5.60	0.0
Fg2	85	2.6785	45-53 (Sf3)	0.01	9.7	5.60	0.0
Fg3	95	2.6787	45-53 (Sf3)	0.01	9.8	5.70	0.0
Fh1	95	2.6787	45-53 (Sf3)	0.01	49.0	5.70	0.0
Fh2	95	2.6787	45-53 (Sf3)	0.01	127.4	5.70	0.0
[a]Fi1	95	2.6787	45-53 (Sf3)	0.01	49.0	5.70	0.0

[a]Experiment was pre-saturated with O_2 (medical grade) at 1000 kPa gauge and kept constant

Table F.1: Initial conditions of the oxidative batch experiments at higher pulp densities, continue

Experiment	Temperature (°C)	Slurry Density (g/L)	Size fraction (µm)	LS (g/L)	$[H_2SO_4]_0$ (g/L)	$[Fe^{3+}]_0$ (g/L)	$[Fe^{2+}]_0$ (g/L)
Fj1	95	2.6786	45-53 (Sf3)	0.01	49.0	1.12	0.0
Fj2	95	2.6786	45-53 (Sf3)	0.01	48.9	11.10	0.0
Fj3	95	2.6786	45-53 (Sf3)	0.01	49.0	19.60	0.0
Fj4	95	2.6786	45-53 (Sf3)	0.01	48.9	39.10	0.0
Fk1	95	2.6787	25-38 (Sf1)	0.01	48.9	19.60	0.0
Fk2	95	2.6786	38-45 (Sf2)	0.01	48.9	19.80	0.0
Fk3	95	2.6786	53-75 (Sf4)	0.01	48.8	19.60	0.0
Fk4	95	2.6786	75-90 (Sf5)	0.01	48.9	19.60	0.0
Fk5	95	2.6785	90-106 (Sf6)	0.01	48.9	19.70	0.0
Fl1	95	2.6857	38-45 (Sf2)	0.01	48.8	19.60	14.1
Fl2	95	2.6787	38-45 (Sf2)	0.01	48.9	19.60	27.9
Fl3	95	2.6787	38-45 (Sf2)	0.01	48.9	19.60	42.2
Fm1	95	2.6786	38-45 (Sf2)	0.01	48.9	5.60	0.0
Fm2	95	2.6786	38-45 (Sf2)	0.01	48.8	5.60	14.0
Fm3	95	2.6785	38-45 (Sf2)	0.01	48.9	5.60	27.9
Fm4	95	2.6786	38-45 (Sf2)	0.01	48.9	5.60	41.9
Fn1	95	2.6786	38-45 (Sf2)	0.01	9.8	5.60	0.0
Fn2	95	2.6785	38-45 (Sf2)	0.01	9.8	5.60	27.9
Fn3	95	2.6787	38-45 (Sf2)	0.01	127.4	5.60	0.0
Fn4	95	2.6786	38-45 (Sf2)	0.01	127.4	5.60	27.9
Fo1	75	2.6786	38-45 (Sf2)	0.01	48.9	5.60	0.0
Fo2	75	2.6785	38-45 (Sf2)	0.01	48.8	5.60	27.8
Fo3	85	2.6786	38-45 (Sf2)	0.01	49.0	5.60	0.0
Fo4	85	2.6786	38-45 (Sf2)	0.01	48.9	5.60	27.8
[a]Fp1	95	2.6798	45-53 (Sf3)	0.01	127.3	5.60	0.0
Fp2	95	15	45-53 (Sf3)	0.1	99.8	17.3	0

[a]Experiment was pre-saturated with O_2 (medical grade) at 1000 kPa gauge and kept constant

Table F.2: Experimentally obtained intrinsic rate constants within the respective evaluation ranges and corresponding average solution concentrations

Experiment	Evaluation Range		Mean particle size	Intrinsic rate constants		Average Concentrations			
	Extent	Time	d_p	k_s	k_l	$[H_2SO_4]$	$[Fe^{3+}]$	$[Fe^{2+}]$	$[Zn^{2+}]$
	(fraction)	(min)	(µm)	(1/min)	(µm/min)	(g/L)	(g/L)	(g/L)	(g/L)
Fa1	0.10	48	63.9	8.34E-04	0.0266	9.75	0.28	0	0.00287
Fa2	0.15	32	63.9	2.02E-03	0.0645	9.75	0.27	0	0.00029
Fa3	0.20	32	63.9	2.60E-03	0.0832	9.84	0.27	0	0.00187
Fb1	0.10	42	63.9	1.04E-03	0.0331	49.02	0.26	0	0.00238
Fb2	0.20	39	63.9	2.18E-03	0.0698	48.96	0.27	0	0.00328
Fb3	0.20	16	63.9	4.82E-03	0.1539	48.85	0.27	0	0.00188
Fc1	0.30	33	63.9	4.20E-03	0.1343	9.84	0.26	0.023	0.00210
Fc2	0.26	35	63.9	3.29E-03	0.1051	9.83	0.22	0.054	0.00185
Fc3	0.30	25	63.9	4.97E-03	0.1586	127.46	0.27	0.012	0.00191
Fd1	0.30	8	63.9	1.54E-02	0.4923	127.52	27.91	0.099	0.13250
Fd2	0.30	9	63.9	1.43E-02	0.4583	127.42	27.75	0.181	0.12550
Fd3	0.30	8	63.9	1.49E-02	0.4776	127.43	27.76	0.260	0.13100
Fe1	0.30	17	63.9	7.62E-03	0.2435	9.73	27.63	0.282	0.20600
Fe2	0.30	13	63.9	9.72E-03	0.3105	9.64	27.79	0.242	0.19150
Fe3	0.30	11	63.9	1.10E-02	0.3521	9.72	27.61	0.300	0.20200
Ff1	0.30	20	63.9	5.78E-03	0.1847	49.02	27.69	0.223	0.17300
Ff2	0.40	27	63.9	5.72E-03	0.1828	49.03	27.61	0.309	0.22250
Ff3	0.40	20	63.9	7.92E-03	0.2530	48.95	27.59	0.350	0.22500
Fg1	0.45	57	63.9	3.35E-03	0.1071	9.82	5.18	0.472	0.26950
Fg2	0.45	39	63.9	5.01E-03	0.1602	9.77	5.14	0.502	0.27950
Fg3	0.45	27	63.9	7.65E-03	0.2446	9.86	5.34	0.407	0.27150
Fh1	0.45	22	63.9	9.00E-03	0.2875	49.07	5.37	0.365	0.31700
Fh2	0.45	25	63.9	8.27E-03	0.2643	127.48	5.32	0.405	0.28950
Fi1	0.45	21	63.9	9.89E-03	0.3161	49.06	5.38	0.339	0.32350
Fj1	0.15	14	63.9	4.22E-03	0.1349	49.05	1.05	0.080	0.08300
Fj2	0.40	20	63.9	9.19E-03	0.2937	48.97	10.78	0.353	0.25500
Fj3	0.32	12	63.9	1.10E-02	0.3509	49.03	19.42	0.199	0.21000
Fj4	0.32	11	63.9	1.18E-02	0.3782	48.93	38.92	0.200	0.22850

Table F.2: Experimentally obtained intrinsic rate constants within the respective evaluation ranges and corresponding average solution concentrations, continued

Experiment	Evaluation Range		Mean particle size	Intrinsic rate constants		Average Concentrations			
	Extent (fraction)	Time (min)	d_p (µm)	k_s (1/min)	k_l (µm/min)	$[H_2SO_4]$ (g/L)	$[Fe^{3+}]$ (g/L)	$[Fe^{2+}]$ (g/L)	$[Zn^{2+}]$ (g/L)
Fk1	0.40	9	43.90	1.75E-02	0.3847	48.92	19.43	0.190	0.24300
Fk2	0.40	13	56.11	1.37E-02	0.3839	48.94	19.57	0.259	0.25600
Fk3	0.32	16	81.35	8.81E-03	0.3583	48.85	19.39	0.234	0.21700
Fk4	0.32	18	105.32	7.10E-03	0.3740	48.93	19.42	0.202	0.19850
Fk5	0.20	12	127.34	6.09E-03	0.3875	48.92	19.55	0.158	0.11400
Fl1	0.40	16	56.11	1.01E-02	0.2828	48.85	19.32	14.436	0.28900
Fl2	0.40	20	56.11	8.18E-03	0.2296	48.95	19.31	28.259	0.25050
Fl3	0.40	28	56.11	6.11E-03	0.1713	48.96	19.23	42.663	0.23350
Fm1	0.40	14	56.11	1.23E-02	0.3460	48.94	5.36	0.258	0.24000
Fm2	0.40	23	56.11	7.24E-03	0.2032	48.88	5.27	14.378	0.27400
Fm3	0.40	42	56.11	4.16E-03	0.1166	49.04	5.15	28.490	0.23650
Fm4	0.30	46	56.11	2.61E-03	0.0733	49.00	5.12	42.431	0.22350
Fn1	0.40	19	56.11	9.10E-03	0.2554	9.85	5.30	0.320	0.25700
Fn2	0.20	38	56.11	2.02E-03	0.0568	9.88	5.39	28.345	0.12250
Fn3	0.40	14	56.11	1.18E-02	0.3309	127.45	5.38	0.241	0.23150
Fn4	0.40	24	56.11	6.85E-03	0.1922	127.47	5.25	28.315	0.26100
Fo1	0.40	39	56.11	4.32E-03	0.1213	49.01	5.12	0.525	0.25000
Fo2	0.20	62	56.11	1.22E-03	0.0343	48.98	5.39	28.084	0.14700
Fo3	0.40	24	56.11	6.86E-03	0.1925	49.05	5.24	0.387	0.26550
Fo4	0.20	34	56.11	2.17E-03	0.0610	48.96	5.42	28.041	0.13550
[a]Fp1	0.40	11	63.9	1.47E-02	0.4682	127.32	5.48	0.134	0.27300
Fp2	0.40	20	63.9	7.56-03	0.2382	99.8	7.3	10.2	5.46

[a]Experiment was pre-saturated with O_2 (medical grade) at 1000 kPa gauge and kept constant

F.2 Summary of reaction extents

Figures presented in this section contains the relevant species concentration responses during the respective batch experiment. Each figure contains graphs showing the factional conversion of sphalerite (a), a corresponding shrinking core model plot (b). Only the initial and final sulphuric acid, ferric and ferrous concentration were measured and, hence, is assumed to follow linear behaviour through the batch test or remained approximately constant (see average solution composition within the evaluation rage in Table F.2.

Solid lines in the figures represents the best fit of the shrinking core model (SCM), within the respective evaluation rages and modelled according to the regressed intrinsic rate constants (k_s), as tabulated in Table F.2.

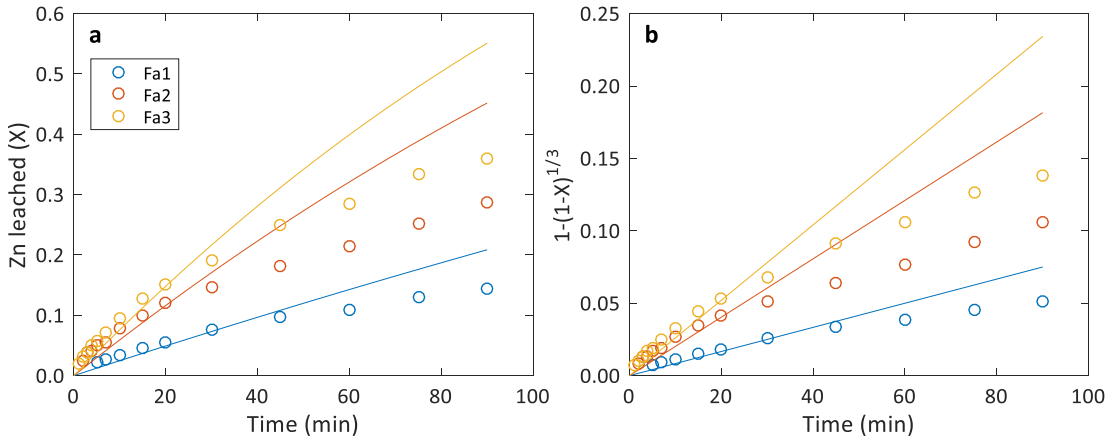

Figure F.1: Effect of temperature at 0.1 M H_2SO_4 a) reaction extent b) shrinking core model

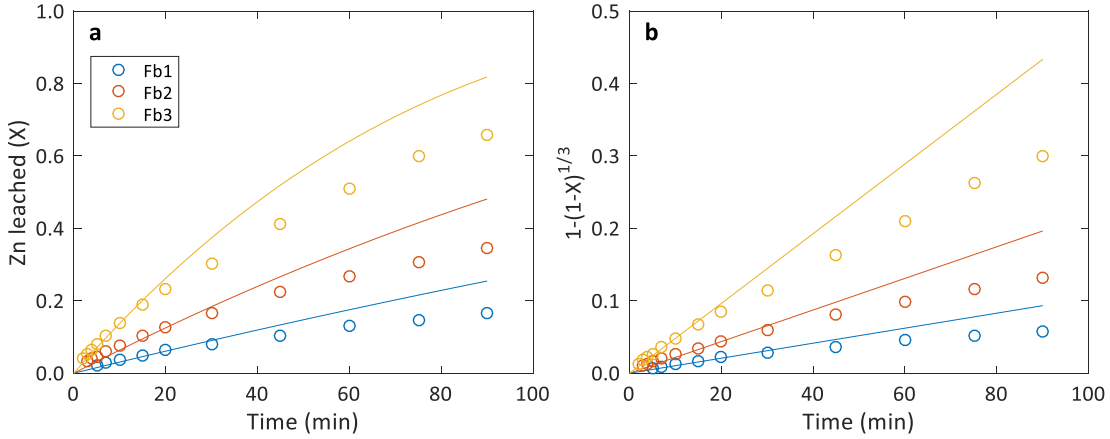

Figure F.2: Effect of temperature at 0.5 M H_2SO_4 a) reaction extent b) shrinking core model

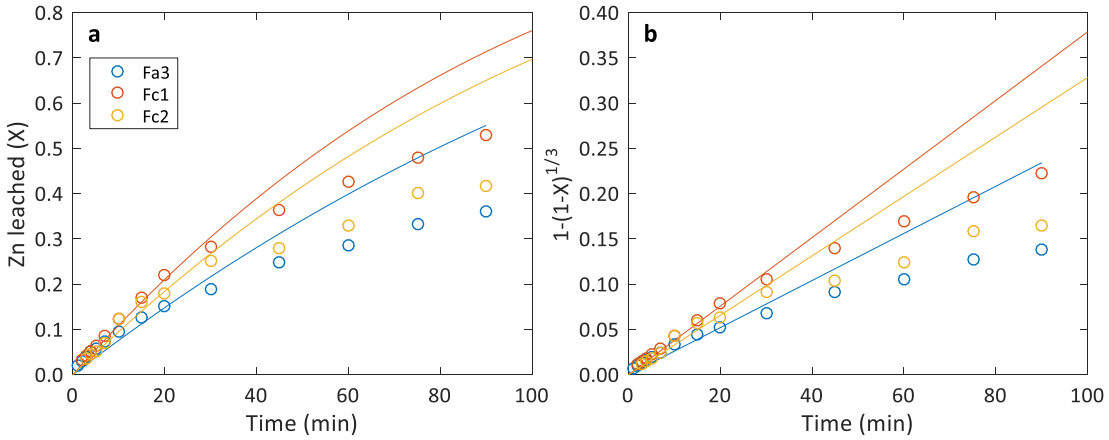

Figure F.3: Effect of lignosulphonate concentration at 0.1 M H_2SO_4 a) reaction extent b) shrinking core model

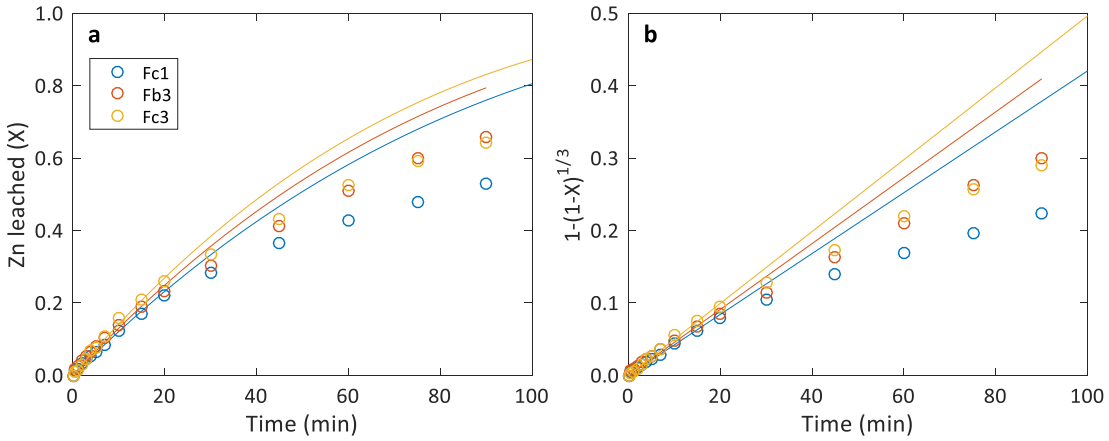

Figure F.4: Effect of acid concentration at 0.27 g/L Sf3 concentrate a) reaction extent b) shrinking core model

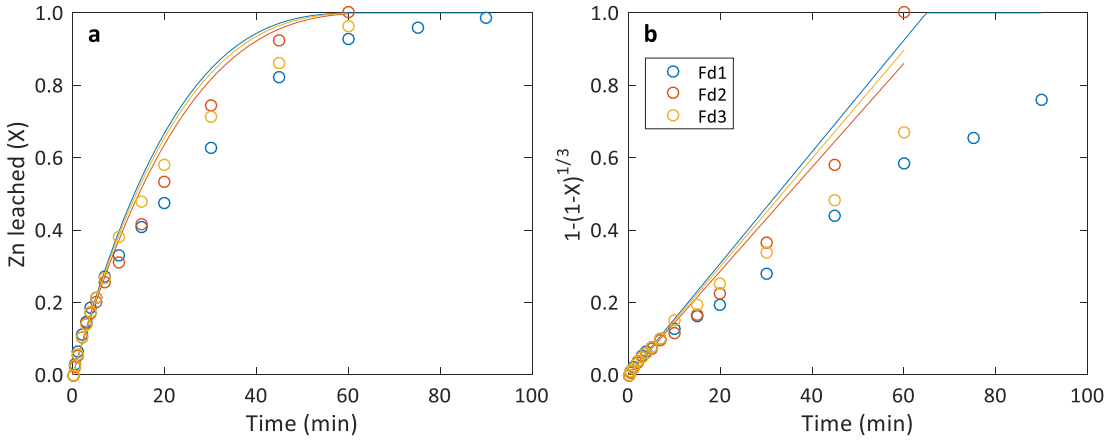

Figure F.5: Effect of lignosulphonate concentration a) reaction extent b) shrinking core model

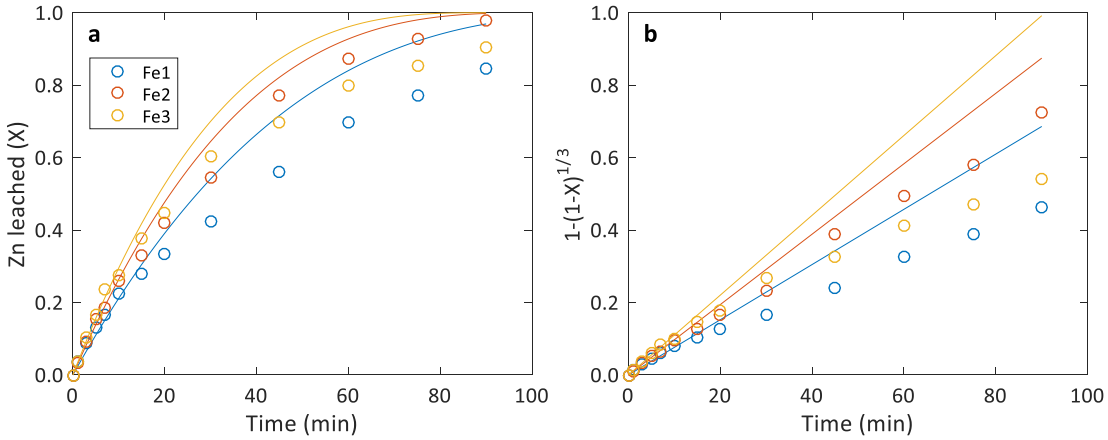

Figure F.6: Effect of lignosulphonate concentration a) reaction extent b) shrinking core model

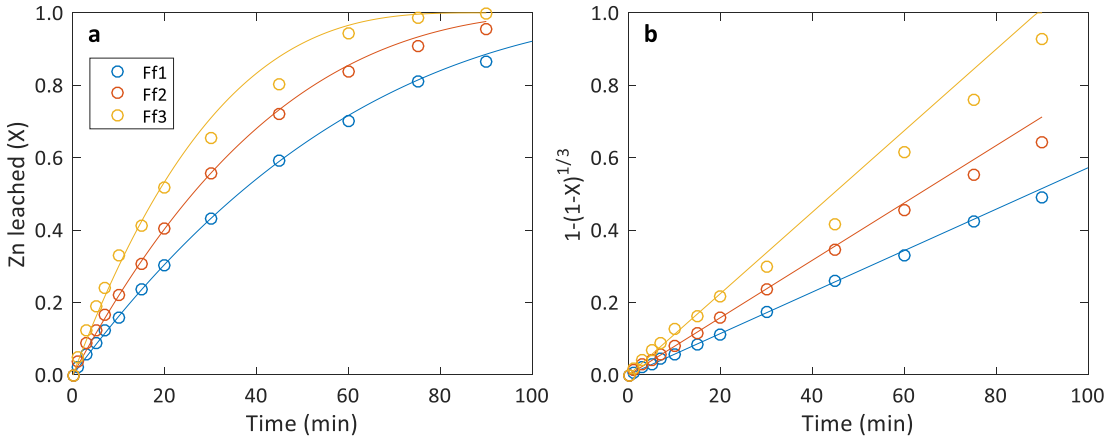

Figure F.7: Effect of temperature at 0.5 M H_2SO_4 a) reaction extent b) shrinking core model

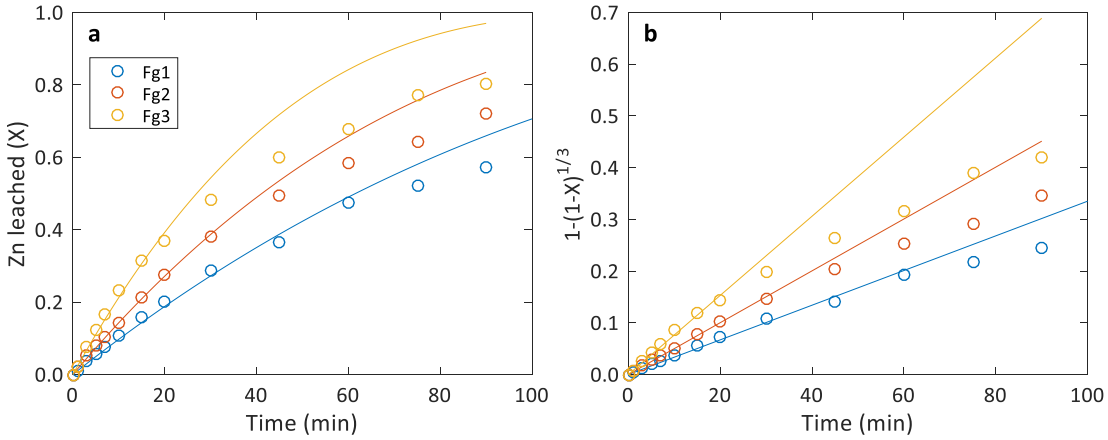

Figure F.8: Effect of temperature at 0.1 M H_2SO_4 a) reaction extent b) shrinking core model

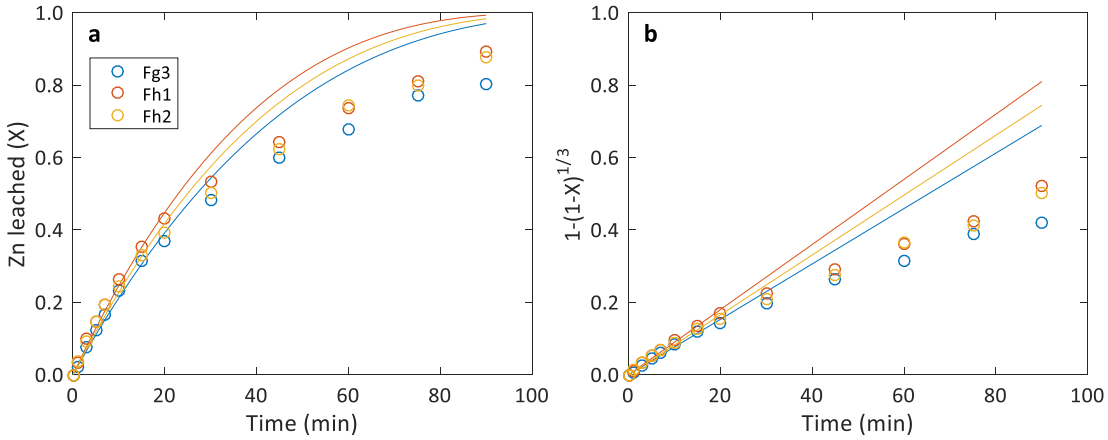

Figure F.9: Effect of acid concentration a) reaction extent b) shrinking core model

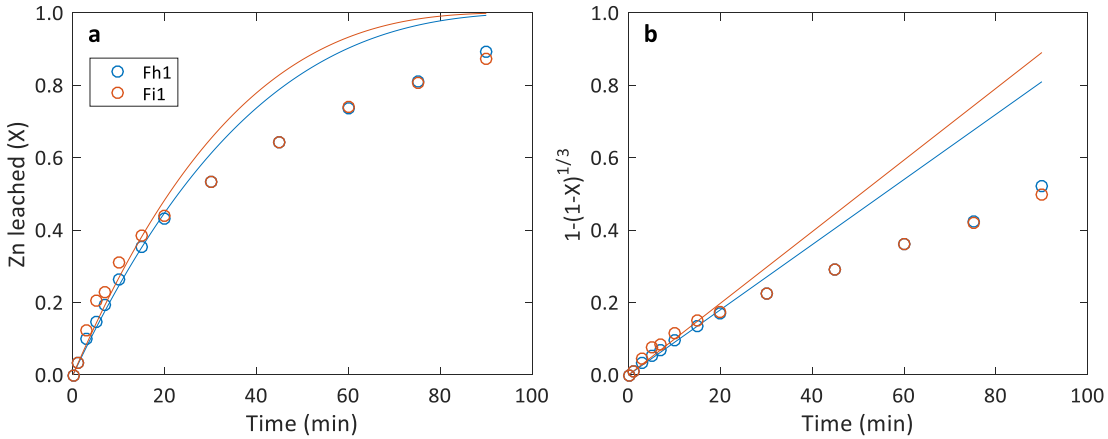

Figure F.10: Repeated experiments a) reaction extent b) shrinking core model

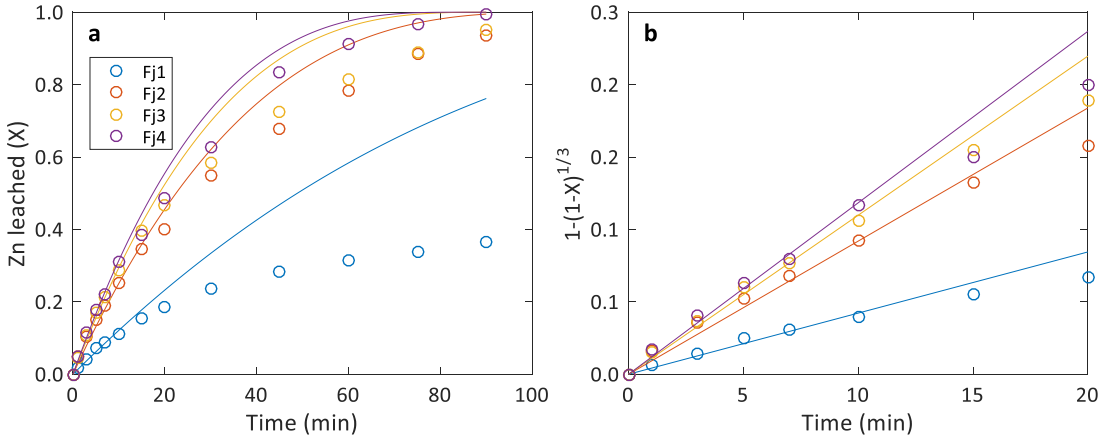

Figure F.11: Effect of ferric concentration a) reaction extent b) shrinking core model

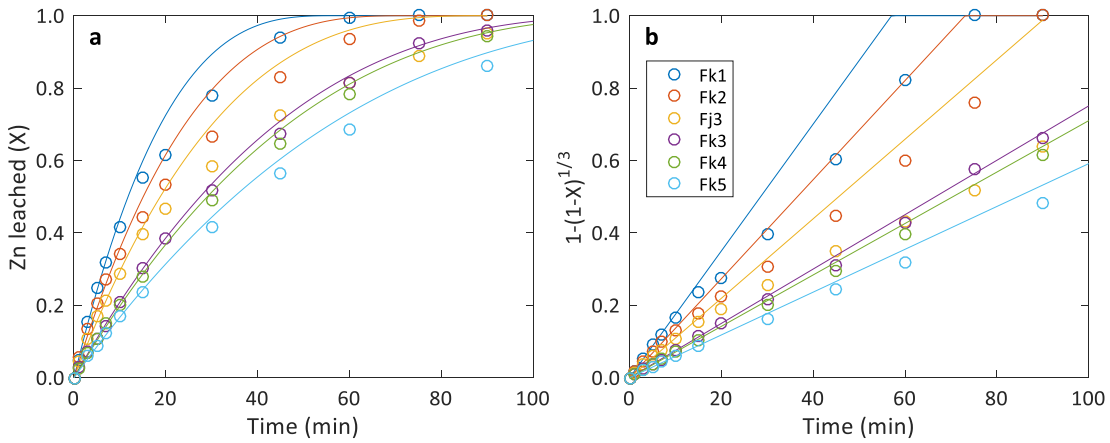

Figure F.12: Effect of particle size a) reaction extent b) shrinking core model

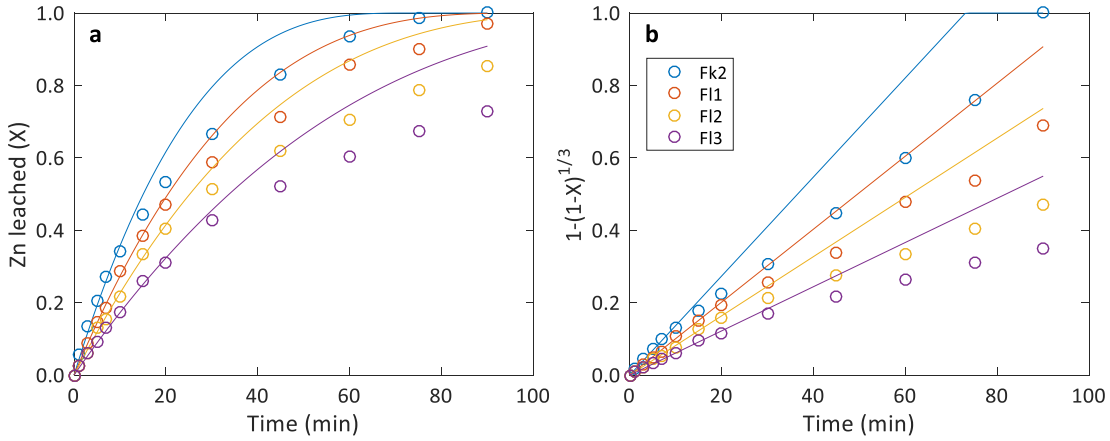

Figure F.13: Effect of ferrous (Fe^{2+}) concentration a) reaction extent b) shrinking core model

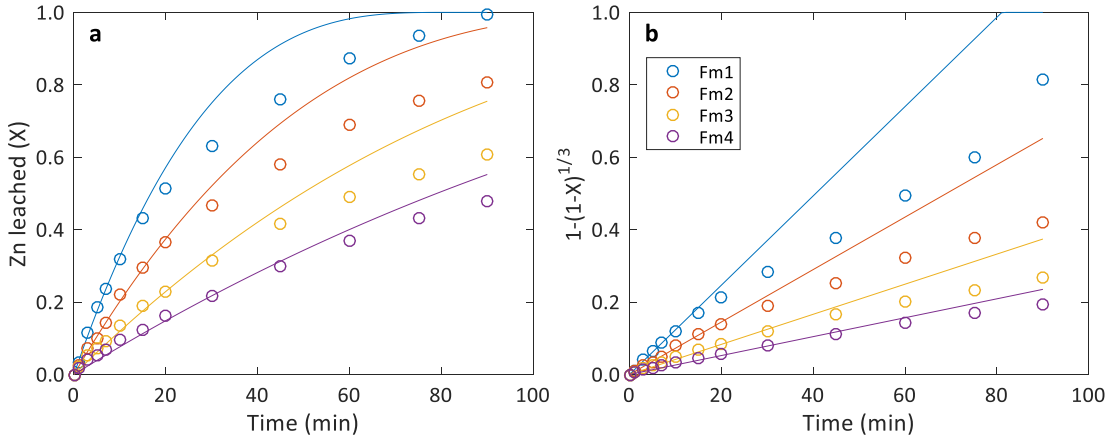

Figure F.14: Effect of ferrous (Fe^{2+}) concentration a) reaction extent b) shrinking core model

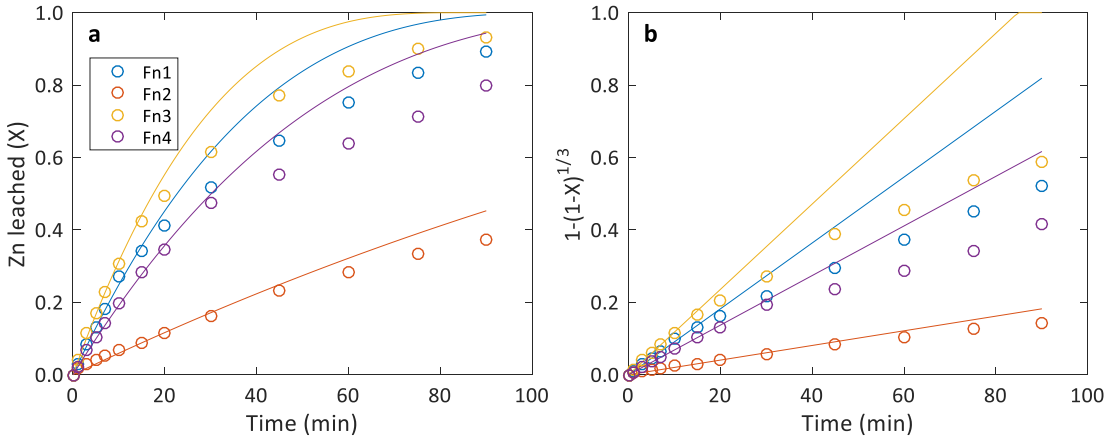

Figure F.15: Effect of ferrous (Fe^{2+}) and acid (H_2SO_4) concentration a) reaction extent b) shrinking core model

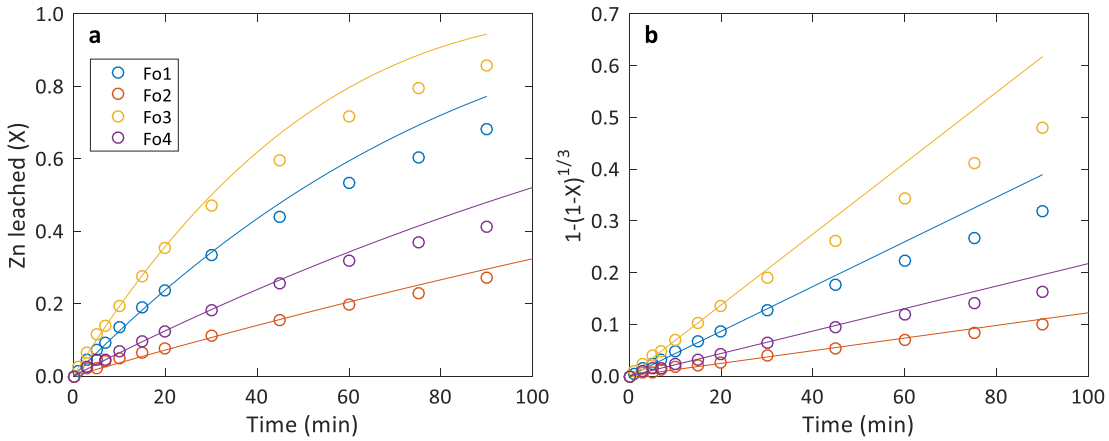

Figure F.16: Effect of temperature at various ferric to ferrous ratios concentration a) reaction extent b) shrinking core model

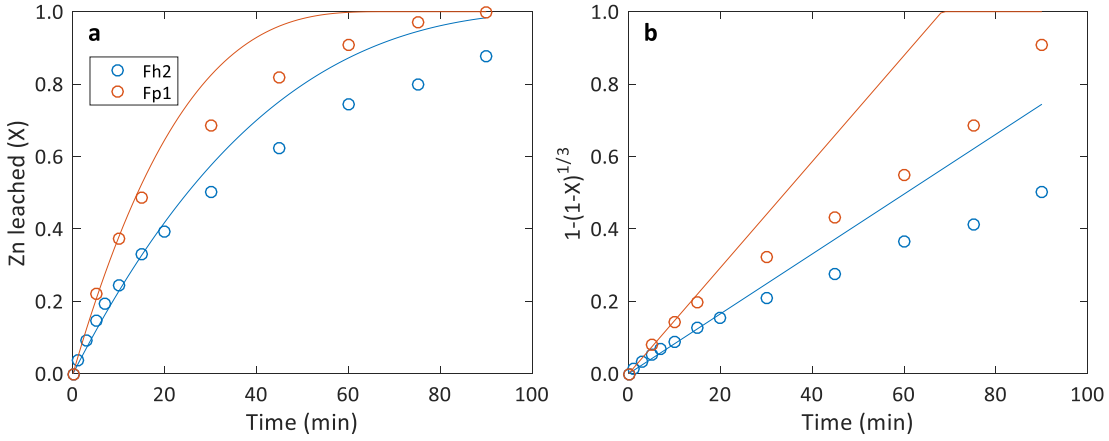

Figure F.17: Effect of oxygen partial pressure a) reaction extent b) shrinking core model

Appendix G Statistical Calculations

G.1 Statistical descriptions

- Sum of squared error (SSE)

Measures the total deviation of the response values from the fit to the response values. A value closer to 0 indicates that the model has a smaller random error component, and that the fit will be more useful for prediction.

$$SSE = \sum_{i}^{n} \left(x_i^{exp} - x_i^{sim}\right)^2 \quad \text{G.1}$$

- Coefficient of determination (R^2)

Measures how successful the fit is in explaining the variation of the data. Defined as the ratio of the sum of squares of the regression (SSR) and the total sum of squares (SST).

$$SSR = \sum_{i}^{n} \left(x_i^{sim} - \bar{x}_i\right)^2 \quad \text{G.2}$$

$$SST = \sum_{i}^{n} \left(x_i^{exp} - \bar{x}_i\right)^2 \quad \text{G.3}$$

$$R^2 = \frac{SSR}{SST} = 1 - \frac{SSE}{SST} \quad \text{G.4}$$

A value closer to 1 indicates that a greater proportion of variance is accounted for by the model, hence a better fit. Note that comparison of R squired between models can only be done if they have the same number of degrees of freedom.

- Root mean squared error (RMSE)

RMSE is an estimate of the standard deviation of the random component in the data. Just as in SSE, if the RMSE value is closer to 0 it indicates a fit that is more useful for prediction.

$$RMSE = \sqrt{\frac{1}{n}\sum_{i}^{n} \left(x_i^{exp} - x_i^{sim}\right)^2} \quad \text{G.5}$$

- Mean absolute error (MAE)

The mean absolute error is a quantity used to measure how close repeated or predicted data are to the eventual outcome. Hence, measures the average magnitude of the errors in a set of data, without considering their direction. It measures accuracy for continuous variables.

$$MAE = \frac{1}{n}\sum_{i}^{n}\left|x_i^{exp1} - x_i^{exp2\ or\ sim}\right| = \frac{1}{n}\sum_{i}^{n}|\varepsilon_i| \quad \text{G.6}$$

- Average absolute relative error (AARD) or mean absolute percentage error (MAPE)

AARD is a measure of prediction accuracy of a forecasting method in statistics, e.g. in trend estimation. It usually expresses accuracy as a percentage.

$$AARD = \frac{100}{n}\sum_{i}^{n}\left|\frac{x_i^{exp1} - x_i^{exp2\ or\ sim}}{x_i^{exp1}}\right| \quad \text{G.7}$$

- Uncertainty and uncertainty propagation

While many scientific investigations make use of data, statistics is concerned with the use of data in the context of uncertainty and decision making in the face of uncertainty. Expressing uncertainty in terms of uncertainty parameter:

$$\bar{x} + \Delta_x \quad \text{G.8}$$

where $\bar{x}$ is the sample mean and Δ_x is the uncertainty associated with the mean. Uncertainty is calculated by either one of two methods based on the sample size, as follows:

$$\Delta_x = \pm k(\alpha) \cdot \sigma \text{ for large samples, } n \geq 30 \quad \text{G.9}$$

$$\Delta_x = \pm t(\alpha, n-1) \cdot \sigma_n \text{ for small samples, } n < 30 \quad \text{G.10}$$

With:

- n = sample size
- α = significance level (selected as 0.05 for a 95 % confidence level)
- σ = standard deviation
- $\sigma_n = \sigma/\sqrt{n}$ standard error
- $k(\alpha)$ = standard normal distribution inverse (two-tailed)
- $t(\alpha, n-1)$ = student's t distribution inverse (two-tailed)

Uncertainty propagation from one variable to another is calculated based on the following formulas:

$y = f(x)$ functional relationship

$$\Delta_{\bar{y}}^2 = \left(\left[\frac{dy}{dx} \right]_{\bar{x}} \cdot \Delta_x \right)^2 \qquad \text{G.11}$$

G.2 Error and uncertainty calculations of repeated experiments

To quantify the experimental error of during this project a statistical description of three repeated experiments are provided. The experimental error is defined as the average error plus the calculated uncertainty within the error (equation G.8).

Table G.1: Error calculation of repeated experiments (repeat 1) of series C

Time (min)	X (Ca1) (%)	X (Ca2) (%)	Error	AARD (%)	Statistics Type	Value
0	0	0	0.00	-	Absolute Mean	0.07
5	1.55	1.78	-0.23	14.9	Standard Error	0.66
15	3.44	3.79	-0.35	10.2	Standard Deviation	2.08
30	7.21	7.58	-0.37	5.1	MAE	1.60
60	13.75	15.82	-2.07	15.1	RMSE	1.97
90	20.29	22.95	-2.66	13.1	AARD (%)	9.97
120	26.72	29.42	-2.69	10.1	Uncertainty	1.49
180	34.59	31.87	2.73	7.9	Minimum	-2.69
240	36.70	34.32	2.38	6.5	Maximum	2.73
300	37.92	35.32	2.60	6.9	**Error**	**1.55**

Table G.2: Error calculation of repeated experiments (repeat 2) of series D

Time (min)	X (Dk2) (%)	X (Dr4) (%)	Error	AARD (%)	Statistics Type	Value
0	0	0	0.00	-	Absolute Mean	4.39
5	22.63	14.85	7.79	34.4	Standard Error	1.27
15	35.31	27.16	8.15	23.1	Standard Deviation	3.81
30	46.17	39.83	6.34	13.7	MAE	3.29
60	67.90	57.94	9.96	14.7	RMSE	5.67
120	89.62	85.10	4.53	5.1	AARD (%)	11.72
180	95.05	94.15	0.91	1.0	Uncertainty	2.93
240	96.87	95.96	0.91	0.9	Minimum	0.00
300	98.68	97.77	0.91	0.9	Maximum	9.96
					Error	**7.31**

Table G.3: Error calculation of repeated experiments (repeat 3) of series F

Time (min)	X (Fh1) (%)	X (Fi1) (%)	Error	AARD (%)	Statistics Type	Value
0	0	0	0.00	-	Absolute Mean	1.44
1	3.26	3.26	0.00	0.0	Standard Error	0.63
3	9.93	12.44	-2.52	25.3	Standard Deviation	2.29
5	14.62	20.67	-6.05	41.4	MAE	1.93
7	19.18	22.92	-3.74	19.5	RMSE	2.63
10	26.52	30.87	-4.35	16.4	AARD (%)	9.74
15	35.29	38.42	-3.13	8.9	Uncertainty	1.38
20	43.11	44.00	-0.88	2.1	Minimum	-6.05
30	53.18	53.45	-0.27	0.5	Maximum	1.77
45	64.19	64.19	0.00	0.0	**Error**	**2.83**
60	73.78	73.92	-0.14	0.2		
75	81.05	80.51	0.54	0.7		
90	89.15	87.38	1.77	2.0		

With the experimental error in conversion estimated, propagation of the error to the shrinking core model (SCM) needs to be quantified. Using equation G.11, the uncertainty in the SCM results can be obtained by substitution of the uncertainty in conversion (Δ_X) as well as the absolute mean error ($\bar{e}$) into the differential of the surface reaction shrinking core model differential equation below:

$$\frac{d(k_s t)}{dX} = \frac{1}{3} \cdot \frac{1}{(1-X)^{2/3}} \qquad \text{G.12}$$

Table G.4: Uncertainty propagation and average experimental error calculations

Repeat	Absolute Mean Error		Uncertainty		Differential	Error	
	X (fraction)	SCM	Δ_X (fraction)	Δ_{SCM}	$d(k_s t)/dX$	X (fraction)	SCM
1	0.0007	0.000225	0.0149	0.00495	0.333	0.0155	0.0052
2	0.0439	0.01484	0.0293	0.01006	0.343	0.0731	0.0249
3	0.0144	0.00484	0.0138	0.00466	0.337	0.0283	0.0095
					Average	**0.039**	**0.0132**

Appendix H Feed Particle Properties

H.1 Particle size distribution

The method used to determine the particle size distribution of each of the three feed concentrates and seven screened size fractions is described, as well as presenting the experimental data.

A Malvern MasterSizer 1000 were used to measure particle size distributions. The instrument makes use of a laser diffraction technique. A monochromatic beam of light (Helium-Neon laser) is passed through the measurement cell, and then sample is introduced. Solid particles scatter the light beam and a series of detectors (at different angles) measures the intensity of the scattered light. Every particle of a specific size produces light with unique intensity measure. The intensity is then related by least squares fitting to produce the relative volume distribution of particles sizes in the sample. It is important to note that because particles are never spherical, there is always a discrepancy between the measured size distribution and the distribution obtained from screening through a series of sieves. The laser scattering technique deducts the particle size from the light energy measurement by assuming all particles are spherical, which may give a false impression of the real size. The error is reduced by the size of the population of particles and averaging over a total measurement time. All measurements were repeated twice and excellent reproducibility was obtained. No percentile passing diameter (Dv10, Dv50 and Dv90) differed more than 1% between repeated measurements. The raw data from the size measurements are presented below (Table H.1).

Table H.1: Detailed cumulative volume % (under) for the feed and screened particles

Particle size µm	Fc1 %	Fc2 %	Fc3 %	Sf1 %	Sf2 %	Sf3 %	Sf4 %	Sf5 %	Sf6 %	Sf7 %
1.2	0.15	0.3	-	-	-	-	-	-	-	-
1.32	0.25	0.5	0.1	-	-	-	-	-	-	-
1.46	0.35	0.7	0.1	-	-	-	-	-	-	-
1.61	0.45	0.8	0.1	-	-	-	-	-	-	-
1.78	0.5	0.9	0.1	-	-	-	-	-	-	-
1.97	0.65	0.9	0.15	-	-	-	-	-	-	-
2.17	0.75	0.9	0.2	-	-	-	-	-	-	-
2.39	0.9	0.95	0.2	-	-	-	-	-	-	-
2.64	1.05	0.95	0.25	-	-	-	-	-	-	-
2.92	1.2	1	0.3	-	-	-	-	-	-	-
3.22	1.4	1.05	0.35	-	-	-	-	-	-	-
3.55	1.6	1.05	0.4	-	-	-	-	-	-	-
3.92	1.85	1.15	0.5	-	-	-	-	-	-	-

Table H.1: Detailed cumulative volume % (under) for the feed and screened particles, continue

P. Size µm	Fc1 %	Fc2 %	Fc3 %	Sf1 %	Sf2 %	Sf3 %	Sf4 %	Sf5 %	Sf6 %	Sf7 %
4.33	2.15	1.15	0.55	-	-	-	-	-	-	-
4.77	2.45	1.2	0.65	-	-	-	-	-	-	-
5.27	2.75	1.25	0.85	-	-	-	-	-	-	-
5.82	3.15	1.3	0.95	-	-	-	-	-	-	-
6.42	3.55	1.35	1.25	-	-	-	-	-	-	-
7.08	4.05	1.4	1.55	-	-	-	-	-	-	-
7.82	4.55	1.5	1.9	-	-	-	-	-	-	-
8.63	5.15	1.5	2.4	-	-	-	-	-	-	-
9.52	5.85	1.6	3.1	-	-	-	-	-	-	-
10.5	6.6	1.7	3.95	-	-	-	-	-	-	-
11.6	7.5	1.8	5.1	-	-	-	-	-	-	-
12.8	8.55	2	6.6	-	-	-	-	-	-	-
14.1	9.65	2.2	8.4	-	-	-	-	-	-	-
15.6	11.05	2.5	10.7	-	-	-	-	-	-	-
17.2	12.7	2.9	13.6	-	-	-	-	-	-	-
19	14.55	3.5	17.15	-	-	-	-	-	-	-
21	16.7	4.35	21.15	0.14	-	-	-	-	-	-
23.1	19.1	5.55	25.65	0.46	-	-	-	-	-	-
25.5	21.9	7.15	30.6	1.19	0.1	-	-	-	-	-
28.2	25.05	9.35	36.05	2.88	0.2	-	-	-	-	-
31.1	28.5	12.3	41.7	6.41	1	0.1	-	-	-	-
34.3	32.3	16.15	47.35	13.26	3	0.1	-	-	-	-
37.9	36.45	20.65	53.1	25.01	5.9	1	0.1	-	-	-
41.8	41.05	26.45	58.8	41.02	12.5	3.8	0.2	-	-	-
46.2	45.9	33.3	64.4	59.19	23.1	7.8	1.1	0.1	-	-
50.9	50.85	40.7	69.4	74.79	35.2	16	3.4	0.25	-	-
56.2	55.9	48.4	74	86.35	50.3	29.2	6.7	0.55	0.05	-
62.1	61.05	56.3	78.15	93.40	64.1	45.1	13.9	1.4	0.1	-
68.5	66.05	63.9	81.85	97.03	75	60.7	25.5	3.9	0.45	0.1
75.6	70.75	70.7	84.95	98.73	82.5	73.2	39.2	8.95	1.4	0.3
83.4	75.2	76.65	87.6	99.44	88.6	82	53.7	15.65	2.95	0.5
92.1	79.45	81.95	90	99.70	92.7	88.4	67.6	27.65	6.95	2.2
102	83.3	86.45	92.05	99.79	95.5	93.5	78.5	44	15.2	3.4
112	86.75	90.05	93.75	99.8	97.3	96.5	86.1	60.25	28.15	7.6
124	89.85	93	95.25	99.9	98.4	98.1	92.3	74.75	44.8	15.5
137	92.55	95.3	96.5	99.9	99.2	99.1	96.2	86.35	63.05	29.4
151	94.8	97	97.5	100	99.6	99.7	98.3	93.3	79.15	45.3
166	96.5	98.2	98.3	100	99.9	99.9	99.3	96.6	89.75	64.1
184	97.7	98.9	98.85	100	100	100	99.7	98.9	95.1	79.4
203	98.5	99.35	99.2	100	100	100	99.9	99.75	97.65	90.2
224	99.1	99.6	99.5	100	100	100	100	99.9	99.25	95
247	99.4	99.75	99.65	100	100	100	100	99.95	99.8	98.1
273	99.6	99.85	99.8	100	100	100	100	100	99.9	99.4
301	99.85	99.9	99.8	100	100	100	100	100	99.9	99.9

Appendix I Acknowledgement of Mintek data

Mintek Experimental Data for MSc (modelling) study of Adriaan Henning

Modelling study using experimental non-oxidative & oxidative leaching data generated by JDT Steyl at Mintek (1996-1999)

April 2015

Johann Steyl
PrEng PhD
Post-Graduate Supervisor, Senior Lecturer
Stellenbosch University
johannsteyl@sun.ac.za
0218084053

1. Background & Context

During full-time employment at Mintek, Johann Steyl undertook a part-time MSc study to investigate the atmospheric non-oxidative and oxidative leaching of sphalerite in acidic sulphate solutions. Due to the various pilot plants (incl. the Bindura Project) and other research responsibilities (incl. developing the autoclave facility), time spent on this study was limited to a few weeks per year, usually over the December holidays. Most of the chemical analyses (incl. AA & calorimetric titrations) were conducted by Johann Steyl himself. The 'green money' spent on this project covered the study (WITS registration) fees, autoclave spare parts, chemical reagents and other 'typical' testwork consumables. This study was also used to commission the then new (Bindura) alloy autoclave at Mintek under low temperature (Albion type) leaching conditions, i.e., the opportunity was also used to generate low temperature steady state data for this study. Involvement by the other departments was limited to the Mintek Library (ordering hard-copies, mainly from the British Library), Mineralogy Department (taking SEM images & measuring PSDs) and the Analytical Services Department (analysing leach residues). Before the MSc study was completed, an international research opportunity (incl. Lakefield Research in Canada & Oretest in Australia, now SGS,) was pursued. Since there was no commercial 'angle' to this MSc project, the only requirement was to refund Mintek for the yearly registration fees, as required by the (then) post-graduate study contract. The raw data, albeit of high quality, was never reported or analysed in detail (saved on stiffy discs in QPRO format).

An opportunity has now presented itself to extract value from this data. Mr. Adriaan Henning has recently registered for a full-time MSc study at the Process Engineering Department of Stellenbosch University. The study (student bursary) sponsor is GE Intelligent Platforms (www.ge-ip.com) – they are only interested in the 'human capital' and in utilising the student for 3 months per year to work on-site on non-related projects. They only sponsor the top students and have a long history with the department, i.e., there are no intellectual property or other requirements from GE-IP related to the data or the specifics of the MSc study.

2. Primary study Objective, Scope & Deliverables

The main study objective is to develop a phenomenological leaching model of non-oxidative/oxidative sphalerite leaching based on the above-mentioned experimental data and information from the literature. This will also require detailed understanding of particle surface, solution thermodynamic and reaction engineering principles. Besides the normal Engineering Faculty requirements for obtaining an MSc, the work will be reported in thesis format.

3. Undertaking to acknowledge Mintek

The Process Engineering Department of Stellenbosch University hereby undertakes to formally acknowledge Mintek when reporting the study results in the public domain, i.e., in the thesis itself, in any peer-reviewed journal publications and/or in any conference proceedings and presentations.

Signed: Dr. Johann Steyl

Process Engineering Department, Stellenbosch University 19/04/2015

Acceptance email from Leon Krüger:

From: Leon Kruger <Leonk@mintek.co.za>
Sent: Monday, April 20, 2015 7:50 AM
To: Steyl, JDT, Dr <johannsteyl@sun.ac.za>
Subject: RE: Using experimental data generated at Mintek for SUN MSC study

Dear Johann

Please accept this e-mail as confirmation that Mintek accepts your proposal and authorises you to use the data in the proposed MSc. Study.

Kind regards
Leon

Leon Krüger, Ph.D (Chem.)
Manager: Hydrometallurgy Division
Mintek
leonk@mintek.co.za

Tel: +27 (0)11 709 4656
Cellular: +27 (0)82 573 4934
Fax: +27 (0) 709 4160
Block 6, Level 5 Office No. 6574A
200 Malibongwe Drive, Strijdom Park, Randburg, Gauteng Province, South Africa
Private Bag X3015, Randburg 2125, Gauteng Province, South Africa
Website: www.mintek.co.za/

MINTEK – A global leader in mineral and metallurgical innovation

From: Steyl, JDT, Dr <johannsteyl@sun.ac.za> [mailto:johannsteyl@sun.ac.za]
Sent: 2015 April 19 01:00 PM
To: Leon Kruger
Subject: Using experimental data generated at Mintek for SUN MSC study

Dear Leon

Attached is the 1 pager, as requested.
Please let me know is you want any changes, additions, etc. made to the document.

Regards & thank you!
Johann

Dr. Johann Steyl Pr.Eng.
Senior Lecturer
Departement Prosesingenieurswese
Department of Process Engineering

Tel: +27 21 808 4053
E-pos/E-mail: johannsteyl@sun.ac.za
Universiteit Stellenbosch University
Privaat Sak/Private Bag X1 Matieland 7602
Suid-Afrika/South Africa
www.processengineering.sun.ac.za